UNIVERSITÀ
DEGLI STUDI
DI PADOVA

Sede Amministrativa: Università degli Studi di Padova
DIPARTIMENTO DI FISICA E ASTRONOMIA “GALILEO GALILEI”

CORSO DI DOTTORATO DI RICERCA IN ASTRONOMIA
Ciclo XXXVI

AGN FRACTION AND METALLICITY IN CLUSTERS AND FIELD: THE ROLE OF RAM PRESSURE STRIPPING

Coordinatore:
Prof. Giovanni Carraro
Supervisore:
Dr. Bianca Maria Poggianti
Co-Supervisore:
Dr. Benedetta Vulcani
Co-Supervisore:
Dr. Alessia Moretti
Co-Supervisore:
Dr. Mario Radovich

Dottorando:
Giorgia Peluso

ABSTRACT

The research project presented in this Thesis has been funded by the European Research Council (ERC) under the Horizon 2020 research and innovation program (grant agreement N. 833824) and has been conducted within the framework of the Ph.D. program in Astrophysics in the Padova University.

Active Galactic Nuclei (AGN) are supermassive black holes (SMBHs) accreting gas that emit a great amount of energy over the entire electromagnetic spectrum. A tight connection exists between the active nucleus and the host galaxy, as the activity of the SMBH relies on the gas supply of the galaxy, which in turn is regulated by the AGN feedback throughout outflows and jets able to heat or even remove the gas. AGN activity is one of the many processes involved in the so-called *baryonic cycle*, which broadly speaking is how the gas enters and exits the galaxy disks. Other mechanisms can affect the baryon cycle and some of them depend on the environment in which galaxies reside. In clusters, the largest structures in the universe, the ram-pressure (RP) exerted by the hot plasma filling the intra-cluster medium (ICM) is certainly one of the most efficient processes affecting gas inflows and outflows.

This Thesis aims to probe the interplay between the ram-pressure stripping (RPS) phenomenon and the AGN activity in nearby galaxies through the use of integral field spectroscopy (IFS) and the comparison of the observed data with ionization models. Throughout this dissertation, I present the results obtained by exploiting four large samples of galaxies divided according to the host galaxy's environment (in clusters, showing signs of stripping, or in the field, undisturbed by environmental effects) and on the stage of AGN activity (active or inactive/star-forming (SF) galaxies). In this context, I select RP-stripped galaxies from the Gas Stripping Phenomena (GASP) survey, which targets 114 galaxies with the optical integral field spectrograph MUSE at the VLT and aims at studying the gas removal mechanisms in galaxies in different environments, in the local universe. Also, I select galaxies from the integral field unit Mapping Nearby Galaxies at APO (MaNGA) survey to build a control sample of undisturbed galaxies.

First, I measure the incidence of AGN in clusters and in the field, in order to find for the first time statistical evidence of a link between RPS and the AGN activity. One hypothesis is that the RPS triggers massive gas inflows towards the galaxy centers, which eventually light up or enhance the BH activity. A way to probe this hypothesis is to compare the fraction of AGN in galaxies disturbed and undisturbed by the RPS. This allows me to reveal an enhanced AGN fraction in RP stripped galaxies with respect to undisturbed galaxies located in field.

Second, I present a project focused on the measurement of the gas-phase metallicity in the nuclear regions of galaxies, in order to understand first of all the impact of the AGN on the **global** metallicity of the galaxy, also as a function of the host galaxy's stellar mass and the AGN's luminosity. With this project, I also aim to investigate the role of RPS on the AGN metallicity, since the two phenomena seem to work in synergy to quench star formation (thus, halting the metal production and the consequent ISM enrichment) in galaxies when acting together. I find that the AGN activity is somehow releasing metals into the ISM. Particularly, I observe an enhancement of the metallicity at the centers of AGN hosts, but I conclude that the RPS is not playing a significant role in regulating the metal content in their nuclear regions.

The final part is dedicated to a project aimed at deriving reliable gradients of metallicity by measuring in a **spatially-resolved** and homogeneous way the metallicity of the gas phase in regions ionized by stars, AGN, or a mixing of both. I find that the metal enrichment is actually tracing the impact of the AGN on the host galaxy since the enhanchment is limited to the nuclear regions, while H II regions in the galactic disk of SF and AGN galaxies are equally more metal-poor with respect to the centers.

Overall, this Thesis demonstrates the power of multi-wavelength IFS studies to explore the impact of the environment on the properties of local galaxies. The use of large IFS programs, such as the GASP and MaNGA surveys, allowed me to study in a statistically robust way the interplay between RPS and AGN activity by comparing the galaxies properties, disturbed or not by the RPS, both in a global and spatially-resolved way. The results obtained represent a unique test bench for the new generation of photoionisation models given both the capability of the HII models to reproduce even the strongest emission of the forbidden lines observed in HII regions and the ability to measure the gas metallicity with an homogeneous method in case of different ionization sources, thanks to the consistent assumptions made to generate the AGN and HII models.

CONTENTS

List of Figures

List of Tables

1

INTRODUCTION

A huge variety of processes can drive the evolution of a galaxy by altering the baryonic content of the disk. These processes, that cause the gas to flow in and out of galaxies providing the fuel both for star formation (SF) and black hole (BH) accretion, are known as the galaxy baryon cycle. Their origin can be internal to the galaxies, such as galactic winds due to SF or an active galactic nucleus (AGN, Veilleux et al., 2005; King & Pounds, 2015) or external, such as ram pressure stripping (RPS), thermal evaporation (Boselli et al., 2006) affecting the gas or tidal mechanisms (Barnes et al., 2015) affecting both gas and stars. Particularly, the presence of a powerful AGN influences the properties of the interstellar medium (ISM) by heating, compressing and/or removing the gas through AGN-driven gas outflows in the vicinity of the supermassive BH (SMBH).

More than that, several physical processes have been proposed as "feeding mechanisms" able to trigger the AGN activity. The availability of gas, or lack thereof, is an essential ingredient for feeding the black hole, and mechanisms affecting the gas are also believed to influence the AGN (e.g. Maier et al., 2019). Given that the gas content of galaxies is especially sensitive to environmental effects, AGN studies as a function of environment are of interest, though they often find contrasting results (Miller et al., 2003; Kauffmann et al., 2004; Martini et al., 2007; Popesso & Biviano, 2006; Von der Linden et al., 2010; Marziani et al., 2017).

This Chapter aims at providing a brief description of the main ISM properties, surrounding the SMBH, after being ionized and/or heated by the AGN radiation (Section 1.1.1). Furthermore, it gives a broad view of the current knowledge on the incidence of AGN as a function of the environment (Section 1.1.2), and a summary of all those processes which are mostly impacting the disk composition and causing gas instabilities necessary for the AGN feeding, when the galaxy passes from the field to the cluster environment (Section 1.1.3). It also provides a brief review of those processes linked to the cluster environment that are considered candidates (i.e. major mergers, chaotic cold gas accretion, RPS) for the SMBH feeding in galaxies, according to the predictions by simulations and detections in observations. Finally, it provides a comprehensive dissertation about the methods used to derive the AGN chemical compositions (e.g., temperature-sensitive auroral lines, photo-ionization models) and concludes with an overview of the state-of-the-art of integral field spectroscopy (IFS), underlying its importance in modern astrophysics.

1.1 Interplay between SMBH activity and environmental mechanisms

1.1.1 Unified Model of AGN

An AGN is a supermassive black hole (SMBH), located at the galaxy center, accreting gas in its vicinity and photoionizing the surrounding medium in a wide range of radii, ionization states, gas densities and velocities (Hickox & Alexander, 2018). The SMBH is located beyond the so-called 'event horizon', which is defined as the radius where a particle needs to move as fast as the speed of light (c) in order to escape from the gravitational field (also called Schwarzschild or gravitational radius, $R_G = 2GM_{\mathrm{BH}}/c^2$, Beckmann & Shrader, 2012, where G is the gravitational constant and M_{BH} is the BH mass). Around the SMBH, the gas forms a thin accretion disk by spiraling inward on scales down to a few gravitational radii, losing angular momentum and a considerable fraction of its gravitational energy. The high temperature (T> 10^4 K) reached by the gas in the accretion disk, due to heating from friction, accounts for the continuum emission observed from optical through soft X-ray. SMBH masses typically range between 10^5 to 10^{10} $M_\odot$, as deduced by the motion of the accreted mass buried in the SMBH's gravitational field. One parameter used to quantify how efficiently the mass is accreted by the SMBH is the ratio between the bolometric luminosity and the Eddington luminosity, the so-called *Eddington ratio* ($\lambda_{edd} = L_{bol}/L_{EDD}$), where L_{EDD} is defined as the luminosity at which the radiation pressure by the accretion of the infalling plasma balances the gravitational attraction of the black hole.

The gas at distances below 1 pc from the central source, which is ionized by the radiation arising from the accretion disk, is characterized by high densities ($n_e \approx 10^9 - 10^{10}\mathrm{cm}^{-3}$), high temperature ($\sim 10^4$ K) and high velocity dispersions ($\sigma \sim 2000$ km/s). Thus, the permitted lines emitted by the gas are very broad (full width at half maximum FWHM $\approx 10^3 - 10^4$ km/s), and this region is typically called broad-line region (BLR). The electron density is high enough to collisionally de-excite forbidden lines.

In the favored picture for the physical structure of AGN (termed the “unified model” of AGN; e.g. Antonucci et al., 1993), the accretion disk is surrounded by an optically thick dusty and molecular “torus”. The torus is expected to be within the gravitational influence of the SMBH and could be considered, in a broad sense, the cool outer regions of the accretion disk where molecules and dust grains can form. The torus emits the reprocessed radiation in the IR band, while it appears to be opaque at all the other wavelengths, obscuring the central source along the line of sight.

Further away, the gas reaches a lower temperature and emits narrower lines (with a FWHM $\approx 10^2$ km/s), in the so-called Narrow Line Region (NLR) where the electron density is sufficiently low ($\sim 10^4$ cm^{-3}) to allow the presence of forbidden lines. The growth of SMBHs can also release an enormous amount of energy capable of launching highly collimated jets.

Finally, a hot rarefied gas ($T \sim 10^8$ - 10^9 K), located at ~ 3 - 10 R_G above the disc, constitutes the so-called hot corona. In this region, the soft thermal photons produced by the disc are scattered to X-ray via inverse Compton.

Figure 1.1, taken from Hickox & Alexander (2018), shows a scheme of the AGN physical model.

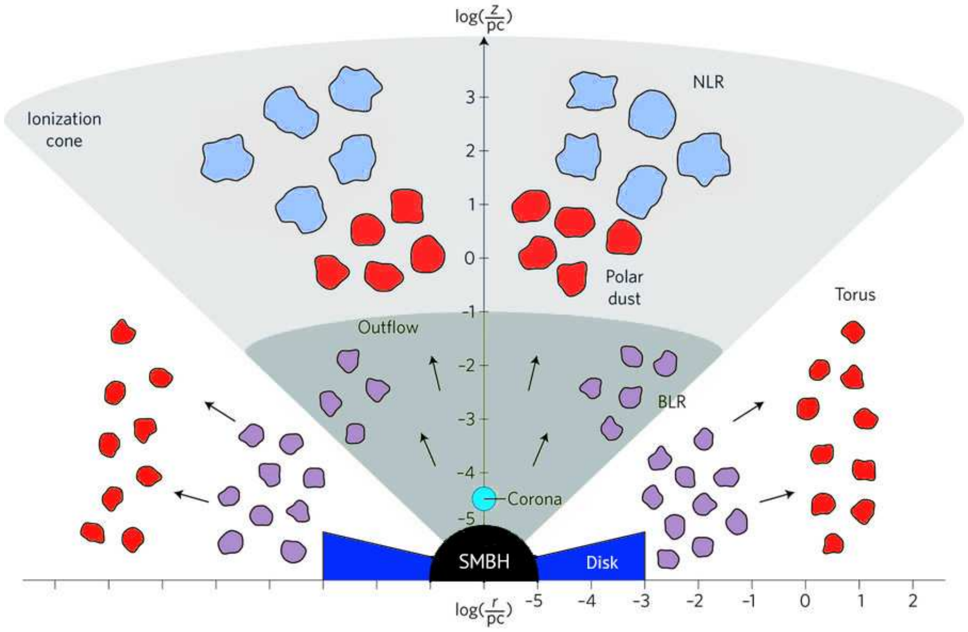

Figure 1.1: Scheme of the AGN physical model. The accretion disc, corona, BLR and dusty torus are within the gravitational influence of the SMBH, while the NLR extends on large scales and is under the gravitational influence of the host galaxy (Hickox & Alexander, 2018).

According to the Unified Model, the different classes of known AGN differentiate from each other depending on the inclination of the torus of dust, inside which the BLR and the accretion disk are located, with respect to the line of sight. More than that, Padovani (1997) introduces a further distinction between jetted and non-jetted sources. Among the non-jetted AGN, I will consider in this Thesis the LINER (Low Ionization Nuclear Emitting Region), Seyfert 1 (or Sy1) and Seyfert s (or Sy2) classes, for which I give a brief description of the main spectral features:

- **Seyfert 1** emit optical spectra characterized by narrow forbidden lines, such as [O III]λ5007 [O I]λ6300 and [N II]λ6583, and broad permitted lines emitted by abundant elements such as hydrogen (e.g., Hα, Hβ) and helium (e.g., He II λ4686). The emission of this source is consistent with an unobscured AGN, which is the case when the torus of dust is not blocking the emission coming from the BLR and the accretion disk. As a result, both broad and narrow lines are visible since they are emitted by the gas in the BLR and NLR, respectively;

- **Seyfert 2** present only the narrow lines, both forbidden and permitted, emitted by the gas in the NLR, while the BLR is obscured;

- **LINERs** (Low Ionization Nuclear Emitting Region) are characterized by an accretion disk with a lower luminosity than Seyfert galaxies. A lower luminous accretion disk is also used to explain the lower ionization parameter impacting the surrounding gas of the BLR and NLR. The most intense emission lines are broaden of $\sim 200 - 400$ km/s (Blandford et al., 1990).

1.1.2 AGN incidence in different environments

It is still debated if factors such as a dense galaxy environment or galaxy clusters (e.g. Pimbblet et al., 2013) have an impact on the presence of AGN in galaxies, where a cluster is defined as a structure of galaxies bound together by gravity with masses above 10^{14} $M_{\odot}$. Despite the vast literature on this topic (e.g. Kauffmann et al., 2004; Best et al., 2007; Silverman et al., 2009; Von der Linden et al., 2010; Hwang et al., 2012; Sabater et al., 2013; Martini et al., 2013; Ehlert et al., 2014; Silverman & David, 2015; Coldwell et al., 2017; Lopes et al., 2017; Marziani et al., 2017; Gordon et al., 2018; Magliocchetti et al., 2018; Koulouridis et al., 2018; Argudo-Fernández et al., 2018), different studies have reached quite opposite results, most likely due to the different techniques adopted to identify AGNs, select the samples and characterise the environment.

Using a spectroscopic sample, Dressler et al. (1985) first suggested that the fraction of AGN in clusters ($\sim 1\%$) is significantly lower than in the field (~5%). Similarly, Lopes et al. (2017), identifying AGN in the Sloan Digital Sky Survey (SDSS) using optical emission lines and Baldwin, Philips & Terlevich (BPT, Baldwin et al., 1981) diagrams, found that AGN favor environments typical of the field, low mass groups or cluster outskirts. It is interesting, however, the comparison between Figure 4 in Pimbblet et al. (2013) and Figure 4 in Lopes et al. (2017). In both these works, as shown in Figure 1.2, the AGN fraction increases as a function of the cluster-centric distance, peaking at 1.5 $\mathrm{R_v}$ (i.e. 1.5 times the virial radius) to finally drop again at $\sim 2-3$ $\mathrm{R_v}$, reaching an AGN fraction in field of $f_{AGN} \sim 0.11$. However, Lopes et al. (2017) consider only Seyfert galaxies and find their fraction in clusters to be lower than in the field. While Pimbblet et al. (2013) consider Seyfert and LINER-like nuclei, finding higher values than Lopes et al. (2017) in cluster at all radii and an AGN fraction within 1.5 R_v comparable to that at 2.0–3.0 R_v (AGN fractions of 0.11 ± 0.02 and 0.11 ± 0.03, respectively). This result shows how conclusions can vary depending on the classification criteria adopted among different works. Another interesting aspect is that the trend of the AGN fraction in cluster is qualitatively the same in both these works (even though quantitatively numbers change due to the different classification criteria adopted) and shows that the AGN fraction peaks in the cluster outskirt at distances where the effects of environmental processes are typically the most intense. Finally, the AGN fraction in the outer part of the cluster measured by Pimbblet et al. (2013)

Von der Linden et al. (2010) show that the fraction of powerful ($\mathrm{L_{[OIII]}} \geq 10^7$erg/s) AGN hosted by late-type (LT) galaxies does not change as a function of environment, nor of clustercentric distance. Similar conclusions were obtained by Martini et al. (2007), Lehmer et al. (2007), Sivakoff et al. (2008), Arnold et al. (2009), exploiting X-ray data. Hwang et al. (2012), considering also composite (i.e. AGN+stars emission in their centers) galaxies to compute the fractions, find that the value for the LTs starts to

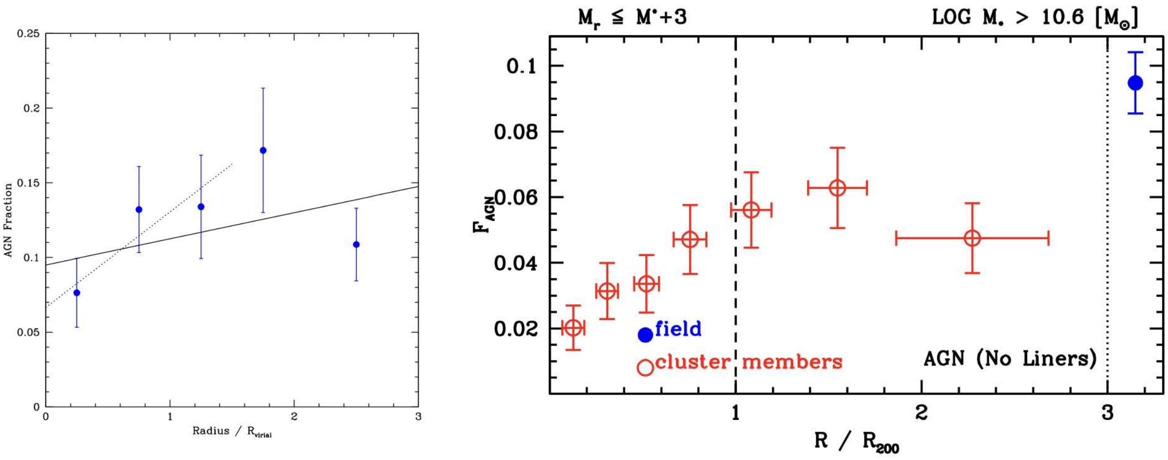

Figure 1.2: AGN fraction as a function of distance from Pimbblet et al. (2013) (left) and Lopes et al. (2017) (right). Distances are expressed in units of virial radius (R_{vir}) of the clusters, and the field outside the cluster environment is measured between 2.0 and 3.0 R_{vir}. Pimbblet et al. (2013) consider six SDSS galaxy clusters in the redshift range 0.070 < z < 0.084, selected according to the Abell (1958)'s criteria. Lopes et al. (2017) consider 6415 galaxies belonging to 152 groups and clusters from the Northern Sky Optical Cluster Survey (NoSOCS Gal et al., 2003) and 4676 selected as field galaxies at $z < 0.1$. Lopes et al. (2017) consider only Seyfert galaxies, classified according to BPT diagrams, while Pimbblet et al. (2013) include also LINER-like sources.

decrease close to the cluster center (0.1-0.5 R_v), but they also show that the *mean* AGN fractions of late-type cluster galaxies are similar to those of late-type field galaxies. On the contrary, the AGN fractions among early-type cluster galaxies, on average, are found to be lower than those of early-type field galaxies by a factor ∼ 3.

Yet, the radio AGN fraction seems to be much higher in clusters than in the field (Sabater et al., 2013; Best et al., 2007). Moreover, Sabater et al. (2013) found that (at fixed mass) the incidence of optical AGN is a factor of 2-3 lower in the densest environments (see also Man et al., 2019), but increases by a factor of ∼2 in the presence of strong one-to-one interactions.

To conclude, the expected connection between AGN incidence and the environment has roots in the fact that the characteristics of AGN are strongly linked to the conditions of the available gas, which in turn can be affected by the galaxy environment by a plethora of processes, which are briefly reviewed in the following Section 1.1.3.

1.1.3 Environmental processes affecting galaxies in clusters

Galaxies falling onto clusters change dramatically their properties, due to a wide variety of mechanisms. These can be divided into two main categories: gravitational or tidal interactions and hydrodynamical (gas-gas) interactions. Tidal interactions affect both the gas and stars distribution and consist in interactions with the cluster as a whole (cluster-galaxy tidal interaction e.g., Merritt et al., 1984; Miller, 1986; Byrd et al., 1990; Valluri, 1993, 1994) or in high-speed encounters with other cluster members in the so-called "galaxy harassment" (galaxy-galaxy tidal interaction e.g., Moore et al., 1996, 1997; Mastropietro et al., 2005; Bialas et al., 2015). According to Merritt et al. (1984), the morphology of galaxies in clusters is mainly fixed during cluster collapse and change little afterward. Moore et al. (1996), on the other hand, showed with their simulations how low-mass spirals transform into spheroidal galaxies after a series of fast and at high-speed encounters with other cluster members. Mergers between galaxies are more common in the group environment than in clusters, due to the large relative velocities in the most massive haloes.

Other mechanisms affect only the gas component. Cooling of gas and consequent gas inflows towards the galactic plane can be stopped by the removal of the gas halo envelope in the so-called strangulation (or starvation) scenario (e.g., Larson et al., 1980; Bekki et al., 2002; Van Den Bosch et al., 2008; Peng et al., 2015). Larson et al. (1980) show how in this way spirals transition into S0 galaxies, consuming their gas reservoir into stars without being replenished by infall from the halo. Star-formation can be reduced significantly within ~ 5 Gyrs from the removal of the hot halo, with the additional help of SN feedback and AGN-driven outflows. Starvation becomes more important around 3 - 4 R_{200} (Boselli et al., 2014), when galaxies become satellites of larger structures. However, since the effect is mild and requires long timescales, it soon becomes not important when other, more efficient mechanisms are at work. Thermal evaporation (Cowie & Songaila,

1977) acts on relatively shorter timescales ($\sim 10^8$-10^9 yrs in clusters with masses around 10^{14}-10^{15} $M_\odot$) when high-temperature (about 100 million K) intergalactic gas interacts with cooler halo gas within galaxies and extragalactic clouds.

All these processes, however, cannot affect the gas in the galaxy disk. The interaction between the interstellar medium (ISM) and the intra-cluster medium (ICM) can instead directly affect the disk gas by stripping. The main mechanisms causing the stripping are:

- Ram-pressure stripping (RPS) exerted by the hot ICM on the colder ISM (Gunn et al., 1972). The ICM pressure can be expressed as p = $\rho_{ICM} v_\perp^2$, where $v_\perp$ is the component perpendicular to the galactic disk of the galaxy's velocity relative to the ICM and ρ_{ICM} is radial density profile of the ICM. The gas is removed if $\rho_{ICM} v_\perp > 2\pi G \Sigma_* \Sigma_{gas}$, where Σ_* and Σ_{gas} are the density profiles of the stars and the gas components, respectively and the second term is the anchoring force of a disk galaxy;
- Kelvin-Helmholtz instability (Livio et al., 1980) which is developed at the interface between the moving galaxy, due to the velocity difference between the two fluids (e.g., ISM and ICM);
- Viscous stripping (Nulsen et al., 1982) can also strip the gas at a rate that can exceed that due to pressure alone.

Finally, the remaining gas disk can be affected by the Rayleigh-Taylor instability (Roediger & Hensler, 2008), which occurs when a denser fluid is accelerated by a lighter one, e.g. when a dense gas cloud moves through a wind of rarefied gas. A gas cloud is expected to be destroyed by the RT instability, and subsequent Kelvin-Helmholtz instability, unless stabilising mechanisms take place such as (self-)gravity, surface tension, magnetic fields (Chandrasekhar & Subrahmanyan, 1961), or heat conduction (Vieser & Hensler, 2007). In the latter case, finger-like structures at the leading edge of the gas disk can form.

Two observable characteristics of galaxies experiencing RPS are a gaseous truncated disk (due to the fact that RP stripping proceeds outside-in in the disk) and the formation of tails of stripped gas emitting at different wavelengths (radio continuum, Hα, HI, CO). HI and CO trace the neutral and molecular gas distribution, respectively, while the UV and Hα are tracers for the star-formation acting on different timescales (see Boselli et al., 2022, for a review).

In this Thesis, I will mainly focus on the RPS phenomenon and its effects on the surviving gas in the disk.

1.2 Feeding processes of SMBHs

Both theoretical and observational studies concur on the fact that there is a strong connection between the presence of an AGN and the host galaxy properties (see Kormendy et al., 2013, and references therein), suggesting that internal processes might regulate the AGN activity and, conversely, the AGN activity might be relevant for shaping galaxy properties. AGN are preferentially found in more massive galaxies ($M_* > 10^9 M_\odot$, see e.g. Juneau et al., 2011; Sabater et al., 2013; Lopes et al., 2017; Pimbblet et al., 2013; Kauffmann et al., 2003; Sánchez et al., 2018) and the mass of the host galaxy is the main parameter driving the level of AGN activity (Magliocchetti et al., 2020). Many studies have attempted to detect and characterize inflows of gas in the very inner regions of galaxies (see Storchi-Bergmann & Schnorr-Müller, 2019, for a review). In particular, with the AGNIFS project it was possible to detect and map such gas inflows by studying the inner few hundred parsecs of a sample of 20 local Seyfert galaxies by using Gemini Near-Infrared Integral Field Spectrograph (NIFS) adaptive optics. In this section, I am going to talk about the main processes advocated to push such gas inflows, thus feeding SMBHs with a special focus on those more connected to the galaxy environment.

1.2.1 Major Mergers

Theoretical studies suggest that the violent disturbances induced by major mergers are the main drivers of massive inflows of gas towards the galaxy center at high BH masses (e.g., $M_{\mathrm{BH}} \geq 10^8 M_\odot$, Menci et al., 2014; Hopkins et al., 2014; Gatti et al., 2015), which, in turn, trigger bursts of star formation in the galaxy circumnuclear regions. Part of the gas pushed by the subsequent supernovae (SN) explosions is able to fuel the SMBH.

Observationally, Treister et al. (2012) find that the fraction of AGN hosts showing signs of mergers increases with the AGN bolometric luminosity (see also e.g., Urrutia et al., 2008; Glikman et al., 2012, 2015; Fan et al., 2016), across a wide range of bolometric luminosities ($10^{43} \leq L_{\mathrm{bol}}(erg/s) \leq 5 \times 10^{46}$). This trend is independent of the redshift, across a range $0 < z < 3$. This means that only the most luminous AGN phases seem to be connected to major mergers, while less luminous AGNs appear to be driven by secular processes. In support of this, Araujo et al. (2023) find that nuclear activity in type 2 QSO host galaxies (QSO 2) is triggered by close galaxy interactions, by investigating the role of the close environment on the nuclear activity of a sample of 436 nearby (z < 0.3) QSO 2's (selected from SDSS-III spectra) and a control sample of 1308 galaxies. In the case of lower luminous ($L_{\mathrm{AGN}} \leq 10^{44}$ erg/s) Seyferts, a number of studies also found a higher incidence of AGN in galaxies with signatures of interaction with respect to a control sample of undisturbed galaxies (e.g., Koss et al., 2010; Hernández-Toledo et al., 2023). Hernández-Toledo et al. (2023) find a statistically significant higher incidence of major mergers in an optical AGN sample compared to a non-AGN sample matched in redshift, stellar mass, colour, and morphological type.

Nevertheless, other studies also find the opposite result, that is a fraction of mergers in AGN hosts equal to the fraction of mergers in a sample of non-AGN (e.g., Böhm et al., 2013; Gabor et al., 2009; Grogin et al., 2005; Cisternas et al., 2011; Kocevski et al., 2012; Villforth et al., 2014; Karouzos et al., 2013; Mechtley et al., 2016; Villforth et al., 2017). Among the reasons for this discrepancy, selection effects can play a role since the fractions are computed by selecting AGN in different wavebands, going from the X-rays to the optical or radio (Padovani et al., 2017). Another possible explanation of this consists in the fact that the merger, other than activating the BH, cause also the obscuration of the central regions of interacting galaxies, which thus make the AGN undetectable from the optical. This is shown, for example, in the work presented by Satyapal et al. (2014) for a sample of galaxy pairs and post-mergers, observed both in the optical and IR bands, which show a factor of 10-20 excess in the AGN fraction compared with the control sample. In the same work, it is also shown that the excess in the post-mergers increases much more dramatically for mid-infrared-selected AGN than for optical AGN. These results suggest that optically obscured AGNs become more prevalent in the most advanced mergers, consistent with theoretical predictions.

1.2.2 Chaotic Cold Accretion (CCA)

According to the Chaotic Cold Accretion (CCA) theory (Gaspari et al., 2013, 2015; Gaspari, 2016, 2017), the hot intergalactic medium (IGM) in galaxy clusters cools down into warm filaments and cold clouds rain towards the inner region chaotically accreted via inelastic collisions. Several observational findings indicate this process as being the fueling mode of the most massive SMBHs in the near universe, hosted by classical bulges, usually in the brightest central galaxies (BCGs) of rich galaxy clusters.

Temi et al. (2018) show CO (2-1) ALMA observations of three group-centered elliptical galaxies revealing the presence of a non-diffuse component of molecular gas, consistent with a scenario of hot gas cooling accretion. The central galaxy of the Perseus cluster, NGC 1275, hosting the radio-loud AGN 3C 84 (Perseus A), shows kpc-sized cold gas filaments with ALMA, resulting from jet-induced cooling of cluster gas that are flowing towards the galaxy centre and feeding the circumnuclear accretion disc (100 pc diameter) of the SMBH (Oosterloo et al., 2023). For this galaxy, warm filaments of ionized gas emitting in Hα have also been detected with HST (see Figure 1.3 Fabian et al., 2008). Similar inflows traced by Hα filaments falling into the nucleus of the elliptical galaxy NGC5044 are shown in Diniz et al. (2017).

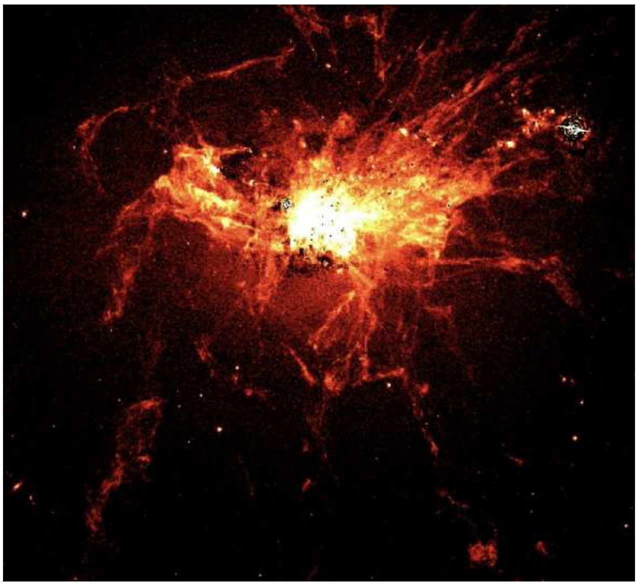

Figure 1.3: Image of the Hα emission from the core of the Perseus cluster (Fabian et al., 2008), showing complex filamentary structures. The image was created by subtracting a scaled green image from the red image, removing the smooth galactic continuum, using the following HST/ACS filters: F625W in the red, which contains the Hα line; F550M which is mostly continuum; F435W in the blue which highlights young stars.

1.2.3 Ram-Pressure Stripping

As introduced before, the RPS phenomenon is the interaction between the interstellar medium (ISM) with the intra-cluster medium (ICM) which is able to produce many visible effects on the galaxy, such as altering its less bound gas, giving rise to wakes of stripped material departing from the main galaxy body (e.g., Kenney et al., 2004; Poggianti et al., 2017a; Fumagalli et al., 2014) and inducing a quenching of star formation (Vollmer et al., 2001; Tonnesen et al., 2007; **?**). Prior to complete gas removal, it has been observed that ram pressure can also increase the star formation rate in galaxies (Crowl & Kenney, 2006; Merluzzi et al., 2013; Vulcani et al., 2018, 2020, 2023) and simulations support this finding (Kronberger et al., 2008; Kapferer et al., 2009; Tonnesen et al., 2009; Bekki, 2013), suggesting that the increased pressure initially helps compressing the gas and triggering star formation. The same mechanism that initially promotes star formation can also fuel the AGN during the RPS process: gas can be funnelled towards the galaxy centres, due to local pressure torques and the loosing of angular momentum of the gas spiraling towards the center (Schulz & Struck, 2001; Tonnesen et al., 2009; Ramos-Martínez et al., 2018; Akerman et al., 2023). The funneling of gas towards the galaxy center can also ignite the central SMBH. Theoretical models (Tonnesen et al., 2009) have indeed demonstrated that gas inflows can fuel the central AGN in ram-pressure stripped galaxies, possibly also aided by the presence of magnetic fields (Ramos-Martínez et al., 2018). The enhanced accretion onto the black hole can then produce heating and outflows due to AGN feedback (Ricarte et al., 2020).

The scenario of RPS feeding BH's activity has been first proposed by Poggianti et al. (2017b, hereafter P17b), to explain the very high incidence (6/7) of AGN detected in a sample of galaxies strongly affected by RPS (i.e. jellyfish galaxies). That analysis is based on Integral Field spectroscopic data coming from the GAs stripping Phenomena in galaxies (GASP, Poggianti et al., 2017a). According to this idea, RPS might be simultaneously responsible for an enhanced AGN activity and the appearance of tails of stripped material. In this Thesis, I will present statistical and observation evidence in support of this hypothesis.

1.3 Gas-phase metallicity of local AGN

The chemical evolution of a galaxy is regulated by a plethora of processes, from stellar winds and supernovae explosions within the galaxy body (e.g., Larson, 1974; Larson & Dinerstein, 1975; Maiolino & Mannucci, 2019, for a review) to the exchange of material with its environment (e.g., Ellison et al., 2009; Peng & Maiolino, 2014). The global gas-phase metallicity is well-known to be strongly correlated with the assembled stellar mass of a galaxy (e.g., Lequeux et al., 1979) through the so-called mass-metallicity relation (MZR) which has been shown to hold from low z (e.g., Tremonti et al., 2004; Pérez-Montero et al., 2013) to high z (up to $z \sim 6.5$ based on recent JWST measurements, Shapley et al., 2023; Curti et al., 2023a,b). At a given stellar mass, Mannucci et al. (2010)

found for the first time an anti-correlation between the star-formation rate (SFR) and the metallicity (at fixed stellar mass) which is the so-called Fundamental MZR (FMZR), while Peng & Maiolino (2014) find that satellite galaxies in denser environments, in terms of local density, are more metal-rich than galaxies in lower-density environments. In addition to stellar evolution and environmental effects, also the presence of a central AGN potentially can have an impact on the galaxy metallicity. In the following, I am going to present the main techniques used to measure the metallicity in case of ionization from an AGN, the main findings obtained using these measurements in the different regions around SMBHs, focusing on the results at low redshifts, and the expected link between the metallicity of AGN hosts and the galaxy environment.

1.3.1 Metallicitiy estimates in AGN-ionized regions

The global gas-phase metallicity (Z) is defined as the ratio of all metals' mass[1] over the baryon mass, dominated by hydrogen and helium. Since oxygen is the most abundant among the metals [2], the oxygen abundance indicated as 12 + log(O/H) is commonly used as a proxy of Z. The abundance of a given element is generally estimated using the emission-line fluxes emitted by the ions of that element. Once the temperature and the gas pressure (or, equivalently, the gas density) are known, the observed strength of a line gives information on the total number of ions in the nebula responsible for the emission of that line (Osterbrock, 2006).

There are two main techniques generally used to derive the element abundances:

- **Direct method**: this method infers directly the metallicity from the gas temperature (T_e), thanks to the use of line ratios sensitive to T_e. These two quantities are connected since metals are efficient coolants of the gas mainly due to collisions between free electrons and ions that cause the formation of forbidden lines. T_e can be estimated by comparing the flux of auroral lines to the flux of nebular lines

---

[1] A metal is every element heavier than hydrogen and helium.

[2] The oxygen is ~ 48 per cent by number at solar metallicity, followed by carbon and nitrogen that are respectively ~ 26 and ~ 6 per cent by number (Gutkin et al. 2016).

from the same species, such as the most used one involving the oxygen lines:

$$R_{[OIII]} = \frac{I_{4959} + I_{5007}}{I_{4363}} = \frac{7.73 \times e^{\frac{3.29 \cdot 10^4}{T_e}}}{1 + 4.5 \cdot 10^{-4} \frac{N_e}{\sqrt{T_e}}} \tag{1.1}$$

A list of emission line ratios used to estimate the electron temperaure follows: [O II] (λ3726 + λ3729)/(λ7320 + λ7330), [Ne III] (λ3869 + λ3969)/λ3342,[O III] (λ4959 + λ5007)/λ4363, [O I] (λ6300 + λ6363)/λ5577, [N II] (λ6548 + λ6583)/λ5755, [S II] (λ6716+λ6731)/(λ4068+λ4076), [Ar III] (λ7136+λ7751)/λ5192, [S III] (λ9069 + λ9532)/λ6312.

- **Indirect method** An indirect way to estimate the ISM chemical abundance stems from the calibration of ratios of strong emission lines (SEL), that are bright typically forbidden lines, and Balmer lines. Calibrations can be extrapolated from measurements of metallicity derived with the direct method (e.g., Pettini & Pagel, 2004; Flury & Moran, 2020, for H ii and AGN ionized regions, respectively), which however relies on the detection of auroral lines, that are typically faint for higher metallicities. Alternatively, calibrations can be inferred theoretically, estimating the oxygen abundance via photoionisation models (e.g. Dopita et al., 2013; Storchi-Bergmann et al., 1998; Castro et al., 2017; Carvalho et al., 2020, for H ii and AGN ionized regions, respectively). Photoionisation codes, such as CLOUDY (e.g. Ferland et al., 2017) and MAPPINGS (e.g., Dopita et al., 2013) generate grids of models out of which line ratios can be extracted and proposed as metallicity diagnostics (Gutkin et al., 2016; Feltre et al., 2016). Typically, chemical abundances scale proportionally to solar, except for nitrogen that shows a secondary origin. In particular, nitrogen is assumed to be a secondary nucleosynthesis element above metallicities of 0.23 solar ((Z/H)>0.23 (Z/H)$_\odot$ Dopita et al., 2000), but as a primary nucleosynthesis element at lower metallicities.

Chemical abundance estimates in gas nebula ionized by hot, young stars abound. On the contrary, there is very little literature concerning the chemical abundances of the gas surrounding AGNs. Metallicity determinations of the BLR and NLR have mostly relied on photoionization models (e.g., Nagao et al., 2006), although attempts have been made to use the direct-T$_e$ method (Dors et al., 2015), which unfortunately have revealed the inadequacy of this method for AGNs. In any case, despite the fact that AGN have high ionization degree, their typically high (e.g., Groves et al., 2006) metallicity leads to faint auroral lines (such as the [OIII] λ4363), hampering the use of the T_e-method. Many SEL calibrations for the NLR have been computed in the last decades in the literature, derived either with photoionization models (e.g., Carvalho et al., 2020; Storchi-Bergmann et al., 1998) or with the direct method (Flury & Moran, 2020; Dors et al., 2021). However, calibrators obtained from the same set of measurements (either direct or indirect) in case of ionization from star formation and AGN are still not available in the literature. Some works (e.g., Thomas et al., 2019; Pérez-Díaz et al., 2021) have developed consistent AGN and stellar photoionization models and used them to determine the metallicity in both star-forming (SF) and AGN-ionized regions. Observed and predicted line ratios are compared making use of the Bayesian inference with codes such as NEBULABAYES (Thomas et al., 2018a) or H II-CHI-MISTRY (Pérez-Montero, 2014; Pérez-Montero et al., 2019).

1.3.2 BLR metallicity

A general finding is that the metallicity of the BLR in quasars is very high, nearly always supersolar and up to several times solar (e.g., Hamann & Ferland, 1999; Dietrich et al., 2003; Nagao et al., 2006; Simon & Hamann, 2010; Matsuoka et al., 2010; Wang et al., 2012; Xu et al., 2018). Matsuoka et al. (2010) and Xu et al. (2018) also find a relationship between BLR metallicity and BH mass, which is thus expected to translate into a relationship between the BLR metallicity and the host galaxy stellar mass, due to the well-known BH mass - host galaxy stellar mass relation (Reines & Volonteri, 2015). High nuclear metallicities (a few/several times solar) are confirmed by the iron emission and absorption features observed in the X-ray emission coming from the nuclear region (e.g., Jiang et al., 2018). Such high metallicities in the nuclear region of AGN are not really unexpected. Among the mechanisms that can explain this, there are star formation with a top-heavy IMF in the accretion disk (e.g., Nayakshin & Sunyaev, 2005; Collin & Zahn, 2008; Bartko et al., 2010) and tidal disruption events, which may be more frequent in active nuclei (Karas et al., 2012) and may cause “tidal detonation” of stars (e.g., Carter et al., 1982; Bicknell et al., 1983; Alexander, 2005). Top-heavy IMF star-formation in the accretion disk seems to be the most likely scenario to explain the emission from the young stars orbiting around Sgr A*, the SMBH at the center of the Milky Way. By studying a few dozen young high-mass stars, orbiting around Sgr A* at distances as short as ~0.1 pc, Nayakshin & Sunyaev (2005) attempted to constrain two different scenarios of formation via the expected X-ray emission using Chandra observations. The presence of young stellar populations is explained in one of two ways: (i) by very massive star clusters at several tens of parsecs, characterized by ‘normal’ star formation, which then spiraled in; or (ii) by *in situ* star formation in a massive self-gravitating disc. In this study, they conclude that the young stars in the Galactic Centre are the first solid observational evidence for star formation in AGN discs and also require the IMF of these stars to be top-heavy. Later on, Bartko et al. (2010) confirm these results, finding a large number of Wolf Rayet (WR), O-, and B-stars in two strongly warped disks close to Sgr A*, as well as a central compact concentration (the S-star cluster) centered on Sgr A*. The stellar mass function of the disk stars is extremely top heavy and WR/O-stars were formed in situ in a single star formation event ~ 6 Myr ago. Thus, this mass function reflects the initial mass function. On the other side, Karas et al. (2012) investigated the idea that a self-gravitating accretion disc around a SMBH increases the rate of gradual orbital decay of stellar trajectories (and hence tidal disruption events), by setting some stars on eccentric trajectories. They find that the cooperation between the gravitational field of the disc and the dissipative environment can provide a mechanism explaining the origin of stars that become bound tightly to the central black hole. Then, stars undergo a tidal disruption event as they plunge below the tidal radius of the SMBH.

1.3.3 NLR metallicity

Other studies focused on the metallicity of the NLR, i.e., which extends out to much larger galactic scales in AGN hosts. In this case studies have generally focused on type 2 AGNs, in which the BLR (whose strong, broad lines would otherwise prevent a proper disentangling of the flux of the narrow lines) is obscured along the line of sight. Studies have both exploited optical narrow nebular lines ratios, especially in local galaxies, and UV nebular lines, especially in distant galaxies whose UV lines are redshifted into the observed optical bands.

In contrast to the BLR, the metal content of the NLR is still highly debated: regardless of the stellar mass of the host galaxy, some works find an enrichment of metals in type 2 AGN with respect to star-forming galaxies of similar mass (e.g.. Coil et al., 2015; Thomas et al., 2019; Pérez-Díaz et al., 2021, see also Figure 1.5), while other works measure lower metallicity than in star-forming galaxies (e.g., Do Nascimento et al., 2022; Armah et al., 2023, see also Figure 1.4).

The origin of the high metal content may be explained in this case by AGN-driven outflows of high-metallicity gas, which are actually observed on kpc scales from the BLR (e.g., D'Odorico et al., 2004; Arav et al., 2007). Another contribution to the metal enrichment of the gas surrounding the BLR may also come from *in-situ* star-formation inside the AGN-driven outflows, which has been recently detected by several works (e.g. Maiolino et al., 2017; Gallagher et al., 2019).

On the other side, a possible way to explain the results in those works finding low AGN metallicities is that AGN-driven winds halt the production of metals by quenching star formation in the circumnuclear regions around the galaxy center (Choi et al., 2022).

In support of this hypothesis, Armah et al. (2023) find that the BASS sample of AGN show an anti-correlation between the X-ray luminosity-NLR metallicity and the Eddington ratio, which indicates that the low-luminous AGN (and therefore likely those with the weakest feedback) are more actively undergoing ISM enrichment through star formation, as opposed to the most luminous X-ray AGN. Similarly, EAGLE simulations

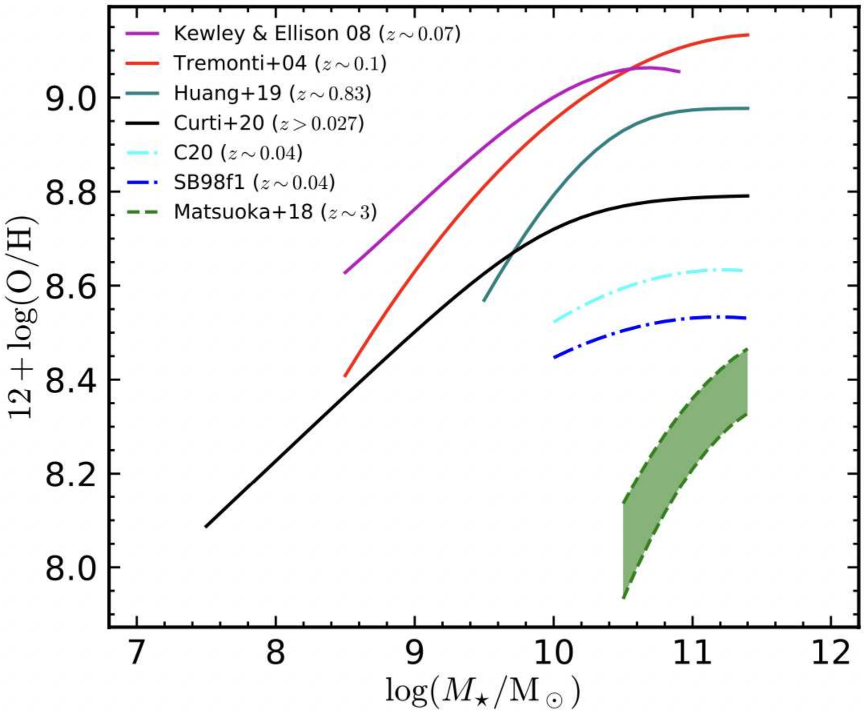

Figure 1.4: Comparison between the mass-metallicity relations of the BASS sample (with a median redshift at $z \sim 0.04$) and from the literature. The solid magenta, red, teal and black curves denote the MZRs for star-forming galaxies at $z \sim 0.07$, $z \sim 0.1$, $z \sim 0.83$ and $z > 0.027$ derived by Kewley & Ellison (2008), Tremonti et al. (2004), Cid Fernandes et al. (2011), Curti et al. (2020) respectively. The dashdot cyan and blue curves represent estimates from C20 and SB98 calibrations respectively. Finally, the green filled area is from type-2 AGNs at $z \sim 3$ by Matsuoka et al. (2018).

predict that the scatter from the MZR at $M_* > 10^{10.4}M_\odot$ depends on the mass of the central black hole, and in particular that black hole mass and gas-phase metallicity are anti-correlated (Van Loon et al., 2021). AGN feedback can also play a role by removing both gas and metals from the nucleus of the galaxy and dispersing this material to larger radii (Choi et al., 2022).

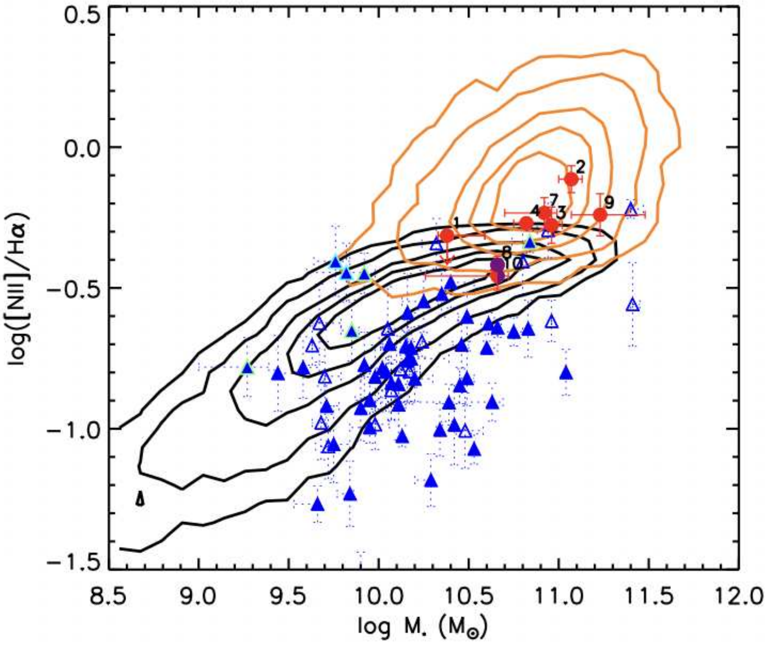

Figure 1.5: By considering the ratio [N II]/Hα as a proxy of the metallicity, Coil et al. (2015) shows the [NII]/Hα ratios of MOSDEF galaxies (blue triangle) and AGNs (red circles) as a function of stellar mass, compared to galaxies (black contours) and AGNs (orange contours) in SDSS. In this way, they conclude the narrow-line region of AGNs at z ∼ 2 (MOSDEF sample) are less enriched than those at z ∼ 0 (SDSS sample), at a given host stellar mass.

1.3.4 The role of the environment on the metallicity of local AGN

In this context, a dedicated study of the gas-phase metallicity in the nuclear regions of galaxies hosting an AGN (AGN metallicity, hereafter) and its scaling relation with the host galaxy stellar mass in different environments is still missing. A possible link between the AGN metallicity and the environment may have roots in the fact that environmental processes such as the ram pressure stripping (RPS) phenomenon have been proven to quench rapidly star formation in galaxies falling into clusters (Boselli & Gavazzi, 2006), and that AGN feedback may aid in the quenching of star formation together with ram pressure (Ricarte et al., 2020). The ROMULUS C cosmological simulations of a high-resolution galaxy cluster by Ricarte et al. (2020) find that RPS triggers enhanced gas accretion onto the black hole, which then produces heating and outflows due to AGN feedback. Growing evidence has been found, both observationally (Poggianti et al., 2017b; Peluso et al., 2022) and theoretically (Tonnesen et al., 2009; Akerman et al., 2023), in support of the hypothesis that RPS is able to trigger or enhance the AGN activity in cluster galaxies. Recent studies have clearly identified AGN-driven outflows (Radovich et al., 2019) and AGN feedback in action (George et al., 2019) in strongly stripped galaxies.

1.4 Integral Field Spectroscopy of nearby galaxies

Our understanding of galaxy formation and evolution, either at low redshift (e.g., MaNGA Bundy et al., 2015) or at high redshift (e.g., Epinat, 2010), has greatly advanced thanks to the advent of integral-field spectroscopy (IFS) techniques, which allowed the study of spatially-resolved properties within the whole galaxy body. The development of IFS techniques was motivated by the need to fill the gap between the increasing spatial resolution of imaging instruments with the still poor spatial resolution and spatial coverage of the long-slit spectroscopic observations.

Generally speaking, the IFS data cubes are generated in the following way: the galaxy is divided into smaller regions (spaxel or slices), inside which a 1D spectrum is extracted; then a 2D map of the intensity of the flux at a given wavelength is obtained, combining the information from 1D spectra acquired throughout the whole field of view of the detector. The resulting 3D data cubes can then be used to study spatially resolved spectroscopic quantities such as gas kinematics (derived from nebular emission lines), stellar kinematics (derived from absorption lines and stellar spectral templates), chemical composition, ionization profiles, and more. Figure 1.6 shows three different methods to obtain the final data cube, that differ from each other in the way in which the sky is sampled. Briefly, the lenslet array technique distributes short spectra originating from each spaxel over the detector surface. The microlens is tilted in order to prevent the spectra from overlapping, but this limits the length of the spectrum. The most common

Parameter	MaNGA (Abdurro et al., 2022)	SAMI (Croom et al., 2021)	CALIFA (Sánchez et al., 2012)	AMUSING++ (López-Cobá et al., 2020)
Sample size	11’273	2’400	974	635
Selection	Mass flat distribution	Volume limited	Diameter	Compilation
Redshift range	0.01-0.15	0.01-0.1	0.005-0.03	0.0002-0.1
Coverage	1.5 R_e (2/3), 2.5 R_e (1/3)	1 R_e	>2.5 R_e	>2 R_e
Wavelength range (Å)	3600-10300	3700-5700/6250-7350	3700-7500	4650-9300
Spectral resolution (σ)	80 km/s	75/28 km/s	85/150 km/s	40 km/s
Spatial resolution	2.5 ”	2.3”	2.5”	0.7”
Telescope size	2.5 m	3.6 m	3.5 m	8.2 m

Table 1.1: Main characteristics of the largest IFS surveys of nearby ($z < 0.15$) galaxies. References are to the latest release of each survey.

technique is the one that uses a 2D bundle of optical fibres to transfer the input light to the spectrograph. Finally, in the image-slicer technique, the telescope focal plane is sampled using an array of slicing mirrors, each of which then directs its light to a dispersive element to produce a long slit spectrum of each slice on a detector.

Table 1.1 lists the largest surveys, using the fiber technique, aimed at studying the properties of nearby galaxies in the visible and infrared. All these surveys target very large sample of galaxies to give an unbiased view of the galaxy population of the local universe.

As a part of the fourth generation of the Sloan Digital Sky Survey (SDSS-IV), the MaNGA project bundles single fibers into an integral field unit (IFU) from the Baryon Oscillation Spectroscopic Survey (BOSS) spectrograph (Smee et al., 2013), installed at the Cassegrain focus of the Sloan Digital Sky Survey 2.5 m telescope at Apache Point Observatory (Gunn et al., 2006). Over the six year lifetime of the survey (2014–2020) MaNGA obtained spatially resolved optical+NIR spectroscopy of 10’000 galaxies at redshifts $z \sim 0.02 - 0.1$. The MaNGA field of view covers up to 1.5 galaxy effective radii (e.g. R_e) for two-third of the sample, while covers up to 2.5 R_e for the remaining one-third of the sample. The rest-optical ($\lambda\lambda$0.36–1.0 μm) spectral resolution R $\sim$ 2000 implies an instrumental spectral line-spread function (LSF) with typically 1σ width of about 80 km/s.

The Sydney-AAO (Australian Astronomical Observatory) Multi-object Integral field spectrograph (SAMI Croom et al., 2012; Bryant et al., 2012) uses revolutionary new imaging fibre bundles, called hexabundles (e.g. Bland-Hawthorn et al., 2011). 13 of these hexabundles can be positioned anywhere over a 1-degree diameter FoV. SAMI feeds the AAOmega spectrograph (Sharp et al., 2006), installed at the prime focus of the 3.6 m Anglo Australian Telescope (AAT), which for the survey is set up to have resolutions of R = 1730 in the blue arm (3700-5700 Å) and R = 4500 in the red arm (6250-7350 Å).

The Calar Alto Legacy Integral Field Area survey (CALIFA Sánchez et al., 2012) survey aims to obtain spatially resolved spectroscopic information for ~900 galaxies of all Hubble types in the local universe ($0.005 < z < 0.03$). The survey has been designed to allow three key measurements to be made: (a) two-dimensional maps of stellar populations (star formation histories, chemical elements); (b) the distribution of the excitation mechanism and element abundances of the ionized gas; and (c) kinematic properties (velocity fields, velocity dispersion), both from emission and from absorption lines. To cover the full optical extension of the target galaxies, CALIFA uses the large field of view of the PPAK/PMAS IFU at the 3.5m telescope of the Calar Alto observatory. Two grating setups have been used, one covering the wavelength range between 3700 and 5000 Å at a spectral resolution R~1650, and the other covering 4300 to 7000 Å at R~850 (Sánchez et al., 2010).

While galaxy surveys such as MaNGA, CALIFA, and SAMI have enabled investigations at kiloparcec scales in the nearby universe, all of those explorations have been limited by the spatial resolution of ~2.5”. On the other side, AMUSING++ is the largest compilation of nearby galaxies observed with the MUSE integral-field spectrograph so far. This collection consists of 635 galaxies from different MUSE projects covering the redshift interval $0.0002 < z < 0.1$. The MUSE instrument provides a wide field of view (FoV) of $1' \times 1'$, with a spatial sampling of $0.2'' \times 0.2''$ per spaxel, and seeing-limited spatial resolution of $\sim 0.7''$. MUSE covers the whole optical range from 4750 to 9300 Å, with a spectral sampling of 1.25 Å, and a FWHM that depends slightly on the wavelength

(Bacon et al., 2017), being ~ 2.4 Å at the red part of the spectrum (at 7500 Å).

Another novel MUSE large program is GAs Stripping Phenomena in galaxies (GASP, Poggianti et al., 2017a), that is aimed at studying gas removal processes in galaxies, investigating the ionized gas phase and the stellar component both in the discs and in the extra-planar tails of local morphologically disturbed galaxies, in different environments (galaxy clusters and groups), as well as a control sample of disc galaxies with no morphological anomalies.

In this Thesis, I will exploit data mainly from the GASP survey (which will be described in details in Chapter 2, when the sample selection is introduced) and from the Data Release 15 (DR15, Bundy et al., 2015) of the MaNGA survey.

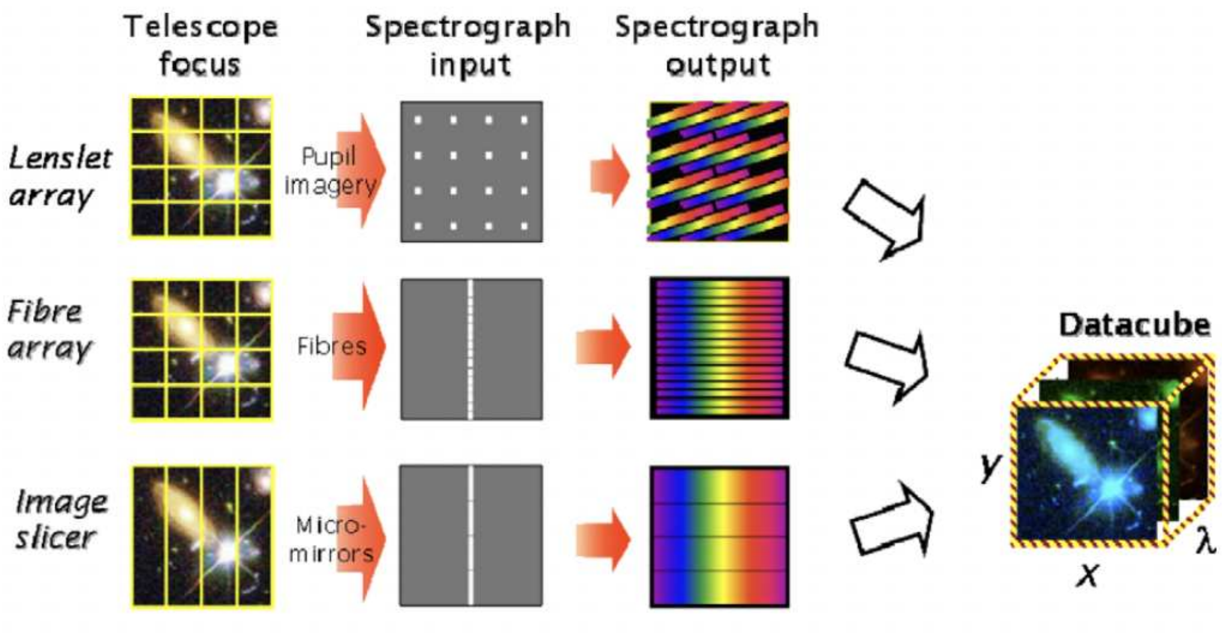

Figure 1.6: A summary of the three main techniques of integral field spectroscopy.

1.5 Thesis Outline and Aims

The aim of this dissertation is to understand the effects of RPS on the nuclear activity of SMBHs located at the center of massive star-forming galaxies, and the impact on the

ISM properties of the synergy between the presence of an AGN, acting on the nuclear regions, and the RPS, altering the gas distribution in the surviving disk of the host galaxy. In fact, AGN and RPS are key processes able to shape the gas properties of their host galaxy, as they are both able to hugely alter the ISM distribution, kinematics, and chemical composition in the innermost and outermost parts of the disk, respectively.

To explore this, I build up the samples of galaxies described in Chapter 2, exploiting the statistical power of the GASP and MaNGA surveys. In particular, I select two samples of late-type RP-stripped galaxies from GASP, located in clusters, either hosting AGN activity or showing star formation in the nuclear regions. In a similar way, I select two control samples of undisturbed galaxies from the MaNGA survey, either hosting or not an AGN.

In Chapter 3 I show the diagnostics power of IFS data to disentangle the ionization sources using strong optical emission lines such as the [NII] and [OIII] , but also the capability of these SEL to constrain the ionization parameter and the oxygen abundance of the gas phase by modeling and predicting their emission through the most updated version of photoionization codes. In this context, I also present photoionization models generated to measure in a homogeneous way the gas oxygen abundance of the ISM ionized by different kinds of ionization sources (e.g., stars and AGN).

Chapter 4, 5, and 6 show the results of the analysis performed with the datasets and method described in the first parts of this dissertation. Chapter 4 shows the AGN fraction as a function of the RPS, investigated in a project published in Peluso et al. (2022). Chapter 5 presents the nuclear metallicity and the relationship between the host galaxy mass and the nuclear metallicity of SF and AGN galaxies, to investigate the effect of the presence of an AGN on the global properties and scaling relationships in nearby galaxies. The MaNGA and GASP samples also allowed to disentangle the role of the ram-pressure stripping in shaping the chemical content at the centers of AGN hosts, and the results are presented in Peluso et al. (2023). Finally, Chapter 6 presents an ongoing project in which I perform for the first time a spatially resolved study of the chemical composition in AGN hosts galaxies using photoionization models. This allows to assess the extent of the AGN impact on the galaxy ISM metallicity, within the limit of the ~ 1 kpc spatial resolution of the observations.

2 GALAXY SAMPLES

In this Chapter, I describe the three main datasets of galaxies used to construct the samples to perform the analysis presented throughout this Thesis. In particular, I present the GAs Stripping Phenomena in galaxies with MUSE (GASP) survey along with its main goals, observing strategy, data analysis and target galaxies for which I give details on the most significant properties. Together with the GASP galaxies, I also built a catalog of all the known RP-stripped galaxies in the literature using as RP tracers the gas emission at different wavelengths. For each galaxy, I give a brief description by reviewing their main properties, especially those regarding the stripping process and the ionization source in the inner central regions where any AGN emission is expected to be located. Finally, I present the MaNGA survey from which I draw a control sample of undisturbed galaxies, presumably not experiencing any stripping, which will be used to obtain a statistically significant comparison to the RP stripping effects on galaxies.

2.1 GASP

GAs Stripping Phenomena in galaxies with MUSE (GASP, hereafter) is an integral-field spectroscopic (IFS) survey carried out with the spectrograph MUSE, mounted at the Very Large Telescope (VLT).

The main goal of the survey is to study the gas removal processes in galaxies as a function of the environment in order to investigate their effects on the galaxy's evolution. Specifically, the key drivers of GASP are:

(a) identify the physical processes responsible for the gas outflow among the possible external (ram pressure stripping, tidal interactions, harassment etc.) and internal (winds due to stars or AGN) mechanisms, clarifying where and how it happens;

(b) measure the time-scale and the efficiency of the stripping phenomenon in galaxies as a function of galaxy environment and galaxy mass (Werle et al., 2022; **?**);

(c) quantify the amount of stars formed in the stripped gas (Gullieuszik et al., 2023; Giunchi et al., 2023);

(d) monitor the evolution of the galaxies that are being depleted of their gas content, looking at their transition from the blue cloud to the red sequence;

(e) study the possible interplay between the gas physical conditions and the activity of the supermassive black holes (SMBH) at the center of galaxies (Peluso et al., 2022);

(f) estimate the spatially resolved star formation history and metallicity distribution in ram-pressure stripped galaxies, understanding how this process is affecting their global properties (e.g., Franchetto et al., 2020)

Multi-wavelength auxiliary data (covering the spectral range from radio to X-ray and collected by instruments such as APEX, VLA, ALMA and ALMA, Astrosat, Meerkat, HST) allowed further characterization of the gas in all the phases.

2.1.1 Observing strategy and Sample selection

The GASP survey targeted 114 galaxies located in clusters, groups, filaments, and in isolation, spanning more than four orders of magnitude in halo mass. The observations were carried out with the MUSE spectrograph in wide field mode with natural seeing $leq1''$ (WFM-noAO). The redshift range of the targeted galaxies is $0.04 < z < 0.07$, translating into a spatial resolution of ∼ 1 kpc. The WFM-noAO MUSE FoV of $1' \times 1'$ allows good coverage of the targets out to several effective radii. The majority of GASP galaxies were observed with four exposures of 675 seconds each, each rotated by 90 °. Some galaxies (e.g. JO206) required two or three further offset pointings to extend the sky coverage to include the longest tails. Galaxy stellar masses range between $\log\ (M_{*}/M_{\odot}) = 10^{8.7}$ and $10^{11.5} M_{\odot}$, consenting to explore the mass dependence of the efficiency of gas removal processes. The vast majority of the sample is composed of cluster galaxies, but a third of the sample is located in less dense environments (Vulcani et al., 2021). The GASP primary targets are selected from the atlas of jellyfish candidates of Poggianti et al. (2016), which provides a large sample of disk galaxies, candidates to undergo gas-only removal processes. By using the B-band images of the WINGS (Fasano et al., 2006), OMEGAWINGS (Gullieuszik et al., 2015) surveys, and the PM2GC catalog (Calvi et al., 2011), this atlas collects those galaxies whose optical morphology presents unilateral debris or asymmetrical/disturbed star formation on one side. The galaxies are divided into classes, the so-called JSTAGE (Poggianti et al., in prep.) according to the intensity of the disturbed signatures (see Section 2.1.3 for further details on how the JSTAGE is assigned).

Galaxies in the GASP control sample are galaxies in clusters and the field with no optical signs of stripping, i.e., no signs of debris or unilaterally disturbed morphologies in the optical images. This sample allows to contrast the properties of stripping candidates with those of galaxies that show no optical evidence of gas removal. Control sample galaxies were selected from WINGS, OMEGAWINGS, and PM2GC visually inspecting the same B-band images used for the primary targets.

2.1.2 Data reduction and analysis

The MUSE data cubes are reduced using the MUSE pipeline presented in (Bacon et al., 2010), following the GASP reduction procedures described in Poggianti et al. (2017a).

The datacubes are average smoothed in the spatial direction with a 5×5 pixel kernel, with a pixel size of $0.2''$. This procedure does not significantly alter the spatial resolution of the data, as the filter size almost corresponds to the seeing (e.g., $\sim 1''$).

Stellar masses have been computed with the code SINOPSIS (Fritz et al., 2017) assuming a Chabrier et al. (2003) IMF.

The fluxes of the main emission lines and the corresponding errors are measured with the IDL software KUBEVIZ (Fossati et al., 2016). KUBEVIZ can attempt a single- or double-component Gaussian fit. The code also fits the continuum+emission spectra to estimate the redwards and bluewards continuum underlying the main emission lines, between 80 and 200 Å. The lines used in this Thesis are: Hβ, [OIII]λ5007, [OI]λ6300, Hα, [NII]λ6583, [SII]λ6716, and [SII]λ6731. The emission-line fluxes are computed from the emission-only spectrum (obtained by subtracting the stellar continuum) and are corrected for the dust internal extinction by applying the extinction law of Cardelli et al. (1989) and assuming a Balmer decrement of $\mathrm{H}\alpha/\mathrm{H}\beta = 2.86$. In all the Thesis only spaxels with signal-to-noise ratio $\mathrm{S/N} \geq 3$ in the involved emission lines are considered. As an example, 2.1 shows the stellar continuum (in grey) and the gas emission (in pink) in four galaxies from GASP, revealing the RPS in action: in fact, the stellar distribution is mainly undisturbed, while the gas distribution is highly disturbed.

The emission line fluxes were used to build the so-called BPT diagrams which are commonly used to classify the ionization mechanism acting on the gas (Baldwin et al., 1981; Veilleux & Osterbrock, 1987; Kauffmann et al., 2003; Kewley et al., 2001, 2006).

2.1.3 Useful galaxy properties

In Table 2.1.3, the galaxy properties used throughout this Thesis are listed. The ionization mechanism acting on the gas was determined by adopting the standard NII-BPT diagrams (Baldwin et al., 1981). Specifically, I use the BPT diagram involving the line ratios [NII]λ6583/Hα over [OIII]λ5007/Hβ (e.g., [NII]-BPT)[1]. In this case, the Kewley et al. (2001) relation based on photoionization models is used to delimit the region where Seyfert/LINER spaxels are located, and the empirical Kauffmann et al. (2003) relation to isolate star-forming spaxels. The region in between the two demarcation lines is populated by spaxels with line ratios usually classified as Composite (SF+AGN). I finally use the Sharp et al. (2010) relation to further distinguish Seyfert from LINER line ratios. In Table 2.1.3, I list the classification (i.e. AGN flag) of the main ionization mechanism acting on the gas in the nuclear regions of the GASP galaxies. Specifically, the AGN flag is 0 when the galaxy is dominated by photo-ionization from young stars in the center, while the AGN flag is: 1 in case of Seyfert-1 like nucleus, 2 in case of Seyfert-2 like nucleus, 3 in case of LINER-like nucleus and 4 in case of dust-obscured AGN classified by the X-ray emission.

The Jstage was assigned with the following workflow: two or three classifiers (first independently, then together) visually inspected the OMEGAWINGS and PM2GC and WINGS-only B-band images searching for any type of evidence suggestive of gas stripping, selecting galaxies that have (a) one-sided debris of gas or tails and/or (b) asymmetric morphologies suggestive of unilateral external forces, and/or (c) distribution of star-forming regions and knots suggestive of triggered SF on one side of the galaxy. The images were first inspected independently by each classifier and then each galaxy was inspected together until a consensus was found in 100 % of the cases. Six classes were assigned according to the visual evidence for stripping signatures in the optical bands:

1. no signs of stripping : JSTAGE = 0
2. almost undisturbed/tentative candidates: JSTAGE = 0.3
3. pre or initial-stripping: JSTAGE = 0.5

---

[1] The only exception is the GASP galaxy JW100 for which I use the [SII]-BPT, involving the [SII]$\lambda\lambda$6716,6731/Hα instead of [NII]λ6583/Hα, because at the galaxy's redshift the [NII] line is contaminated by a sky line

4. stripped: JSTAGE = 1

5. jellyfish with tails longer than the galaxy's diameter: JSTAGE = 2

6. truncated disk / late stage of the stripping process: JSTAGE = 3

In Table 2.1.3 the JSTAGE of each GASP galaxies is listed.

It is important to keep in mind that the JSTAGE depends not only on the intrinsically stronger or weaker evidence for stripping signatures but also on the galaxy orientation with respect to the line of sight, the galaxy size (number of pixels) and the signal-to-noise of the images, thus it is only crudely indicative of the intensity of the stripping.

The stellar mass is computed with the code SINOPSIS, which uses a stellar population synthesis technique that reproduces the observed optical spectra of galaxies performing a spectral fitting of the stellar content and extinction, to derive the spatially resolved properties of the stellar populations. Total stellar masses are obtained by summing the stellar mass inside each spaxel within the galaxy (Vulcani et al., 2018).

The structural parameters (effective radius, inclination, position angle) are derived as described in detail in Franchetto et al. (2020), from the I-band images obtained from the integrated MUSE data cubes using the Cousins I-band filter response curve. The luminosity growth curve L(R) of the galaxies was computed by trapezoidal integration of their surface brightness profiles. By definition, the effective radius (Re) is the radius such as $\mathrm{L}(R_e)/\mathrm{L}_{\mathrm{tot}}$=0.5. The $\mathrm{L}_{\mathrm{tot}}$ is the total luminosity within the most externally fitted isophote, which encloses entirely the full optical extent of the galaxy. The ϵ (ellipticity) and PA (position angle) of the disk were derived as the average values of the elliptical isophotes corresponding to the galaxy disk. The galaxy inclination i is computed as:

$$\cos^2 i = \frac{(1-\epsilon)^2 - q_0^2}{1 - q_0^2} \tag{2.1}$$

where an intrinsic flattening for galaxies of $q_0 = 0.13$ is assumed (Giovanelli et al., 1994). Note that four stripping galaxies (JO95, JO156, JO153 and JO149) have an irregular I-band morphology that prevents a good estimate of their structural parameters.

With the quantities just described, I deproject the position of each spaxel to derive its physical galactocentric distance.

Table 2.1:

ID	z	RA	DEC	CLUSTER	Jstage	$\log\left(\frac{M_*}{M_\odot}\right)$	AGN	R_e(kpc)	PA°	i°
JO85	0.0355	351.1307	16.8682	A2589	10.7	1.0	3	7.0	158	25
JO93	0.0370	350.7989	14.9014	A2593	10.5	0.5	0	9.4	145	25
JW56	0.0387	201.7626	-27.2162	A1736	9.1	2.0	0	2.2	90	65
JO36	0.0407	18.2476	15.5915	A160	10.8	3.0	4	9.0	14	81
JO194	0.0420	359.2528	-34.6806	A4059	11.2	2.0	3	10.8	60	39
JO89	0.0424	351.5025	14.3073	A2593	9.7	0.5	0	6.4	80	66
JO204	0.0424	153.4451	-0.9142	A957x	10.6	2.0	2	5.2	149	72
JO45	0.0426	18.3191	0.2016	A168	9.2	0.5	0	3.8	99	57
JO47	0.0427	18.9903	0.6933	A168	9.6	1.0	0	6.1	81	45
JW29	0.0431	194.4562	-17.6659	A1644	9.5	0.5	0	8.7	122	77
JO95	0.0433	356.1111	9.1155	A2657	9.4	2.0	0	–	–	–
JO149	0.0438	202.0439	-31.1639	A3558	8.8	2.0	0	–	–	–
JO201	0.0446	10.3762	-9.2628	A85	10.8	2.0	2	7.1	176	42
JO17	0.0451	17.1472	1.9436	A147	10.2	0.5	0	6.8	64	60
JO49	0.0451	18.6827	0.2861	A168	10.7	2.0	3	6.5	117	54
JO162	0.0454	202.8747	-33.0554	A3560	9.4	2.0	0	4.0	150	72
JO175	0.0468	312.8233	-52.8227	A3716	10.5	2.0	0	3.6	56	44
JO153	0.0469	202.0631	-31.0327	A3558	9.4	1.0	0	–	–	–
JO10	0.0471	14.4234	-1.3122	A119	10.8	3.0	0	5.5	3	62

Continued on next page

Table 2.1: (Continued)

JW108	0.0477	90.1998	-39.9187	A3376	10.5	3.0	0	5.2	148	76
JO41	0.0477	193.4783	-15.7889	A1631a	10.2	0.5	0	5.1	77	26
JO13	0.0479	13.9153	-0.8767	A119	9.8	0.5	0	4.8	109	36
JO159	0.0480	201.6488	-30.9936	A3558	9.8	0.5	0	3.8	70	40
JO160	0.0483	202.3693	-31.6570	A3558	10.1	2.0	0	5.4	87	59
JO27	0.0493	17.7023	-15.0782	A151	9.5	0.5	0	5.2	52	79
JO128	0.0500	193.7368	-29.8364	A3530	9.9	0.5	0	6.7	95	23
JO147	0.0506	201.7072	-31.3960	A3558	11.0	2.0	3	8.4	53	82
JO156	0.0511	202.1436	-31.0241	A3558	9.6	1.0	0	–	–	–
JO206	0.0511	318.4475	2.4762	IIZW108	11.0	2.0	2	9.4	118	64
JO144	0.0515	201.1351	-31.1164	A3556	10.5	1.0	0	3.8	29	66
JO171	0.0521	302.5613	-56.6418	A3667	10.6	2.0	2	12.1	113	18
JO200	0.0527	10.5210	-9.5344	A85	10.8	1.0	0	9.1	10	46
JO28	0.0543	17.5388	-15.5735	A151	9.4	1.0	0	5.4	32	66
JO135	0.0544	194.2679	-30.3751	A3532	11.0	2.0	2	4.6	43	64
JO69	0.0550	329.3300	-7.7788	A2399	9.9	1.0	0	5.4	49	44
JO123	0.0550	193.2543	-28.6146	A3528b	9.9	0.5	0	4.3	100	37
JO23	0.0551	17.0338	-15.5116	A151	9.7	3.0	0	3.4	29	73
JO113	0.0552	55.4549	-53.4038	A3158	9.7	2.0	0	3.5	22	73
JO197	0.0562	136.6358	-9.5242	A754	10.0	1.0	0	4.1	3	57
JO138	0.0572	194.2438	-30.1017	A3532	9.7	0.5	0	4.2	1	75
JO70	0.0578	329.0170	-7.3272	A2399	10.5	1.0	0	3.9	24	40

Continued on next page

Table 2.1: (Continued)

JO112	0.0583	55.0251	-54.0409	A3158	9.6	0.5	0	3.3	33	37
JO141	0.0587	194.6599	-30.7923	A3532	10.7	1.0	0	5.4	71	70
JO102	0.0594	52.2695	-52.8348	A3128	10.0	0.5	0	2.9	33	71
JO181	0.0599	337.0158	-30.3011	A3880	9.1	0.5	0	3.0	136	66
JO179	0.0618	326.7795	-43.7051	A3809	9.5	0.5	0	3.6	88	24
JW100	0.0619	354.1044	21.1507	A2626	11.4	2.0	2	6.9	0	75
JO60	0.0622	223.4649	18.6518	A1991	10.4	2.0	0	4.4	44	70
JO180	0.0647	326.3125	-44.0087	A3809	10.0	1.0	0	3.6	151	26
JW39	0.0663	196.0321	19.2107	A1668	11.2	2.0	3	8.3	100	53
JW115	0.0725	180.1998	-31.2282	A3497	9.7	1.0	0	4.2	99	69

2.2 LIT-RPS sample

I also performed a systematic literature search of all the ram pressure stripped galaxies identified by December 2020. These galaxies were studied exploiting a wide variety of observational techniques, including radio (e.g., Gavazzi et al., 1995); sub-mm (e.g. Scott et al., 2013; Jáchym et al., 2014, 2019); infrared (e.g., Sivanandam et al., 2010, 2014); optical (e.g., Gavazzi et al., 1995, 2001; Sun et al., 2007, 2010; Yagi et al., 2010; Sivanandam et al., 2010; Fumagalli et al., 2014; Gavazzi et al., 2017; Fossati et al., 2016; Roberts et al., 2020); UV (e.g., Smith et al. 2010) and X-ray (e.g., Sun et al., 2006, 2010). The assembled sample is therefore greatly heterogeneous and while for some galaxies it has been confirmed that RPS is the only acting mechanism, in some other cases galaxies are most likely undergoing both RPS and tidal interactions. As my aim is to include all RPS galaxies and collect a sample as large as possible, I consider also the latter cases.

I narrow down the search to galaxies for which I retrieve information at any wavelength on the ionization mechanism of the central emission, obtaining a total sample of

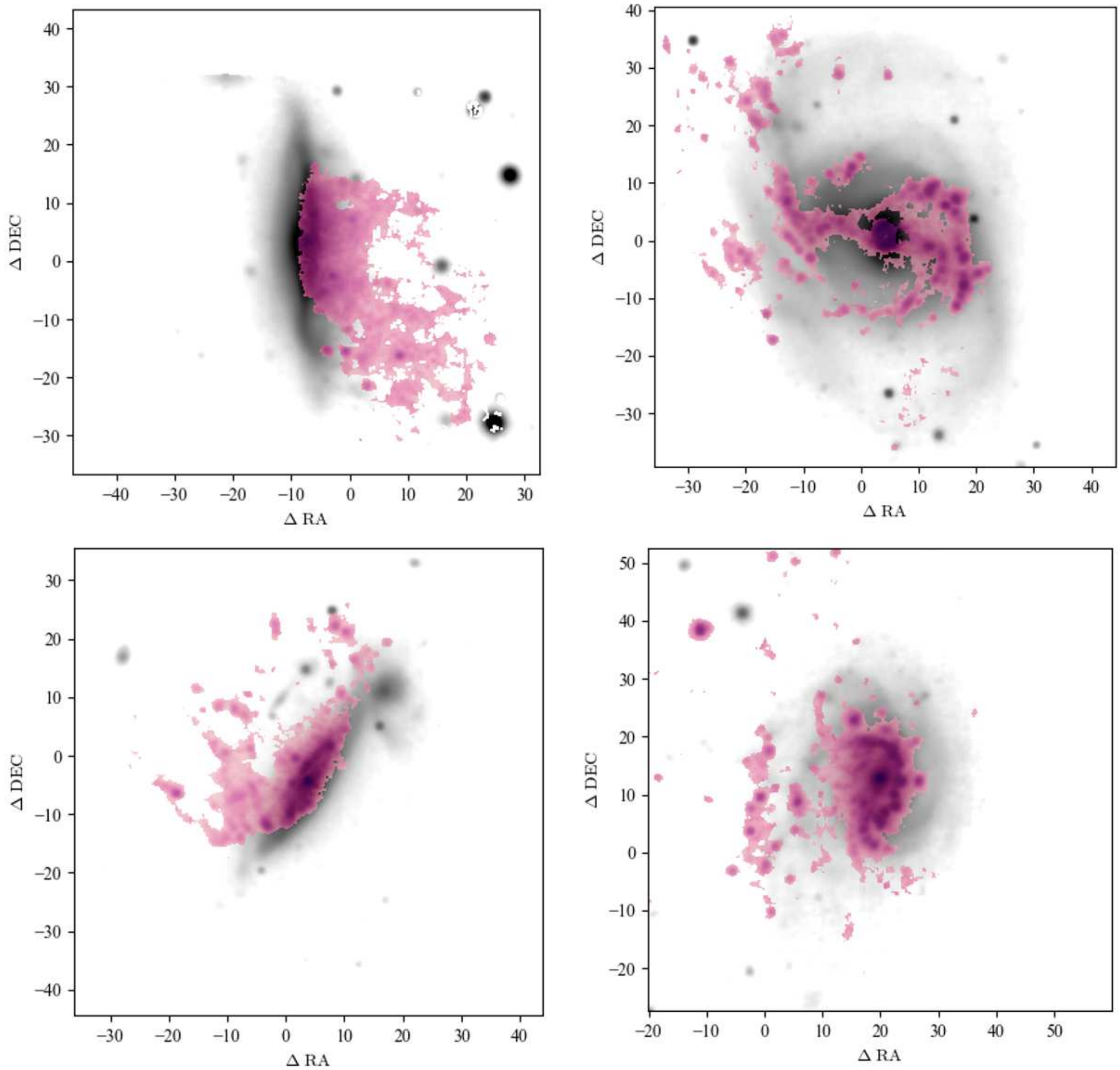

Figure 2.1: Stellar continuum (grey) and emission-only Hα flux (pink) of four jellyfishes sampled randomly from the GASP survey. The ram pressure stripping is evident from the highly disturbed morphology of the gas component, in contrast with the mostly undisturbed stellar distribution.

80 galaxies (from now on LIT-RPS sample). All these turn out to have some active star formation (in addition to the eventual AGN activity) in the available literature.

The LIT-RPS sample is located in the redshift range $0.001 \leq z \leq 0.34$, plus a galaxy at $z = 0.73$, and covers a stellar mass range of $1.3 \times 10^8 < M_*/M_\odot < 2.0 \times 10^{11}$. Stellar masses have been collected from the literature and homogenized to the same Chabrier et al. (2003) IMF (as in GASP). When a stellar mass estimate was not available (4/80), I computed it using the available photometric data following the Bell et al. (2001) approach. In particular, I use the Bell et al. (2001) relation between the mass-to light ratio of a galaxy and its color:

$$\log\left(\frac{M}{L_\lambda}\right) = a_\lambda + b_\lambda \cdot \mathrm{COL} \tag{2.2}$$

where L_λ is the luminosity in a band, indicated with λ, COL is a photometric color and a_λ and b_λ are coefficients depending on both λ and COL. For the calculations, I used the Bell et al. tables for a solar metallicity $Z = 0.02$ and a Bruzual & Charlot (2003) SSP model, converting from a Salpeter et al. (1955) to a Chabrier et al. (2003) IMF subtracting a factor -0.24. For one galaxy, 235144-260358 (Cortese et al., 2007), in order to use the formula (2.2) I first converted *HST* magnitudes to an UBV phometric system with the use of calibration equations for the Advanced Camera for Surveys (ACS) presented in Sirianni et al. (2005). I assume a typical 0.3 dex uncertainty on the computed stellar masses, which I take as bin size of the stellar mass distribution.

To assess the strength of RPS signatures and compare with the GASP Jstage classification, four of us (GP, BMP, BV, AM) visually inspected the available images in the literature for all the galaxies. Following the scheme described in §2.1.2, we assign a flag indicating the extent of the tail (same Jstage scheme as for GASP) based on the Hα emission (if available) and also a general Jstage based on any wavelength observed (Jstage$_{gen}$). In the case of multiple images with different resolutions or at different wavelengths showing a different extent of the tail, we always consider the wavelength with the longest visible tail to assign the Jstage$_{gen}$. The classifiers agreed in most of the cases. In the discrepant cases, each galaxy was inspected together by the classifiers to ensure homogeneity and to find a consensus. This visual inspection also confirmed that the LIT-RPS sample is composed of morphologically late-type galaxies (spirals or irregulars).

In Table 2.2 and Table 2.3 I present the main properties of each galaxy of the sample and a brief description of each galaxy follows:

name	RA	DEC	z	cluster	Jstage$_{H\alpha}$	Jstage$_{gen}$	Other names
MIP001417-302303	3.5693	-30.3843	0.2955	A2744	–	2.0	F1228
HLS001427-302344	3.61065	-30.39581	0.3033	A2744	–	2.0	F0083
NGC1566	65.00175	-54.93781	0.005	Dorado	0.0	0.0	–
ID345	149.9191	2.5281	0.727	CGr32	2.0	2.0	–
LEDA36382	175.73523	19.96621	0.02427	A1367	2.0	2.0	CGCG97073
UGC6697	175.95446	19.96844	0.02243	A1367	2.0	2.0	CGCG097-087
2MASXJ11443212+2006238	176.13385	20.10662	0.02398	A1367	2.0	2.0	–
NGC4254	184.70668	14.41651	0.00803	Virgo	1.0	2.0	MESSIER099
NGC4388	186.44508	12.66207	0.00856	Virgo	1.0	2.0	UGC07520, VCC 0836, VPC 0438, CGCG070068
NGC4402	186.53189	13.11332	0.0008	Virgo	3.0	0.5	VCC873
NGC4424	186.79838	9.42067	0.0015	Virgo	0.5	2	–
NGC4438	186.93997	13.00883	0.0003	Virgo	–	–	–
IC3418	187.43301	11.40469	0.00013	Virgo	0.5	2.0	VCC1217
NGC4501	187.9965	14.42039	0.00761	Virgo	–	0.5	MESSIER088
NGC4522	188.41546	9.17502	0.0077	Virgo	3.0	1.0	–
NGC4548	188.86022	14.49634	0.00164	Virgo	0.0	0.0	MESSIER091
NGC4569	189.20747	13.16294	0.0008.0	Virgo	2.0	2.0	MESSIER090, UGC07786, VCC 1690
GMP6364	193.67526	27.63897	0.02874	Coma	–	2.0	SDSS J125442.05+273820.2
GMP5821	193.93454	28.75464	0.0275	Coma	–	–	SDSS J125544.29+284516.6
IC3913	194.11905	27.29128	0.0251	Coma	–	–	GMP5422, KUG 1254+275, CGCG160026
GMP5382	194.11967	29.13708	0.03163	Coma	–	0.0	2MASX J12562871+2908140
GMP4688	194.43215	29.00331	0.0231	Coma	–	1.0	LEDA 1852727

GMP4629	194.4593	28.17036	0.0231	Coma	1.0	1.0	SDSSJ125750.2+281013
GMP4570	194.48665	27.99176	0.0152	Coma	2.0	2.0	SDSSJ125756.79+275930
GMP4555	194.4905	28.06178	0.0271	Coma	2.0	2.0	SDSSJ125757.7+280342, KUG1255+283
MACSJ1258-JFG1	194.49833	47.0461	0.3424	MACSJ1258.0+4702	–	2.0	–
NGC4848	194.52352	28.24274	0.0314	Coma	2.0	2.0	GMP4471, CGCG 160-055, SDSSJ125805.6+281433
GMP4437	194.53846	28.70859	0.0254	Coma	–	0.0	–
GMP4463	194.53858	26.66409	0.0243	Coma	–	0.0	–
GMP4281	194.60575	28.12897	0.0274	Coma	–	0.0	–
GMP4236	194.6285	26.99494	0.0249	Coma	–	1.0	–
NGC4853	194.64663	27.59633	0.0256	Coma	0.0	0.0	–
GMP4159	194.64717	27.26486	0.0245	Coma	–	0.5	SDSSJ125835.2+273547, GMP4156, CGCG160068
GMP4135	194.65538	27.17625	0.0256	Coma	–	1.0	Mrk 56, KUG1256+27
GMP4106	194.66637	26.7595	0.0249	Coma	–	1.0	Mrk057, KUG1256+274
IC3949	194.73338	27.83336	0.0253	Coma	1.0	1.0	–
NGC4858	194.7585	28.11575	0.0314	Coma	2.0	2.0	SDSSJ125856.0+275000, GMP3896, CGCG160212
Mrk58	194.772	27.64446	0.0181	Coma	2.0	2.0	GMP3816, SDSSJ125902.0+280656
GMP3618	194.81937	27.10608	0.028	Coma	–	0.5	GMP3779, KUG1256+279, CGCG160073
GMP3271	194.91621	27.57625	0.0167	Coma	0.5	1.0	–
GMP3253	194.91721	28.63081	0.0178	Coma	–	0.5	D41, SDSSJ125939.8+273435, KUG1257+278
GMP3143	194.95524	26.97433	0.0235	Coma	–	0.0	KUG 1257+288B
GMP3071	194.9838	27.74633	0.0298	Coma	2.0	2.0	–
SDSSJ130006.15+281507.8	195.02568	28.25234	0.0212	Coma	–	2.0	–
D100	195.03809	27.86649	0.0177	Coma	2.0	2.0	Mrk60, GMP2910
GMP2625	195.13003	28.95054	0.0233	Coma	–	0.5	–
GMP2599	195.14031	27.63777	0.025	Coma	0.0	1.0	–

IC4040	195.15777	28.05809	0.0255	Coma	2.0	2.0	KUG1258+279A, 7W 1258+27W06
NGC4911	195.23357	27.79087	0.0266	Coma	1.0	1.0	–
GMP2073	195.35448	28.67723	0.0292	Coma	–	0.0	GMP2374
NGC4921	195.35884	27.886	0.0183	Coma	0.0	0.0	–
GMP1616	195.53284	27.64831	0.023	Coma	–	0.0	GMP2059
GMP1582	195.54739	28.17326	0.0299	Coma	–	0.0	–
GMP713	195.97679	28.31054	0.0268	Coma	–	–	LEDA 83761
GMP672	195.98809	26.72948	0.022	Coma	–	1.0	–
GMP597	196.0547	28.54245	0.0271	Coma	–	0.5	–
GMP522	196.09452	28.81077	0.0265	Coma	–	1.0	–
GMP455	196.11063	27.30431	0.0184	Coma	–	2.0	–
GMP406	196.16159	28.97269	0.0253	Coma	–	0.0	–
GMP223	196.27764	28.64115	0.0182	Coma	–	1.0	–
SDSSJ130545.34+285216.8	196.439	28.87133	0.0266	Coma	–	1.0	–
SDSSJ130553.48+280644.7	196.47287	28.11244	0.0246	Coma	–	0.0	–
JO147	201.707304	-31.39575	0.0506	A3558	2.0	2.0	SOS114372
SOS90630	202.368875	-31.657111	0.049	SC1327-312	2.0	2.0	–
SOS61086	202.999167	-31.822833	0.045	SC1329-313	2.0	2.0	–
d4	203.135758	50.564581	0.272	A1758	–	0.5	–
A1758N_JFG1	203.146583	50.52675	0.2733	A1758	0.0	1.0	–
d5	203.17445	50.525994	0.2716	A1758	–	0.5	–
d7	203.184258	50.518794	0.2875	A1758	–	0.0	–
d6	203.1906	50.527164	0.2668	A1758	–	0.5	–
d3	203.208908	50.555894	0.2755	A1758	–	1.0	–
d1	203.224104	50.526292	0.2686	A1758	–	2.0	–

d2	203.226979	50.516425	0.2719	A1758	–	1.0	–
C153	235.2875	66.26222	0.2525	A2125	–	1.0	–
ESO137-001	243.363771	-60.764053	0.01557	A3627	2.0	2.0	–
ESO137-002	243.398546	-60.865167	0.0191	A3627	2.0	2.0	–
Sausage9	340.671125	52.974631	0.1839	CIZAJ2242.8+5301	–	–	–
Sausage7	340.740125	53.087431	0.1832	CIZAJ2242.8+5301	–	–	–
Sausage6	340.749375	53.037381	0.1836	CIZAJ2242.8+5301	–	–	–
Sausage8	340.787	53.090289	0.1843	CIZAJ2242.8+5301	–	–	–
Sausage5	340.80375	53.0028	0.1825	CIZAJ2242.8+5301	–	–	–
235144-260358	357.933458	-26.066555	0.2265	A2667	–	2.0	–

Table 2.2: Columns are: 1) name; 2) and 3) equatorial coordinates of the galaxy center from SIMBAD; 4) galaxy redshift; 5) host cluster; 6) and 7) Jstage and general Jstage, defined in section §3.2; 8) alternative names.

Name	$\log(M_*/M_\odot)$	AGN	Refs
MIP001417-302303	9.6 [Rawle et al. (2014)]	0 [Owers et al. (2012)]	Owers et al. (2012), Rawle et al. (2014)
HLS001427-302344	10.9 [Rawle et al. (2014))]	1 [Owers et al. (2012))]	Owers et al. (2012), Rawle et al. (2014)
NGC1566	10.8 [Elagali et al. (2019)]	1 [Veron-Cetty et al. (2006)]	Elagali et al. (2019)
ID345	10.3 [Boselli et al. (2019)]	1 [Boselli et al. (2019)]	Boselli et al. (2019)
LEDA36382	9.5 [Mendel et al. (2014)]	0 [SDSS (2004)]	Gavazzi et al. (1995), Gavazzi et al. (2001), Sivanandam et al. (2014), Boselli et al. (2018), Yagi et al. (2017)
UGC6697	9.8 [Yagi et al. (2017)]	0 [Consolandi et al. (2017)]	Gavazzi et al. (1984), Gavazzi et al. (1989), Gavazzi et al. (1995),Gavazzi et al. (2001), Scott et al. (2010), Fruscione et al. (1990), Sun et al. (2005), Yagi et al. (2017), Consolandi et al. (2017)
2MASXJ11443212+2006238	9.9 [Yagi et al. (2017)]	0 [SDSS (2004)]	Gavazzi et al. (1989), Gavazzi et al. (1995), Gavazzi et al. (2001), Yagi et al. (2017), Gavazzi et al. (2017)
NGC4254	10.1 [Boselli et al. (2018)]	2 [Davies et al. (2020)]	Boselli et al. (2018), Weżgowiec et al. (2012), Chyży et al. (2007), Kantharia et al. (2008), Rahman et al. (2011)
NGC4388	9.9 [Boselli et al. (2015)]	2 [Boselli et al. (2015)]	Vollmer et al. (2003), Vollmer et al. (2009), Oosterloo et al. (2005), Chung et al. (2009), Yoshida et al. (2004), Yoshida et al. (2002), Yagi et al. (2013), Gu et al. (2013),Damas-Segovia et al. (2016)
NGC4402	10.0 [Boselli et al. (2015)]	0 [?]	Lee et al. (2017), **?**, W. J. et al. (2020), Abramson et al. (2016)
NGC4424	10.2 [Boselli et al. (2015)]	0 [Ho et al. (1997)]	Chung et al. (2007)
NGC4438	10.4 [Boselli et al. (2015)]	3 [Veron-Cetty et al. (2003)]	Boselli et al. (2005), Vollmer et al. (2009), Wang et al. (2020), Kenney et al. (1995), Chemin et al. (2005), Kenney et al. (2008)

IC3418	8.4 [Boselli et al. (2015)]	0 [Fumagalli et al. (2011)]	Hester et al. (2010), Fumagalli et al. (2011), Kenney et al. (2014)
NGC4501	10.7 [Boselli et al. (2015)]	2 [Boselli et al. (2015)]	–
NGC4522	9.1 [Boselli et al. (2015)]	0 [SDSS (2004)]	Kenney et al. (2004), Abramson et al. (2016), Lee et al. (2018), Minchin et al. (2019), Stein et al. (2017), Vollmer et al. (2004)
NGC4548	10.5 [Boselli et al. (2015)]	3 [Boselli et al. (2015)]	–
NGC4569	10.4 [Boselli et al. (2015)]	3 [Boselli et al. (2015)]	Boselli et al. (2016), Boselli et al. (2006), Tschöke et al. (2001), Vollmer et al. (2004), Weżgowiec et al. (2012)
GMP6364	8.5 [Salim et al. (2016)]	0 [SDSS (2004)]	Roberts et al. (2020), Salim et al. (2018), Salim et al. (2016)
GMP5821	8.9 [Salim et al. (2016)]	0 [SDSS (2004)]	Roberts et al. (2020), Salim et al. (2018), Salim et al. (2016)
IC3913	11.0 [Salim et al. (2016)]	0 [Mahajan et al. (2010)]	Salim et al. (2018), Salim et al. (2018), Salim et al. (2016)
GMP5382	9.3 [Salim et al. (2016)]	0 [SDSS (2004)]	Roberts et al. (2020), Salim et al. (2018), Salim et al. (2016)
GMP4688	8.5 [Salim et al. (2016)]	0 [SDSS (2004)]	Roberts et al. (2020), Salim et al. (2018), Salim et al. (2016)
GMP4629	8.6 [Salim et al. (2016)]	0 [SDSS (2004)]	Salim et al. (2018), Chen et al. (2020), Roberts et al. (2020), Gavazzi et al. (2018), Salim et al. (2018), Salim et al. (2016)
GMP4570	8.1 [Salim et al. (2016)]	0 [Mahajan et al. (2010)]	Salim et al. (2018), Chen et al. (2020), Roberts et al. (2020), Gavazzi et al. (2018), Salim et al. (2018), Salim et al. (2016)
GMP4555	9.9 [Salim et al. (2016)]	0 [Mahajan et al. (2010)]	Salim et al. (2018), Chen et al. (2020), Salim et al. (2018), Salim et al. (2016), Gavazzi et al. (2018)
MACSJ1258-JFG1	10.5 (*)	1 [Rakshit et al. (2017)]	Ebeling et al. (2014), McPartland et al. (2016)

NGC4848	10.8 [Salim et al. (2016)]	0 [Mahajan et al. (2010)]	Chen et al. (2020), Salim et al. (2018), Roberts et al. (2020), Salim et al. (2018), Salim et al. (2016), Fossati et al. (2012), Yagi et al. (2013), Gavazzi et al. (2018)
GMP4437	10.4 [Salim et al. (2016)]	0 [Mahajan et al. (2010)]	Roberts et al. (2020), Salim et al. (2018), Salim et al. (2016)
GMP4463	9.3 [Salim et al. (2016)]	0 [SDSS (2004)]	Roberts et al. (2020), Salim et al. (2018), Salim et al. (2016)
GMP4281	9.7 [Salim et al. (2016)]	0 [Mahajan et al. (2010)]	Roberts et al. (2020), Salim et al. (2018), Salim et al. (2016)
GMP4236	8.4 [Salim et al. (2016)]	0 [Mahajan et al. (2010)]	Roberts et al. (2020), Salim et al. (2018), Salim et al. (2016)
NGC4853	10.8 [Salim et al. (2016)]	2 [Mahajan et al. (2010)]	Yagi et al. (2010), Salim et al. (2018), Salim et al. (2016), Chen et al. (2020), Gavazzi et al. (2018)
GMP4159	9.8 [Salim et al. (2016)]	0 [Mahajan et al. (2010)]	Roberts et al. (2020), Salim et al. (2018), Salim et al. (2016)
GMP4135	9.8 [Salim et al. (2016)]	0 [Mahajan et al. (2010)]	Roberts et al. (2020), Salim et al. (2018), Salim et al. (2016)
GMP4106	9.1 [Salim et al. (2016)]	0 [SDSS (2004)]	Roberts et al. (2020), Salim et al. (2018), Salim et al. (2016)
IC3949	10.6 [Salim et al. (2016)]	2 [Mahajan et al. (2010)]	Yagi et al. (2010), Chen et al. (2020), Gavazzi et al. (2018), Salim et al. (2018), Salim et al. (2016)
NGC4858	10.2 [Salim et al. (2016)]	0 [SDSS (2004)]	Chen et al. (2020), Yagi et al. (2010), Salim et al. (2018), Roberts et al. (2020), Gavazzi et al. (2018), Salim et al. (2018), Salim et al. (2016)
Mrk58	9.8 [Salim et al. (2016)]	0 [SDSS (2004)]	Chen et al. (2020), Yagi et al. (2010), Roberts et al. (2020), Gavazzi et al. (2018), Salim et al. (2018), Salim et al. (2016)
GMP3618	10.1 [Salim et al. (2016)]	6 [Mahajan et al. (2010)]	Roberts et al. (2020), Salim et al. (2018), Salim et al. (2016)

GMP3271	9.1 [Salim et al. (2016)]	0 [Mahajan et al. (2010)]	Yagi et al. (2010), Chen et al. (2020), Roberts et al. (2020), Gavazzi et al. (2018), Salim et al. (2018), Salim et al. (2016)
GMP3253	9.4 [Salim et al. (2016)]	0 [Mahajan et al. (2010)]	Roberts et al. (2020), Salim et al. (2018), Salim et al. (2016)
GMP3143	8.9 [Salim et al. (2016)]	0 [Mahajan et al. (2010)]	Roberts et al. (2020), Salim et al. (2018), Salim et al. (2016)
GMP3071	9.3 [Salim et al. (2016)]	0 [SDSS (2004)]	Chen et al. (2020), Roberts et al. (2020), Yagi et al. (2010), Yoshida et al. (2012)
SDSSJ130006.15+281507.8	8.8 [Salim et al. (2016)]	0 [SDSS (2004)]	Roberts et al. (2020), Salim et al. (2018), Salim et al. (2016)
D100	9.3 [Salim et al. (2016)]	2 [Mahajan et al. (2010)]	Chen et al. (2020), Yagi et al. (2010), Smith et al. (2010), Jáchym et al. (2017), Roberts et al. (2020), Cramer et al. (2019), Salim et al. (2018), Salim et al. (2016)
GMP2625	9.1 [Salim et al. (2016)]	0 [SDSS (2004)]	Roberts et al. (2020), Salim et al. (2018), Salim et al. (2016)
GMP2599	9.9 [Salim et al. (2016)]	4 [Nucita et al. (2017), Birchall et al. (2020)]	Chen et al. (2020), Smith et al. (2010), Roberts et al. (2020), Salim et al. (2018), Salim et al. (2016)
IC4040	10.3 [Salim et al. (2016)]	5 [Best et al. (2012)]	Chen et al. (2020), Smith et al. (2010), Yagi et al. (2010), Yoshida et al. (2012), Roberts et al. (2020), Salim et al. (2018), Salim et al. (2016)
NGC4911	11.3 [Salim et al. (2016)]	2 [Mahajan et al. (2010)]	Chen et al. (2020), Yagi et al. (2010), Roberts et al. (2020), Salim et al. (2018), Salim et al. (2016)
GMP2073	10.4 [Salim et al. (2016)]	0 [SDSS (2004)]	Roberts et al. (2020), Salim et al. (2018), Salim et al. (2016)
NGC4921	11.0 [Salim et al. (2016)]	6 [Mahajan et al. (2010)]	Kenney et al. (2015), Chen et al. (2020), Salim et al. (2018), Salim et al. (2016)
GMP1616	10.3 [Salim et al. (2016)]	0 [Mahajan et al. (2010)]	Roberts et al. (2020), Salim et al. (2018), Salim et al. (2016)

GMP1582	8.7 [Salim et al. (2016)]	0 [SDSS (2004)]	Roberts et al. (2020), Salim et al. (2018), Salim et al. (2016)
GMP713	9.0 [Salim et al. (2016)]	0 [Mahajan et al. (2010)]	Roberts et al. (2020), Salim et al. (2018), Salim et al. (2016)
GMP672	8.7 [Salim et al. (2016)]	0 [SDSS (2004)]	Roberts et al. (2020), Salim et al. (2018), Salim et al. (2016)
GMP597	8.7 [Salim et al. (2016)]	0 [SDSS (2004)]	Roberts et al. (2020), Salim et al. (2018), Salim et al. (2016)
GMP522	9.9 [Salim et al. (2016)]	0 [SDSS (2004)]	Roberts et al. (2020), Salim et al. (2018), Salim et al. (2016)
GMP455	9.4 [Salim et al. (2016)]	0 [Mahajan et al. (2010)]	Roberts et al. (2020), Salim et al. (2018), Salim et al. (2016)
GMP406	9.0 [Salim et al. (2016)]	0 [SDSS (2004)]	Roberts et al. (2020), Salim et al. (2018), Salim et al. (2016)
GMP223	8.5 [Salim et al. (2016)]	0 [SDSS (2004)]	Roberts et al. (2020), Salim et al. (2018), Salim et al. (2016)
SDSSJ130545.34+285216.8	9.2 [Salim et al. (2016)]	0 [SDSS (2004)]	Roberts et al. (2020), Salim et al. (2018), Salim et al. (2016)
SDSSJ130553.48+280644.7	10.1 [Salim et al. (2016)]	0 [SDSS (2004)]	Roberts et al. (2020), Salim et al. (2018), Salim et al. (2016)
JO147	10.8 [Merluzzi et al. (2010)]	3	Merluzzi et al. (2013), Merluzzi et al. (2016), Gullieuszik et al. (2020)
SOS90630	10.0 [Merluzzi et al. (2016)]	0 [Merluzzi et al. (2016)]	Merluzzi et al. (2016)
SOS61086	9.6 [Merluzzi et al. (2016)]	0 [Merluzzi et al. (2016)]	Merluzzi et al. (2016)
d4	9.8 [Ebeling et al. (2019)]	0 [Ebeling et al. (2019)]	Ebeling et al. (2019)
A1758N_JFG1	10.9 [Ebeling et al. (2019)]	0 [Kalita et al. (2019)]	Ebeling et al. (2019)
d5	10.1 [Ebeling et al. (2019)]	0 [Ebeling et al. (2019)]	Ebeling et al. (2019)
d7	9.8 [Ebeling et al. (2019)]	4 [Ebeling et al. (2019)]	Ebeling et al. (2019)

d6	8.9 [Ebeling et al. (2019)]	0 [Ebeling et al. (2019)]	Ebeling et al. (2019)
d3	8.4 [Ebeling et al. (2019)]	0 [Ebeling et al. (2019)]	Ebeling et al. (2019)
d1	8.5 [Ebeling et al. (2019)]	0 [Ebeling et al. (2019)]	Ebeling et al. (2019)
d2	9.5 [Ebeling et al. (2019)]	0 [Ebeling et al. (2019)]	Ebeling et al. (2019)
C153	10.4 (*)	3 [Owen et al. (2006)]	Owen et al. (2006)
ESO137-001	9.6 [Sun et al. (2010)]	0 [Fossati et al. (2016)]	Sun et al. (2010), Sun et al. (2006), Sun et al. (2007), Sun et al. (2010), Sivanandam et al. (2010), Jáchym et al. (2019), Jáchym et al. (2014), Fossati et al. (2016), Fumagalli et al. (2014), Zhang et al. (2013)
ESO137-002	10.3 [Sun et al. (2010)]	4 [Sun et al. (2010)]	Zhang et al. (2013), Ruszkowski et al. (2014), Sun et al. (2007)
Sausage9	10.6 [Sobral et al. (2015)]	2 [Sobral et al. (2015)]	Stroe et al. (2020)
Sausage7	10.5 [Sobral et al. (2015)]	0 [Sobral et al. (2015)]	Stroe et al. (2020)
Sausage6	9.4 [Sobral et al. (2015)]	0 [Sobral et al. (2015)]	Stroe et al. (2020)
Sausage8	10.6 [Sobral et al. (2015)]	2 [Sobral et al. (2015)]	Stroe et al. (2020)
Sausage5	9.6 [Sobral et al. (2015)]	0 [Sobral et al. (2015))]	Stroe et al. (2020)
235144-260358	9.3 (*)	0 [Cortese et al. (2007)]	Cortese et al. (2007)

Table 2.3: Columns are 1) galaxy most common name 2) logarithm of the stellar masses, homogenizing them to our adopted Chabrier IMF (in parenthesis the reference from which the value has been taken is reported) 3) AGN classification (see Table 4.1) and relative reference 4) references which present a characterization of the galaxy as a RPS candidate. The four galaxies with classification equals to 4 and 5 (e.g. where the AGN is spotted observing them in X and radio) resulted to be Star-Forming in the optics. In the text we analyze the consequence to change their AGN flag to 0.

- MIP001417-302303 hosts a trail of blue knots, the most distant of which is $\sim$ 11 kpc from the galaxy's main component. The AAOmega nuclear spectrum (Owers et al., 2012) has been used to derive ratios of log [N II]/Hα = -0.64 and log [O III]/Hβ = -0.04 that are consistent with a star-forming origin.

- HLS001427-302344 hosts a spectacular trail of blue knots and filaments not associated with the disk, extending up to ~35 kpc from the galaxy center to the southwest. The slightly irregular disk structure and a faint tidal feature may indicate that a tidal interaction has taken place (Owers et al., 2012). X-ray suggests the presence of an AGN (Rawle et al., 2014), confirmed by optical AAOmega spectroscopy in which the combination of broad and narrow lines indicates that this galaxy hosts a Seyfert 1 nucleus (Owers et al., 2012).

- NGC1566 is a candidate for initial stripping as Elagali et al. (2019) observe an asymmetric and mildly warped HI disc which, based on a simple analytic model, is consistent with ram pressure interactions with the IGM. According to the Veron-Cetty et al. (2006) "Quasars and Active Galactic Nuclei" catalog (V2006c hereafter), this galaxy hosts a Seyfert 1.5 (Winkler et al., 1992).

- ID345 is a galaxy hosting a long tail of ionized gas without any old stellar counterpart, suggesting that the galaxy is now undergoing a ram-pressure stripping episode. This is evident from the F814W HST ACS and *i*-band Supreme-Cam images coupled with the spatially-resolved maps of [O II]emission detected by MUSE. At the galaxy's redshift (z = 0.73), the Hα line is outside the spectral domain of MUSE. However, the presence of an AGN is suggested by the strong radio emission at 1.4 GHz. Also, the asymmetric shapes of the emission lines [O III] and Hβ could be explained by a contribution from an AGN.

- LEDA36382 reveals through radio continuum observations with the VLA (Gavazzi et al., 1995) a tail extending up to 75 kpc (Gavazzi et al., 2001) on the side opposite to bright H II regions. The star formation takes place in bright H II regions distributed along curved paths on the galaxy periphery facing the cluster center, but no obvious extraplanar star-forming regions or dust trails are seen at 8μm (Sivanandam et al., 2014). Observations in the 21 cm line of HI (e.g., Gavazzi et al., 1989) revealed that the galaxy has a slightly deficient HI content, displaced in the direction marked by the radio continuum tail. Finally, Sivanandam et al. (2010) detect significant emission of warm H2 within the galaxy and in a portion of its tail in the extracted spectra. The galaxy is classified as star-forming in the DR7 (Abazajian et al., 2009) and DR8 (Aihara et al., 2011).

- UGC6697 presents a 100 kpc tail of ionized gas mapped with MUSE that detected Hα emission, and to a lesser extent, Hβ, [OIII]λ5007, and [OI]λ6300 (Consolandi et al., 2017). According to the BPT classification (see Figure 14 in Consolandi et al., 2017), compact knots of star formation lie outside the stellar disk along the northern and to a lesser extent the southern periphery of the tail. Roughly half of the spaxels are consistent with 70% of the ionization coming from shocks. The main body of the galaxy appears to be consistently photoionized by stars. Thus, this galaxy does not seem to host an AGN at its center. This galaxy also shows an impressive HI tail, coinciding with a radio continuum tail (Gavazzi et al., 1995), that extends at least 70 kpc to the north-west of the nucleus, with an increasing offset from the plane of the optical galaxy (Scott et al., 2010). CGCG 97087, the nearby galaxy of UGC 6697, was detected in X-rays (although no tails are observed) by Sun & Vikhlinin (2004), who speculated that the X-ray emission arises from the gas heated by active star formation triggered by the tidal force of UGC 6697. However, the large difference between the recessional velocity of UGC 6697 and CGCG 97087 suggests that, if any, only a mild gravitational interaction occurred (Consolandi et al., 2017). On the other side, other gravitational interactions, for instance, with the giant elliptical NGC 3842, cannot be excluded a priori.

- 2MASXJ11443212+2006238 shows of an Hα trail of 85 kpc projected length behind the galaxy (Gavazzi et al., 2001). Also, Yagi et al. (2017) observe a truncated star formation at the southern side (opposite to the tail). According to the SDSS DR8 classification, the galaxy center is dominated by star-formation.

- NGC4254, with deep Hα + [NII]narrow-band and GALEX UV images, reveals the presence of 60 compact (70-500 pc radius) star-forming regions up to ~ 20 kpc outside the optical disc of the galaxy (Boselli et al., 2018). The stripped material has been detected in HI out to 250 kpc, thus H II regions clearly visible only in the GALEX UV bands are totally absent in the outer HI tail. Finally, the presence of a radio continuum extended tail (Kantharia et al., 2008) suggests that the galaxy is suffering ram pressure stripping. The X-ray distribution is disturbed along a similar pattern to radio and optical emission, but shows no out-of-disk emission or shocks that could imply strong ram pressure forces (Chyży et al., 2007). Davies et al. (2020) show the NII-BPT diagram of the galaxies in the LLAMA survey, among which NGC4254 is part. By using an X-shooter long-slit spectrum extracted from a $1.8'' \times 1.8''$ aperture, the central emission of the galaxy is consistent with ionization from an AGN.

- NGC4388 is a rare example in which the tail is observable in the X-ray, Hα, and H I phases. From deep Hα imaging Yoshida et al. (2002) discovered a very extended ionized region near the galaxy. The region was spectroscopically observed with the Faint Object Camera and Spectrograph (FOCAS) at the Subaru Telescope (Yoshida et al., 2004), confirming that the region has a recessional velocity comparable to that of NGC4388 and that the Hα tail would have been made by ram-pressure stripping. Oosterloo et al. (2005) observed the region in H I 21 cm with the Westerbork Synthesis Radio Telescope and found that the H I tail extends to $>$ 120 kpc from NGC4388. X-ray gas near the tail of NGC 4388 was associated with the galaxy by Weżgowiec et al. (2012). The ram-pressure stripped gas observed out to 35 kpc from the galaxy disk was found to be ionized mostly by the radiation of an active nucleus (Boissier et al., 2012). Boissier et al. (2012) observe no obvious optical or FUV counterparts in the tail with GALEX data. This source is classified as 'S1h' (i.e., broad polarized Balmer lines detected) in the V2006c

(Veron-Cetty et al., 2006; Boselli et al., 2015).

- NGC4402 has been established as being actively ram pressure stripped via the detection of a prominent radio continuum tail (Crowl & Kenney, 2006) and of an HI tail (Abramson et al., 2016). Also, the galaxy has radially truncated star formation (Abramson et al., 2016). Furthermore, Crowl et al. (2005) found the stellar disk of NGC4402 to be undisturbed, ruling out any strong influence from tidal interactions on the structure of the galaxy.

- NGC4424 shows a H I tail of ~ 110 kpc (in projected distance) in the southern direction indicating that this galaxy is undergoing a ram pressure stripping event (Boissier et al., 2012; Boselli et al., 2018). The FUV image shows no wide-spread star formation in the gas outside the galaxy (Boissier et al., 2012). Boselli et al. (2018) observe the gas is photo-ionized in the inner regions and shock-ionized in the outer parts though MUSE BPT diagrams. The activity of star formation in the outer disc is thus completely quenched. Chandra and XMM X-ray data do not show a compact source in the nucleus or an extended tail of hot gas (Boselli et al., 2018).

- NGC4438 shows extraplanar gas in all ISM phases, from molecular hydrogen observed in CO to atomic hydrogen, warm ionized gas observed in Hα, hot ionized gas observed in X-ray, magnetic fields and cosmic ray electrons observed in the radio continuum (see Vollmer et al., 2009, and references therein). The extraplanar H I gas in NGC 4438 has an approximately linear structure with a total size of ~9.8 kpc and is displaced from the disc by ~4.1 kpc (Hota et al., 2007). GALEX NUV and FUV images show an extended (~ 20 kpc) tail at the northwest edge of the galaxy (Boselli et al., 2005). While it is agreed that the distortion of the stellar content of NGC 4438 is due to a high-velocity tidal interaction with NGC4435 (Kenney et al., 1995), different mechanisms were put forward to explain the displacement of all ISM phases. In fact, ram pressure plays a key role in the evolution of the gaseous component of NGC 4438 together with the tidal interaction. The displacement of the line profiles to higher velocities in the southwestern region of the galaxy, the lack of CO emission in the eastern optical disk, and the presence of double line profiles in the southwest of the galaxy center are clear signs of RPS (Vollmer et al., 2009). Recent star formation events are also present at the edge of the northern arm and in the southern tail, while totally lacking in the other regions, which are dominated by the old stellar population that was perturbed during the dynamical interaction with NGC 4435 (Boselli et al., 2005). This source is classified as LINER (i.e., S3b, meaning "Seyfert 3 or LINER with broad Balmer lines") in the Veron-Cetty Catalogue (2003) (V2003c, hereafter Veron-Cetty et al., 2003; Ho et al., 1997).

- IC3418 has a spectacular 17 kpc length UV-bright tail comprised of knots associated to star formation triggered by the interaction with the intergalactic medium (Arrigoni et al., 2010). The only Hα emission detected in the imaging is from 8 discrete HII regions in the outer half of the tail, at distances ranging from 10 to 17 kpc from the galaxy center (Kenney et al., 2014). The galaxy is classified as LINER in the (Toba et al., 2014) catalog [2].

- NGC4501 presents an enhanced polarized emission in its southeastern region due to a stripping event, with the ICM hitting the disk ISM nearly edge-on. The observed southwestern ridge of 6 cm polarized radio-continuum emission (Vollmer et al., 2007) is located at the outer edge of the Hi distribution. Both show the same rapid increase at the edge, which is expected in a ram pressure scenario. Along the gas ridge, a faint Hα emission ridge is also present. The galaxy is classified as Seyfert 2 in the V2003C (Veron-Cetty et al., 2003).

- NGC4522 is particularly interesting as it is the nearest example among only a few ram-pressure-stripped cases where extraplanar molecular gas has been identified (e.g., Vollmer et al., 2008; Jáchym et al., 2014, 2017) with 30% of H I and 15% of CO (2–1) found outside of the stellar disk (Lee et al., 2018). NGC 4522 also

---

[2] link to the catalog: Catalog:2017yCat..17880045T

exhibits a warm H_2 tail approximately 4 kpc in length (Sivanandam et al., 2014). Ten percent of the Hα emission arises from extraplanar H II regions that are exclusively located to the west of the galactic disk (Vollmer et al., 2004). Both 20 and 6 cm total emission distributions are asymmetric with an extended component to the west, where the extraplanar atomic gas and Hα emission are located (Vollmer et al., 2004). On the easter side of the galaxy (the other side with respect to the direction of the gas stripping) there is an extraplanar arm of young, blue stars, but only one area with ISM and ongoing star formation, which is located at the top of the upturn, ~2 kpc from the disk plane (Abramson et al., 2016). It has been proposed that the extraplanar SF regions are part of a distinct extraplanar arm or arm-like structure formed during stripping (Vollmer et al., 2008).

- NGC4569 shows strong evidence for ongoing ICM–ISM interaction. H I gas is located within the stellar disc of the galaxy and has a truncated radial distribution that is typical of H I-deficient cluster galaxies (Chung et al., 2009). This is also the case for the distribution of the molecular gas (Helfer et al., 2003). The diffuse soft X-rays emission extends to the west coinciding with a giant H I and Hα arm, which likely represents the gas stripped from the disc about 300 Myr ago (Vollmer et al., 2004). It is conceivable that the observed tail of ionized gas is just a projection on the plane of the sky, thus 80 kpc is a lower limit to the real height of the cylinder. This source is classified as “Seyfert" in the V2003c (Veron-Cetty et al., 2003).

- The following list of galaxies are presented in the catalog of RPS candidates by Roberts et al. (2020) and, according to SDSS DR8, do not host AGN activity at their centers: GMP6364, GMP5821, GMP5382, GMP4688, GMP4437, GMP4463, GMP4281, GMP4236, GMP4159, GMP4135, GMP4106, GMP3618, GMP3253, GMP3143, GMP2625, SDSSJ130006.15+281507.8, GMP2073, GMP1616, GMP1582, GMP713, GMP672, GMP597, GMP522, GMP455, GMP406, GMP223, SDSSJ130545.34+285216.8, SDSSJ130553.48+280644.7, see Roberts et al. (2020); Salim et al. (2018, 2016)

- IC3913 has been observed with GALEX by Smith et al. (2010). It is a spiral with a distinct opening of the spiral arms to the south-west, and an enhancement of star formation to the north-east. Studies in H I (Bravo-Alfaro et al., 2001), in Hα (Gavazzi et al., 1998) and in radio continuum (Miller et al., 2009) have not suggested strong stripping in this galaxy. However, the opening arm is suggestive of ongoing unwinding (see e.g., Vulcani et al., 2022), as also confirmed by Roberts et al. (2020) which present this galaxy among the list of RPS candidates. The galaxy is classified as star-forming both by Mahajan et al. (2010) and the SDSS DR8.

- GMP4629, among the RPS candidate in Roberts et al. (2020), shows an asymmetric extension in the GALEX image (Smith et al., 2010). In the MegaCam data, multiple blue knots are seen to the north-west of the galaxy, away from the cluster centre. The Hα imaging shows secondary emission peaks to the north and north-west of the core. GMP 4629 lies close in projection ($0.7'$ or 20 kpc) to an elliptical galaxy (GMP4648), with 300 km/s radial velocity difference, and hence a tidal interaction is possible in this case. Chen et al. (2020) observed a very faint and small tail of 2.8 kpc in the radio continuum. The galaxy does not host an AGN according to the SDSS DR8 classification.

- GMP4570 is a distorted spiral galaxy, for which the GALEX image shows a clumpy UV extension to the west, away from the cluster centre, and is confirmed as an RPS candidate in Roberts et al. (2020). Hα is not detected from this object in the INT narrow-band imaging, because its large velocity with respect to the cluster shifts the emission line outside of the filter profile. In the Hα image shown by Chen et al. (2020), though, it is visible a clumpy and faint tail. The u-band MegaCam image in Smith et al. (2010) shows some trails and knots, coincident with the UV peaks, extending at least $0.4\,'$ (12 kpc) from the galaxy centre. The galaxy has a radio tail of 3.9 kpc (Chen et al., 2020) and does not show AGN activity according to Mahajan et al. (2010).

- GMP4555 in the GALEX imaging reveals a UV plume to the west, oriented away from the cluster centre (Smith et al., 2010). In the MegaCam u-band data, the inner part of the plume is delineated by faint filaments extending to the south-west. The Hα emission is also asymmetric and extended to the south-west, as also shown in Chen et al. (2020). Miller et al. (2009) note that the radio emission is offset from the galaxy and suggestive of ram-pressure stripping and Chen et al. (2020) confirm a radio tail of 9.1 kpc in extent. The X-ray morphology also appears extended to the west in Fig. 3 of Finoguenov et al. (2004). Interestingly, this is not a confirmed RPS candidate in Roberts et al. (2020). It has a star-forming nucleus according to Mahajan et al. (2010).

- NGC4848 is the brightest galaxy in the sample, a spiral with a disturbed inner morphology and a faint extension to the north-west visible in the MegaCam imaging (see also Roberts et al., 2020). GALEX data show trails pointing north-west away from cluster centre, certainly to 1.4 ′ (40 kpc), and tentatively to twice this distance. The INT Hα images show an asymmetric distribution of emission in the core, and a stream of emitting knots to the north-west of the galaxy, some of which are coincident with compact blue sources in the MegaCam imaging, also observed in the Subaru Hα map in Chen et al. (2020). GMP 4471 is also deficient in total H I (Gavazzi et al., 2005). Vollmer et al. (2001) discussed the peculiar morphology in CO, H I and Hα, and proposed this object as a 'post- stripping' galaxy, i.e. one which has already passed through the cluster. Finally, Finoguenov et al. (2004) noted a tail of X-ray emission to the north-west of GMP 4471, making it one of very few galaxies known to exhibit a stripping trail in hot gas. Finally, Chen et al. (2020) observe a radio tail of 12.6 kpc and Mahajan et al. (2010) classify the nuclear emission as SF.

- NGC4853 shows detached clouds in the Suprime-Cam Hα image (Yagi et al., 2010). This galaxy is, however, not presented as an RPS candidate in Roberts et al. (2020) nor shows an Hα or radio tails according to Chen et al. (2020). Thus this galaxy represents a really weak case of RPS. The SDSS spectrum shows a high [NII]/Hα ratio of ~ -0.85, which may indicate a weak active galactic nucleus (AGN).

- IC3949 exhibits core star formation and extended Hα emission connected to the core (Yagi et al., 2010) and is classified as a Seyfert 2 according to Mahajan et al. (2010). Chen et al. (2020) detects a really faint Hα tail but without an associated radio continuum emission.

- NGC4858 is confirmed as an RPS candidate in Roberts et al. (2020). This disturbed barred spiral presents a 'jellyfish' morphology in the GALEX image and in the MegaCam data, especially in the u band (Smith et al., 2010). Several tails and knots, are seen in a broad fan-like distribution (see also Yagi et al., 2010), extending 0.5 ′ (15 kpc) to the north-west, away from cluster centre. There are strong variations in Hα versus UV flux ratio among the various filaments; in particular the brightest UV structure is not coincident with the strong central Hα feature. The galaxy is deficient in H I, based on the upper limit to the gas mass published by Gavazzi et al. (2005). The galaxy is observed close in projection (0.6 ′ or 20 kpc) to a large elliptical, GMP3792, with 1500 km/s radial velocity difference. It is possible that these galaxies are physically interacting, although their relative velocity is quite large compared to the characteristic internal velocities, and hence strong mutual interactions are unlikely. The Hα tail is also reported by Chen et al. (2020) together with a radio tail. The galaxy is SF in the SDSS DR8.

- Mrk 58 is confirmed as an RPS candidate in Roberts et al. (2020). According to Yagi et al. (2010), the galaxy exhibits core star formation and extended Hα emission connected to the core. Chen et al. (2020) observe a radio tail of 5.8 kpc. The galaxy is SF in the SDSS DR8.

- GMP3271 is confirmed as an RPS candidate in Roberts et al. (2020). According to Yagi et al. (2010), GMP3271 shows galaxy-wide star formation and some regions of Hα emission have flown out of the galaxies entirely. Chen et al. (2020) observe a radio tail of 2.9 kpc. The galaxy is SF in the SDSS DR8.

- GMP3071, according to Chen et al. (2020), does not show a radio tail, but shows along Hα tail with knots and diffuse emission, as also reported from Yagi et al. (2010) previously. It is not among the Roberts et al. (2020) RPS candidates, though. The galaxy is classified as SF in the DR8.

- D100 is an irregular or spiral galaxy, which has a post-starburst spectrum in the disc region, with the burst age estimated at 250 Myr and ongoing star formation (Caldwell et al., 1999). Mahajan et al. (2010) classify this galaxy as an AGN based on SDSS DR7 data. The GALEX image shows a narrow tail of length $\sim 0.5'$ (15 kpc), extending to the north-east. Stripping in this galaxy was first discussed by Yagi et al. (2001), who reported a 60-kpc Hα tail, which is also seen in the INT Hα imaging of Smith et al. (2010). This remarkably narrow and straight feature is also clearly seen in deep u-band images, and is co-located with the UV trail. The presence of continuum emission suggests that star formation is taking place in the stripped material, not merely ionization of a purely gaseous tail as proposed by Yagi et al. (2001). In Chen et al. (2020), they reported a radio tail of 8.1 kpc. The galaxy is also among the Roberts et al. (2020) RPS candidates.

- GMP2599 appears distorted in the GALEX image, showing broad streaks that point south-east away from the cluster centre, in the same direction of the long radio tail detected by Chen et al. (2020). Some faint knots are visible in the MegaCam images (Smith et al., 2010). Gavazzi et al. (2005) detected the galaxy in H I but indicating that it is strongly gas deficient. The galaxy is among the Roberts et al. (2020) RPS candidates. This galaxy is considered as an AGN candidate due to the presence of an X-ray point-like source in the galaxy center detected by Nucita et al. (2017) and Birchall et al. (2020). However, the AGN is not visible in the optical (see Mahajan et al., 2010).

- IC4040 shows a long Hα tail and a smaller radio tail of 9.1 kpc (Chen et al., 2020). Smith et al. (2010) show the GALEX image which reveals a plume of emission towards the south-east, and three compact sources to the south-west. At very low surface brightness levels, the region between these two features appears to be filled by faint diffuse UV emission. Co-located with the UV plume, also Smith et al. (2010) observe an Hα trail extending at least 1.4 $'$ (40 kpc), with secondary Hα peaks at 12, 23 and 28 kpc from the nucleus.

- NGC4921, shown in Kenney et al. (2015), present HST V and I images of the face-on Coma cluster spiral galaxy NGC4921 showing remarkable dust extinction features. VLA H I maps show a truncated and highly asymmetric H I disk with a compressed H I distribution in the NW, providing evidence for ram pressure acting from this side. Where the H I distribution is truncated in the NW region, HST images show a well-defined, continuous front of dust that extends over 90 degrees and 20 kpc. This dust front separates the dusty from dust-free regions of the galaxy, and the authors interpret it as galaxy ISM swept up near the leading side of the ICM-ISM interaction. The morphology of these features strongly suggests that dense gas clouds partially decouple from surrounding lower density gas during stripping, but decoupling is inhibited, possibly by magnetic fields that link and bind distant parts of the ISM. The galaxy is classified as 'Broadline' AGN in the SDSS DR8.

- NGC4911: Bravo-Alfaro et al. (1999) show that the galaxy is H I deficient in the disk. Chen et al. (2020) detect a short Hα tail and radio emission in the galaxy, but not in the tail. However, the radio continuum is asymmetric, with an extension towards the short Hα tail. NGC4911 is classified as a LINER in Mahajan et al. (2010) and it has a strong X-ray point-like source at its center. The classification criteria applied by this work consists, in brief, of computing the [NII]/Hα ratio from DR7 SDSS spectra and seeing if this is greater than -0.2, i.e. the so-called Miller et al. (2003) criteria.

- ESO 137 - 001 is located in the Norma cluster (A3627; $M_{dyn} \sim 1 \times 10^{15}$ $M_{\odot}$, σ = 925 km/s, where M_{dyn} is the dynamical mass of the cluster and σ is the cluster galaxies' velocity dispersion) and is one of the nearest "jellyfish galaxies" ($z = 0.016$,

$M_*/M_\odot = 9.6$ Sun et al., 2010, see Figure 2.2) with an 80 kpc-long X-ray (Jáchym et al., 2014) associated with a shorter and broader Hα tail with over 30 HII regions up to 40 kpc from the galaxy (Sun et al., 2007), a warm H2 tail and compact CO regions extending to nearly 60 kpc in length and 25 kpc in width (Jáchym et al., 2019) (Sun et al., 2006, 2010, 2007; Sivanandam et al., 2010; Fossati et al., 2016). By exploiting MUSE IFU data, Fossati et al. (2012) observe modest ratios for [OIII]/Hβ, [NII]/Hα, and [OI]/Hα consistent with ionization from a soft spectral energy distribution. Thus, in agreement with the X-ray analysis of Sun et al. (2010), the nuclear emission of ESO 137-001 is powered by star formation activity and the galaxy does not host a strong AGN.

- MACSJ1258-JFG1 shows signature of RPS in images of clusters from the Massive Cluster Survey (MACS Ebeling et al., 2001) obtained with ACS aboard HST according to Ebeling et al. (2014) and (McPartland et al., 2016). MACSJ1258-JFG1 is known to host an active galactic nucleus (AGN) and is classified as a QSO in the DR8, and has an X-ray point-like source overlapping the optical center according to RASS data (Anderson et al., 2007).

- JO147: Merluzzi et al. (2013) report extraplanar gas in the MMTF Hα image combined with the UKIRT K-band (red) image in Figure 6. The most noticeable feature of the Hα image are the compact knots of Hα emission seen all along the NW side of the disc and there are no such Hα features on the SE side. Some of these knots seem 'tethered' to the disc by faint filamentary strands. The most distant knot is seen at ~13 kpc (in projection) from the galaxy major axis, but most knots are much closer, within 3–4 kpc of the disc. All of these knots and filamentary structures are completely absent in the MMTF continuum image, confirming that this is from Hα emission with little if any underlying stellar continuum component. They plot in the NII-BPT - built up using WiFes IFU spectra - 114 regions of the galaxy and find that star formation and shocks are the predominant ionization mechanisms in the tails.

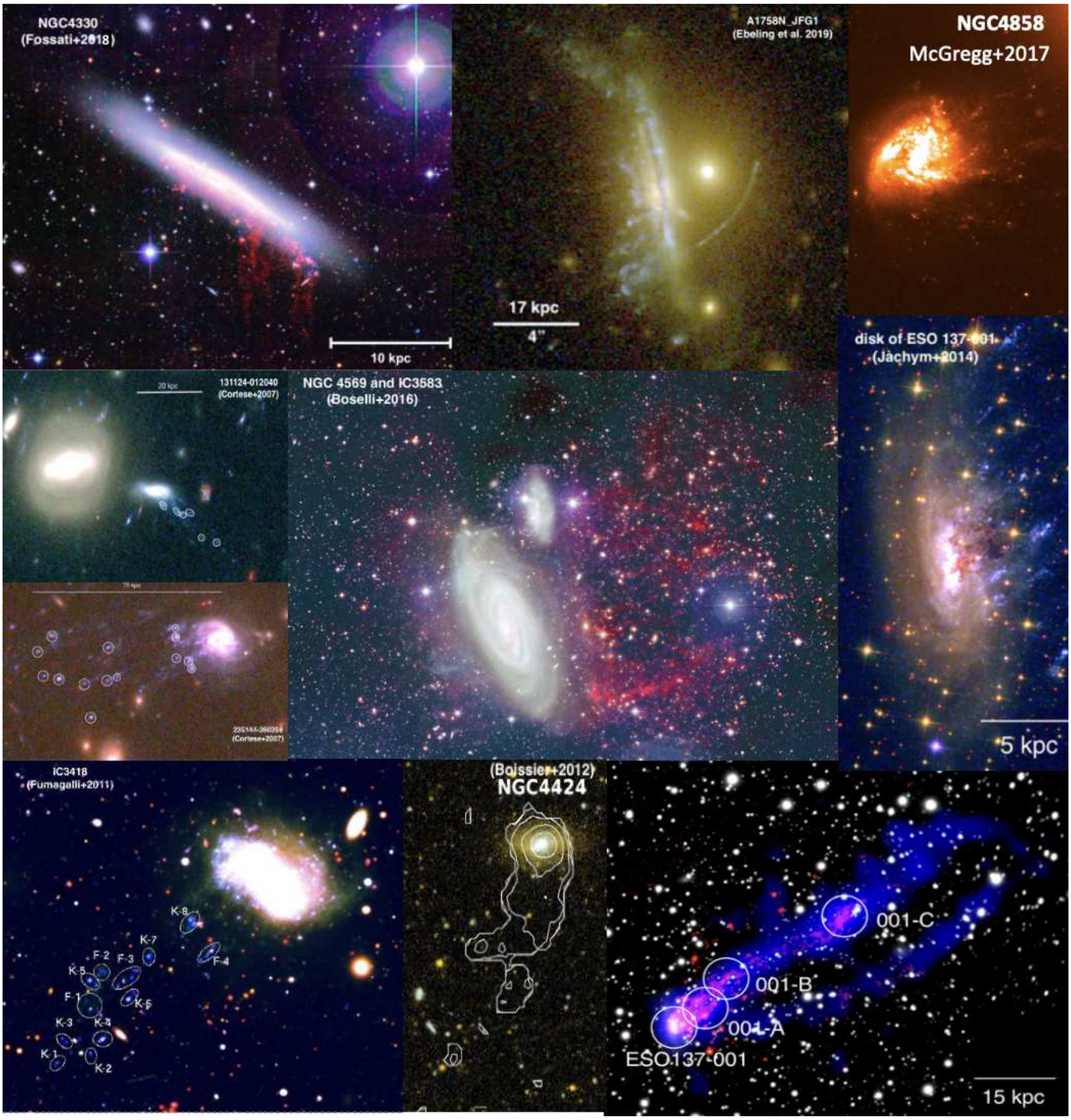

Figure 2.2: Mosaic of jellyfish galaxies from the LIT-RPS. *Top row (from left to right panel)*: pseudo-colour image of NGC 4330 obtained from CFHT NGVS broad-band and VESTIGE narrow-band images (Hα emission is in red Fossati et al., 2018); HST/ACS image of A1758N_JFG1 (Elagali et al., 2019); image of NGC4858 with the extremely wide (X) and long-pass (LP) filter F350LP on the WFC3/UVIS camera mounted on HST (Gregg et al., 2017). *Middle row (from left to the right panel):* RGB colour image of 235144-60358 in Abell 2667 (upper panel) and of 131124-012040 in Abell 1689 (lower panel) with the F450W, F606W and F814W filters on HST (Cortese et al., 2007); pseudo-colour image of the system NGC 4569 + IC 3583 obtained combing the CFHT MegaCam NGVS optical g (blue) and i (green) images with the Hα+[NII] narrow-band image (red) (Boselli et al., 2016); HST image of the disk of ESO 137-001 (Jáchym et al., 2014); *Bottom row (from left to right panel):* high contrast RGB picture of IC3418 obtained from the LBT images combininf the U-spec, g-SDSS, i-SDSS filters (Fumagalli et al., 2011); GALEX FUV/NUV image of NGC4424 with VLA HI surface density contthes superimposed (Boissier et al., 2012); composite X-ray Chandra (blue) / Hα SOAR (red) image of ESO 137-001 with CO (2–1) beams (FWHM = 25″ ≈ 8.4 kpc) of the APEX telescope.

- SOS61086: Merluzzi et al. (2016) show the WiFeS narrow-band Hα image and the distribution of Hα emission, which are complementary and together show different aspects of the distribution of ionized gas. The IFS data show that ionized gas spreads out from the disc of the galaxy in an approximately triangular region with a vertex in the central disc and one side at ~16 kpc north and directed approximately EW. No ionized gas is found in the disc beyond ~6 kpc from the centre along the major axis. Along the minor axis, instead, the ionized gas appears to extend far out from the disc in projection. Other clumps of gas extend further in the north reaching ~30 kpc in projection. The [NII]- and [SII]- BPT show that there is no emission consistent with ionization from an AGN in the galaxy. Although some of these features can be suggestive also of tidal interaction, the hydrodynamical simulations of RPS well reproduce the overall gas velocity field of the galaxy and supports a scenario where ongoing RPS is the dominant mechanism at work.

- SOS90630 appears truncated in the ESE side from Hα image and the distribution of Hα emission from IFS . Gas extending ~4 kpc in projection out of the disc is seen in the NW side, and more prominently along a tail extending by more than 41 kpc to the west. The maximum of Hα emission takes place in the centre of the galaxy, and is resolved into two clumps about 1 kpc apart in the narrow-band image. The MMTF image resolves an arc-shaped crown composed of Hα-emitting knots all long the leading edge of the galaxy. Other knots of Hα flux are detected along a western arm and in the tail. The overall morphology of the Hα emission is a remarkable example of the classic 'jellyfish' forms reproduced in simulations of galaxies undergoing RPS. The SFR drops abruptly in the external disc and is low in the tail. The BPT diagrams for SOS90630 show that the galaxy is SF at its center and present no evidence that shocks play a role in the excitation of the gas within the main body of the galaxy, or within its extended tail.

- d1, d2, d3, d4, d5, d6, d7 and A1758N, see Figure 2.2), are located in the A1758 cluster and are proposed as RPS candidates by Ebeling et al. (2019) based on their disturbed morphology in HST/ACS images. By analyzing their gas properties with DEIMOS spectra, Ebeling et al. (2019) demonstrate that all eight RPS candidates are undergoing a period of intense star formation. In addition, the location of the most massive galaxies (A1758N and d5) among the targets in the composite region of the BPT diagram is consistent with modest nuclear activity.

- C153 exhibits a plume stretching toward the cluster center seen in soft X-rays by Chandra, parts of which are also seen in [OII] emission and near-UV continuum light (Owen et al., 2006). C153 shows AGN-like emission in the NII-BPT using KPNO 4 m Mayall telescope (slit widths $1.5''$-$2''$) and GEMINI optical spectra (Owen et al., 2006). Also, the presence of a steep and compact radio core in VLA observations suggests that this galaxy is hosting an AGN.

- ESO137-002 shows a ~ 40 kpc narrow X-ray tail (Sun et al., 2010; Zhang et al., 2013) with a constant width of ~3 kpc (Zhang et al., 2013). ESO 137-002 also features double Hα tails extending ~20 kpc from the nucleus without any H II regions identified (Sun et al., 2010). The secondary tail (~12 kpc) resides at a distance of ~7.5 kpc from the nucleus at a ~23° to the main tail. The Hα main tail is spatially coincident with the X-ray tail. Laudari et al. (2022) do not detect any active SF in the X-ray and Hα tails of ESO 137-002 with the HST data. Also, there is no CO upstream and abundant CO downstream and in the inner tail region, according to APEX observations (Laudari et al., 2022). ESO 137-002's nucleus hosts an obscured, Seyfert2-like AGN from the X-ray data (Sun et al., 2010; Zhang et al., 2013). The HST data reveal that the nuclear region is indeed heavily obscured by dust, without a nuclear point-like source in the optical and NIR (Laudari et al., 2022)

- Sausage 5, Sausage 6, Sausage 7, Sausage 8 and Sausage 9 are galaxies in the CIZAJ2242.8+5301 cluster showing tails and gas outflows, thus proposed as RPS candidates (based on Gemini/GMOS-N integral field unit (IFU) observations) by Stroe et al. (2020). More than that, Sausage 8 and 9 have [NII]/Hα and [OIII]/Hβ

ratios consistent with AGN ionization according to DEIMOS optical spectra (Stroe et al., 2015).

- 235144-260358 shows a disturbed morphology in the HST RGB image, with clear indications of stripping within its optical disc and a prominent one-armed spiral component as is typically observed in gravitationally perturbed systems (Cortese et al., 2007). The radio contours appear elongated in the direction of the trail. A similar morphology seems also to be present in the Spitzer 8-μm map, which has the appearance of a head on the galaxy, with a tail tracing the current star formation associated with the blue knots. The [OII] emission, not associated with any of the blue knots, extends from the galaxy for a total length of at least ≈ 50 kpc (see Fig. 8), suggesting the presence of diffuse ionized gas along the trails as already observed in nearby ram pressure stripped galaxies. Finally, the 2– 10 keV/24 μm flux ratio is at least four times too low to lie within the range of typical AGN, and also from line ratios in the optical emission a significant contribution from an AGN is ruled out: log([OIII]/Hβ) -0.45, log([NII]/Hα) -0.33 (Cortese et al., 2007).

2.3 MaNGA sample

2.3.1 Observing Strategy and Data Reduction

MaNGA (Mapping Nearby Galaxies at Apache Point Observatory, Bundy et al. 2015) is an integral-field spectroscopic survey observing galaxies at $0.01 \leq z \leq 0.15$ using the BOSS Spectrograph (Smee et al., 2013) mounted at the 2.5 m SDSS telescope (Gunn et al., 2006). The MaNGA survey is one of the three components of SDSS-IV (Blanton et al., 2017). MaNGA galaxies are selected to be representative of the overall galaxy population for $\log(\mathrm{M}_{\odot}/\mathrm{M}_{\odot}) > 9$. The sample is drawn from an extended version of the NASA-Sloan catalogue (NSA v1_0_13 Blanton et al., 2011). MaNGA observations are carried out with 17 hexagonal fiber-bundle integral field units (IFUs) that vary in diameter from 12″ (19 fibers) to 32″ (127 fibers). Each fiber has a diameter of 2″ (Drory et al., 2015). The IFUs feed light into the two dual-channel BOSS spectrographs, that provide simultaneous wavelength coverage in the 3600–10300 Å wavelength range, with a resulting spectral resolution of R ~ 1400 at λ ~ 4000 Å and R ~ 2600 near λ 9000 Å (R ~ 2000 corresponds to a velocity dispersion of σ ~ 70 km/s Smee et al., 2013). A uniform radial coverage to radii of 1.5 R_e and 2.5 R_e is achieved for 2/3 (Primary sample) and 1/3 (Secondary sample) of the final sample, respectively. In order to compensate for light loss during observations, a three-point dithering pattern is used, allowing also to obtain a uniform point spread function (PSF Law et al., 2015).

The data analysed in this work are part of the fifteenth SDSS Data Release (DR15 Aguado et al., 2019), reduced according to the algorithms described in Law et al. (2016) and Yan et al. (2016) and subsequent updates. The data release includes the output of the MaNGA data analysis pipeline (DAP Westfall et al., 2019; Belfiore et al., 2019) for a sample of 4688 spatially-resolved galaxies. Integrated galaxy global properties such as redshift and star-formation rate are drawn from the Pipe3D-v2_4_3[3] catalog, which contains integrated properties, characteristic and gradients of different quantities for 4656 galaxies. I draw properties such as emission line fluxes (*gflux*), elliptical effective radius (R_e), inclinations and de-projected distances from the drpall-v2_4_3 using the online tool MARVIN[4] (Cherinka et al., 2019). The de-projected coordinates are computed using the ellipticity (ϵ = 1-b/a) and position angle (θ) measured from the r-band surface brightness. Effective radii and inclinations are used throughout this work to construct de-projected radial gradients. I select spaxels having a S/N > 1.5 (which is the value typically adopted in MaNGA Belfiore et al., 2019) for the same emission line fluxes listed in Section §2.1.2. The emission lines are fitted with a Gaussian function and are corrected for stellar absorption, since the Data Analysis Pipeline (DAP; Westfall et al., 2019; Belfiore et al., 2019) simultaneously fits the continuum and emission lines with the latest version of the pPXF software package (Cappellari, 2017). All lines are also

---

[3] https://www.sdss.org/dr16/data_access/value-added-catalogs/?vac_id=manga-pipe3d-value-added-catalog:-spatially-resolved-and-integrated-properties-of-galaxies-for-dr15

[4] https://www.sdss.org/dr16/manga/marvin/

corrected for Galactic extinction, using the Schlegel et al. (1998) maps (Westfall et al., 2019) and the reddening law of O'Donnell et al. (1994). Following the same approach used in GASP, I correct the emission lines for host galaxy dust attenuation using the Cardelli et al. (1989) law and assuming an intrinsic Balmer decrement $\mathrm{I(H\alpha)/I(H\beta)} = 2.86$, appropriate for an electron density n_e=100 cm^{-3} and electron temperature $T_e = 10^4$ K (Osterbrock, 2006).

2.3.2 Total galaxy masses

Spatially resolved stellar masses in the MaNGA sample are available in the MaNGA FIREFLY VAC (Sánchez et al., 2016) variants (1) FF- Mi and (2) FF-Ma; (3) in the Principal Component Analysis (PCA) VAC (Pace et al., 2019a,b); (4) in the Pipe3D VAC, and (5) total galaxy masses in the NASA SLoan Atlas (Blanton et al., 2011; Wake et al., 2017, NSA;). The total mass in (1)-(4) is simply the sum across the MaNGA field-of-view, where the mass inside each spaxel is computed by performing a spectral fitting of the stellar component and retrieving the mass-to-light ratio from the best fit. Instead, the NSA stellar masses are estimated by the k correct code (Blanton & Roweis, 2007) applied to the five-band SDSS photometric images of the total galaxy. I chose to use the stellar masses in the Pace et al. (2019b) catalog since the authors use a method similar to that in GASP to compute the stellar mass inside the MaNGA fiber and provide also approximate aperture corrections to estimate total galaxy stellar mass. The mass within the fiber is computed by fitting the optical spectra of galaxies with a basis set of six vectors obtained from principal-component analysis of a library of synthetic spectra of 40'000 star-formation histories (SFHs). Then, the aperture correction takes into account the galaxy mass residing in the region extending outwards with respect to the 1.5 R_e aperture and is recovered with the Color-Mass-To-Light Relations (CMLR) method, which employs relations (as the one in Pace et al., 2019a) between the mass-to-light ratio and the photometric colors of the galaxy's light outside the MaNGA IFU.

3 | METHODS

In this Chapter, I will give an overview of the tools typically used to discriminate among the different ionization sources acting on the gas, and the main methods employed to measure the gas-phase metallicity in case of ionization due to young stars or the presence of an AGN.

Among the diagnostics used to state which mechanism is the main driver of the gas emission, the Baldwin, Philips and Terlevich (BPT) diagrams are typically the most commonly used, which make use of the diagnostic power of a combination of line ratios (e.g., [N II]/Hα versus [O III]/Hβ). For completeness, I will also discuss strengths and weaknesses of the so-called WHAN (Fernandes et al., 2010) diagram, which are used to spot 'fake AGN' (i.e. ionization from old stars) by combining the information coming from the Hα line equivalent width and the line ratio [N II]/Hα (used in the BPTs). As I will show in this dissertation, the galaxies in this Thesis' samples globally do not show a significant contribution to the ionization from old stellar populations, presumably as a consequence of the fact that these are active and star-forming galaxies. For this reason, in the end, I sticked to the commonly used BPT classification to state the spaxel-by-spaxel ionization mechanisms acting on the gas (see Section 3.1).

Secondly, I will summarize the different methods developed up to now to compute the gas metallicity, either directly through temperature-sensitive auroral lines or indirectly through the comparison between observations and photoionization models from Cloudy or Mappings. I will briefly describe the main reasons why, if one side the direct method is preferable to measure the metallicity in star-forming galaxies when auroral lines are detectable, on the other side this is not the preferable method for the AGN-ionized regions (see Section 3.2) To give a complete census of the main methods employed to measure the AGN metallicity, I will present the strong emission line (SEL) calibrators, based on photoionization models, available in the literature (Storchi-Bergmann et al., 1998; Carvalho et al., 2020) and I will compare the results obtained by using different SEL calibrators (see Section 3.2.4).

However, the main aim of this work was to measure the gas metallicity in both H II and AGN-ionized regions. The results obtained with calibrators generated in different works in case of SF and AGN ionized regions strongly depend on the assumptions made to obtain these calibrators and, for this reason, the use of a set of photoionization models generated in a coherent way assuming ionization from stars and AGN was necessary. Particularly, I will describe the sets of AGN and H II models available in the literature generated by making consistent assumptions, and I will present in this Thesis photoionization models generated ad hoc for this work. I will discuss the reasons that lead me to generate a new set of models, which encompass the main issues affecting those already available from previous works.

3.1 Classification of the ionization mechanism: BPT and WHAN diagrams

Baldwin et al. (1981) (BPT herefater) demonstrated that it was possible to distinguish type 2 AGNs from normal star-forming galaxies by considering the intensity ratios of two pairs of relatively strong emission lines (but see also, Dessauges-Zavadsky et al., 1987).

In fact, the physical difference that distinguishes a narrow-line AGN (e.g., Seyfert 2, without broad lines) from an H II region-like object resides in the weakness of low-ionization lines such as [N II]λ6583, [S II]$\lambda\lambda$6716, 6731, and especially [O I]λ6300. The [N II], [S II] and [O I] emission lines arise preferentially in a zone of partly-ionized hydrogen (Veilleux & Osterbrock, 1987). This zone is quite extended in objects photo-ionized by a spectrum containing a large fraction of high-energy photons, but is nearly absent in galaxies photo-ionized by OB stars. Thus, the BPT diagrams are an efficient tool to distinguish narrow-line AGNs and H II region-like galaxies that takes full advantage of the physical distinction between the two types of objects, since they are based on line ratios involving [O III]λ5007, [N II]λ6583, [S II]$\lambda\lambda$6716, 6731, [O I]λ6300, and the Balmer lines.

However, the exact demarcation between star-forming galaxies and AGN is subject to considerable uncertainty. Kewley et al. (2001) used a combination of photoionization and stellar population synthesis models to place a theoretical upper limit on the location of star-forming models in the BPT diagrams. Galaxies with emission-line ratios that place them above this line cannot be explained by any possible combination of parameters in a star-forming model. Thus, the Kewley et al. demarcation between starbursts and AGN in the [N II]-BPT (e.g., the diagram involving the [N II]/Hα line ratio):

$$\log([\text{O III}]/\text{H}\beta) = 0.61 \times (\log([\text{N II}]/\text{H}\alpha) - 0.47) + 1.19$$

represents a very conservative lower limit on the true number of AGN, according to Kauffmann et al. (2003) which studied the properties of 22’623 narrow-line active galactic nuclei (AGN) with $0.02 < z < 0.3$. Based on these data, they have chosen to revise the demarcation between starburst galaxies and AGN as follows:

$$\log([\text{O III}]/\text{H}\beta) = 0.61 \times (\log([\text{N II}]/\text{H}\alpha) - 0.05) + 1.3$$

Galaxies with higher values of log([O III]/Hβ) are classified as AGN. In Figure 3.1, I show the [N ɪɪ]-BPT diagrams for the 10 AGN-host galaxies from the GASP survey [1], where each point represents a spaxel of the galaxy, together with the spatially-resolved maps of the galaxy color-coded according to the BPT classification. Also, I show the maps based on the classification obtained by another kind of diagnostic: the so-called WHAN diagram (Fernandes et al., 2010).

The WHAN diagram exploits the diagnostic power of the line ratio log [N ɪɪ]/Hα coupled with the equivalent width of the Hα line ($W_{H\alpha}$). Five classes of galaxies are identified within the WHAN diagram:

- pure star-forming galaxies: log[N ɪɪ]/Hα < -0.4 and $W_{H\alpha}$ > 3 Å ;
- strong AGN (i.e. Seyferts): log[N ɪɪ]/Hα > -0.4 and $W_{H\alpha}$ > 6 Å ;
- weak AGN: log[N ɪɪ]/Hα > -0.4 and $W_{H\alpha}$ between 3 and 6 Å ;
- retired galaxies (RGs): $W_{H\alpha}$ < 3 Å ;
- passive galaxies (PGs): $W_{H\alpha}$ and W [N ɪɪ] < 0.5 Å .

The advantage of the WHAN diagram is to allow the differentiation between two very distinct classes that overlap in the low-ionization nuclear emission-line region (LINER) of BPT diagrams. These are galaxies hosting a weakly active galactic nucleus (wAGN) and ‘retired galaxies’ (RGs), i.e. galaxies that have stopped forming stars and are ionized by their hot low-mass evolved stars (Fernandes et al., 2010). On the other hand, the division line between SF and AGN in the WHAN diagram is set at log[N ɪɪ]/Hα = -0.40 and corresponds to the optimal transposition of the Stasińska et al. (2006) (S06 hereafter) BPT-based SF/AGN division, designed to differentiate sources where star formation provides all ionizing photons from those where a harder ionizing spectrum is required. It follows that the WHAN diagram do not define a ‘SF+AGN composite’ category, which are the points between the Kauffmann et al. (2003) and Kewley et al. (2001) demarcation

---

[1] The galaxy JW100 also hosts an optical AGN, though the classification is based on the [S II]-BPT at the galaxy’s redshift the [N II] line is contaminated by a sky line

lines in the [N II]-BPT. Thus, Composite line ratios as classified by the [NII]- BPT are transposed into the SF/AGN categories of the WHAN. Similarly, the division at $W_{H\alpha}$ = 6 Å represents an optimal transposition of the Kewley et al. (2006) division between Seyferts and LINERs. Even though the WHAN diagram are a powerful tool to spot fake AGN from true ones, I decided to employ the more commonly used BPTs and the Kewley et al. (2001) demarcation line to spot the AGN-ionized regions, which represents the best choice to minimize the contamination from star-forming regions. Also, as shown in Figure 3.1, the GASP-AGN hosts - with the only exception of JO49 - do not show signs of emission from evolved stars (e.g. classified as RG in the WHAN). Therefore, in our cases, this new diagnostic does not seem to add information with respect to the commonly-used BPTs.

3.2 Gas-phase metallicity measurements

As descrobed in details in the Introduction (Chapter 1), there are two main techniques generally used to derive the element abundances: the direct method (T-e method) and the SEL method. The direct method makes use of both auroral and nebular lines to infer the gas temperature, T_e: once this quantity is known, the emissivity of a given ion should depend only on its abundance. This method is also affected by several caveats: (i) auroral lines are often weak and faint; (ii) a wide spectral coverage is needed to observe all the required lines. The strong-line method makes use of equations that are function of strong emission lines, calibrated either with the direct method (e.g., Dors et al., 2020b; Flury & Moran, 2020) or with photo-ionization models (Castro et al., 2017; Carvalho et al., 2020, e.g., SB98,). Photoionization models have the advantage to span a wide range of parameter values, but they can also experience a series of uncertainties linked to some simplistic assumptions (e.g. dust-free gas, N/O fixed relation). On the other hand, the direct method tends to predict lower values of 12 + log(O/H) compared to the photoionization models. The discrepancy between the results obtained with the two methods has already been studied (see e. g.

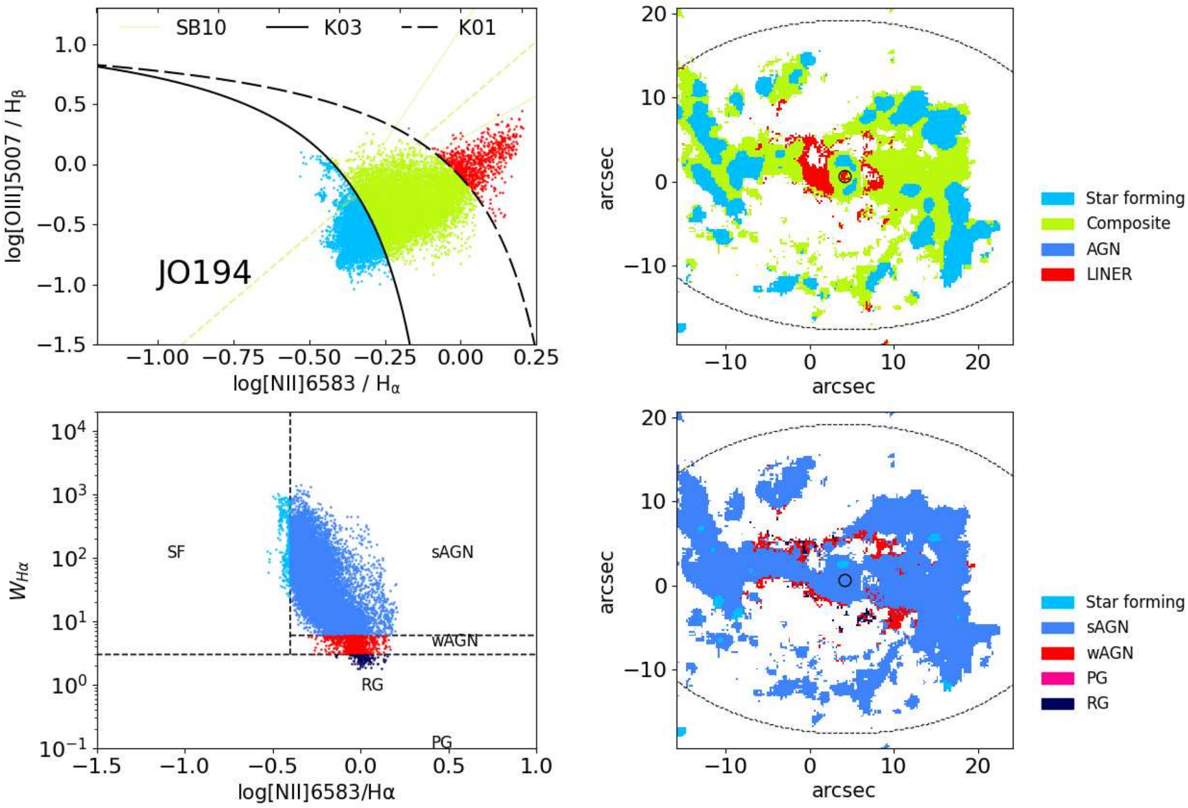

Figure 3.1: For each of the 10 AGN-host galaxies in the GASP sample, classified on the basis of the [N II]-BPT, I show the BPT and WHAN diagrams tracing the ionization mechanisms affecting the gas, and the corresponding spatially-resolved galaxy maps color-coded according to the classification. For the BPT diagrams and maps, I use the color light blue in case of the SF-like line ratios, dark blue for the AGN-like ratios, light green for line ratios arising from a mixing between stars' and AGN's ionization, and red for the LINER-like ratios. For the WHAN, I use the color light blue for the SF-like ratios, dark blue for the strong-AGN line ratios, red for the weak-AGN line ratios and dark blue for the 'Retired Galaxy' like ratios, tracing the ionization from old stars (see Fernandes et al., 2010). In the AGN-GASP sample, there are no 'Passive Galaxy'-like line ratios. With the only exception of the galaxy JO49, the WHAN diagram does not seem to add information on the ionization mechanism with respect to the BPT. On the contrary, the information about the Composite-like emission is lost, due to the fact that Fernandes et al. (2010) consider the Kewley et al. (2006) dividing line between SF and AGN-like ratios [O III]/Hβ and [N II]/Hα in the BPT, without considering the Composite region delimitated by the Kauffmann et al. (2003) and Kewley et al. (2001) dermarcation lines (see Chapter 3.1 for further details).

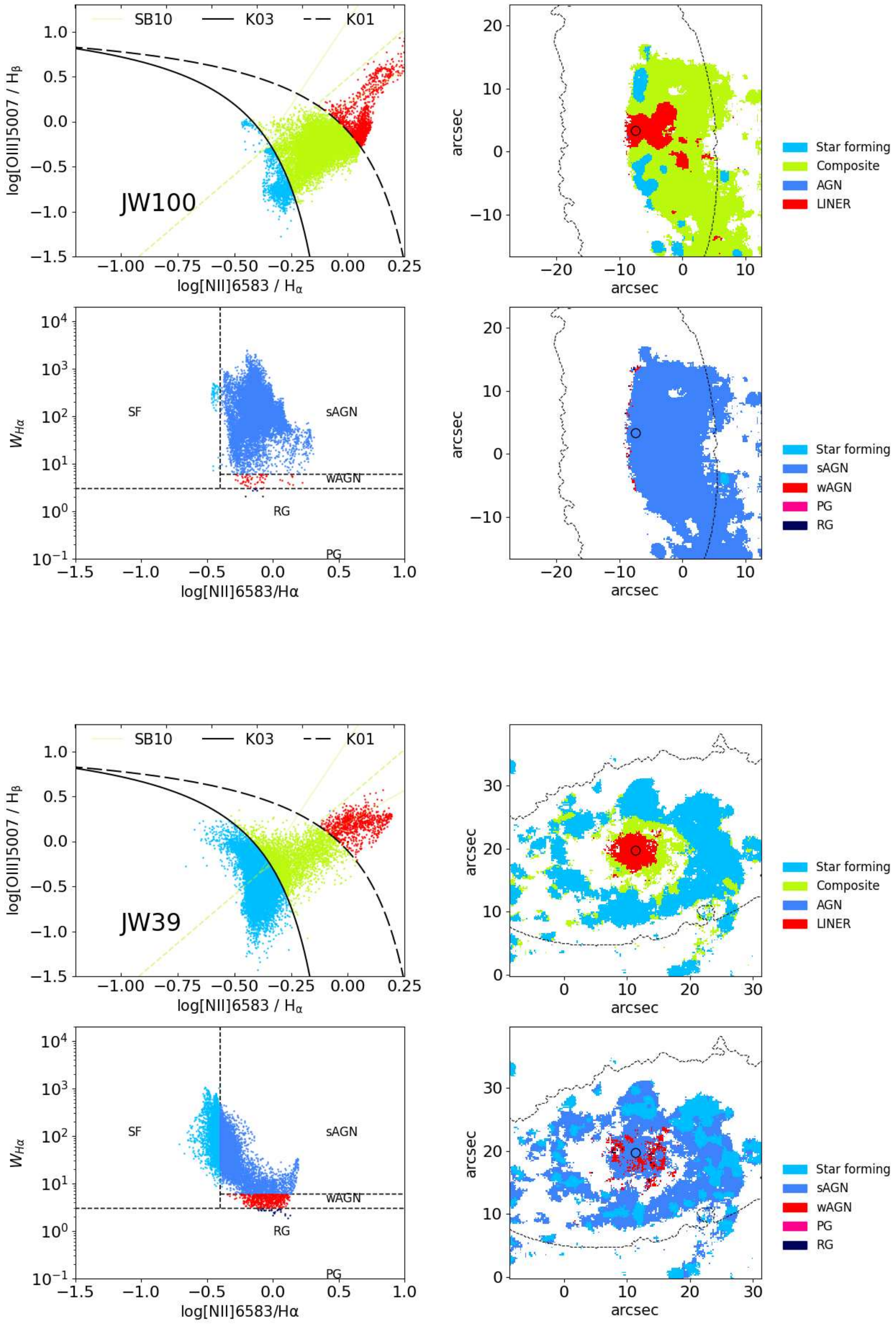

Figure 3.1 : *(continued)*

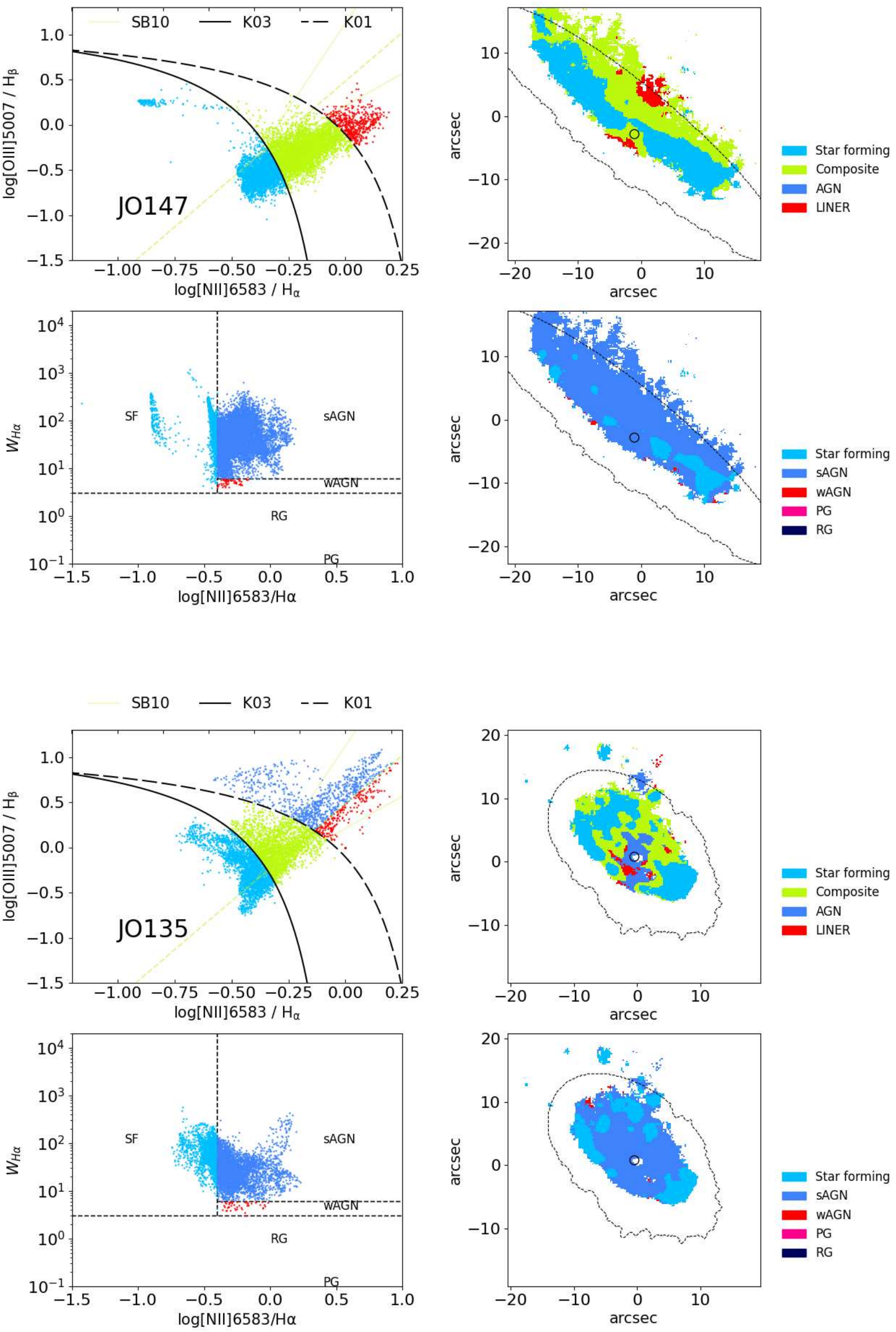

Figure 3.1 : *(continued)*

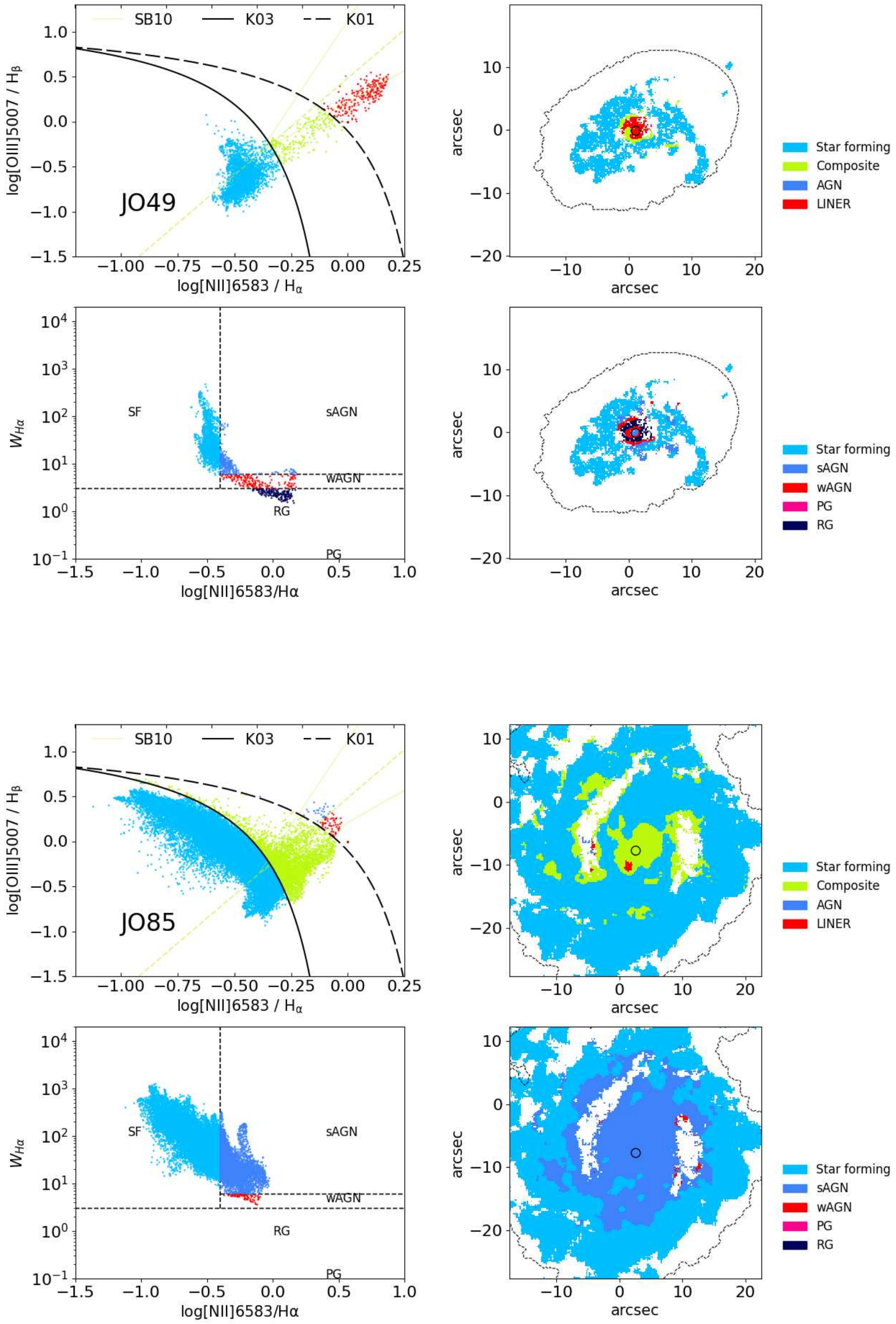

Figure 3.1 : *(continued)*

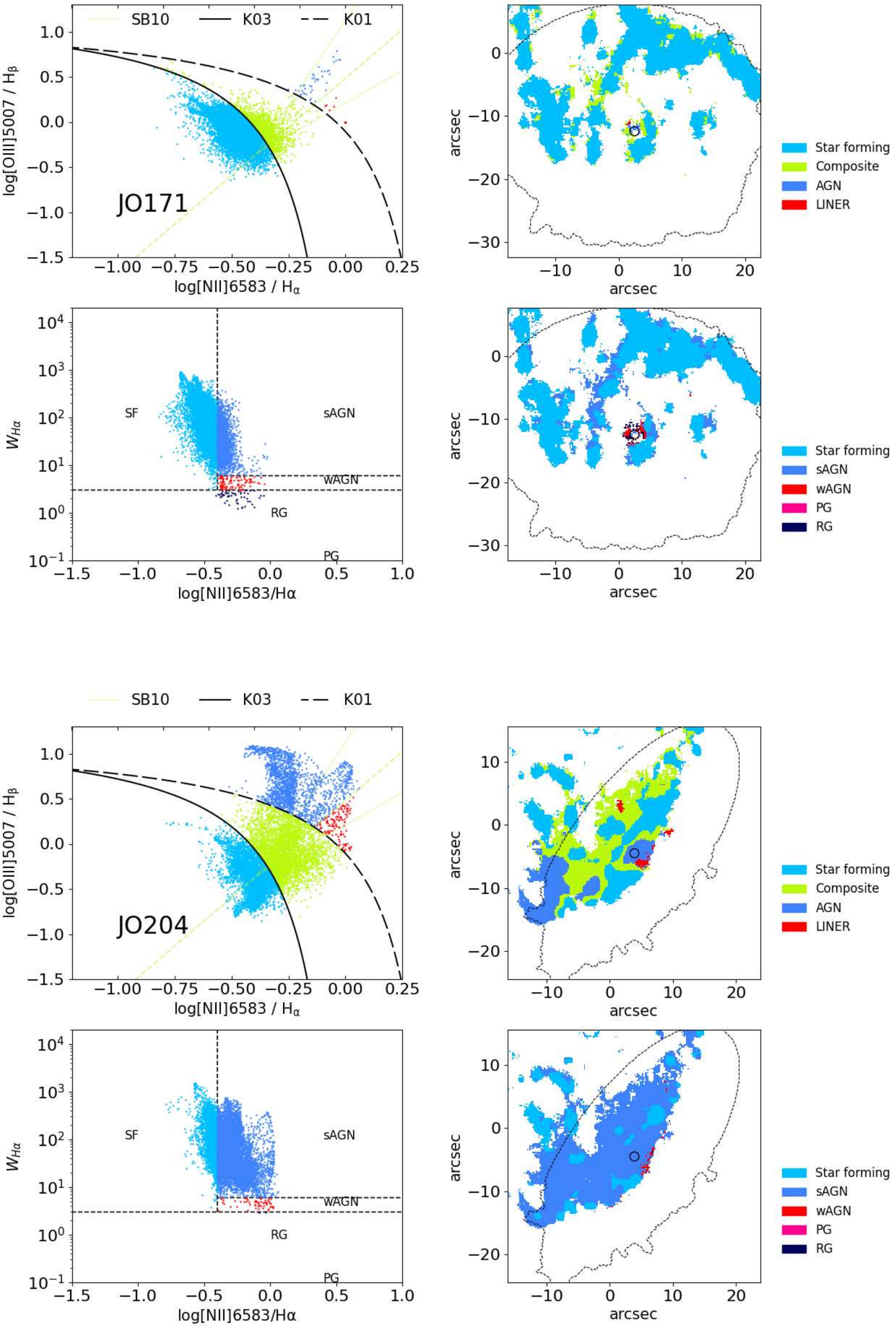

Figure 3.1 : *(continued)*

Dors et al., 2020b) and is possibly linked with uncertainties in the direct method, such as:

- **Systematics**: the assumed t2-t3 relation in the direct method usually used for AGNs was previously derived from models or observations of H II regions, where t3 and t2 are the electron temperatures in the high ionization zone and in the low ionization zone of the gas phase, respectively, and are used to compute the O^{++} and O^{+} abundances in relation to H^{+} abundance. Recently, Dors et al. (2020a) investigated the discrepancy between O/H abundance estimations for narrow-line regions (NLRs) of Seyferts 2 derived by using T_e-method and those derived from photoionization models. These authors found that the derived discrepancies are mainly due to the inappropriate use of the relations between temperatures of the low (t2) and high (t3) ionization gas zones derived for H II regions in AGN chemical abundance studies. In addition, Dors et al. (2020b), using a photoionization model grid, derived a new expression for the t2-t3 relation valid for Seyfert 2 nuclei which reduces the O/H discrepancies between the abundances obtained from strong-line methods and those derived from T_e-method, but still persist as a shift of ~ 0.4 dex.
- **Shocks**: shocks can affect the measured electron temperature and impact the inferred chemical abundance (Riffel et al., 2021; Dors et al., 2021). However, the effects of shocks on the t2-t3 relation are usually neglected.

The application of the direct method was not possible in this work since the auroral line [OIII]λ4364 is too faint in MaNGA and outside the MUSE spectral range for GASP targets. However, to test that the direct method underestimates the oxygen abundances in AGN-ionized regions, I apply the SEL calibrator of Flury & Moran (2020) (Section §1.4), that is based on directly-measured abundances, and I find that the method predicts values of $12 + \log(O/H)$ lower than 0.6 dex with respect to photoionization model predictions, as expected for the reasons discussed above. For these reasons, I will adopt in this Thesis an indirect method based on photoionization models.

Particularly, by means of photoionization models and the code NebulaBayes, used to compare models and observations, I will obtain spatially-resolved maps of 12+log(O/H), with a resolution of ~ 1 kpc for both the GASP and MaNGA samples of AGN.

Due to the lack of calibrators for both H ii and AGN-like regions (generated using the same codes, assumptions on the model's parameters, etc.), I will not apply SEL calibrators in this Thesis. However, for completeness, I will give an overview of the main SEL calibrators available in the literature to measure the AGN metallicity (3.2.1,3.2.2) and I will compare the results obtained by using different SEL calibrators (3.2.4).

3.2.1 Storchi-Bergmann et al. 1998 (SB98) calibrator

SB98 present an indicator based on the line ratios x = log([N ii]λ6548+6583/Hα) = [N ii]/Hα and y = log([O iii]λ4959+5007/Hβ) = [O iii]/Hβ:

$$\begin{aligned}12 + \log(\mathrm{O/H}) = 8.34 + 0.212\mathrm{x} - 0.0122\mathrm{x}^2 - 0.002\mathrm{y} + 0.007\mathrm{xy}\\ -0.002x^2y + 6.52 \cdot 10^{-4}y^2 + 2.27 \cdot 10^{-4}xy^2 + 8.87 \cdot 10^{-5}x^2y^2\end{aligned} \tag{3.1}$$

They use a set of photoionization model grids built with the code Cloudy to mimic the AGN emission. Three different approximations for the AGN ionizing continuum are considered: a typical AGN continuum (a combination of power laws; see Mathews et al., 1987) and two power laws F ~ ν^α, with α = 1 and 1.5, respectively. The ionization parameter $\log U$ varies over the interval -4 ≤ $logU$ ≤ -2 and the oxygen abundance within the range 8.4 ≤ 12+log(O/H) ≤ 9.4. In this way, it was possible to reproduce the observed range in emission-line ratios for typical NLRs. The solar abundance is assumed to be 8.91. The nitrogen-to-oxygen abundance is fixed by the relationship $\log(\mathrm{N/O}) = 0.96 \times [12 + \log(\mathrm{O/H})] - 9.29$. The dust-to-gas ratio is assumed to be solar. They fit, with a two-variable polynomial, the theoretical curves in the diagram [N ii]/Hα vs [O iii]/Hβ finding the calibrator expressed in equation (3.1). The fitted values are within 0.05 dex of the model values.

Since the authors fix the electron density N_e at 300 cm^{-3}, they also provide a correction factor to account for different values of the electron density, valid for N_e = 100-10 000 cm^{-3} (see equation 3.2).

$$12 + \log(\mathrm{O/H})_{\mathrm{corr}} = 12 + \log(\mathrm{O/H}) - 0.1 \cdot \log(\mathrm{N_e}/300) \tag{3.2}$$

Thus, the correction factor can range from 0.052 for N_e = 100 cm^{-3} and 0.048 for N_e = 1000 cm^{-3}, that are the values of gas density typically observed in Seyfert/LINER-like nuclei. The reason why I decided to not apply this correction resides in the low-gain of the procedure: indeed the correction is relatively small if compared to the spread of metallicity values obtained with the formula 3.1 (see Section 3.2.4) .

3.2.2 Carvalho et al. (2020) calibrator

Carvalho et al. (2020) find a relationship between the metallicity Z and the line-ratio $N2 = \log([\mathrm{N\,II}]\lambda6583/\mathrm{H}\alpha)$ ($N2$ index, see also Groves et al., 2006) expressed as:

$$Z/Z_{\odot} = a^{N2} + b \tag{3.3}$$

with a = 4.01 and b = - 0.07. The validity range of the expression is $-0.7 \leq N2 \leq 0.6$. They use the CLOUDY code to generate 399 dust-free photoionization models. They assume four parameters: (i) the AGN Spectral Energy Distribution (SED) with three different spectral indexes for the ionizing continuum, equals to -0.8, -1.1, and -1.4 (ii) the ionization parameter, log(U), which varies from -4 to -0.5 with a step of 0.5 dex (iii) the metallicity, ranging from 8.0 to 9.0 (iv) the electron density which goes from 100 to 3000 cm^{-3}. They use the diagram [O III]λ5007/[O II]λ3272 vs [N II]λ6583/Hα to obtain the calibrator in Equation (3.3), by matching the model grids and the observed points in this plane through a linear interpolation. The nitrogen-to-oxygen ratio is fixed by the relation log(N/O) = 1.29 × [12 log(O/H)] - 11.84. This is slightly different from the one assumed in SB98 and this is why the authors find differences, according to them, between their estimates and the ones obtained with the SB98 calibrator. Indeed, as any other theoretical calibration based on nitrogen lines, one of the drawbacks of the N2 index resides in its dependence on the assumed (N/O) - (O/H) relation. Moreover, calibrators involving nitrogen lines are not valid in the low-metallicity regimes, since the dependence between the nitrogen lines and Z is due to the N secondary stellar nucleosynthesis origin in the "high" metallicity regime. Finally, the N2 index saturates in the very high metallicity regime, which is $Z/Z_\odot \leq 2$. The advantages on the other side are that (i) the N2 index is not sensitive to reddening corrections or to flux calibration uncertainties, thanks to the vicinity of the lines involved (ii) it is not affected by a strong dependence on the ionization parameter as other calibrators (such as R_{23}).

3.2.3 Flury & Moran (2020) calibrator

As already mentioned in Section 3.2, the direct method underestimates the 12 + log(O/H) values of the NLR gas, relatively to photoionization predictions. Nevertheless, I present for completness the results obtained using the semi-empirical relation of Flury & Moran (2020) between oxygen abundances measured from the direct method and the strong line ratios [O III]λ5007/Hβ and [N II]λ6583/Hα

$$\begin{aligned} 12 + \log(\mathrm{O/H}) = 7.863 + 1.170\mathrm{x} + 0.027\mathrm{y} - 0.369\mathrm{x}^2 + 0.208\mathrm{y}^2 - 0.406\mathrm{xy} \\ -0.100x^3 + 0.323y^3 + 0.354x^2y - 0.333xy^2 \end{aligned} \tag{3.4}$$

where x = log([O III]λ5007/Hβ) and y = log([N II]λ6583/Hα). To obtain this expression, the authors measure the electron temperature T_e of the gas, from which they deduce the oxygen abundance 12 + log(O/H) for a sample of 8720 optically-selected AGNs in the SDSS DR8. They fit the T_e - 12 + log(O/H) relation (also called cooling-sequence), finding a strong correlation between these two quantities. They also obtain an empirical relationship between the nitrogen-to-oxygen ratio (N/O) and the oxygen abundance. Finally, assuming a three-ionization-zone approximation for the NLR and making use of the empirical relationships described above, they obtain grids of values for [NII]λ6583/Hα and [OIII]λ5007/Hβ varying 12 + log(O/H) between 7.51 and 8.76

and η from 0.1 to 0.9, where η is the O^{+2} ion fraction. The equation 3.4 is obtained with a linear interpolation of the grids in the NII-BPT diagram.

3.2.4 Comparison between SEL calibrators

In this section, I compare the results obtained with the sets of calibrators described in Sections 3.2.1, 3.2.2 and 3.2.3.

Figure 3.2 shows that Flury & Moran (2020)'s metallicities are a factor 0.5-0.6 dex lower than those computed with the SB98 and C20 calibrators, in each galaxy from the AGN GASP sample, as expected from the fact that the Flury & Moran (2020) calibrator is based on direct estimates which are well-know to be affected by caveats (see Section 3.2 for the details).

On the other hand, there is also a discrepancy between metallicites measured by C20 and SB98 calibrators, even though not systematic. The discrepancy ranges between 0.2 dex and 0.4 dex, depending on the ([O III]λ4959+5007/Hβ) ratio (e.g., the 'y'-term in the Equation 3.1). To visualize it better, I show in details the comparison between the metallicities computed with SB98 and C20 calibrators for the galaxy JO135, selected from the GASP AGN sample. In particular, in Figures 3.3 and 3.4 each point represents a spaxel of the galaxy, classified either as Seyfert or LINER in the NII-BPT. The points are color-coded according to the value of x = log([NII]λ6548+6583/Hα) measured inside a given spaxel in Figure 3.3 and according the values of y = log([OIII]λ4959+5007/Hβ) in Figure 3.4. The following trend shows up. The datapoints which deviate the most from the one-to-one relation are those with the highest values of the y-term. In particular, I tested that the shift is mainly driven by the terms $0.007 \cdot x \cdot \mathbf{y}$ and $6.52 \cdot 10^{-4}\mathbf{y}^2$ of Equation 3.1. When these two terms cannot be approximated to zeros due to the high values of [OIII]λ4959+5007/Hβ, the plume of points (see e.g. Figure 3.4) appears.

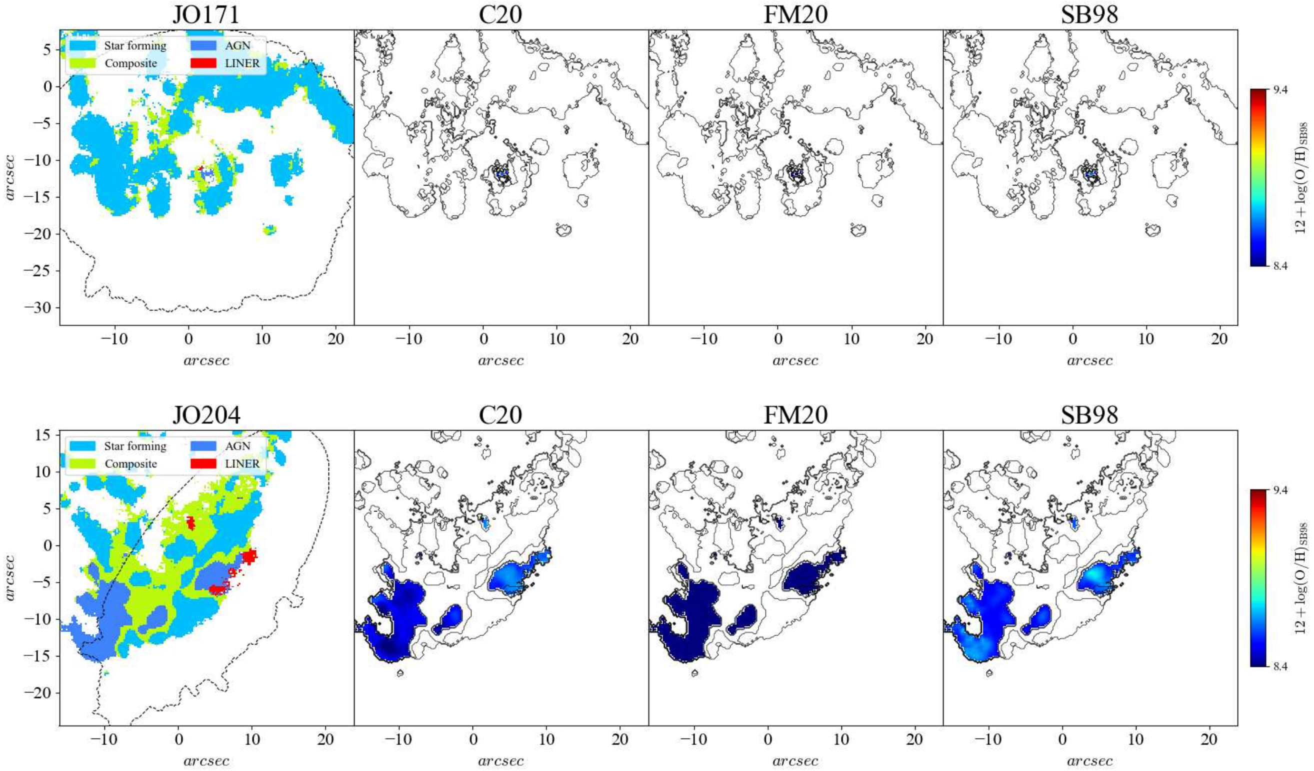

Figure 3.2: GASP AGN's galaxy maps color-coded according to the N ɪɪ-BPT classification, and spatially-resolved maps of oxygen abundances inside the Seyfert/LINER regions estimated with (from left to right) Equation 3.3 from C20, Equation 3.4 from (Flury & Moran, 2020) and Equation 3.1 from SB98.

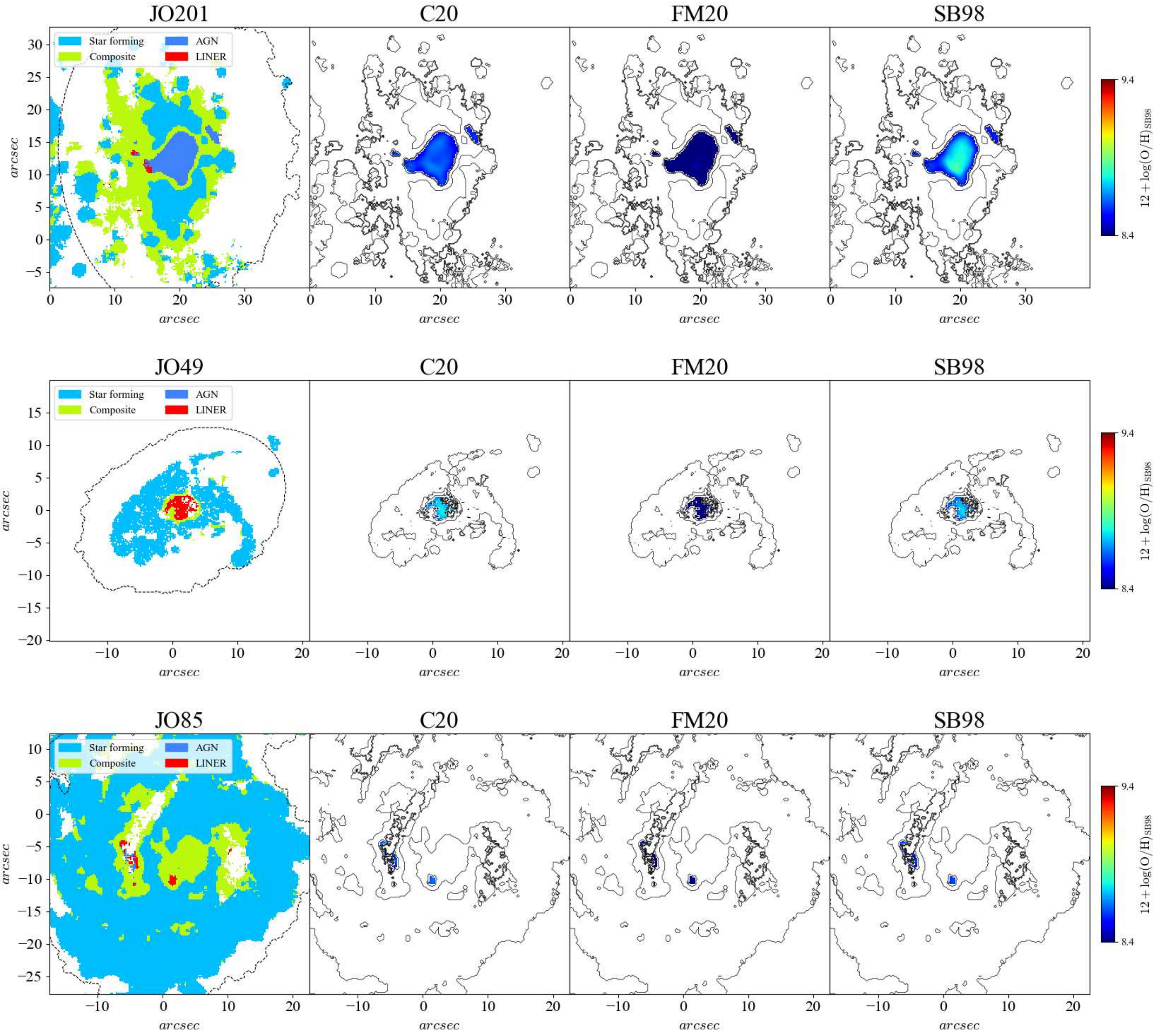

Figure 3.2 : *(continued)*

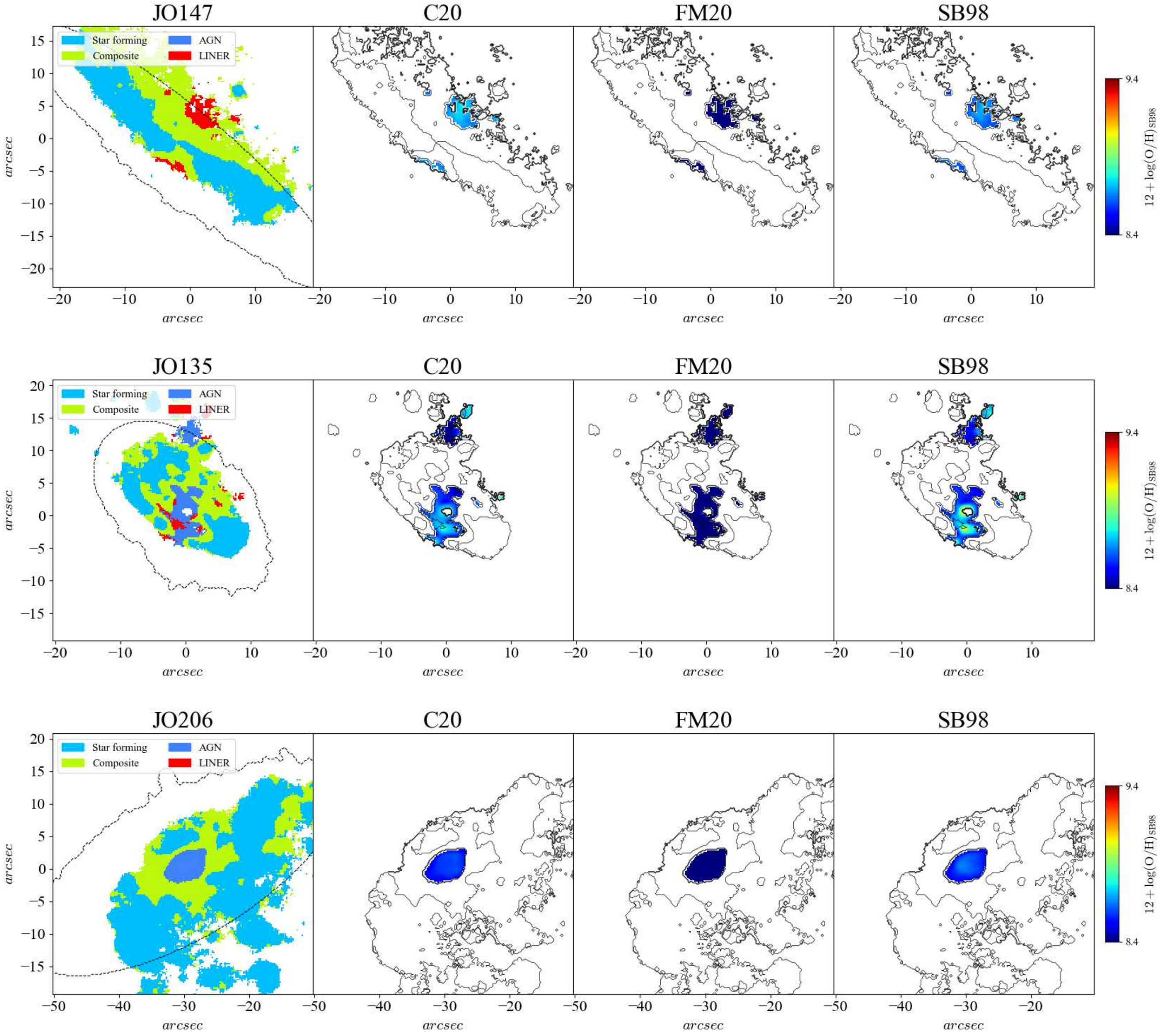

Figure 3.2 : *(continued)*

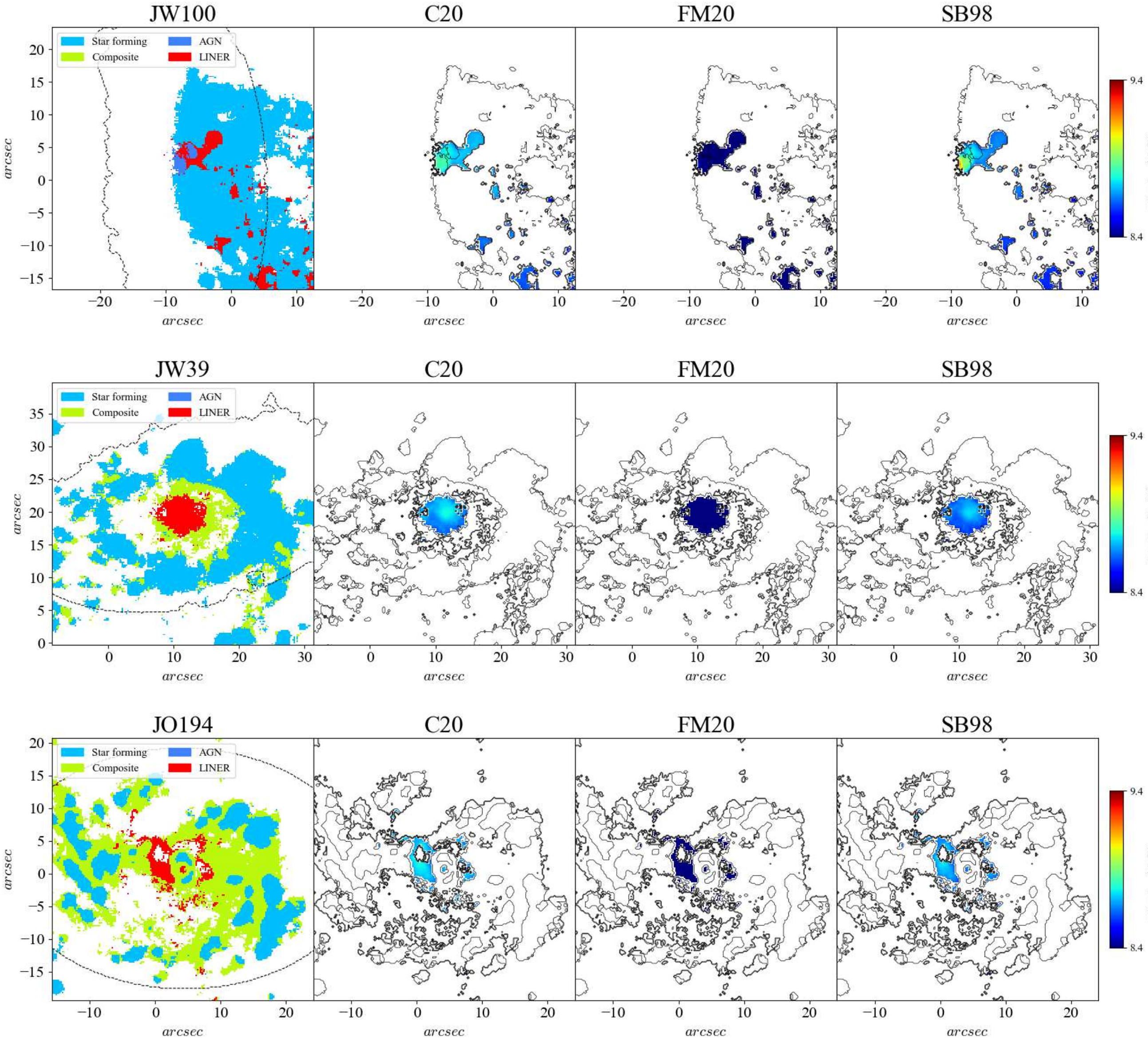

Figure 3.2 : *(continued)*

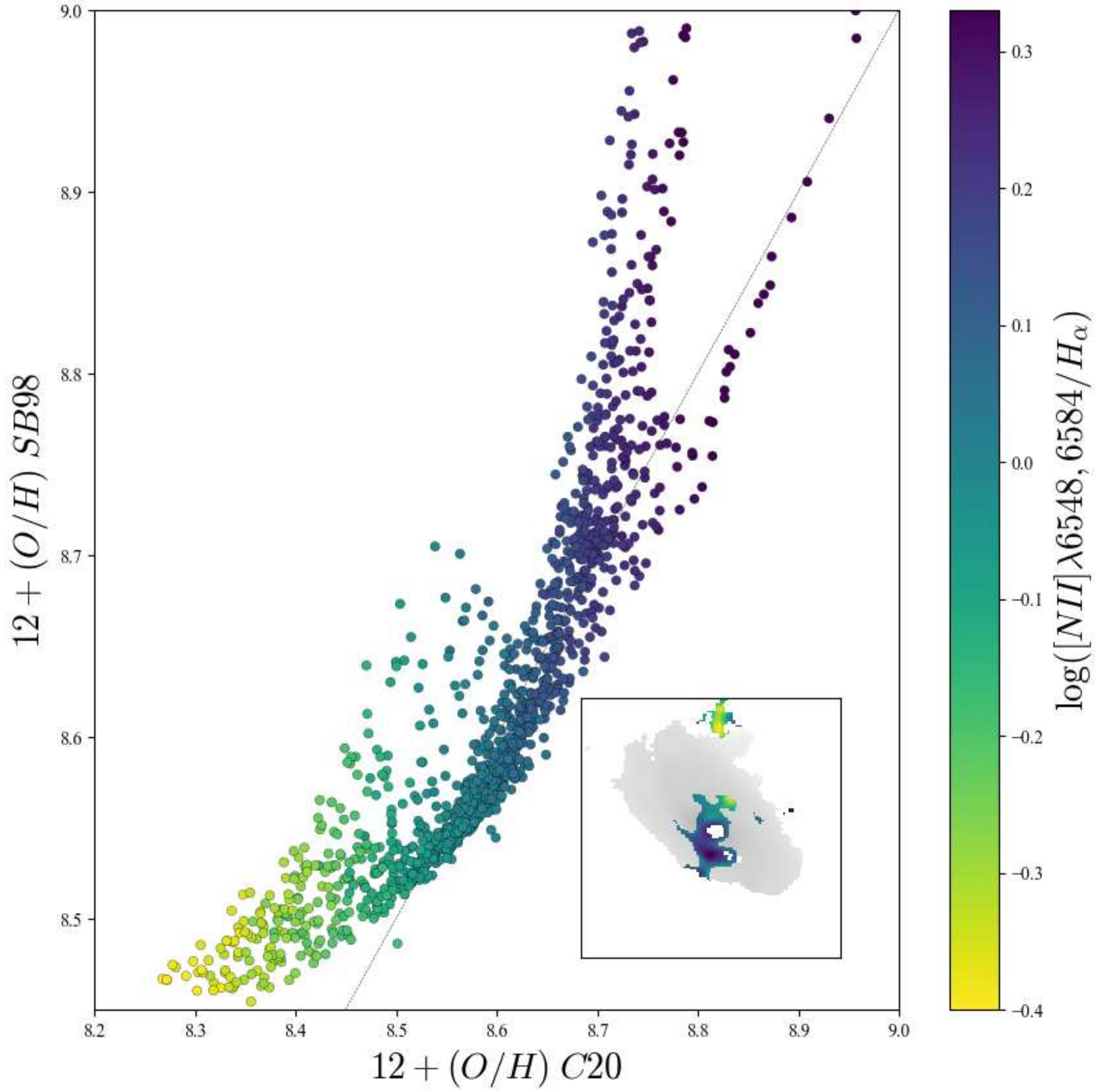

Figure 3.3: Spaxel-by-spaxel comparison between SB98 and C20 calibrators, for the galaxy JO135. In the x-axis, 12 + log(O/H) values computed with Equation 3.3 from C20, in the y-axis 12 + log(O/H) values computed with the Equation 3.1 from SB98. The points are color-coded according to the value of x = log([NII]λ6548+6583/Hα. The dotted-black line represents a line with slope equals to 1. To visualize the locations of each point within the galaxy, in the bottom-right panel I show the galaxy map color-coded according to the x values in the Seyfert/LINER spaxels, superimposed to the stellar continuum (in gray) under the Hα line.

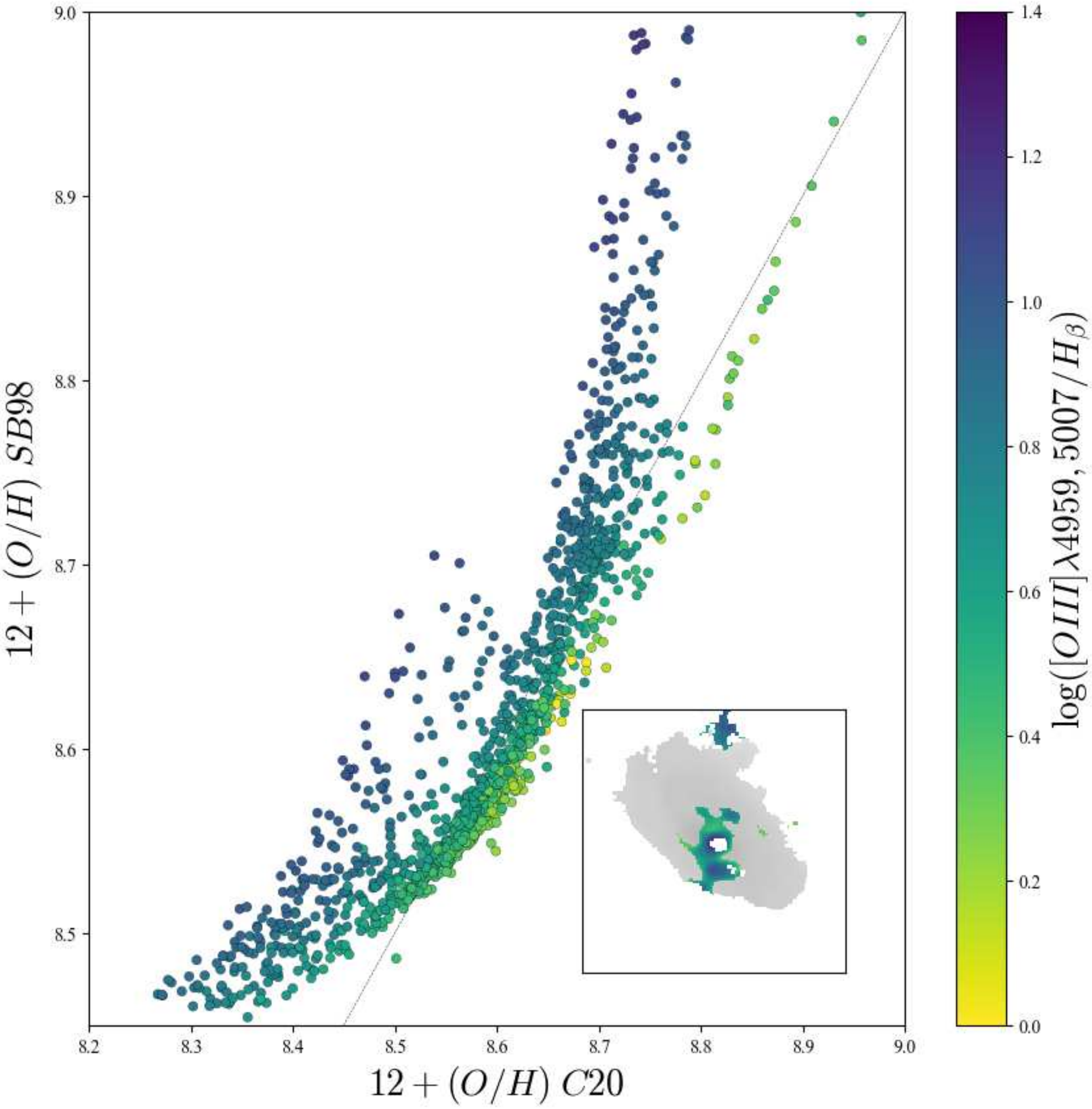

Figure 3.4: Spaxel-by-spaxel comparison between SB98 and C20 calibrators, for the galaxy JO135. In the x-axis, 12 + log(O/H) values computed with Equation 3.3 from C20, in the y-axis 12 + log(O/H) values computed with the Equation 3.1 from SB98. The points are color-coded according to the value of y = log([OIII]λ4959+5007/Hβ. The dotted-black line represents a line with slope equals to 1. To visualize the locations of each point within the galaxy, in the bottom-right panel I show the galaxy map color-coded according to the x values in the Seyfert/LINER spaxels, superimposed to the stellar continuum (in gray) under the Hα line.

3.2.5 Photoionization models

In this section, I will describe MAPPINGS photoionization models generated in case of ionization from both AGN or stars by Thomas et al. (2018b) (T18 models, hereafter), as well as AGN (Feltre et al., 2016) and H II (Gutkin et al., 2016) CLOUDY photoionization models available in the literature. Then, I will discuss the reasons which lead me to generate a new sets of models.

Gutkin et al. (2016)

Gutkin et al. (2016) present models for the nebular emission in star-forming galaxies that are appropriate to interpret observations of galaxies at all cosmic epochs. In particular, they use the Charlot & Longhetti (2001) approach to parametrize their models. In this approach, the rate of ionizing photons produced by a star cluster evolves as the stellar population ages and the nebular emission from an entire galaxy is computed by convolving that of individual star clusters with the star formation history. The metallicity of the ionizing stars (Z_*) is assumed to be equal to the metallicity of the nearby gas, $\mathrm{Z_{ISM}}$ (e.g. $Z_* = \mathrm{Z_{ISM}}$). The nebular emission is modeled by the photoionization code CLOUDY (v13.03 Ferland et al., 2013). The models account for the presence of dust in the gas surrounding the stars and for the consequent depletion of metals into dust grains, parametrized by the dust-to-metal mass ratio ξ_d. These HII grids have a total number of 21'168 gridpoints. The physical conditions of the photoionized gas can be described by the following parameters:

Ionization parameter U_S at the Strömgren radius. The authors compute the rate of ionizing photons produced by a star cluster with effective mass M_* (i.e. Q(t')) and use it to compute the ionization parameter at a distance r from the ionizing source as U(t',r) = Q(t')/($4\pi r^2 n_H c$). Finally, they parametrize models in terms of the zero-age ionization parameter at the Strömgren radius (i.e. R_S), $\mathrm{U}_S \equiv \mathrm{U}(0,R_S)$. The values of this parameter vary in the range -4.0 $\leq \log U_S \leq$ -1.0 with a step of 0.5 dex.

Hydrogen density, n_H. They consider values of this parameter in the range $10^2 \leq n_H/cm^3 \leq 10^4$.

Gas metallicity, Z_{ISM}. The relative abundances and the depletion factors for the heavy elements are reported in Table 1 of Gutkin et al. (2016). The content of Z increases with time since the byproduct of stellar evolution enriches the ISM and all the heavy elements expect nitrogen are supposed to scale linearly with Z. Studies on galactic and extragalactic H II regions suggest that N has primary and secondary nucleosyhthetic components. Both components are thought to form by the conversion of carbon and oxygen in the CNO cycles in stars with M_* from 4 to 8 $M_\odot$. The abundance of N depends on the initial content of CO in stars: while the first stars have a low CO abundance and produce the nitrogen by burning H in the CNO cycle, the following generations grow in their CO content (C/H $\propto Z$) and this leads to an ulterior increase of N (N/C $\propto Z$). In broad terms, N/H $\propto Z^2$. The abundance of primary+secondary nitrogen is related to the [O/H] through the expression:

$$\mathrm{N/H} \approx 0.41\ \mathrm{O/H}\ [10^{-1.6} + 10^{2.33+\log\mathrm{O/H}}] \tag{3.5}$$

Carbon-over-oxygen abundance, (C/O)/(C/O)$_\odot$. Since some studies of HII regions suggest a connection between the C/O and the O/H content in galaxies, the C/O ratio is left to be an adjustable paramater and its values vary in the range 0.10 to 1.40. The solar ratio is $(\mathrm{C/O})_\odot = 0.44$.

Dust-to-haevy element mass ratio, ξ_d. They adopt the default dust properties of CLOUDY, which is a mixture of silicates and graphite with a standard Mathis et al. (1977) size distribution and optical properties from Malina et al. (1991). They consider values in the range $0.1 \leq \xi_d \leq 0.5$.

The main issue that prevents the usage of these models is the fact that only a part of them (10'621 over the expected total of 21'168, based on the list of parameters presented in the paper) are available online [2].

Feltre et al. (2016)

Feltre et al. (2016) construct CLOUDY (v13.3 Ferland et al., 2013) photoionization models to reproduce the emission in the NLR ionized by an AGN. The composition of the gas nebula is the same of Gutkin et al. (2016), except for the C/O ratio that is set simply equal to the solar value 0.44. The ranges of the paramaters are listed in Table 3.1. The emission from the accretion disk in an AGN is approximated by a broken power-law:

$$S_\nu \propto \begin{cases} \nu^{\alpha} \quad at \quad 0.001 \leq \lambda \mu m \leq 0.2 \\ \nu^{-0.5} \quad at \quad 0.25 \leq \lambda \mu m \leq 10.0 \\ \nu^{2} \quad at \quad \lambda \mu m \geq 10.0 \end{cases} \tag{3.6}$$

and the spectral index α in the UV regime is left to be an adjustable parameter, which varies in the range -2.0 $\leq \alpha \leq$ -1.2. The total number of grid points are 5'184 (4 values of the spectral index x 9 values of the ionization parameter x 3 values of hydrogen density x 16 values of metallicity x 3 values of the dust-to-metal mass ratio).

Thomas et al. 2018

Thomas et al. (2018a) (hereafter T18) present models generated with the code MAPPINGS 5.1 (Sutherland & Dopita, 2017) for both the H II and AGN-ionized regions (H II and NLR models, hereafter). To do so, they use the work of Nicholls et al. (2017), which involves a scaling of abundances accounting for the changing contributions of primary and secondary nitrogen with metallicity and for the changing ratio of α-process elements to iron-peak elements as a function of metallicity.

The H II T18 models are generated using the ionizing spectra derived with the SLUG2 (Krumholz et al., 2015) stellar population synthesis code, taking into account the Lejeune/Schmutz extended stellar atmosphere models as in STARBURST99 (Schmutz et al.,

---

[2] The models can be downloaded at the link:http://www.iap.fr/neogal/sf-models.html

1992; Lejeune et al., 1997), a Chabrier initial mass function, constant SFH over 10 Myr with SFR = $10^{-3} M_{\odot} yr^{-1}$ and Padova stellar tracks with five explicitly calculated values of metallicity (Z= 0.0004, 0.004, 0.008, 0.02, 0.05, where Z=0.02 is Solar). The gas pressure samples 12 values in the range $4.2 \leq \log\ \mathrm{P/k(cm^{-3}K)} \leq 8.6$. The ionization parameter varies in the range log U = [-4.2, -0.5]. The models are plane-parallel and dusty, even though dust destruction is not allowed. Interestingly, Thomas et al. (2019) find a systematic offset between predicted and observed O III fluxes in case of star-forming galaxies. In particular, they find that the [OIII] is systematically underpredicted by a factor of ~ 3-5 at supersolar metallicities. Because of it, they need to set the prior [NII]/[OII], to constrain the O/H, in order to get a smooth distribution of O/H for the star-forming galaxies. The authors attribute this offset to some issues affecting the H II models. To explain the origin of the H II models' 'inadequacy', Thomas et al. (2019) propose as sources of uncertainty the stellar model sensitivity to properties such as stellar rotation, dredge-up of helium, and mass-loss rates. Other issues are related to the stellar tracks and stellar atmosphere models, such as the poor-parameter space coverage, for example. Also, there is an inconsistency between the abundances of stellar track and atmosphere models, which implies that the stellar and nebular abundances were approximately matched (i.e. the HII models are not fully self-consistent).

The NLR T18 models are generated using an ionizing spectrum (Thomas et al., 2016) which is characterized by three parameters: the energy of the peak of the accretion disk emission ($\mathrm{E_{peak}}$), the photon index of the inverse Compton scattered power-law tail (Γ), and the proportion of the total flux of the non-thermal tail (p_{NT}). The OXAF model does not account for the soft X-ray excess emission, since Thomas et al. (2016) showed that including the soft excess does not have a major effect on predictions of the strong optical emission lines. For the T18 NLR grid, the only OXAF parameter is E_{peak}, while the other parameters are fixed to the fiducial values $\Gamma = 2.0$ and $\mathrm{p}_{NT} = 0.15$. Therefore, the final NLR grids have the following four parameters: metallicity, ionization parameter, pressure, and E_{peak}. The ranges of these parameters are listed in Table 3.1, together with those of the H II models.

	MAPPINGS 5.1 models	
Parameter	Thomas et al. (2018a) (Star-forming regions)	Thomas et al. (2018a) (AGN narrow-line regions)
log P/k	4.2, 4.6, 5.0, 5.4, 5.8, 6.2, 6.6, 7.0, 7.4, 7.8, 8.2, 8.6	4.2, 4.6, 5.0, 5.4, 5.8, 6.2, 6.6, 7.0, 7.4, 7.8, 8.2, 8.6
log U	-4, -3.75, -3.5, -3.25, -3, -2.75, -2.5, -2.25, -2	-4.2, -3.8, -3.4, -3, -2.6, -2.2, -1.8, -1.4, -1, -0.6, -0.2
12 + log O/H	7.061, 7.663, 8.061, 8.362, 8.605, 8.76, 8.874, 8.99, 9.082, 9.158, 9.237, 9.304	7.061, 7.663, 8.061, 8.362, 8.605, 8.76, 8.874, 8.99, 9.082, 9.158, 9.237, 9.304
log E_{peak}	–	-2,-1.75, -1.5, -1.25, -1, -0.75
	CLOUDY v13.3 models	
	Feltre et al. (2016) (AGN narrow-line region)	Gutkin et al. (2016) (Star-forming region)
Ionizing spectrum	α = -1.2,-1.4,-1.7,-2.0	SFR=1 $M_\odot\ yr^{-1}$ for 10^8 yr
log U	-1, -1.5,-2,-2.5,-3,-3.5,-4,-4.5,-5	-1,-1.5,-2,-2.5,-3,-3.5,-4
$\log(n_H/cm^{-3})$	2.0,2.0,4.0	2.0,3.0,4.0
Z	0.0001,0.0002,0.0005,0.001,0.002,0.004,0.006, 0.008,0.014,0.01774,0.03,0.04,0.05,0.06,0.07	0.0001,0.0002, 0.0005, 0.002,0.004,0.006 0.008,0.014,0.01774,0.03,0.04
ξ_d	0.1,0.3,0.5	0.1,0.3,0.5

Table 3.1: Adjustable parameters of the photo-ionization models retrieved from the literature.

The lack of H ii models with N ii/Hα and S ii/Hα ratios close to BPT demarcation lines

Figure 3.5 shows clearly the lack of T18 H ii models with N ii/Hα and S ii/Hα line ratios close to the BPT demarcation lines, which are the Kauffmann et al. (2003) empirical relationship in the NII-BPT and the theoretical Kewley et al. (2001) relationship in the SII-BPT (see Law et al., 2021, for a review of these demarcation lines). The discrepancy between models and observations is consistent with that found in H ii models generated with the previous version of the code Mappings IV (Nicholls et al., 2012; Dopita et al., 2013, D13 models). The H ii models described in Kewley et al. (2019b) partly recover models with generally higher N ii/Hα and S ii/Hα than T18 and Dopita et al. (2013), but still too weak to approach the line ratios of the Kauffmann et al. (2003) and Kewley et al. (2001) relations (Fig. 11 in Kewley et al., 2019a). Byler et al. (2017) generate H ii models with the code Cloudy v13 which come much closer to the BPT demarcation lines in both the NII- and SII- BPT diagrams, but only the use of the version of the code Cloudy v17 (Ferland et al., 2017) leads to model predictions that are capable to follow exactly the S ii/Hα and N ii/Hα line ratios of the demarcation relations (Law et al., 2021; Belfiore et al., 2022).

Because of it, we generate H ii models with the code Cloudy v17 as described in the following Section §3.2.5 based on the prescription presented in Byler et al. (2017) (see Belfiore et al., 2022, for a similar approach).

This thesis's photoionization models

Models are generated with Cloudy v17.02 (Ferland et al., 2017) in case of ionization from stars (H ii models, hereafter) and AGN (AGN models, hereafter), so that the metallicity is measured in a homogeneous way from the central AGN region to the star formation-dominated outskirts of galaxies with AGN activity. To compute the metallicity in Composite (AGN+SF) regions, we mix the H ii and AGN models.

The files used as input by Cloudy are built using the CloudyFSPS library (Byler,

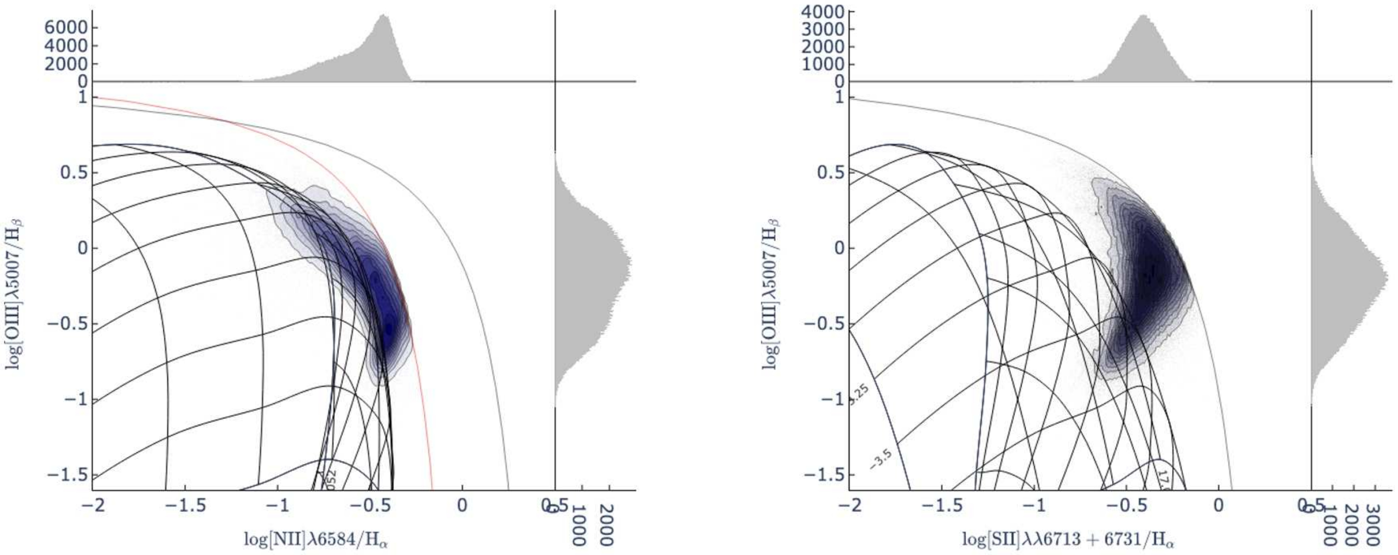

Figure 3.5: NII- and SII- BPT diagrams with overlaid the H II models (black lines) provided with the code NebulaBayes. The model's gas pressure is log P/k (cm^{-3}/K) = 5. The red line is the empirical Kauffmann+2003 relation, while the black lines are the theoretical Kewley et al. (2001) relationships. The distribution of the observed star-forming line ratios (from GASP and MANGA galaxies) is shown by density curves filled with shades of purples, where darker colors indicate higher densities.

2018), modified to handle both H II and AGN models. All models span the following parameter space:

- The ionization parameter [$\log(U)$] ranges between $-4 \leq \log(U) \leq -1$ with a step of 0.5 dex;

- Gas-phase abundances are those in CloudyFSPS that are based on the solar values from Dopita et al. (2000) (see Byler et al., 2017). With the exception of nitrogen and helium, abundances scale with the gas-phase metallicity ($\log Z = -1, -0.6, -0.4, -0.3, -0.2, \ -0.1, 0.0, +0.1, +0.2, +0.3, +0.4, +0.5$), corresponding to oxygen abundance ranging between $7.69 \leq 12 + \log(\mathrm{O/H}) \leq 9.19$ ($12 + \log\ (\mathrm{O/H}) = 8.69$ for the solar value). For nitrogen and helium, the relations with $\log Z$ are those defined in Dopita et al. (2000) to take into account the effects of non primary nucleosynthesis. The effects of abundance depletion by grains is also taken into account in CloudyFSPS, following Dopita et al. (2000).

We run our grids of Cloudy models, iterating till the temperature is above 100 K or until convergence: since in the outer regions the ionization rate may fall below the galactic background rate, cosmic ray background emission (Ferland, 1984) was added as a secondary ionization source.

We explored the effect of dust on the line ratios studied here by comparing models with and without dust grains. To this end I assumed for the grains the default size distribution and abundances in the diffuse interstellar medium of our galaxy (van Hoof et al., 2001; Van Hoof et al., 2004; Ferland et al., 2013), described by the grains ISM command in Cloudy. Consistently with Byler et al. (2017) I find that its effect is minimal, with dusty models producing slightly higher O III /Hβ (i.e. $\sim$ 0.19 dex, on average) at fixed N II /Hα for high metallicities and ionization parameters.

We also explored the effect of varying the dust-to-metal abundance, without observing any significant effect.

Finally, I select models with a gas density of $n_H = 10^2$ cm^{-3} since they fully recover the observed line ratios in our GASP and MaNGA samples, as shown in Figure 3.6. In particular, in Figure 3.6 I show the line ratios [OIII] λ5007/[SII] $\lambda\lambda$6713, 6731 and [NII] λ6583/[SII] $\lambda\lambda$6713, 6731 (top left), Composite (top right), AGN (bottom) models and the observed line ratios inside the spaxels in MaNGA and GASP classified by the BPT correspondingly. The purple-shaded curves outline the density distribution of the observations, which is fully covered by the model grid.

H II models

H II models are generated following the same prescription as in Byler et al. (2017). The python library python-fsps is used to generate the ionizing continuum produced by a Single Stellar Population (SSP). To this end, we use the SSPs produced by the

Flexible Stellar Population Synthesis code (FSPS, Conroy et al., 2009) and the MESA Isochrones and Stellar Tracks (MIST; Choi et al., 2016; Dotter, 2016). In Cloudy, the stellar continuum models produced by FSPS are read by the Table STAR command, that also takes as input the stellar age and metallicity[3] to be used. For each Cloudy model, the gas phase metallicity equals to the stellar metallicity.

Unlike the Byler et al. (2017) models, we use the version Cloudy v17.02 due to several improvements in the atomic database introduced with respect to Cloudy v13 (Ferland et al., 2013), in particular concerning the rate coefficient for the S^{2+} - S^{+} dielectronic recombination (Ferland et al., 2017; Badnell et al., 2015; Belfiore et al., 2022).

We test models with stellar ages ranging between 1 Myr $\leq t_* \leq$ 7 Myr (similary to Byler et al., 2017) , and we fix $t_* =$ 4 Myr (see also Mingozzi et al., 2020), as models with stellar ages $t_* \leq$ 4 Myr are perfectly capable to reproduce line ratios typically observed in H ii regions (in agreement with e.g., Dopita, 1997), while models with $t_* \geq$ 4 Myr generate line ratios (such as O iii /Hβ and N ii /Hα) too weak to reproduce the entire range of the observed MaNGA and GASP line ratios of our sample.

AGN models

For AGN photoionization models, we adopt as ionizing source a simple power law continuum (command table power law in Cloudy):

$$\mathrm{S}_\nu \propto \begin{cases} \nu^{\alpha} & h\nu_1 < h\nu < h\nu_2 \\ \nu^{5/2} & h\nu < h\nu_1 \\ \nu^{-2} & h\nu > h\nu_2 \end{cases} \tag{3.7}$$

where $h\nu_1 = 9.12 \times 10^{-3}$ Ryd and $h\nu_2 = 3676$ Ryd define the spectral breaks at 10μm and 50 keV respectively. The slope of the continuum, from the infrared to X-ray wavelength ranges, is set equal to $\alpha =$ - 2.0, as in this way the models were able to

---

[3] Stellar metallicities in MIST are defined within $-2.5 \leq \log(Z/Z_\odot) < +0.5$.

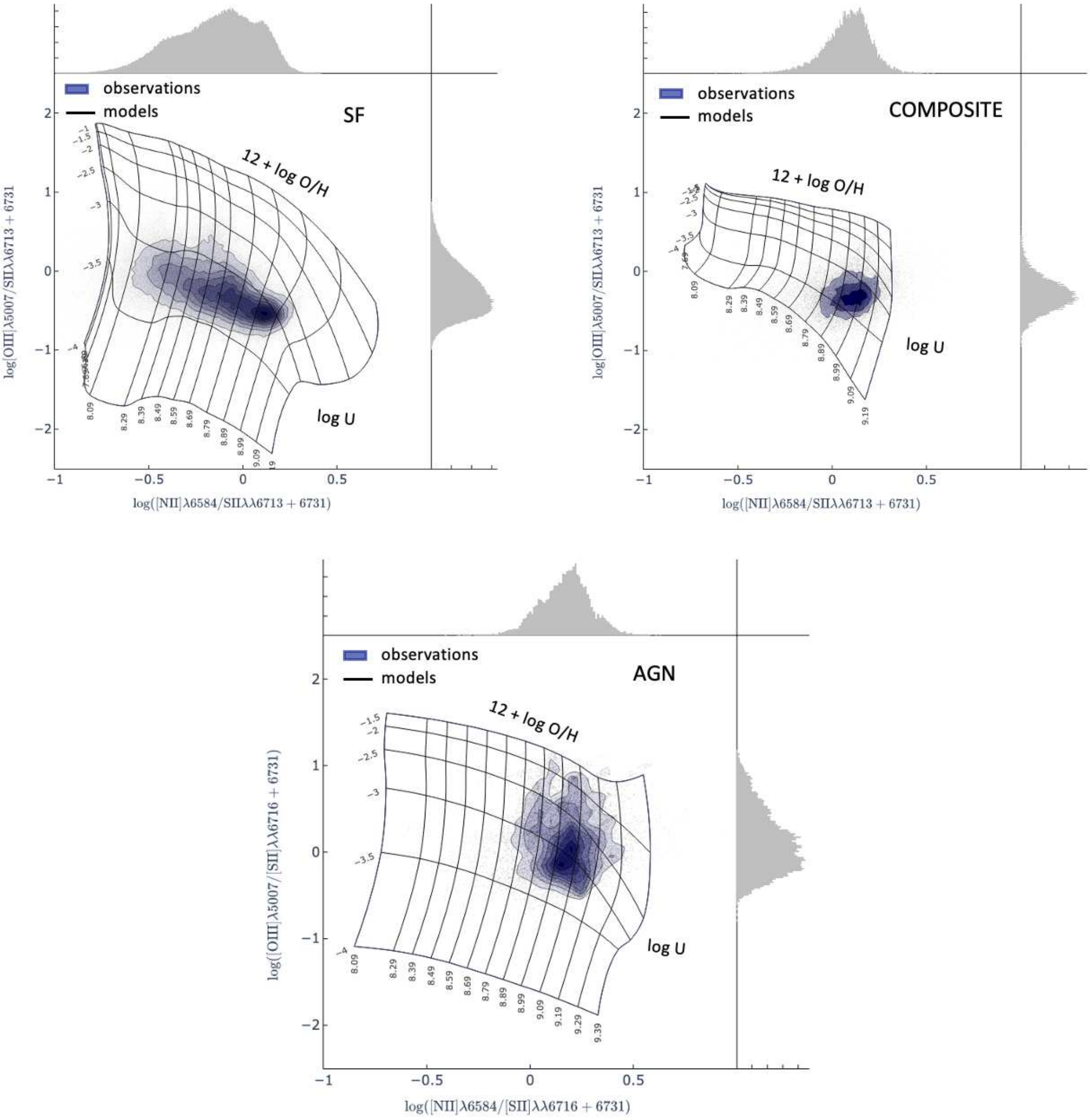

Figure 3.6: O iii /S ii vs N ii /S ii line ratios in case of ionization from SF (top left), AGN+SF (top right), and AGN (bottom). The grey points are the observed line ratios inside the spaxels of the MaNGA and GASP samples together. The distribution of the observed points is outlined by density curves filled with different shades of purple and shown by the grey histograms in the top and right insets. Darker colors indicate regions where the density of data is higher. The black solid lines are the Cloudy models. The H ii models have stellar ages $t_* = 4$ Myr, Composite models have the ionization parameter of the stars $\log U_{\rm Hii}$ is fixed to -3.0 and f_{AGN} is 0.2, AGN models have α = -2.0 (see text for details).

perfectly reproduce the observations. According to the literature, the NLR density is relatively high (i.e., $n_e \approx 300 - 500$ cm^{-3}, Storchi-Bergmann et al., 1998; Feltre et al., 2016; Armah et al., 2023) with respect to the H II regions in the galaxy disc (10 cm^{-3}, e.g., Dopita et al., 2013). However we note that the regions classified as AGN by the BPT can extend well-beyond the sub-kpc scale of the NLR (i.e., the so-called extended narrow line region, ENLR, see e.g. Congiu et al., 2017; Chen et al., 2019) thus we consider $n_{\mathrm{H}} = 10^2$ cm^{-3} as an average value between the high-density (i.e., 500 cm^{-3}) and the low-density (i.e., 10 cm^{-3}) regime.

Composite models

I combine the H II and the AGN models following a similar approach as in Thomas et al. (2018b).

The mixed emission is parametrized by f_{AGN}, defined as:

$$f_{AGN} = \frac{R_{AGN}}{R_{\mathrm{HII}} + R_{AGN}}$$

where R is the flux of the reference line (i.e. Hβ), thus R_{AGN} is the Hβ flux that arises from the AGN and R_{HII} is the the Hβ flux that arises from the HII regions. In other words, f_{AGN} is the fraction of the Hβ flux from the AGN with respect to the total Hβ flux (i.e. $R_{\mathrm{HII}} + R_{AGN}$) of a mixed spectrum, where the emission comes from both stars and AGN.

I obtain the Composite grids with the following steps:

1. we mix the H II and AGN models with the same metallicity and gas density;
2. the mixed emission line ratios are computed as:

$$\left(\frac{L}{R}\right)_{Comp} = \left(\frac{L}{R}\right)_{AGN} \times f_{AGN} + \left(\frac{L}{R}\right)_{\mathrm{HII}} \times (1 - f_{AGN})$$

   where L is the flux of a generic line.

The f_{AGN} is a parameter of the Composite models, which ranges between 0.2 (i.e., 80 % of ionization due to the stars) to 1 (i.e., 100 % of ionizing photons coming from the AGN), with a step of 0.2.

In the Composite models, $\log(U)$ indicates the ionization parameter of the AGN emission, while the ionization parameter of the stars $\log U_{\mathrm{HII}}$ is fixed to -3.0 (i.e., median value observed in pure SF regions), similarly to Thomas et al. (2018b).

3.2.6 NebulaBayes

NebulaBayes (Thomas et al., 2018b) is a code that statistically compares models and observations using the Bayes Theorem. In brief, the code takes as input a set of emission lines from photoionization models and a set of observed emission lines with their relative errors. The line fluxes are then divided for a reference line, specified by the user. By comparing observations and predictions using the Bayes theorem, the code finds the best model to fit the observable. NebulaBayes is provided with models, generated with the code Mappings 5.1 (Sutherland & Dopita, 2017), for both the H II and AGN-ionized regions. However, I will discuss in detail the reasons which lead me to generate and use my own Cloudy models.

Some basic concepts of Bayesian Probability

The user set the density of the parameter space, by choosing the number of parameters (n) and the density of values for each parameter (d_n). Then, the code interpolates the models until the given density ($N = \prod_{k=0}^{n} d_k$) is reached.

After interpolating the models, the code computes the posterior $p(\theta|D, M')$ of the observed data (D), given the set of parameters (θ) of the model (M'):

$$p(\theta|D, M') = \frac{p(\theta|M')p(D|M', \theta)}{p(D|M')} \tag{3.8}$$

where $p(\theta|M')$ is the prior, which is assigned by hand, and $p(D|M', \theta)$ is the likelihood. The likelihood is expressed as follows:

$$p(D|M',\theta) = \prod_{i=1}^{m} p_i \tag{3.9}$$

where m is the number of emission lines used in the analysis and p_i is the probability to measure the emission line's flux f_i:

$$p(f_i|M',\theta) \propto \frac{1}{\sqrt{V_i}} exp\left[-\frac{(f_i - f_i'(\theta))^2}{2V_i}\right] \tag{3.10}$$

$f_i'(\theta)$ is the predicted flux from the model and $V_i = e_i^2 + \epsilon^2 f_i'(\theta)^2$ is the variance, where e_i is the measurement error and ϵ is the model error, which by default is uniformly set $\epsilon = 0.1$.

Given the density of the parameter space (N), Equation (3.8), (3.10) and (3.9) tell us that the posterior is a N dimensional Probability Distribution Function (PDF). The 'best model' is the point in the parameter space which maximizes the posterior PDF. Since the data D is the set of emission lines inside a given spaxel, the code computes the best model inside all the selected spaxels of the galaxy.

To get the posterior PDF of the nth-parameter (e.g. the metallicity), the code computes the marginalized PDF, by integrating the joint PDF over the range of values of the other $n-1$ parameters. The marginalized PDF shows pathological shapes (e.g. double peaks) when multiple values of the given parameter are equally probable.

Application of Nebulabayes

Particular care is necessary when selecting the emission lines to use in a NEBULABAYES analysis (see Thomas et al., 2018a, for details). Among all the emission lines covered by the observational samples, I notice that some widely used combinations are particularly affected by the degeneracy between the ionization parameter and the metallicity (Dopita et al., 2013, and diagnostics therein). In particular, Figure 3.7 shows the N II /Hα versus O III/Hβ for the observational sample with overlaid *this Thesis'* photoionization models, showing that the models are correctly reproducing the observations. However, I also note the well-known folding in the N II -BPT and S II-BPT, which in my models happens around 12 + log (O/H) = 8.6. It follows that, by using the line ratios O III/Hα, N II /Hα and S II/Hα to constrain the parameters, I obtain that NEBULABAYES does not converge to a solution for metallicities around 12 + log (O/H) = 8.59 (similarly to Mingozzi et al., 2020), as it is clear from the blue histogram in Figure 3.8, where I show the results for the MaNGA galaxies. Instead, the choice of using the line ratios O III/S II and N II /S II produces the smooth metallicity distribution shown in Figure 3.8 as a black histogram. I stress that in the latter case the Balmer lines (Hα, Hβ) are not used to constrain the parameter space, but only to estimate the extinction correction.

Choice of lines to use in NebulaBayes

To obtain the metallicity and ionization parameter computed spaxel-by-spaxel, thus, I use our SF/Composite/AGN models inside the spaxels within the galaxy classified by the BPT diagrams correspondingly and compare the predicted and observed emission lines O III and N II normalized for the reference line S II. By using the plane O III /S II (sensitive to $\log U$) versus N II /S II (sensitive to $\log Z$), I was able to distinguish very well models with different values of ionization parameter and metallicity, as shown in Figure 3.6. In this Figure, we plot the H II, AGN, and Composite models on the plane O III /S II vs. N II /S II demonstrating the ability of such lines to unfold the grids. The O III /S II ratio is sensitive to the variation in $\log(U)$ because of the different ionization potentials (IP) needed to create the O++ and S+ ions (35.12 eV and 10.36 eV, respectively). Instead, the ions emitting the N II and S II lines have similar IP and thus the ratio N II /S II has little dependence on $\log(U)$. However, the N II /S II is a good indicator for Z as the growth of N/H scales with Z^2 (Hamann et al., 1993) while S/H is ~ Z (e.g. Dors et al., 2023).

I also summarize, in the following, those works using the Hβ-normalized lines O III λ5007, Hα, N II λ6584, S II λ6716 and S II λ6731 to compute the metallicities, but without finding signs of degeneracy.

Thomas et al. (2019) use the code NEBULABAYES and the Hβ-normalized strong emission lines listed above, with the addition of the lines: O II $\lambda\lambda$3726/29, NE IIIλ3869, O III λ4363 and He I λ5876.

Similarly, Pérez-Díaz et al. (2021) use the Bayesian code HCM (Pérez-Montero, 2014; Pérez-Montero et al., 2019), give in input the same set of lines listed above, with the only addition of the auroral line O III λ4363 (if measured) and normalize them with Hβ. The code HCM assumes a relation between 12 + log (O/H) and $\log(U)$ (from Pérez-Montero, 2014) when the auroral line O III λ4363 is not measured, as predicted 12 + log (O/H)'s values are not valid if the O III λ4363 is not included (see Figure 2 in Pérez-Montero, 2014). Mingozzi et al. (2020) use the lines included in this work, with the only addition of the O II doublet and the S IIi $\lambda\lambda$9069,9532, and an updated version of the code IZI [4] (Blanc et al., 2014), from which NebulaBayes was developed. The authors observe a bimodal metallicity distribution, peaking at 12 + log(O/H) ~ 9 and at 12 + log(O/H) ~ 8.6, with a gap around 12 + log(O/H) ~ 8.8. They discuss how the bimodality is probably caused by the degeneracy between 12 + log(O/H) and log(q), and constrain the ionization parameter with the S III $\lambda\lambda$9069,9532 lines, using the Díaz et al. (1991) relation between the S III/S II and log(q) to set a Gaussian prior on log(q). After this adjustment, the bimodality disappears. We conclude that a relationship (e.g Díaz et al., 1991; Pérez-Montero, 2014) between the ionization parameter and the metallicity, or the use of auroral lines (such as O III λ4363), is necessary to measure 12 + log (O/H) when exploiting line ratios normalized by Hβ line. We also argue more generally that line ratios involving Balmer lines (e.g., Hβ, Hα) are powerful tools to distinguish between star formation and AGN ionization (e.g., BPT diagrams), at the cost to be strongly degenerate in terms of the ionization parameter and not the better-suited choice to estimate the metallicity.

---

[4] https://github.com/francbelf/python_izi

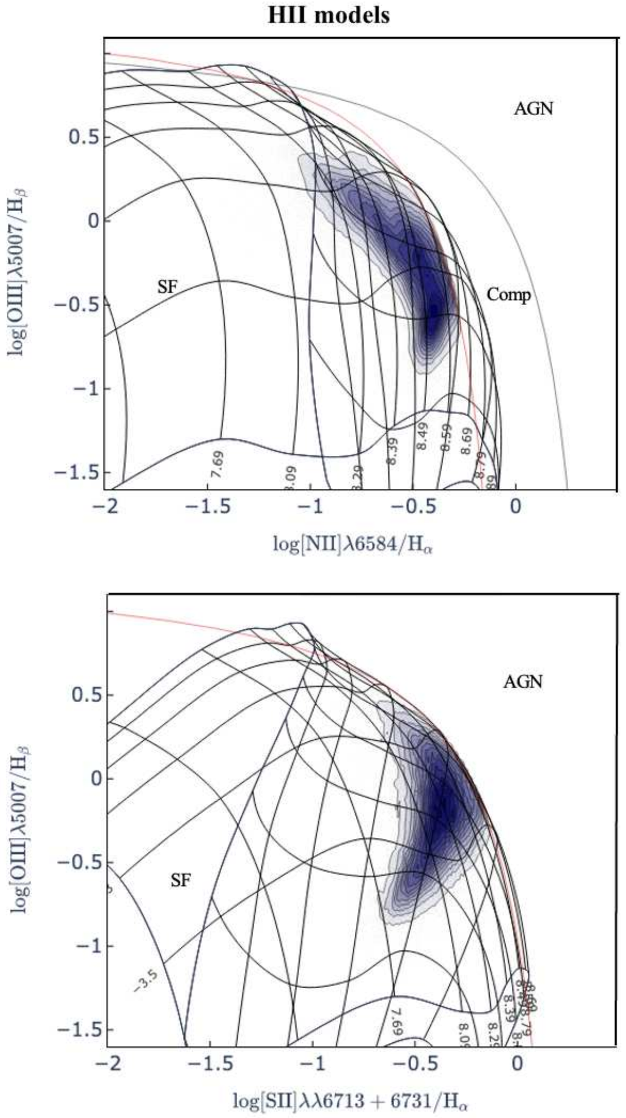

Figure 3.7: H II models (black lines) in the NII-BPT (*top panel*) and in the SII-BPT diagram (*bottom panel*). The H II models, generated with CLOUDY, have $n_H = 100\ cm^{-3}$ and stellar ages t_*= 4 Myr. Density curves, filled with different shades of purple, are drawn to show the distribution of the observed line ratios of the SF spaxels in the MaNGA and GASP samples together. Red lines are the Kauffmann et al. (2003) and Kewley et al. (2001) relations defining the SF regions in the NII-BPT and in the SII-BPT respectively. The black line in the NII-BPT is the Kewley et al. (2001) relationship which distinguishes Composite and Seyfert/LINER. The H II grids fold, due to the degeneracy between the metallicity and the ionization parameter, around 12 + log (O/H) = 8.6 - 8.7.

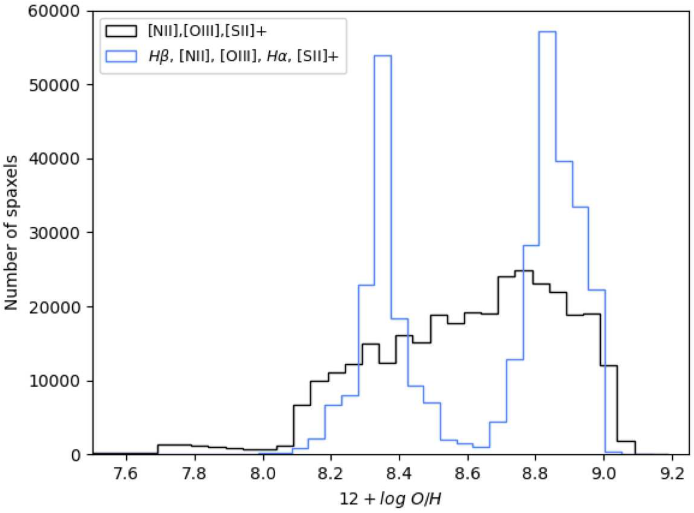

Figure 3.8: Histograms of the 12 + log (O/H) values inside all the spaxels classified as SF by the NII-BPT, in the MaNGA sample. The black histogram shows a uniform distribution in metallicity, obtained when using the O III and N II lines, normalized for S II. The blue histogram shows a strong bimodality, with a gap around 12 + log (O/H) ~ 8.6, and is obtained when normalizing with Hβ the set of lines: Hβ, N II, O III, Hα, S II. The bimodality is caused by the $\log(U)$ - $\log Z$ degeneracy of the models observed in the NII-BPT shown in Figure 3.7.

4

EXPLORING THE AGN-RAM PRESSURE STRIPPING CONNECTION

As mentioned before (see Chapter 1), P17b found a high incidence (6/7) of AGN detected in a sample of jellyfish galaxies. However, the P17b analysis is based on a small sample and importantly is only composed of jellyfish galaxies with very striking tails, and all massive galaxies. Thus, it leaves open the possibility that the AGN activity could be only related to the (rather short) peak phase of stripping and/or only to the galaxy mass regardless of RPS.

A subsequent study did not find a high incidence of AGN: Roman-Oliveira et al. (2018) analyzed a sample of ram pressure stripped galaxies in a supercluster at $z \sim 0.2$ and found only 5/70 AGN, according to optical line diagnostics. Their sample spans a wide galaxy stellar mass range (from 10^9 to $10^{11.5} M_{\odot}$) and is based on visual identification of the candidates. At odds with GASP, none of these candidates have IFS data to confirm they are indeed affected by RPS. It also includes ram pressure stripped candidates with different degrees of stripping, while as said above the P17b study includes only very dramatic cases.

In this Chapter, I aim going to estimate the incidence of AGN on the largest possible sample of ram pressure stripped galaxies up to date in order to find statistically significant evidence of an enhanced AGN fraction in RP-stripped galaxies.

4.1 Galaxy Sample

About the GASP sample, I select only cluster members that have been confirmed to be ram pressure stripped based on the MUSE data: in fact, they all have extraplanar Hα emission in various stages of stripping (B. Poggianti et al. in prep.), from weak/initial stripping (JSTAGE=0.5) to significant tails (JSTAGE=1) to extreme tails longer than the stellar disk diameter (JSTAGE=2, so-called "jellyfish galaxies") to truncated disks corresponding to a late-stage of RPS (JSTAGE=3), for a total of 51 galaxies. From now on I will call this sample GASP-RPS. All of these are morphologically late-type and star-forming galaxies.

For what concern the MaNGA data, I used the DR15. First, I exclude 75 duplicate galaxies and then select only galaxies with a specific Star Formation Rate (sSFR) $>$ $10^{-11}\mathrm{yr}^{-1}$, for a total of 2509 galaxies. The latter selection allows me to consider only star-forming galaxies, as are galaxies in both the GASP-RPS and LIT-RPS samples. To assemble a sample not affected by RPS, I crossmatch the sample with the environmental catalog by Tempel et al. (2014), who provide halo mass estimates based on Navarro et al. (1997) profiles. Using a searching radius of 5″, I obtain a match for 2061 galaxies, 861 of which are located in structures with halo masses $\log(M_h/M_\odot) < 13.0$,[1] therefore are most likely in small groups or isolated. Finally, to reduce the effect of a different morphological

---

[1] I verified that results are insensitive to the exact choice of this threshold, exploring log halo masses up to 13.6. I decided to use a conservative cut (13.0) to avoid the possibility that ram-pressure stripped galaxies in groups contaminate the sample.

mix among the different samples, I use the visual morphological classification from the MaNGA Value Added Catalogs[2] that is based on inspection of image mosaics using a new re-processing of SDSS and Dark Energy Legacy Survey (DESI) images, following the methods from Hernández-Toledo et al. (2010) and exclude 70 early-type (Ellipticals, S0s and S0as) and 2 unclassified galaxies.[3] To assemble the final MaNGA sample, I consider only galaxies that in a circular aperture of 3″ diameter (i.e. the SDSS fibre size) centered on the galaxy have at least 20 spaxels with $\mathrm{S/N} > 3$ for all lines that will be used to detect the presence of an AGN: 782 galaxies pass this selection.

Finally, the sample is further reduced to the 759 galaxies for which I was able to extract the aperture-corrected stellar mass from the Principal Component Analysis (PCA) catalog (Pace et al., 2019a,b). In particular, the aperture correction needed to take into account the galaxy mass residing in the region extending outwards with respect to the 1.5 R_e aperture is recovered with the Color-Mass-To-Light Relations method, which employs relations (as the one in Pace et al., 2019a) between the mass-to-light ratio and the photometric colors of the galaxy's light outside the MaNGA IFU. This constitute the reference sample, called MaNGA-Ref throughout this section. This sample covers a redshift range 0.016< z <0.14. To identify AGN, I inspect the BPT-NII maps provided by the online tool MARVIN and use the same classification criteria as for the RPS samples. By counting the number of spaxels classified as AGN (i.e. Seyfert + LINER), Star-Forming or Composite, if the number of spaxels classified as Seyfert or LINER is larger than 20 in a circular aperture of 3″ diameter, I classify the galaxy as AGN, otherwise as star-forming.

---

[2] https://www.sdss.org/dr16/data_access/value-added-catalogs/?vac_id=manga-visual-morphologies-from-sdss-and-desi-images

[3] For consistency with the other samples, I have applied the morphological cut, but all the results remain unchanged if no morphological criterion is applied.

4.2 The incidence of AGN among ram pressure stripped galaxies

In this section I present the sample of AGN hosts in the GASP-RPS and in the LIT-RPS samples separately and quantify the incidence of AGN among ram pressure stripped galaxies. I also investigate if these fractions depend on the properties of the ram pressure stripped galaxies, such as stellar mass and JSTAGE.

In the following section I will quantitatively compare these fractions controlling for the different mass distribution and comparing them to those of the MaNGA-Ref sample.

4.2.1 GASP-RPS

In the GASP-RPS sample, seven galaxies are already known to host an AGN; six of them were presented in P17b and one (JO36), in Fritz et al. (2017). The latter is an edge-on disk hosting an obscured AGN which is not directly identified using BPT diagrams due to strong dust absorption. However, evidence for the AGN presence comes from extra-nuclear LINER-like emission with a cone morphology and the AGN is detected as a a point-like X-ray Chandra source (Fritz et al., 2017).

Among the P17b candidates, JO194 was classified as a LINER and its combined line ratios are better reproduced by an AGN model (Radovich et al., 2019), while JO201, JO206, JO204, JW100 and JO135 are classified as Seyfert galaxies according to BPT diagrams and are all Seyfert2. JO204 and JO135 also have extended emission line regions ionized by the AGN. Four of these galaxies display AGN outflows (Radovich et al., 2019).

Having inspected all other GASP cluster-members ram-pressure stripped galaxies, I find other 5 AGN candidates.

The stripping characteristics of these galaxies were discussed in previous works and only summarized here, but the analysis of their central ionization mechanism is shown by this work for the first time. JO49 has unwinding tails due to RPS (Bellhouse et al., 2021). It presents a central LINER-like region surrounded by a thin Composite-like ring, which in the BPT diagram correspond to a long finger of points encompassing the

Composite region extending well beyond the K01's line. I note that JO49 is also an XMM source of luminosity $1.2 \times 10^{41}\,\mathrm{erg\,s^{-1}}$ (Webb et al. 2020[4]).

JO85, another unwinding ram pressure stripped galaxy (Bellhouse et al., 2021), has fewer LINER-like points than JO49 embedded in a Composite-like region, but it is highly obscured by dust ($A_V \sim 2.7$ in the central region as measured by the Balmer decrement) and has a central Chandra point source of $5.0 \times 10^{40}\,\mathrm{erg\,s^{-1}}$ (Evans et al., 2020).

JO147 (first described by Merluzzi et al. 2013, see also Poggianti et al. 2019) is an inclined highly-extincted disk, and is stripped in the north-west direction. I find that it has LINER-like opposite cones embedded in wider Composite cones. Its XMM X-ray luminosity is $2.4 \times 10^{41}\,\mathrm{erg\,s^{-1}}$ (Webb et al., 2020).

JO171 is an Hoag-like ring galaxy with long tails stripped in the north direction (Moretti et al., 2018). It has central AGN-powered spaxels (Seyfert2) in the inner kpc.

Finally, JW39 has long tails originating from unwinding spiral arms (Bellhouse et al., 2021). It has a LINER-like circular central region surrounded by a larger circular area with Composite emission.

The latter two galaxies have no available central X-ray counterparts, from neither XMM nor Chandra.

To summarize, with respect to the sample of AGN described in P17b and Radovich et al. (2019), I find an additional Seyfert2 and 4 LINER-like galaxies, yielding a total sample of 12 AGN hosts in the GASP-RPS sample. Their main properties are summarized in Tab. 4.1.

The left panel of Figure 4.1 shows the mass distribution of galaxies hosting an AGN compared to the entire GASP-RPS sample. While RPS galaxies cover a mass range of $8.7 \leq \log(M_*/M_\odot) \leq 11.5$, AGN hosts are among the most massive galaxies in the sample, having all $\log(M_*/M_\odot) \geq 10.5$.

I am now in the position of computing the fraction of AGN (f_{AGN}) over the total (AGN+SF) number of galaxies, considering different subsamples, as summarized in Table

---

[4] The 4XMM-DR10 catalog contains source detections covering an energy interval from 0.2 keV to 12 keV. On the other hand, the Chandra energy range goes from 0.5 to 7 keV.

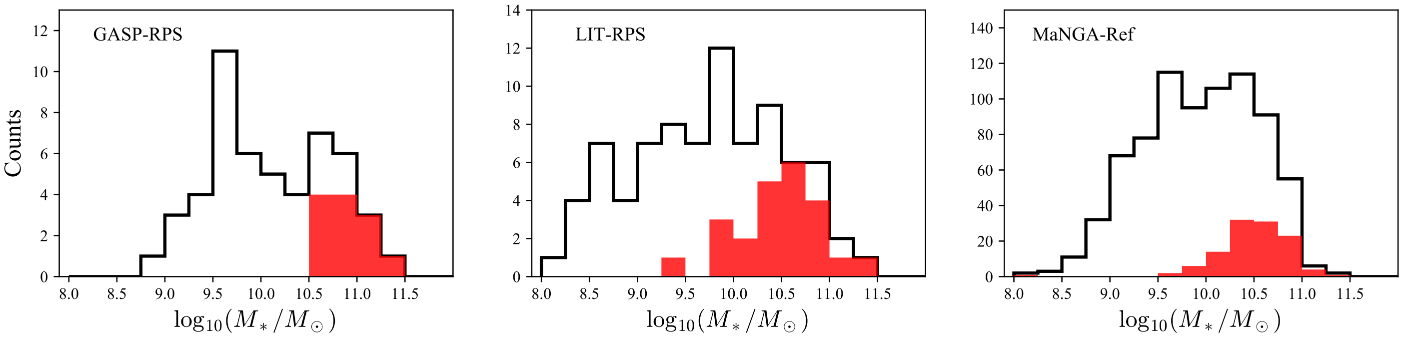

Figure 4.1: Stellar mass distributions for all galaxies (black histogram) and for galaxies hosting an AGN (red histogram). From left to right: the GASP-RPS, LIT-RPS and MaNGA-Ref samples.

4.2. The AGN fraction in the total GASP-RPS sample is $0.24^{+0.06}_{-0.05}$, with uncertainties computed as binonomial errors. Restricting the sample to $\log(M_*/M_\odot) \geq 10.5$, this fraction becomes $0.71^{+0.10}_{-0.12}$.

Considering the various stages of stripping (Fig. 4.2), the frequency of AGN increases with the strength of RPS signatures: no galaxies with AGN activity have Jstage = 0.5, while the AGN incidence increases among moderate-stripping galaxies (Jstage=1, 8%) and is particularly high among Jstage=2 galaxies, where it reaches 56%. Still one out of 4 galaxies in a late stage of RPS (truncated disks, Jstage=3) has an AGN. Interestingly, using the same methods of the current analysis, only two AGNs are found in the GASP non-ram pressure stripped sample of star-forming galaxies, which consists of 49 galaxies (Vulcani et al., 2021, B. Poggianti et al. in prep.).

Among the non-AGN galaxies, there are 8/34 Jstage =2 less massive than $\log(M_*/M_\odot) = 10.5$, while all galaxies more massive than $\log(M_*/M_\odot) = 10.5$ have a Jstage different from 2. This result suggests a tight correlation between stellar mass and Jstage, preventing us from distinguishing which of these two parameters is more connected to the presence of an AGN.

ID	RA	DEC	z	cluster	$\log M_*/M_\odot$	JSTAGE	AGN flag	refs
JO85	351.13068	16.86815	0.0355	A2589	10.7	1	3	P22
JO36	18.247583	15.591488	0.0407	A160	10.8	3	4	F17
JO194	359.25284	-34.680588	0.042	A4059	11.2	2	3	P17b
JO204	153.44513	-0.914182	0.0424	A957	10.6	2	1	P17b
JO201	10.376208	-9.26275	0.0446	A85	10.8	2	1	P17b
JO49	18.682709	0.286136	0.0451	A168	10.7	2	3	P22
JO147	201.70721	-31.395975	0.0506	A3558	11.0	2	3	P22
JO206	318.44754	2.476218	0.0511	IIZW108	11.0	2	1	P17b
JO171	302.56125	-56.641823	0.0521	A3667	10.6	2	1	P22
JO135	194.26791	-30.375088	0.0544	A3532	11.0	2	3	P17b
JW100	354.10443	21.150702	0.0619	A2626	11.4	2	3	P17b
JW39	196.03212	19.210691	0.0663	A1668	11.2	2	3	P22

Table 4.1: AGN candidates in the GASP sample. Columns are: 1) GASP ID; 2-3) coordinates of the optical center; 4) galaxy redshift; 5) host cluster; 6) galaxy stellar masses (Vulcani et al., 2018); 7) JSTAGE (Poggianti et al. in prep.; 8) AGN classification; 9) work in which the source is presented. The adopted AGN flag for both GASP-RPS and LIT-RPS galaxies ranges from 0 to 6: 0 means that star formation is the dominant ionization process at the galaxy center according to BPT-NII classification; 1, 2, 3 if the galaxy hosts a Seyfert 1, Seyfert 2 or LINER-like nucleus, respectively, again according to the BPT diagram; 4 if the AGN has been detected through the X-ray signal, but not in the optical; 5 when the galaxy is classified as a radio galaxy; 6 when the source is classified as AGN, without any specification on the type.

Table 4.2: AGN fractions in the GASP-RPS sample, considering galaxies of different mass and characterized by different JSTAGEs. Errors are binomial.

N_{AGN}/N_{TOT}	f_{AGN}	JSTAGE	$\log(M_*/M_\odot)$
$12/51$	$0.24^{+0.06}_{-0.05}$	≥ 0.5	all
$12/17$	$0.71^{+0.10}_{-0.12}$	≥ 0.5	≥ 10.5
$0/16$	$0.0^{+0.06}_{-0.0}$	$= 0.5$	all
$1/13$	$0.08^{+0.11}_{-0.05}$	$= 1$	all
$10/18$	$0.56^{+0.11}_{-0.12}$	$= 2$	all
$1/4$	$0.25^{+0.25}_{-0.15}$	$=3$	all

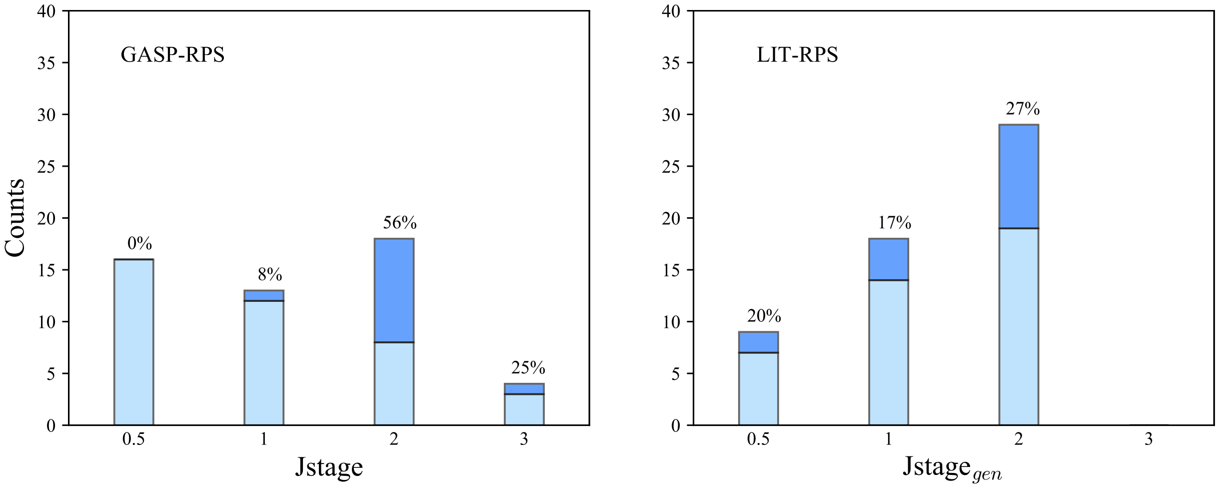

Figure 4.2: Left. Stacked Histograms for galaxies of different JSTAGEs and divided among centrally star-forming galaxies (light blue histogram) and AGN (dark blue histogram) according to the BPT-NII classification for GASP-RPS (left) and LIT-RPS (right). Percentages are AGN fractions in the corresponding bin of JSTAGE and JSTAGE$_{gen}$.

4.2.2 LIT-RPS

The catalog of the 80 literature ram-pressure stripped galaxies us already presented and described in details in .

One of these galaxies has broad optical lines typical of Seyfert1. For all the other galaxies the AGN classification is based on the BPT-NII diagnostic. For $\sim 70\%$ (55/78) of them the classification in published results is based on spectroscopic observations published in dedicated papers, either from integral-field unit (Merluzzi et al., 2013, 2016; Fossati et al., 2016; Boselli et al., 2019; Stroe et al., 2020; Consolandi et al., 2017), long-slit or fiber spectra (Ebeling et al. 2019; Cortese et al. 2007; Owers et al. 2012; Owen et al. 2006; Mahajan et al. 2010[5], Veron-Cetty et al. 2003). We checked that the AGN-like emission was confined in the nuclear regions, while the gas in the galaxy body was ionized by SF, for the galaxies observed in IFU mode. For the other 31% (24/78) of the galaxies I instead use the online AGN classification based on the analysis of emission line ratios extracted from an integrated spectrum of the central circular aperture ($r \sim 3''$) observed with the SDSS fiber (Data Release 8, from now on DR8, Aihara et al. 2011) as analyzed by Brinchmann et al. (2004), Kauffmann et al. (2003), and Tremonti et al. (2004) in the Value Added Catalog MPA/JHU. For 24 galaxies, I had both the DR8 automatic classification and information about the central source from individual publications in the literature. In these cases, I favored the latter.

I note that 4 of the 78 galaxies also have information coming from either X-ray or radio data (Ebeling et al., 2019; Winkler et al., 1992; Owers et al., 2012; Best et al., 2012; Kalita et al., 2019; Caglar et al., 2020). While their position on a BPT-NII diagram suggests they are star-forming, the additional data instead classify them as AGN. In what follows I will therefore discuss how results change if I include or exclude these 4 objects.

Overall, 24/80 galaxies host an AGN (~30%). If I disregard the AGN classification

---

[5] I note that for 2 galaxies, GMP3618 and D100, Mahajan et al. (2010) give different results with respect to the classification reported in the analysis even though they used DR7 data to build up BPT-NII.

based on X-ray or radio data and consistently consider only the BPT-NII classification, the fraction above becomes 20/80 ($\sim 25\%$).

The central panel in Fig.4.1 shows the mass distribution of the galaxies with and without AGN. The entire sample spans a mass range $8.1 < \log(M_*/M_\odot) < 11.4$. Similarly to what found for GASP, most of the AGN are massive galaxies, even though in this sample there are also a few less massive AGN hosts. Above the GASP AGN mass limit ($\log(M_*/M_\odot) > 10.5$) the AGN fraction becomes $0.80^{+0.08}_{-0.12}$.

Table 4.3 reports the AGN fraction for the different subsamples considered, including that for galaxies of different JSTAGE$_{gen}$. The trend of the AGN fraction with JSTAGE$_{gen}$ is weaker than in GASP-RPS (see also Fig. 4.2), with the percentages ranging between 17% and 28% but being consistent within the large errors in all JSTAGES$_{gen}$.[6]

I remind the reader that while the AGN classification and mass estimates among GASP galaxies are homogeneous, for the LIT-RPS sample I based the former on a number of different data and indicators. In addition, stellar masses have been computed following many different approaches and so, even though homogenized to the same IMF, there could be some systematics among the different galaxies. Finally, I recall that the JSTAGE$_{gen}$ flag is based on a very heterogeneous set of images in terms of wavelengths, depth, quality and therefore results must be taken with caution.

4.3 Is the AGN fraction enhanced in RP-stripped galaxies?

In the previous Section, I have quantified the incidence of AGN in RP-stripped galaxies. I have seen that they represent 24% and 25% of the overall GASP-RPS and LIT-RPS samples, respectively. In the following, I will always exclude masses $< 10^9\,M_\odot$, in all samples. Table 4.4 presents the AGN fractions in GASP-RPS and LIT-RPS separately for stellar masses $\geq 10^9 M_\odot$ and $\geq 10^{10} M_\odot$. From now on I exclude from this analysis

---

[6] The subsample of LIT-RPS galaxies with JSTAGE is too small to study trends with the length of the Hα tails.

Table 4.3: AGN fractions for the LIT-RPS sample, considering galaxies of different mass ranges and characterized by different JSTAGE$_{gen}$. Errors on fractions are binomial. Values outside/in brackets are the fractions computed ignoring/considering the 4 galaxies classified as AGN based on radio and X data.

N_{AGN}/N_{TOT}	f_{AGN}	JSTAGE$_{gen}$	$\log(M_*/M_\odot)$
20/80 (24/80)	$0.25^{+0.05}_{-0.05}$ $(0.30^{+0.05}_{-0.05})$	all	all
12/15 (12/15)	$0.80^{+0.08}_{-0.12}$ $(0.80^{+0.08}_{-0.12})$	all	≥ 10.5
4/15 (5/15)	$0.27^{+0.13}_{-0.10}$ $(0.33^{+0.13}_{-0.11})$	=0	all
2/9 (2/9)	$0.22^{+0.16}_{-0.11}$ $(0.22^{+0.16}_{-0.11})$	=0.5	all
3/18 (4/18)	$0.17^{+0.11}_{-0.07}$ $(0.22^{+0.11}_{-0.08})$	=1	all
8/29 (10/29)	$0.28^{+0.09}_{-0.07}$ $(0.35^{+0.09}_{-0.08})$	=2	all

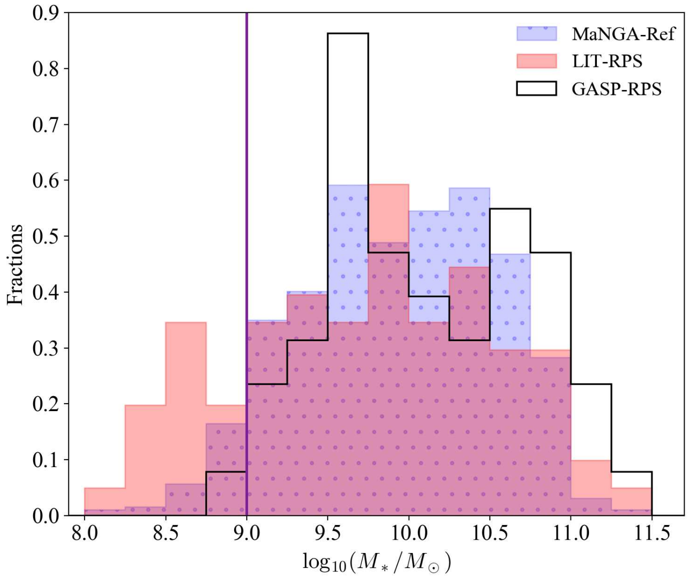

Figure 4.3: Normalized stellar mass distributions of the GASP (black histogram), MaNGA (purple-dotted histogram), and literature sample (light red histogram). For the Montecarlo, I have selected galaxies above the vertical-dotted line, i.e. with masses $\log(M_*/M_\odot) > 9$.

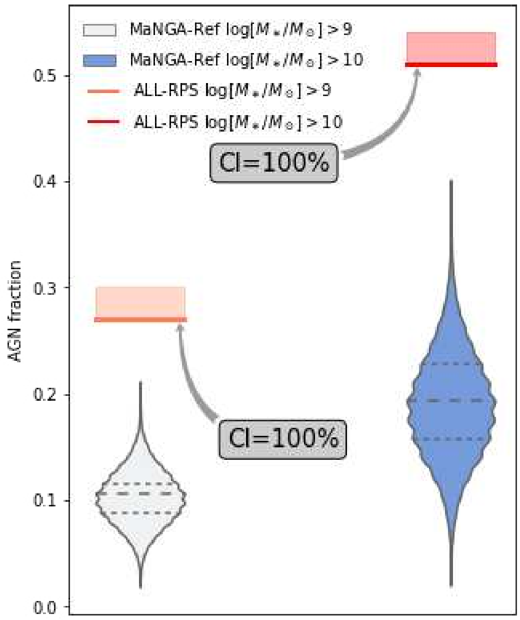

Figure 4.4: Comparison of the AGN fraction in the different samples. Red and orange lines refer to the ALL-RPS sample: the AGN fraction for galaxies with $M_* > 10^9 M_\odot$ is shown by the thick orange line, that for galaxies with $M_* > 10^{10} M_\odot$ by the thick red line. The matched shaded areas indicate by how much fractions change if I consider also the AGN classified on the basis of X-ray or radio data (see text for details). Blue and light blue violin plots refer to the MaNGA-Ref sample, for the two mass bins as indicated in the labels. They show the probability density of the bootstrap random extractions mass-matched to the ALL-RPS sample, at different AGN fraction values, smoothed by a kernel density estimator. Grey horizontal dashed and dotted lines represent median values and 25% and 75% percentiles of the AGN fraction, respectively. Values of the pivotal confidence intervals of the bootstrap distribution are also reported: the mass-matched MaNGA fractions are lower than the ALL-RPS fractions at the confidence level $> 99.9\%$ for galaxies with $M \geq 10^9\, M_\odot$ and for $M \geq 10^{10}\, M_\odot$.

Table 4.4: AGN fractions and binomial errorbars for the GASP-RPS, LIT-RPS and ALL-RPS samples in two different mass bins. For the LIT-RPS and ALL-RPS sample, values in parenthesis are obtained considering also galaxies identified as AGN on the basis of X-ray or radio data.

	GASP-RPS		LIT-RPS		ALL-RPS	
$\log(M_*/M_\odot)$	N_{AGN}/N_{TOT}	f_{AGN}	N_{AGN}/N_{TOT}	f_{AGN}	N_{AGN}/N_{TOT}	f_{AGN}
≥ 9.0	12/50	$0.24^{+0.07}_{-0.06}$	19/63(23/63)	$0.3^{+0.06}_{-0.05}(0.37^{+0.06}_{-0.06})$	31/113(35/113)	$0.27^{+0.04}_{-0.04}$ $(0.31^{+0.05}_{-0.04})$
≥ 10.0	12/25	$0.46^{+0.10}_{-0.09}$	17/29(19/29)	$0.59^{+0.09}_{-0.09}$ $(0.66^{+0.08}_{-0.09})$	29/55(31/55)	$0.53^{+0.07}_{-0.07}$ $(0.56^{+0.07}_{-0.07})$

ID345 at z=0.73, considered a redshift outlier. The fractions in the LIT-RPS sample are always higher than in GASP-RPS (0.30 vs 0.24 and 0.59 vs 0.46, respectively for the two mass bins), but are compatible within the binomial errors. Including also the 4 X-ray/radio AGN in the literature, fractions are slightly higher. I note that also the stellar mass distributions of the two samples are similar (Fig.4.3), and indeed a Kolmogorov-Smirnov (KS) test cannot exclude that they are drawn from the same parent distribution.

It is therefore appropriate to join the two RPS samples, to obtain the largest possible statistics[7], and derive the total AGN fractions: $0.27^{+0.04}_{-0.04}$ at masses $\geq 10^9\,M_\odot$ and $0.53^{+0.07}_{-0.07}$ for masses $\geq 10^{10}\,M_\odot$. These fractions are high, but less extreme than the fraction that would have been inferred from the P17b results, where 6/7 galaxies were AGN with a corresponding fraction of $0.86^{+0.18}_{-0.09}$. This is due to the fact that the 2017 sample was composed of all massive JSTAGE=2 galaxies, and as I have seen in the previous sections these are the most favorable conditions for AGN activity in RPS galaxies.

I now aim at establishing whether the AGN frequency is connected to RPS and therefore I compare the measured fractions to those obtained exploiting the MaNGA-Ref sample, used as representative of non-ram pressure stripped field galaxies.

As for the other samples, also in MaNGA-Ref AGN are located preferentially among the most massive galaxies (right panel of Figure 4.1). The AGN fraction is $0.10^{+0.018}_{-0.02}$

---

[7] Note that the galaxy JO147 appears in both samples, from now on I will just consider it once.

[8] Previous MaNGA works (e.g. Sánchez et al. 2018) have found a significantly lower AGN incidence. However previous analysis has not applied any cut in SSFR as I do, and have adopted much more stringent definitions (emission line ratios above the Kewley demarcation lines considering all the BPT

above $\log(M_*/M_\odot) \geq 9.0$ and $0.19^{+0.04}_{-0.02}$ for $\log(M_*/M_\odot) \geq 10.0$.

A KS test excludes that the MaNGA-Ref mass distribution is drawn from the same parent distribution of the GASP+LIT sample (Fig. 4.3). Since the probability to find an AGN increases with galaxy mass, to properly compare the fractions obtained from MaNGA-Ref and ALL-RPS I need to control for the different mass distributions. I perform a bootstrap random extraction of the MaNGA sample to create 10'000 subsamples with the same mass distribution of the ALL-RPS sample matching the number of ALL-RPS galaxies in bins of 0.3 dex in stellar mass. For each of the extracted samples I compute the AGN fraction f_{AGN}. I repeat the random extraction considering separately two stellar mass ranges, $\mathrm{M}_* \geq 10^9\,\mathrm{M}_\odot$ and $\mathrm{M}_* \geq 10^{10}\mathrm{M}_\odot$. Violin plots with the f_{AGN} distributions for the two mass ranges, their medians and the 25th and 75th percentiles are shown in Fig.4.4. I find that the median f_{AGN} of the 10'000 realizations of mass-matched MaNGA galaxies are f_{AGN} =0.18 for $M \geq 10^9\,M_\odot$ and 0.35 for $M \geq 10^{10}\,M_\odot$. These values are lower than the corresponding values in the ALL-RPS sample, which are 0.27 and 0.53, respectively. In order to assess the significance of the difference between the RPS and non-RPS samples, I compute the pivotal confidence intervals of the bootstrap distribution and find that the mass-matched MaNGA fractions are lower than the ALL-RPS fractions at the $> 99.99\%$ confidence level for galaxies with $M \geq 10^9\,M_\odot$, as well as for galaxies with $M \geq 10^{10}\,M_\odot$.

Since the three samples considered span slightly different redshift ranges, I performed the bootstrap random extractions also limiting all samples to $z \leq 0.075$ (the GASP redshift limit). Results remained unchanged as fractions are affected only at the 1% level at most. Finally, I also tried comparing mass-matched MaNGA samples separately with GASP-RPS and LIT-RPS. Though clearly the statistics decrease, I still find $> 99.99\%$ probabilities that the mass-matched MaNGA sample has lower AGN fractions than the RPS samples, for both GASP-RPS and LIT-RPS samples in the two galaxy mass ranges.

From our analysis, the incidence of AGN activity among ram pressure stripped galax-

---

diagrams simultaneously and Hα equivalent width > 1.5Å in the central regions) for AGN, therefore results are not directly comparable.

ies is significantly higher than that in the MaNGA field control sample. A ram pressure stripped galaxy has a 1.8 times higher probability to host an AGN than a similar non-ram pressure stripped galaxy. This effect is not driven by different stellar mass distributions and points to a connection between RPS and AGN activity.

A larger (of the order of hundreds), homogeneous sample of ram-pressure stripped galaxies with integral-field spectroscopy would be needed to place these results on more solid ground. Since this is currently unavailable, the analysis presented here collects the best available datasets for addressing the question of the AGN-RPS connection. There are however several caveats which are worth stressing.

First of all, the AGN fraction depends strongly on the criteria adopted when using the BPT diagram. In this work, I am including both LINER-like and Seyfert AGN, in order to capture also low-luminosity AGN. This is done in all samples considered in a similar manner, so it should not affect the relative incidence and the main conclusions of this work, but the pure AGN fractions will strongly depend on the initial choice.

Second, although great care has been taken to ensure the most homogeneous analysis possible, the datasets are clearly dishomogeneous. Even GASP and MaNGA, that are both based on integral-field data for every galaxy, have been observed with different instruments, thus have different resolutions, spaxel size etc, and span a slightly different redshift range (see above for invariance of AGN fractions with the redshift interval adopted). The literature sample, obviously, is in itself very heterogeneous, with the spectroscopic information coming from many different sources. The results shown in this paper should therefore be taken with caution, and revisited once large homogeneous samples will become available.

Third, in principle it is possible that the high AGN fraction I observe in RPS galaxies is not a consequence of RPS itself. If the AGN incidence in cluster star-forming galaxies was higher in general than in similar galaxies in the field, the differences with respect to MaNGA would go in the same direction of what I observe. However, as mentioned also above, the AGN fraction in the GASP non-ram-pressure stripped sample is small (2/49) (Vulcani et al., 2021). This sample is composed both of cluster and field “undisturbed" galaxies. If I consider only the GASP cluster control sample (star-forming and late-types), there are no AGN (B. Poggianti et al. in prep). So, this caveat is unlikely to be responsible for our results.

Finally, I note that I am not studying the global AGN fraction in clusters, but the occurrence of AGN activity in a very specific class of cluster galaxies: those with clear signs of ram-pressure stripping, which are all star-forming and late-type galaxies and thus represent a small fraction of the total cluster galaxy population that are dominated by early-type galaxies. Therefore, the results cannot be used to infer the total AGN fraction in clusters and not necessarily show similar trends.

4.4 Summary

I have investigated the occurrence of AGN activity in ram-pressure stripped galaxies in local clusters, comparing it with the AGN frequency in a control sample of field galaxies. In all cases, I rely on BPT diagnostic diagrams based on the [NII] line. All the galaxies analyzed are star-forming and morphologically late-type galaxies.

First, I assembled two samples of ram pressure stripped galaxies. I have used the MUSE data of 51 galaxies observed in the context of the GASP survey (GASP-RPS) finding a Seyfert2 and 4 LINER-like AGN hosts previously unknown, in addition to the 7 galaxies already discussed in P17b and Fritz et al. (2017). I have then conducted a search in the literature assembling a sample of 80 ram-pressure stripped galaxies for which it was possible to retrieve information on their nuclear activity (either from IFU or slit/fibre) (LIT-RPS).

I find similar fractions of AGN in GASP and in literature ram-pressure stripped galaxies, with the AGN incidence being slightly higher in the literature than in GASP, but consistent within the uncertainties. Overall, the AGN fraction in the total GASP-RPS+LIT-RPS sample is $0.27^{+0.04}_{-0.04}$ at masses $M_{*} \geq 10^{9}\,M_{\odot}$ and $0.53^{+0.07}_{-0.07}$ at $M_{*} \geq 10^{10}\,M_{\odot}$. Thus, more than half of the $\geq 10^{10}\,M_{\odot}$ ram-pressure stripped galaxies show AGN activity.

I then compare these findings with those for a sample of galaxies drawn from the

MaNGA survey and inhabiting dark matter haloes with masses $\leq 10^{13} M_{\odot}$. With this halo mass cut I ensure that rich groups and clusters are excluded, hence these galaxies are not undergoing significant RPS and this can serve as a control field sample. I perform a bootstrap random extraction from the MaNGA sample to create 10000 realizations with the same stellar mass distribution of the ram-pressure stripped sample.

The two main results can be summarized as follows:

1) The great majority of galaxies hosting an AGN, in all three samples considered, are high-mass galaxies. There are just very few galaxies with an AGN at masses below $10^{10}\, M_{\odot}$ (no one below $10^{10.5}\, M_{\odot}$ in GASP). As a consequence, the AGN fractions are higher above these limits, and very low below. Another factor that could be playing a role is the ram-pressure strength or phase (JSTAGE): the highest AGN fractions are observed among the most strongly ram-pressure stripped galaxies with the longest tails. However, with the current samples it is hard to disentangle between mass and JSTAGE effects.

2) Even after matching the galaxy mass distributions, the AGN incidence in the field MaNGA sample is lower than in the ram-pressure stripped sample at the $\geq 99.94\%$ confidence level. Overall, a ram pressure stripped galaxy has a 1.5 times higher probability to host an AGN than a similar non-ram pressure stripped galaxy. This supports the hypothesis that ram-pressure can trigger the AGN activity.

5

Gas-phase metallicity of local AGN in the GASP and MaNGA surveys

In this Chapter, I will show how I adopted an approach similar to Thomas et al. (2018a) to compute for the first time the gas-phase metallicity of the central regions of a sample of active galaxies affected by RPS. The aim is to look for signs of metal enrichment or decrement in the nuclear regions of AGN hosts with respect to those in star-forming galaxies without central AGN activity.

To do so, I draw galaxies from the GASP survey and from the MaNGA survey, similarly to Peluso et al. (2022). The use of Integral Field Spectroscopy (IFS) allowed me to derive the global metallicity by exploiting different extraction apertures and to spatially separate regions photo-ionized by stars or by the AGN.

5.0.1 Galaxy sample

From the GASP-RPS sample in Chapter 4, I select the 11 RP-stripped galaxies with Seyfert or LINER-like nuclei (AGN-RPS) according to the spatially-resolved BPT diagnostics and 39 star-forming RP-stripped galaxies without AGN activity (SF-RPS). I excluded four SF galaxies (JO95, JO156, JO153 and JO149) from the RPS sample in Chapter 4 as their irregular I-band morphology prevented a good estimate of their structural parameters (Franchetto et al., 2020), which were necessary to extrapolate the nuclear metallicities.

Moreover, I consider 15 galaxies located in the field and undisturbed by RP (i.e., SF-FS) from the GASP control sample in Vulcani et al. (2018). I exclude only one galaxy (P19482) from the original sample in Vulcani et al. (2018) which was found to be located in a filament in a subsequent work (Vulcani et al., 2021).

For what concerns the control sample, the MaNGA-ref sample used in Chapter 4 covers a redshift range $0.0024 < z < 0.1439$, within which the MaNGA spatial resolution corresponds to a physical size that goes from 0.13 kpc to 6.31 kpc. In fact, the IFU fiber size is 2 and the reconstructed PSF inside the IFU has an FWHM of 2.5, which corresponds to the spatial resolution of the observations (Law et al., 2016). To have approximately a similar spatial resolution in MaNGA and GASP (i.e., $\sim$ 1 kpc), I select the 512 MaNGA galaxies with redshift $z \leq 0.04$. In this way, 30% of the galaxies are at $z \sim 0.025$, where the spatial resolution corresponds to $\sim$ 1 kpc, reaching at most 1.98 kpc of resolution ($z = 0.04$), which is still within a factor of two with respect to the resolution of GASP. Among the 512 galaxies, I include in the sample only those belonging to the Primary+Color-Enhanced sample (Bundy et al., 2015), in order to have a smooth distribution in redshift, while ensuring complete coverage of the i-band magnitudes. The Primary+Color-Enhanced sample covers uniformly the galaxy up to 1.5 times the effective radius (1.5 R_e), which perfectly suits the purposes, as I aim at characterizing the galaxy's central regions. Finally, the sample is further reduced to the 429 galaxies for which I was able to extract the aperture-corrected stellar mass from the

Principal Component Analysis (PCA) catalog (Pace et al., 2019a,b). The final sample spans the stellar mass range $9.0 \leq \log(M_*/M_\odot) \leq 11.3$. Among the 429 galaxies, 52 are Seyfert/LINER (i.e., AGN-FS) according to the spatially-resolved BPT classification with the [NII]/Hα versus [OIII]/ Hβ diagnostic (NII-BPT, Baldwin et al., 1981) and 377 galaxies are classified as star-forming. This sample is part of the so-called star-forming field sample (SF-FS, throughout this section).

5.0.2 Mass-metallicity relation in AGN hosts and SF galaxies in field and clusters.

I estimate the metallicity of the galaxy's central regions, from spatially resolved maps of the oxygen abundance, inside an aperture that scales with the galaxy's mass (or mass-scaled aperture), to address the following question:

i) Does a relation between the stellar mass and metallicity of galaxies with AGN activity exist in RPS galaxies?

To draw the mass-scaled aperture, I compute the projected distances from the galaxy center, using its structural parameters such as the inclination and position angle, and select the spaxels within a projected distance of 0.5 R_e.

In case of AGN host galaxies, I compute the median value of all the 12 + log O/H values inside the AGN, Composite and SF spaxels contained by the aperture, using the corresponding models. In the case of SF galaxies without AGN activity, I discard the emission classified as Composite, which in general is present inside a low fraction of spaxels (i.e., ~5% in the SF GASP sample and ~ 13% in the SF MaNGA sample), since in this case I cannot assume that its origin is the mixed AGN+SF contribution implied to generate our Composite models. Then, I compute the metallicities inside the SF spaxels using the H II models.

By using the same approach, I also estimate the median metallicity inside a fixed aperture of radius $r \sim 1$ kpc (always dominated by AGN emission in case of AGN hosts) to address another open question:

ii) Does the AGN in RPS galaxies show signs of metal enrichment or metal decrement with respect to the same physical region at the center of star-forming galaxies of similar masses?

To understand if the results depend on the RPS, I answer the same questions for the galaxies part of the control samples (SF-FS, AGN-FS) which are located in the field and are undisturbed by RP. The results in the field galaxies are interesting on their own as it is still highly debated in the literature whether an NLR metallicity - stellar mass relation exists (e.g., Thomas et al., 2019; Dors et al., 2020b; Pérez-Díaz et al., 2021) and if AGN are more or less metal-enriched than star-forming regions (e.g., Pérez-Díaz et al., 2021; Armah et al., 2023), since discrepant results have been found even without making a distinction based on the galaxy's environments, as discussed in the Introduction.

5.0.3 The effect of different extraction apertures on spatially-resolved metallicity maps

To illustrate how the choice of the aperture affects the AGN metallicity, I selected two galaxies from the GASP and MANGA samples, shown in Figure 5.1: both galaxies host Seyfert2-like nuclei according to the BPT and have similar stellar masses.

The top panel of Figure 5.1 shows the NII-BPT diagrams of the field galaxy '8993-12705' ($z = 0.030$, log $M_*/M_\odot = 10.96$) and a zoom on the cluster galaxy JO201 ($z = 0.0446$, log $M_*/M_\odot = 10.79$), which is experiencing strong RPS as discussed in Poggianti et al. (2017b).

The other panels of the same figure show the galaxy maps color-coded according to the NII-BPT classification, the metallicity and ionization parameter. On the NII-BPT color-coded map, I overlay the yellow projected aperture extending up to 0.5 R_e and the green on-sky aperture extending up to 1 kpc from the galaxy center.

The 1 kpc aperture includes a higher or lower fraction of the galaxy's total light depending on the stellar mass, as opposed to the $r \sim 0.5\ R_e$ aperture.

However, the 1 kpc aperture has the advantage to include predominantly AGN spaxels, while the $0.5 R_e$ aperture in some galaxies includes a non-negligible fraction of SF/Composite spaxels.

In this sense, the 1 kpc aperture is a better-suited choice to reduce the dependence of the AGN metallicity estimates on processes that are not linked to the presence of the AGN, as shown at the end of Section §5.0.5.

Finally, I briefly comment on the metallicity and ionization parameter maps of the two galaxies shown in Figures 5.1 (c) and (d).

The galaxy '8993-12705' shows a strong inward increase in metallicity, which rapidly increases from 12 + log (O/H) ~ 8.8 in the outer star-forming regions to 12 + log (O/H) ~ 9.2 in the galaxy center. The transition from lower to higher metallicities is co-spatial with the increase of the AGN ionization parameter, which jumps from log(U) ~ -2.5 to log(U) ~ -1.3. Star-forming regions show an average value of log(U) ~ -3.2 (see also Thomas et al., 2019). On the other side, the metallicity in JO201 peaks around 12 + log (O/H) ~ 9.0 in the galaxy center in correspondence to the AGN, and I note that also the gas in the right lower side of the stripped tail shows similar values as well. I also observe two high-metallicity and high-ionization parameter elongated regions symmetrically oriented with respect to the galaxy center. The peak of the AGN ionization parameter (log(U) ~ -1.6) and of the metallicity (12 + log (O/H) ~ 9.0) is presumably tracing the actual position of the AGN, more precisely than the NII-BPT classification map in which the AGN-like region is extending well beyond the NLR.

5.0.4 Gas-phase metallicity of the AGN in RP stripped and undisturbed galaxies

Figure 5.2 shows the metallicity as a function of the host galaxy stellar mass of the AGN-RPS (squares) and AGN-FS (circles) samples. To compute metallicities, I consider the median value of 12 + log (O/H) in all the spaxels within r ~ 0.5 R_e from the galaxy center as a representative value for each galaxy. I have verified that the mass-scaled aperture was always larger than the PSF (e.g., on-sky aperture with diameter d ~ 2.5 in MaNGA, and d ~ 1 in GASP), and therefore includes a well-resolved galactic region. In support of the robustness of the results to a different choice of the extraction aperture,

Figure 3 in Franchetto et al. (2020) clearly shows that the mean (or median) value inside 0.5 R_e is consistent with the median values computed inside smaller apertures or at fixed galactocentric radii in our galaxies (see also Moustakas & Kennicutt, 2006).

Points in Figure 5.2 are color-coded according to the integrated luminosity of the emission line [OIII] λ5007 (i.e., L[OIII] hereafter) inside the fixed aperture of $r \sim 1$ kpc, which is a proxy of the bolometric luminosity of the central AGN (e.g., Berton et al., 2015). I calculated L[OIII] only for galaxies with at least 10 spaxels within $r \sim 1$ kpc powered by the AGN according to the BPT diagram, with S/N > 3 in GASP or S/N > 1.5 in MaNGA for the lines listed in Section 2.1.2. This selection restricts our sample to 9/11 AGN in GASP and 48/52 AGN in MaNGA. AGN with no reliable L[OIII] are shown as dashed white-colored symbols.

The $12 + \log(\mathrm{O/H})$ and stellar mass distributions of the AGN-RPS and AGN-FS are shown as grey and white histograms, respectively, in the subpanels.

The two samples span the same range of L[OIII] and 12 + log (O/H), where the minimum values are 2.5×10^{38} L$_\odot$ and 8.77, respectively, and the maximum values are 1.2×10^{42} L$_\odot$ and 9.22.

A 2D Kolmogorov-Smirnov (KS) test could not exclude that the AGN-FS and AGN-RPS samples are drawn from the same parent distribution. This result suggests that the RPS is not playing a crucial role in shaping the metallicity within $r < 0.5$ R_e and the [OIII] luminosity of the AGN ($r < 1$ kpc) in AGN hosts.

Galaxies of the AGN-RPS sample have slightly higher median L[OIII] $= 41.24^{+0.65}_{-1.28}$ L$_\odot$ than the AGN-FS with median L[OIII] $= 40.19^{+0.88}_{-0.57}$ L$_\odot$. However, the values are consistent within the 16th and 84th percentiles of the L[OIII] and 12 + log (O/H) distributions. The higher L[OIII] luminosities of the AGN-RPS sample are presumably due to the preponderance of Seyfert-like nuclei in this sample. In fact, the AGN-RPS has ∼ 50 % (6/11) of Seyfert 2 galaxies, while in the AGN-FS the Seyfert fraction is 16% (9/53).

Next, I study the relationship between the stellar mass and the AGN metallicity in the AGN-RPS and AGN-FS samples, joined together. The Spearman correlation coefficient is R ∼ 0.27 with a p-value of 0.034, thus the test is not able to conclude that the two quantities are correlated. I argue that this can partially depend on the fact that the galaxies span a very limited range in stellar mass, as AGN are known to be located only in the most massive systems (e.g., Sánchez et al., 2018; Peluso et al., 2022). I also do not see a clear relationship between the stellar mass and L[O III] from Figure 5.2 and, accordingly to that, the Spearman test gives a correlation coefficient of R ~ 0.25 with a p-value of 0.07.

5.0.5 Comparison between metallicities of the nuclear regions in AGN and SF galaxies

To test previous literature findings (Armah et al., 2023; Thomas et al., 2019), I investigate the difference between the metallicity in the nuclear regions of AGN and SF galaxies. Even though the AGN-RPS and AGN-FS show the same MZ distributions (see Section 5.0.4), in the first part of this section I still present the results separately for the two samples.

Figure 5.3 shows the MZR of the SF and AGN galaxies, with different symbols for RP-stripped (squares) and non-RP-stripped (circles) galaxies. The metallicity is computed as the median of all the values of 12 + log (O/H) within $r < 0.5\ R_{\rm e}$.

The AGN galaxies are shown as grey symbols, while the SF galaxies are color-coded according to their SFR $(\mathrm{H}\alpha)_{1.5Re}$, which is the SFR within 1.5 $R_{\rm e}$ computed with the Kennicutt (1998) relation, SFR $(\mathrm{M_\odot yr^{-1}}) = 4.6 \times 10^{-42}\ L_{\mathrm{H}\alpha}$ (erg $\mathrm{s^{-1}}$), using the reddening-corrected Hα-flux. This is the FoV of the MaNGA SF galaxies, while for the GASP SF galaxies I computed the SFR $(\mathrm{H}\alpha)_{1.5R_{\rm e}}$ by excluding the spaxels beyond $1.5 R_{\rm e}$

To fit the mass-metallicity relation of star-forming galaxies (SF MZR), shown in Figure 5.3 as the blue dotted line, I join the SF-RPS and SF-FS and I exploit the SF-FS galaxies to obtain the fit also at high stellar masses where the AGN are located.

In fact, the SF-RPS sample has only 3/37 galaxies with $\log \mathrm{M_*/M_\odot} > 10.5$, since (as seen in Peluso et al., 2022) the GASP-RPS AGN fraction is 51% in the mass bin $\log\ (\mathrm{M_*/M_\odot}) > 10$, while the SF-FS has 33/391 galaxies (i.e., 9%) with $\log\ (\mathrm{M_*/M_\odot}) > 10.8$.

It is worth noticing, though, that the SF-RPS show on average lower metallicities than the SF-FS, but the lowest metallicities of the SF-RPS are consistent with the scatter expected from the Fundamental MZR (Mannucci et al., 2010).

To fit the SF MZR, I use the parametrized function from Curti et al. (2020) (see also Mingozzi et al., 2020):

$$12 + \log(\mathrm{O/H}) = \mathrm{Z}_0 - \gamma/\beta \times \log\left[1 + \left(\frac{\mathrm{M}}{\mathrm{M}_0}\right)^{-\beta}\right] \tag{5.1}$$

where Z_0 is the asymptotic value of metallicity at which the relation saturates, M_0 is the characteristic turnover mass above which the metallicity asymptotically approaches the upper metallicity limit (Z_0) and β quantifies how rapidly the curve approaches its saturation value. For $\mathrm{M}_* < \mathrm{M}_0$, the SF-MZR is a power law of index γ. I fix the turnover mass $\mathrm{M}_0 = 10^{10.1}\mathrm{M}_\odot$. To obtain the best-fit parameters, I use the non-linear least squares (NLS) method which minimizes the residuals, weighted for the uncertainty on the datapoints (σ_y). σ_y is the lowest value between σ_- and σ_+, where σ_- and σ_+ are the average values of the 16th and 84th percentiles of the metallicity PDF among all the spaxels within $0.5R_\mathrm{e}$.

I obtain the following best-fit parameters: $\mathrm{Z}_0 = 9.045 \pm 0.001$, $\gamma = 0.754 \pm 0.008$ and $\beta = 1.121 \pm 0.064$. The one standard deviation error on the parameter estimates is the squared variance (i.e., the diagonal) of the covariance matrix. I observe a plateau in the SF MZR at $\log(\mathrm{M}_*/\mathrm{M}_\odot) > 10.5$ (similarly to Tremonti et al., 2004) where the metallicity is $<12 + \log\,(\mathrm{O/H})>_{0.5\ R_\mathrm{e}} \sim 9.0$ independently of the stellar mass.

Figure 5.4 shows the residuals of the AGN metallicities from the SF MZR, $\Delta\,(\mathrm{O/H})_{r<0.5\ R_\mathrm{e}}$, which is the difference between the metallicity of the AGN and the one computed with equation (5.1). AGN hosts predominantly lie above the SF-MZR, suggesting that the presence of the AGN is enhancing the oxygen abundance in the galactic nuclei. As expected from the results presented in Section §5.0.5, this result is independent of the presence of RPS, since the AGN-RPS sample shows a similar enhancement in metallicity as the AGN-FS sample.

Overall, I find that the median offset of the combined AGN sample (RPS and FS) from the SF MZR is Δ (O/H) $_{r<0.5\ R_e}$ $= 0.047$ dex, which is consistent with previous findings (e.g., Thomas et al., 2019).

Interestingly, two galaxies (JO206 and JO171) from the AGN-RPS show a metallicity that is lower than that found in SF galaxies, which are the outliers in Figure 5.4. The AGN with the lowest metallicity, JO171, is a very peculiar object as it is a Hoag-like post-merger whose central metallicity is not directly linked with the total mass (Moretti et al., 2018). For the galaxy JO206 the interpretation is less clear and would require further analysis, for example by exploring the possible presence of metal-poor inflows of gas (as recently seen in e.g., Pérez-Díaz et al., 2023, in the IR regime) or a particularly strong AGN feedback (Armah et al., 2023).

$\log(\mathrm{M_0/M_\odot})$	$(12+\log \mathrm{O/H})_{\mathrm{AGN,1kpc}}$	$(12+\log \mathrm{O/H})_{\mathrm{SF,1kpc}}$	$\Delta\ (\mathrm{O/H})_{r<\mathrm{1kpc}}$
10.50	$9.069^{+0.152}_{-0.045}$	$8.989^{+0.152}_{-0.045}$	$0.080^{+0.065}_{-0.055}$
10.70	$9.033^{+0.152}_{-0.045}$	$8.989^{+0.152}_{-0.045}$	$0.044^{+0.108}_{-0.059}$
10.90	$9.119^{+0.152}_{-0.045}$	$9.014^{+0.152}_{-0.045}$	$0.104^{+0.059}_{-0.113}$
11.10	$9.069^{+0.152}_{-0.045}$	$9.014^{+0.152}_{-0.045}$	$0.054^{+0.153}_{-0.046}$

Table 5.1: Columns: 1) central mass of the mass bins ($\log \mathrm{M_0/M_\odot}$) in which there are more than 5 AGN galaxies; 2,3) median metallicities of the AGN and SF galaxies inside the mass bin, with the 16th/84th percentiles of the distribution (12+ log $\mathrm{O/H_{AGN,1kpc}}$ and 12+ log $\mathrm{O/H_{SF,1kpc}}$ respectively); (4) values of $\Delta\ (\mathrm{O/H})_{r<\mathrm{1kpc}}$ which are obtained as the difference between (12+ log $\mathrm{O/H})_{\mathrm{AGN,1kpc}}$ and (12+ log $\mathrm{O/H})_{\mathrm{SF,1kpc}}$; the errors are computed propagating the errors on (12+ log $\mathrm{O/H})_{\mathrm{AGN,1kpc}}$ and (12+ log $\mathrm{O/H})_{\mathrm{SF,1kpc}}$.

To have an estimate of the AGN metallicity without a significant contribution from gas ionized by stars, I also computed the metallicities inside the fixed aperture of radius $r \sim 1$ kpc from the galaxy center, which is always dominated by the emission from Seyfert/LINER-classified spaxels in case of AGN hosts.

Figure 5.5 (left panel) shows the metallicities within 1 kpc for galaxies with $\log(\mathrm{M_*/M_\odot}) > 10.4$. I consider separately galaxies in stellar mass bins of 0.2 dex width (i.e., stripes of different colors), since I want to avoid the dependence of the metallicity estimates on the portion of the galaxy covered by the fixed aperture, which changes with the stellar mass.

I compute the median 12 + log (O/H) of AGN metallicities inside each mass bin (12+log O/H$_{\mathrm{AGN,1kpc}}$, filled-colored circles) only when there are more than five AGN galaxies inside that bin.

Qualitatively, results do not change depending on the chosen aperture and, as for the mass-scaled aperture, the AGN galaxies show higher metallicities than SF galaxies. Figure 5.5 (right panel) shows $\Delta(\mathrm{O/H})_{1kpc}$ which is the difference between the metallicities of the AGN (12+log (O/H)$_{\mathrm{AGN,1kpc}}$) and SF (12+log (O/H)$_{\mathrm{SF,1kpc}}$) galaxies with similar stellar masses, which basically quantifies how much the NLR is enriched in metals with respect to a region with the same physical extension but at the center of star-forming galaxies. The red dotted line remarks the level at which $\Delta(\mathrm{O/H})_{1kpc} = 0$. In Table 5.1 I list the central mass of the bin, (12+log O/H)$_{\mathrm{SF,1kpc}}$, (12+log O/H)$_{\mathrm{AGN,1kpc}}$ and $\Delta(\mathrm{O/H})_{r<\mathrm{1kpc}}$ in each mass bin. The errors on $\Delta(\mathrm{O/H})_{r<1kpc}$ are calculated considering the errors on (12+log O/H)$_{\mathrm{AGN,1kpc}}$ and (12+log O/H)$_{\mathrm{SF,1kpc}}$. The offset $\Delta(\mathrm{O/H})_{r<\mathrm{1kpc}}$ is positive in each bin of mass and ranges between 0.044 dex and 0.065 dex depending on the stellar mass, which is consistent within the errors with the offset of 0.06 dex measured by Thomas et al. (2019). The aperture used by Thomas et al. (2019) to integrate the metallicity is comparable in extension with the fixed aperture of 1 kpc at the targets' redshift, as discussed in detail in the following sections.

5.0.6 Comparison with the literature

By using a similar approach to ours, Pérez-Díaz et al. (2021) find that AGN (both Seyferts and LINERs) galaxies do not follow a mass-metallicity relation and that Seyfert 2 have slightly higher chemical abundances than SF galaxies, in the mass range $9 \leq \log(\mathrm{M}_*/\mathrm{M}_\odot) \leq 12$. However, they also find that LINER galaxies have lower abundances than SF galaxies. Pérez-Díaz et al. (2021) use Bayesian inference to compare CLOUDY v17.01 models and observations by exploiting the code HCM (Pérez-Montero, 2014;

Pérez-Montero et al., 2019) in a sample of 143 SF, LINER and Seyfert galaxies observed with the Palomar Spectroscopic Survey. One of the main differences with our analysis is that Pérez-Díaz et al. (2021) consider galaxies independently from their environments.

On the contrary, I consider here the effects of AGN in determining the metallicity of their host galaxy in the dense cluster environment, even if our sample is biased towards those showing optical signatures of RPS. The field sample of galaxies is, instead, complete.

Being aware of that, I find a consistent offset between SF and AGN metallicities to that found in Thomas et al. (2019), which uses the code NEBULABAYES and SDSS data to compute the MZR in a sample of 7,669 Seyfert 2 galaxies and 231,429 SF galaxies. They also find that the active galaxies follow a mass-metallicity relation in the mass range $10.1 \leq \log\ M_*/M_\odot \leq 11.3$ since the nuclear metallicity in Sy2s increases of ∼ 0.1 dex over a stellar mass range of 1.3 dex. It is worth noticing, though, that the value 0.1 dex is of the same order than the errors on the metallicity estimates derived with NEBULABAYES (see e.g., Table 5.1 of this paper). The offset of the oxygen abundance in Sy2s concerning the MZR of the star-forming galaxies is ∼ 0.09 dex, but reduces to ∼ 0.06 dex when considering the contribution to the offset coming from the fact that the metallicity in the Seyfert 2 and star-forming samples was constrained using different emission lines. The scatter of 0.06 dex is consistent (within the error bars) with the scatter measured in this work using the $r \sim 1$ kpc aperture (i.e., 2 kpc in diameter), which indeed ranges between 0.04 and 0.07 dex. Our fixed aperture has a diameter of ∼ 2.5 at our target's redshifts, which is fairly similar to the Sloan fiber's diameter of 3 used by Thomas et al. (2019).

However, other works find opposite results. Armah et al. (2023) find lower values of 12 + log (O/H) abundances (with a mean difference of 0.2-0.5 dex) in AGN hosts than in SF galaxies, using an unbiased sample of Seyfert nuclei in the local universe ($z \leq 0.31$) from the BAT AGN Spectroscopic Survey (BASS, Oh et al., 2022), which select AGN from their hard X-ray band emission (14-195 keV). These authors compute the AGN metallicities using the Carvalho et al. (2020) and Storchi-Bergmann et al.

(1998) calibrators, based on photoionization models. By using a similar approach, Do Nascimento et al. (2022) study the metallicity profiles of a sample of 107 Seyfert galaxies using the spatially resolved data from the SDSS-IV MaNGA and the Carvalho et al. (2020) and Storchi-Bergmann et al. (1998) calibrators. They compute the integrated AGN metallicity within the central 2.5 and compare it with the value extrapolated from the radial oxygen abundance profile of H II regions in the galaxy disc. The oxygen abundance in the H II regions is obtained with the calibrator from Pérez-Montero & Contini (2009a).

I find 9 AGN galaxies in common with the Do Nascimento et al. (2022)'s sample (which is indeed the number of Seyfert galaxies in our AGN-FS drawn from the MaNGA survey, see also Section §5.0.4). I measure the integrated metallicity inside an on-sky aperture of 2.5 centered on the galaxy, as in Do Nascimento et al. (2022), but using the metallicity maps obtained in this work. I find that the median difference between the 12 + log (O/H) measured in Do Nascimento et al. (2022) and ours is -0.4 dex when considering their estimates with the Carvalho et al. (2020) (C20) calibrator, and -0.43 dex when considering their oxygen abundances computed with Storchi-Bergmann et al. (1998) (SB98). This is larger than the average difference between the NLR metallicity and the extrapolated value found by the authors, which ranges between 0.16 to 0.30 dex. By estimating the metallicities with the SB98 and C20 calibrators inside all the AGN spaxels in our MaNGA and GASP samples, I find that the values of 12 + log(O/H) computed with our method and with these other calibrators are well-correlated with each other (i.e., $r = 0.48$ in case of the $12 + \log(\mathrm{O/H})_{\mathrm{SB98}}$ and $r = 0.57$ in case of the $12 + \log\,(\mathrm{O/H})_{\mathrm{C20}}$). However, following the approach of Pérez-Díaz et al. (2021), I find an offset of 0.387 dex with RMSE = 0.12 dex between the $12 + \log\,(\mathrm{O/H})_{\mathrm{C20}}$ and $12 + \log\,(\mathrm{O/H})_{\mathrm{Nebulabayes}}$, while I find an offset of 0.391 dex with RMSE = 0.11 dex between the $12 + \log\,(\mathrm{O/H})_{\mathrm{SB98}}$ and $12 + \log\,(\mathrm{O/H})_{\mathrm{Nebulabayes}}$. Therefore, I conclude that the Carvalho et al. (2020) and Storchi-Bergmann et al. (1998) calibrators give systematically lower values of metallicity than the method applied throughout this work and this is the reason for the discrepancy between our findings and those in Do Nascimento et al. (2022).

I stress that even higher offsets are found in the literature when comparing different methods: for example, the offset found by Pérez-Díaz et al. (2021) when comparing their method with the code NebulaBayes (but coupled with the Mappings models, instead of the Cloudy models adopted by us) is 0.8 dex.

Pérez-Díaz et al. (2021) attributed this offset to the different power-law slope adopted in the Mappings and their models (α = -2.0 and α = -0.8 respectively). However, in our case α = -2.0 produces a significantly lower offset. I therefore conclude that a detailed treatment of the possible effects that lead to these discrepancies involves a complex combination of the assumptions underlying each model, whose discussion is beyond the scope of this paper.

5.1 Summary and Conclusions

I have investigated the effect of RPS on the AGN metallicity of 11 Seyfert/LINER galaxies, by comparing their mass-metallicity distribution with that of 52 Seyfert/LINER galaxies undisturbed by RP. I also studied the impact of the presence of a central AGN on the metal content of galactic nuclei, both in case of RPS and not, by exploring the difference between the metallicity at the center of AGN and SF galaxies. To do so, I exploit IFU data from the GASP and MaNGA surveys, and I measure their metallicities using the NebulaBayes code and a set of AGN, Composite and H ii photoionization models generated with the version of the code Cloudy v17.02.

The main findings are summarized as follows:

- AGN galaxies either experiencing RPS or not generally have the same distribution in the mass-metallicity diagram and span the same range of L[Oiii] luminosity. This result suggests that the stripping is not impacting significantly the integrated metallicity and [Oiii] luminosity of the central AGN, at least when looking at a relatively large sample of galaxies;
- The AGN-RPS and AGN-FS galaxies do not seem to follow a mass-metallicity relation, as shown in Figure 5.2, within the short range of stellar masses they

cover;

- Thanks to the use of IFU data, I was able to test our results by integrating the metallicities inside different extraction apertures. Independently from the extraction aperture and the RPS, AGN galaxies show on average enhanced metallicity with respect to SF galaxies at fixed stellar mass. The difference between the metallicity at the centers of AGN and SF galaxies reaches values up to 0.2 dex when using the aperture with $r \sim 0.5\ R_{\rm e}$, while the median difference between metallicities computed with the 1 kpc aperture ranges from 0.04 dex to 0.07 dex, depending on the host galaxy's stellar mass. The positive shift of the AGN metallicities is systematic since this holds inside each bin of stellar mass. However, a larger sample of galaxies would be required to assess the significance of this result as the difference measured in this work is higher than the 1σ uncertainty only in the mass bin with $\log(M_*/M_\odot) > 11$.

In summary, the results show that the presence of the AGN implies higher metallicities in the nuclei of galaxies but that the RPS is not playing a role in changing either the AGN metallicity or [OIII] luminosity.

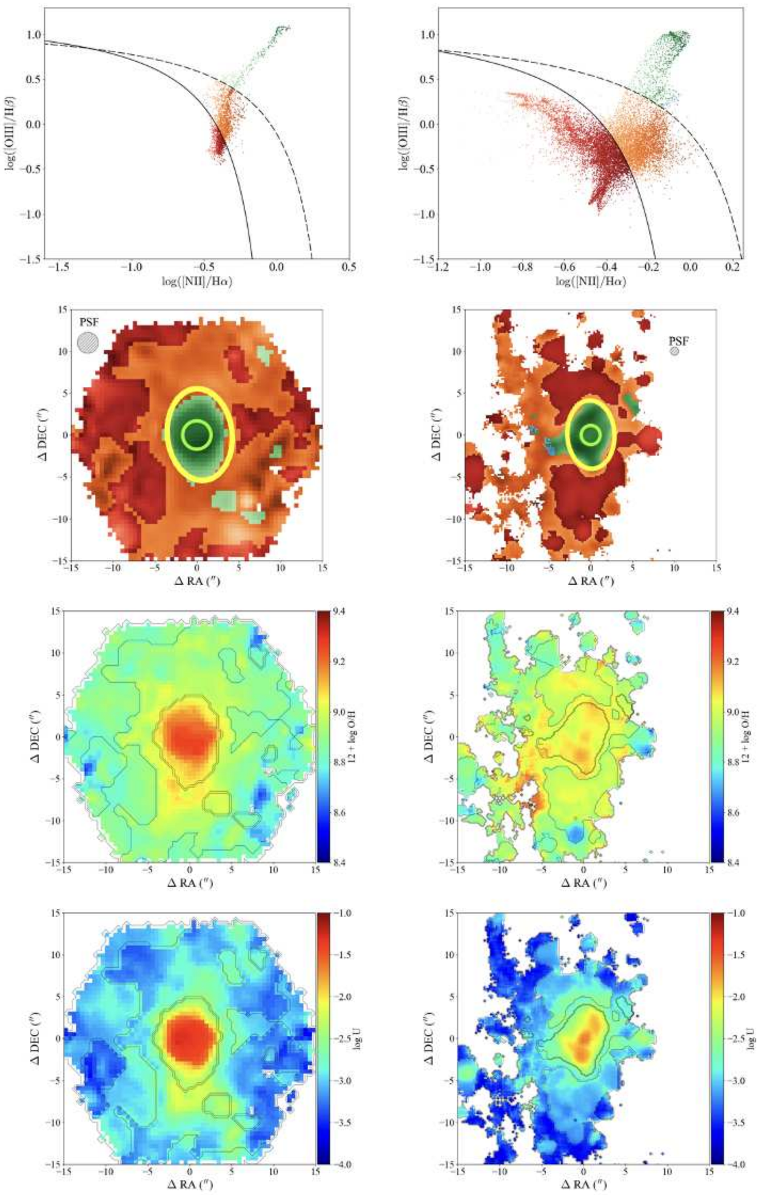

Figure 5.1: NII-BPT diagram and maps of the galaxy '8993-12705' (part of the AGN-FS, on the left) and JO201 (part of the AGN-RPS, on the right). (*top panel*) NII-BPT diagram for all the spaxels in the galaxies, where in the case of JO201 I also include the spaxels of the stripped tail. SF spaxels are in red, Composite spaxels are in orange, LINER spaxels are in light blue and Seyfert spaxels are in green. Darker color shades indicate more intense line ratios, and viceversa. The black line is the Kauffmann et al. (2003) relation and the dotted black line is the Kewley et al. (2001) relation. (*middle panel*) Galaxy map color-coded according to the NII-BPT classification on which I draw the $r \sim 1$ kpc (bright green circle) and $r \sim 0.5R_\mathrm{e}$ (yellow circle) apertures. The $r \sim 1$ kpc aperture is clearly dominated by AGN-only spaxels, while the $r \sim 0.5R_\mathrm{e}$ includes a small fraction of SF/Composite spaxels. The typical PSF size is shown in the top-left corner, with a grey circle. (*bottom panels*) Galaxy map color-coded to the values of 12 + log (O/H) and log(U). The black contours, overlaid on the maps, divide regions classified as AGN/Composite/SF by the NII-BPT. The oxygen abundance 12 + log (O/H) varies between 8.4 and 9.2, the ionization parameter ranges between -4.0 and -1.0.

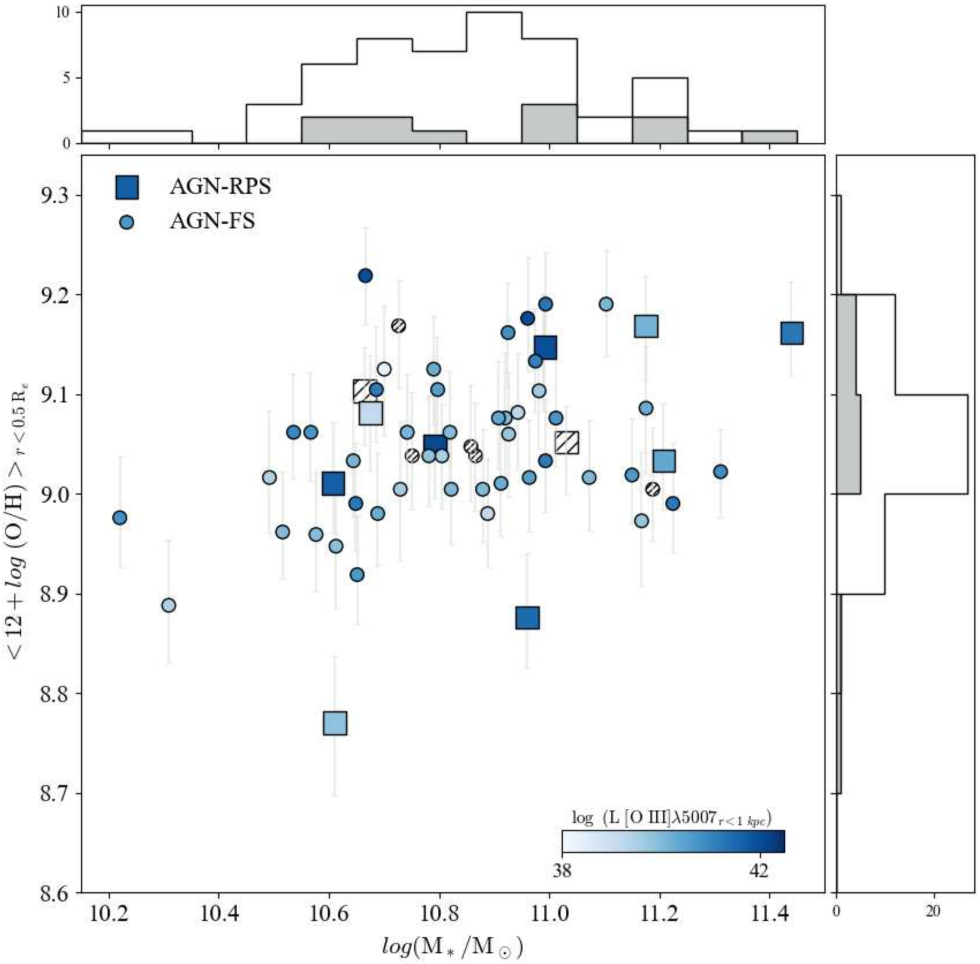

Figure 5.2: MZR of the AGN-RPS (squares) and AGN-FS (circles) color-coded according to their L[OIII] . I show as dashed white symbols those AGN for which I could not estimate L[OIII] (see text for details). The 12 + log (O/H) is computed within the mass-scaled aperture ($r \sim 0.5\ R_e$) and L[OIII] is computed within the fixed aperture ($r \sim 1$ kpc). The error bars are the average values of the 16th and 84th percentiles of the PDF among all the spaxels within $0.5R_e$. The white and grey histograms (in the top and left insets) show the mass and metallicity distributions of the AGN-FS and the AGN-RPS. The two samples have similar ranges of oxygen abundances and L[OIII] .

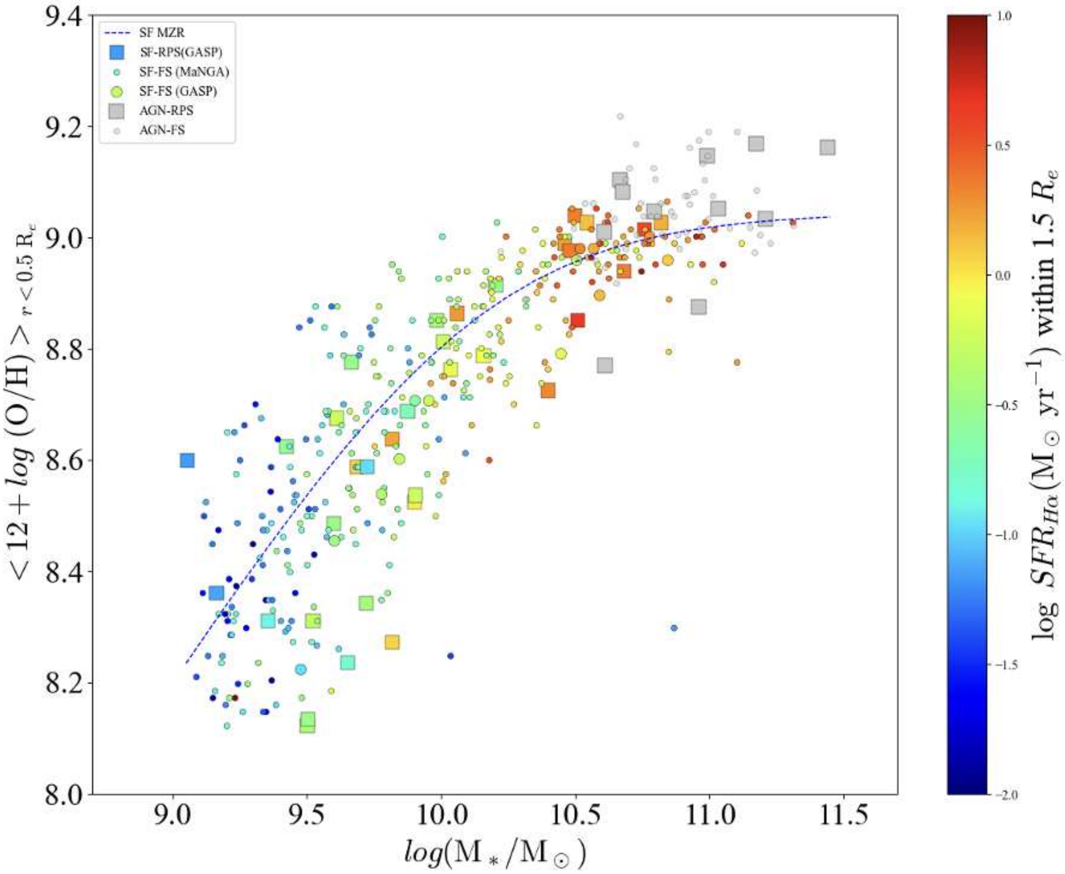

Figure 5.3: Mass-metallicity relation of the SF (colored points) and AGN (grey points) galaxies, with different symbols for the RPS (squares) and non-RPS (circles) samples. Metallicity is computed as the median value in all the spaxels (AGN/SF/Composite) within 0.5 R_e. The blue dotted curve is the best fit for the SF galaxies. SF galaxies are color-coded according to their SFR within 1.5 R_e, a proxy for the total SFR. Overall, AGN galaxies have higher metallicities than SF galaxies.

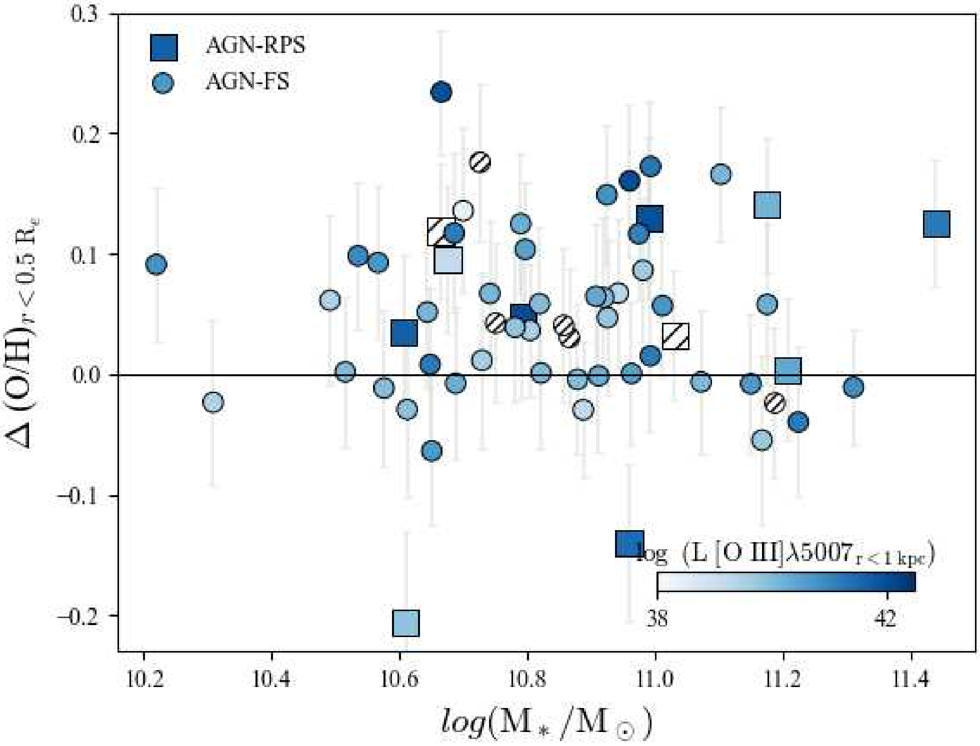

Figure 5.4: Residuals of the AGN-RPS (squares) and AGN-FS (circles) metallicity from the SF MZR, as a function of the galaxy stellar mass, color-coded according to L[OIII] as in Figure 5.2. Dashed white symbols are those AGNs for which I could not estimate L[OIII](see text for details). To compute the error bars on Δ (O/H), I consider the errors on the AGN metallicity and the errors on the SF MZR, computed as described in Section §5.0.5. The horizontal black solid line remarks the level of Δ(O/H) = 0. AGN hosts show Δ(O/H)> 0 on average, except for 2/11 galaxies in the AGN-RPS sample that have lower metallicity than SF galaxies.

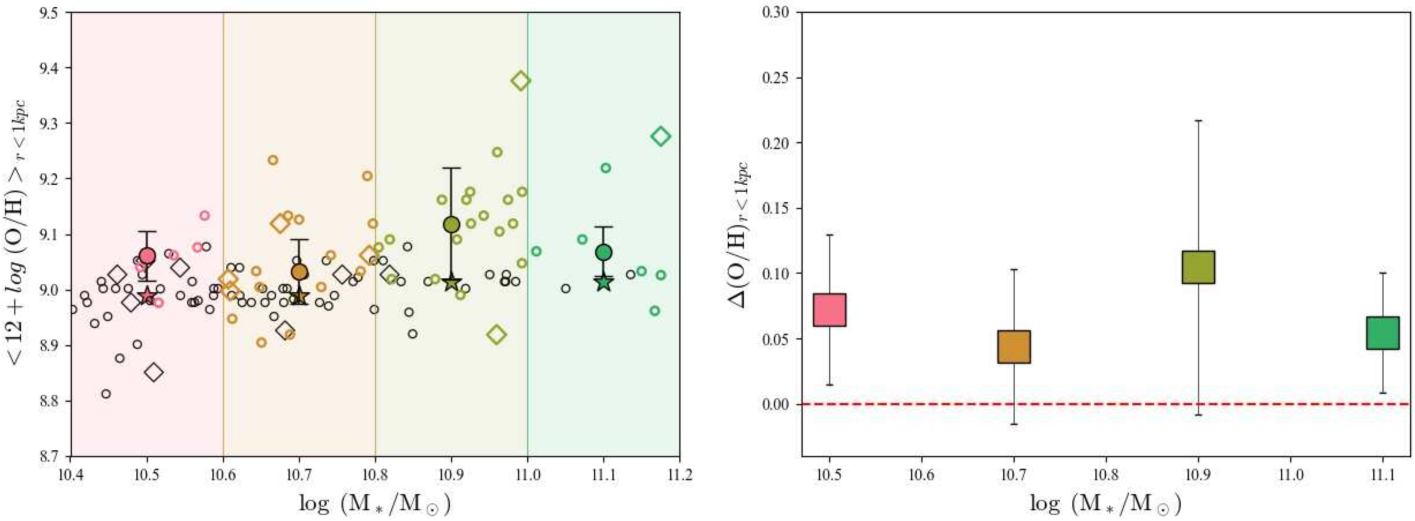

Figure 5.5: (left panel) Mass-metallicity relation of the AGN-RPS galaxies (edge-colored squares), AGN-FS galaxies (edge-colored circles), SF-RPS galaxies (edge-black squares) and SF-FS galaxies (edge-black circles) with stellar masses $\log(M_*/M_\odot) \geq 10.4$, where the metallicities are the median values of 12 + log (O/H) within 1 kpc from the galaxy centers. The filled-colored circles are the median metallicity (12 + log $(O/H)_{AGN,1kpc}$) of the AGN inside the mass bin (i.e., strips of different colors) with the errors given by the 16th/84th percentile of the distribution. The filled-colored stars are the median metallicities (12 + log $(O/H)_{SF,1kpc}$) of the SF galaxies inside the mass bin. (right panel) Difference between (12 + log $(O/H)_{AGN,1kpc}$) and (12 + log $(O/H)_{SF,1kpc}$) as a function of stellar mass. Within the same physical region, galaxies hosting AGN are more enriched in metals than those without AGN activity.

6 METALLICITY GRADIENTS

In this Chapter, I aim to further characterize the impact of the AGN on the host galaxy by studying the spatially resolved gas-phase metallicity in nearby galaxies. Particularly, if the results in Chapter 5 suggest that AGN hosts are more metal-enriched in their central regions with respect to an equivalent area in star-forming galaxies, I aim now to recover the information about the variation of the metallicities *within* the galaxy, in order to check if the central AGN is more/less/equally enriched in metals with respect to the H II regions in the galaxy disk, thus to spatially resolved the effects of the AGN feedback on the surrounding ISM abundances.

To do so, I compute the metallicity gradients in the AGN and SF samples of galaxies already used in Peluso et al. (2023), making use of the photoionization models generated ad hoc for this Thesis and presented in Section 3.2.5. In this way, I find that the metal enhancement is limited to the nuclear regions in AGN hosts since I observe that the gradients in AGN hosts are significantly steeper than in SF galaxies at any given stellar mass.

Do Nascimento et al. (2022) previously attempted to perform a similar analysis, by using the MaNGA survey and SEL calibrators from the literature, and found the opposite result, which is that the NLR in AGN is less metal enriched than the central regions of SF galaxies. I will show in Section 6.1.1 the main differences with the analysis presented in this dissertation and a comparison between the results of this Thesis and those found by Do Nascimento et al. (2022).

6.1 Nuclear versus disk metallicities in AGN and SF galaxies

By considering the same set of galaxies and the same method to compute the gas-phase metallicity described in Chapter 5, I measure the metallicity gradients of the AGN-FS, AGN-RPS, SF-FS and SF-RPS samples. To compute them, I draw radial annuli starting from an inner radius of $r = 0.5\ R_e$ and reaching an outer radius of $r = 1.5\ R_e$ in MaNGA galaxies and $r = 2.6\ R_e$ in GASP. The de-projected distances for the GASP galaxies are computed using the structural parameters in Franchetto et al. (2020).

Proceeding with a step of 0.3 R_e, I compute inside each annulus the median value of the metallicity inside the SF/Composite/AGN spaxels and the errors on the median value, which are the 16th/84th percentiles of the metallicity distribution inside that given annulus.

As an example, Figure 6.1 shows the metallicity maps and gradients of the RP stripped galaxy JO49 hosting an AGN ($\log M_*$= 10.68, $z = 0.0451$) and the SF RP stripped galaxy JO162 ($\log M_* = 9.4$, $z = 0.045$), which does not show signs of AGN activity in its center. If the galaxy JO49 shows a steep metallicity gradient indicative of inside-out galaxy formation (Maiolino & Mannucci, 2019), JO162 on the other hand shows a flatter profile over the entire galaxy body. The same trend shows up for the field AGN galaxy '9024-6102' ($\log M_* = 10.59$, $z = 0.031$) and the SF '8983-12701' ($\log M_* = 10.57$, $z = 0.026$) which are respectively SF and AGN-dominated in their centers (see Figure 6.2).

However, to draw results based on a statistically robust method, I compute the maps and gradients for all the galaxies of the AGN and SF samples. The left panel of Figure 6.1 shows, for each galaxy, the metallicity within 0.3 R_e (12 + log O/H$_{r<0.3R_e}$) versus the metallicity inside the annulus covering the area between r = 0.9 R_e and r = 1.1 R_e (12 + log O/H$_{r=1R_e}$). In this way, I compare the metal content of the nuclear regions of the galaxy and the metal content of the H II regions in the galactic disk. I checked that the inner aperture with $r = 0.3$ R_e was always wider than the smallest spatially-resolved area (e.g., the on-sky aperture with d ~ 1 kpc).

In order not to have a dependency of the results on the host galaxy's stellar mass, I divide the galaxies into two different stellar mass bins: the top panels of Figure 6.1 show the results for galaxies with $10.5 \leq \log M_* \leq 10.8$ and the bottom panels of Figure 6.1 show the results for galaxies with $10.9 \leq \log M_* \leq 11.1$. Red circles are AGN in field, red squares are AGN in clusters and experiencing RPS, blue circles are field SF galaxies and blue squares are the RP stripped galaxies without AGN. I find that RP and non-RP galaxies behave similarly in this plot, thus in agreement with the results in Chapter 5 the RPS is not affecting the metallicities in the nuclear regions of galaxies. For this reason, I will not make any further distinction between the RP and non-RP samples.

Histograms on the right side of the left panels of Figure 6.1 show the distribution of 12 + log O/H$_{r<0.3R_e}$ for the AGN and SF galaxies in red and blue, respectively. It is possible to see that, for a given value of 12 + log O/H$_{r=1\ R_e}$, the AGN hosts on average show higher metallicities in their inner regions (12 + log O/H$_{r<0.3\ R_e}$) than star-forming galaxies, regardless from the galaxy stellar mass. Particularly, the median 12 + log O/H$_{r<0.3\ R_e}$ = $9.05^{+0.08}_{-0.08}$ in AGN host galaxies with $\log M_* \leq 10.8$ is higher than the 12 + log O/H$_{r<0.3R_e}$ = $8.99^{+0.04}_{-0.03}$ in SF galaxies. Similarly, for AGN host galaxies with stellar masses $\log M_* > 10.8$ I found a median 12 + log O/H$_{r<0.3\ R_e}$ = $9.09^{+0.08}_{-0.05}$, which is higher than 12 + log O/H$_{r<0.3\ R_e}$ = $9.014^{+0.02}_{-0.04}$ in SF galaxies. Focusing on the SF galaxies only, an interesting result is that their inner metallicity is always 12 + log O/H$_{r<0.3\ R_e}$ ~ 9.0 in a wide range of values 12 + log O/H$_{r=1\ R_e}$. This flattening of the points is particularly visible in the low-mass bin, $\log M_* < 10.8$.

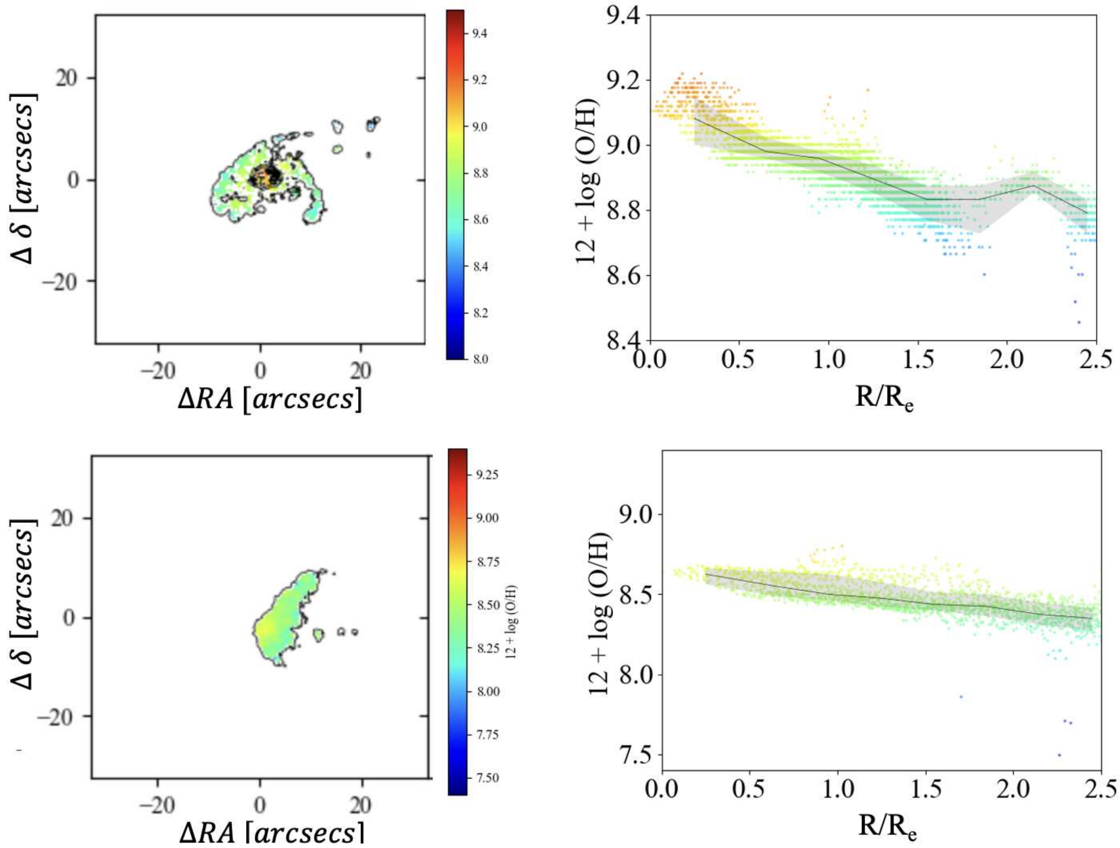

Figure 6.1: Metallicity maps (*left panels*) and metallicity gradients (*right panels*) of the AGN host galaxy JO49 *(top)* and SF *(bottom)* galaxy JO162. I overplot on the metallicity maps the black contours dividing SF, Composite and AGN regions as classified by the N II - BPT. The points of the metallicity gradients are color-coded according to the value of 12 + log O/H inside each spaxel of the galaxy, the black line in the right panels connects the median values of 12 + log O/H inside each annulus and the gray shaded area are the 16th/84th percentiles of the 12 + log O/H's distribution inside the annulus.

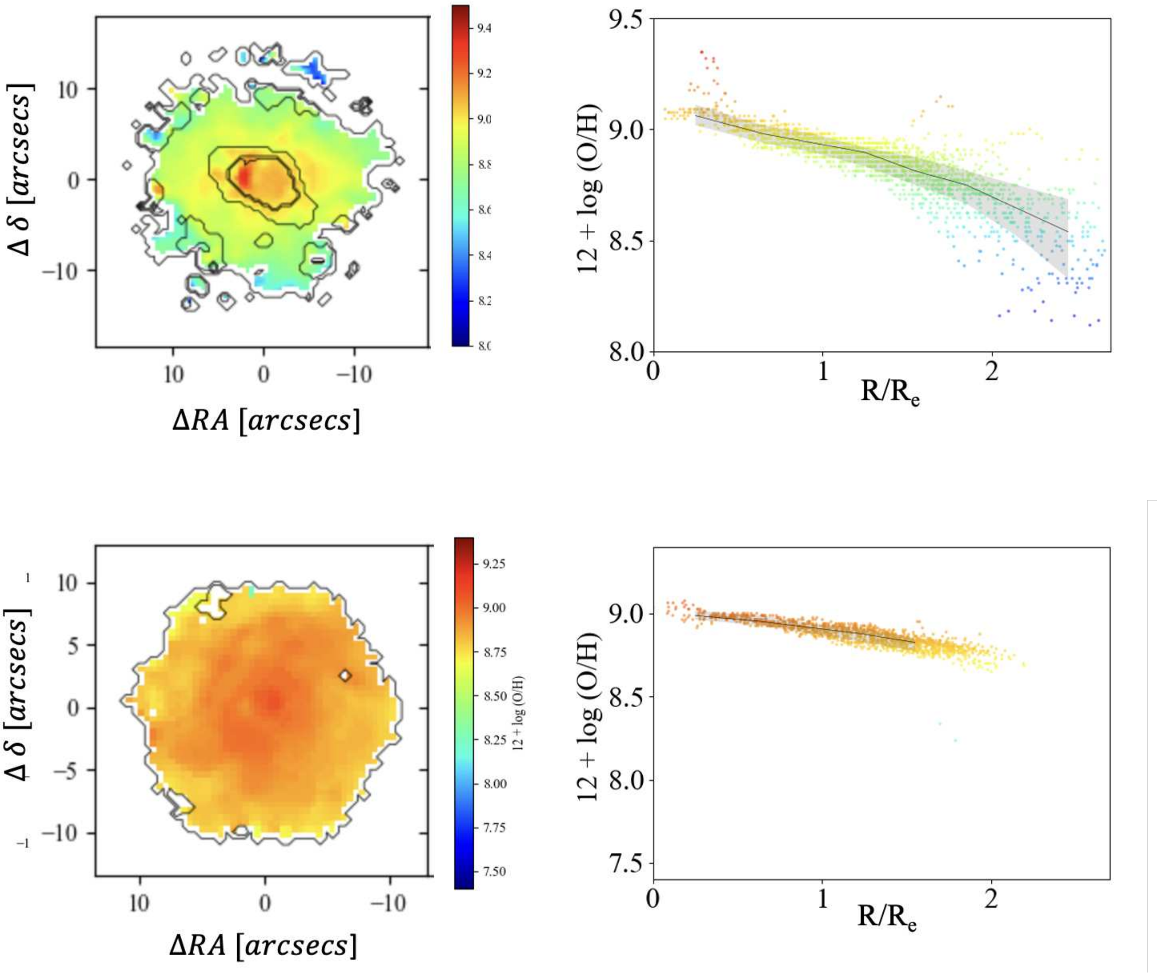

Figure 6.2: Same as in Figure 6.1, but in case of the AGN galaxy ’8983-12701’ and the SF galaxy ’9024-6102’ in field drawn from the MaNGA survey.

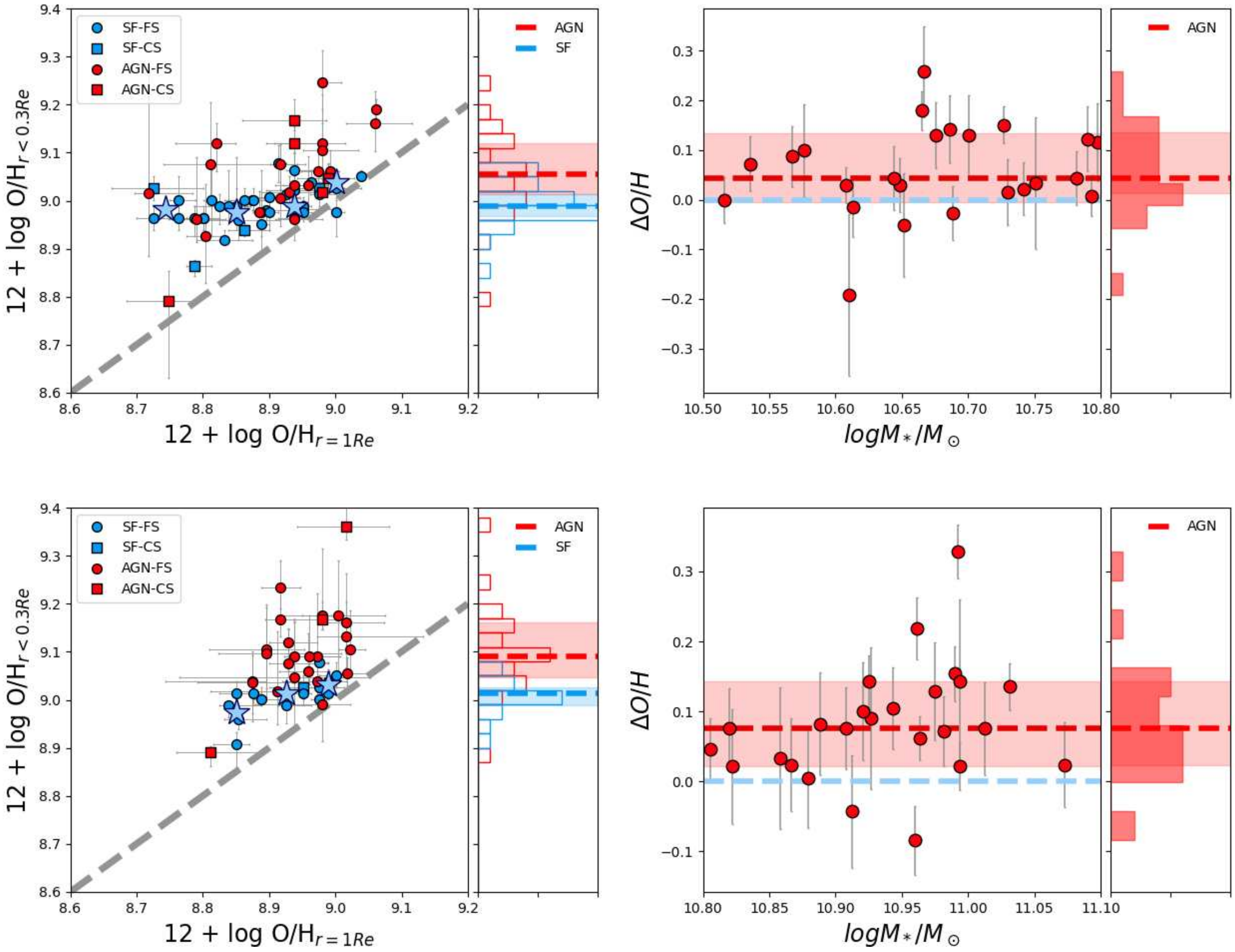

Figure 6.3: Results are presented for AGN and SF galaxies divided into two different mass bins: the *top panels* show the results for galaxies with $10.5 \leq \log M_* \leq 10.8$, while the *bottom panels* show the results for galaxies with $10.8 \leq \log M_* \leq 11.1$. *(Left panels)* 12 + log O/H $_{r<0.3R_e}$ versus 12 + log O/H $_{r=1R_e}$ in case of RP stripped AGN hosts (red squares), non-RP stripped AGN hosts (red circles), RP stripped SF galaxies (blue squares) and non RP stripped SF galaxies (blue circles). The blue stars are the median value of 12 + log O/H $_{r<0.3R_e}$ of the (RP and non-RP stripped) SF galaxies inside bins of 12 + log O/H $_{r=1R_e}$ with width 0.2 dex ($<$ 12 + log O/H $>_{r<0.3R_e}$). The gray dotted line is the one-to-one relation. On the right, the histograms show the distribution of 12 + log O/H $_{r<0.3R_e}$ for the AGN hosts (in red) and for SF galaxies (in blue), with the median value (blue dotted line) with relative errors (shaded area) computed as the 16/84th percentile of the distribution. *(Right panels)* Difference between $<$ 12 + log O/H $>$ $_{r<0.3R_e}$ and the 12 + log O/H $_{r<0.3R_e}$ of AGN hosts (Δ O/H) inside the corresponding bin of 12 + log O/H $_{r=1R_e}$. The blue dotted line is the zero level, while the red dotted line is the median Δ O/H. The shaded area covers the values between the 16/84th percentiles of the distribution, which is also shown on the left-side red histogram.

Then, I compute the median value of 12 + log O/H$_{r<0.3\ R_e}$ dividing the SF galaxies inside bins of 12 + log O/H$_{r=1\ R_e}$ (blue stars) with width 0.2 dex, and I compute the difference between the values marked by the blue stars of SF galaxies and the 12 + log O/H$_{r<0.3\ R_e}$ values of the AGN hosts inside the 12 + log O/H$_{r=1\ R_e}$'s bins (e.g Δ O/H). Finally, I plot Δ (O/H) as a function of the galaxy stellar mass in the right panels of Figure 6.1. In this way, I find that, regardless of the galaxy stellar mass, AGN hosts have steeper gradients, but show a higher steepness in the high-mass bin. In fact, Δ (O/H) = $0.04^{+0.13}_{-0.01}$ for the AGN hosts in the mass bin $10.5 \leq \log(M_*/M_\odot) \leq 10.8$ and Δ (O/H) = $0.08^{+0.14}_{-0.02}$ for the AGN hosts in the mass bin $10.9 \leq \log(M_*/M_\odot) \leq 11.1$.

6.1.1 Comparison with the literature

To test the robustness of these results I compare with the previous study of Do Nascimento et al. (2022). These authors used a slightly different method from the one I presented in Section 6.1 but still aimed at studying the increase or decrease of metallicity in the nuclear regions of AGN hosts, with respect to the galaxy disk.

Do Nascimento et al. (2022) compared the metallicity value measured in the nuclear regions of AGN hosts, selected from the MaNGA survey, with the 12 + log O/H value extrapolated from a linear fit of the metallicity gradient of the extranuclear H II regions. The AGN and H II regions are those with values of [N II]/Hα and [O III/Hβ] above the Kewley et al. (2001) relation and below the Kauffmann et al. (2003) relation, respectively, while Composite regions are discarded in their work. Additionally, the Seyfert-like and LINER-like emission is divided using the Fernandes et al. (2010) demarcation line of the WHAN diagrams. In this way, the authors obtained a sample of 101 Seyfert galaxies and 145 non-active galaxies as part of a control sample. Then, the metallicity inside the AGN-ionized regions was computed using the Storchi-Bergmann et al. (1998) and Carvalho et al. (2020) calibrators, while the metallicity in the H II regions was measured with the Pérez-Montero & Contini (2009b) empirical calibrator. One important difference between the method I used and the one adopted by Do Nascimento et al. (2022) is that I considered photo-ionization models generated making consistent assumptions between the H II, AGN and Composite models, while this is not the case for the AGN and SF calibrators used by Do Nascimento et al. (2022).

Do Nascimento et al. (2022) used the relation Y = Y_0 + grad Y × R to fit the radial abundance distributions, where Y is a given oxygen abundance - in units of 12 + log O/H - R is the galactocentric distance (in units of arcsec), Y_0 is the extrapolated value of the gradient to the galactic centre ($R = 0$), and grad Y is the slope of the distribution (in units of dex/arcsec). Using this method, they were able to obtain the gradients for 61 galaxies containing AGN and for 112 control galaxies. Finally, they measure the quantity D, which is the difference between the O/H abundance of the AGN and the intersect oxygen abundances derived from the radial abundance gradients, Y_0. They find an average value of < D > of 0.16-0.30 dex (depending on the calibration assumed for the AGN regions), meaning that the measured value of the AGN metallicity is lower than the extrapolated oxygen abundances derived from the radial abundance gradients.

Following a similar approach, I select the H II-like spaxels in the galaxies of the AGN-FS drawn from the MaNGA survey and I fit the median 12 + log O/H values computed inside each annulus by using a non-linear least square (NLS) method (an example is shown in panel (b) (bottom) of Figure 6.4 for the MaNGA galaxy '8985-12703'). The uncertainty on the median (σ_y), used to weight the residuals, is the lowest value between σ_- and σ_+, where σ_- and σ_+ are the 16th and 84th percentiles of the metallicity distribution inside the annulus. In this way, I was able to compute the linear fit for 42 galaxies (out of a sample of 52). In Figure 6.5, I compare the value of the linear fit *at* $R = 0.3R_e$ and the median value computed *within* 0.3 R_e, considering the measured values in the AGN, Composite and SF spaxels. In this way, I find that the extrapolated value of 12 + log O/H from the H II regions is on average $9.00^{+0.04}_{-0.02}$, which is lower than the average measured value of 12 + log O/H within r = 0.3 R_e = $9.08^{+0.07}_{-0.07}$, in contrast with the findings in Do Nascimento et al. (2022), as shown in Figure 6.5.

In conclusion, I find that the nuclear regions of a galaxy are more metal-enriched when AGN activity is present, and this does not dependent on the method adopted to obtain the result, meaning that the difference between the results in Do Nascimento et al. (2022)

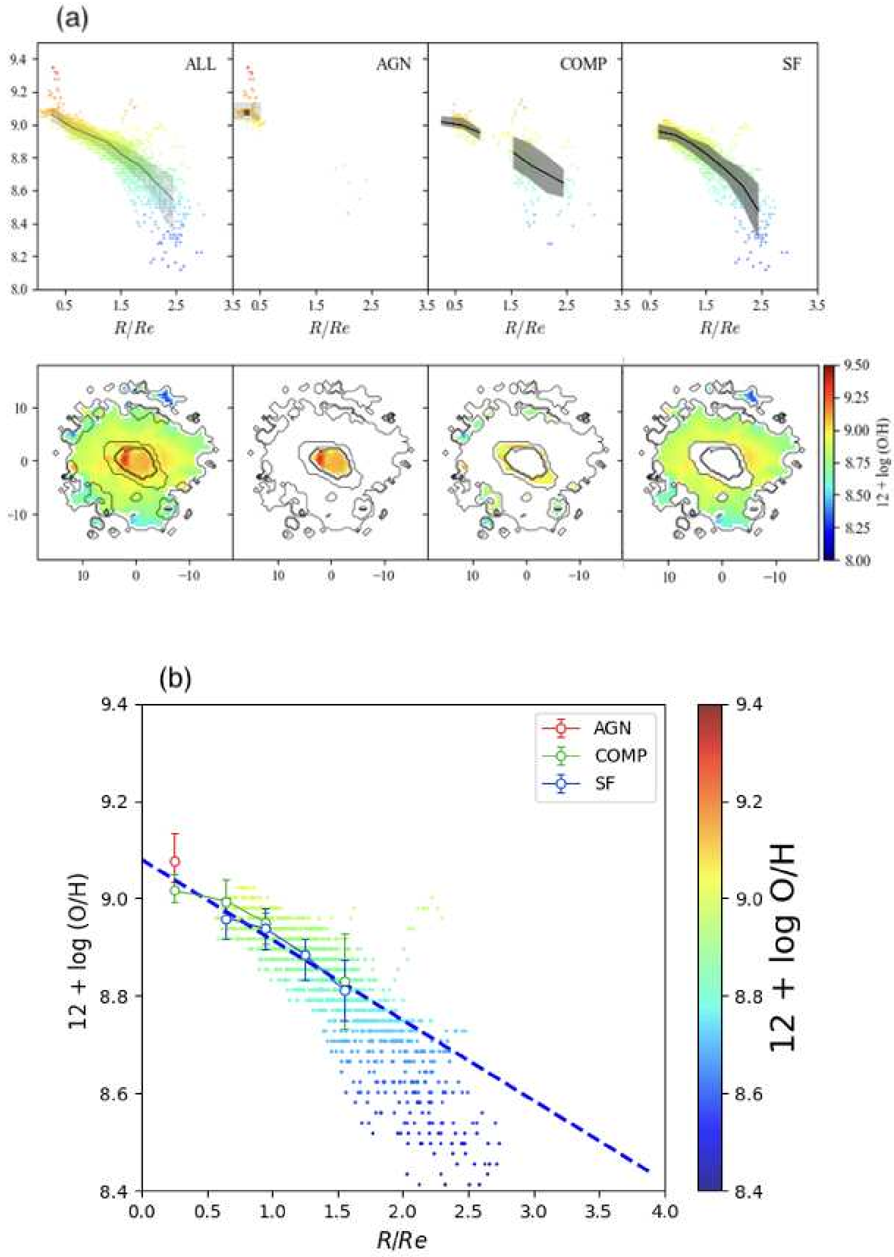

Figure 6.4: *(a)* Metallicity gradients and maps considering all the spaxels (left panel), AGN spaxels (central left panel), Composite spaxels (central right panel) and SF spaxels (right panel) for the galaxy '8983-12701'. The gradients are computed considering the median values of 12 + log O/H inside annuli with inner radii ranging from $r = 0.5R_e$ to $r = 2.5R_e$, spaced between each other of 0.3 dex. *(b)* Median values of the AGN (red points), Composite (grey points) and SF (blue points) metallicities, inside each annulus. The spaxel-by-spaxel SF metallicities are also overplotted, color-coded according to their value of 12 + log O/H. The blue dotted line is the linear fit of the SF gradient obtained with a NLS using as weights the errorbars on the blue points, which are the 16th/84th percentiles of the 12 + log O/H's distribution inside the annulus.

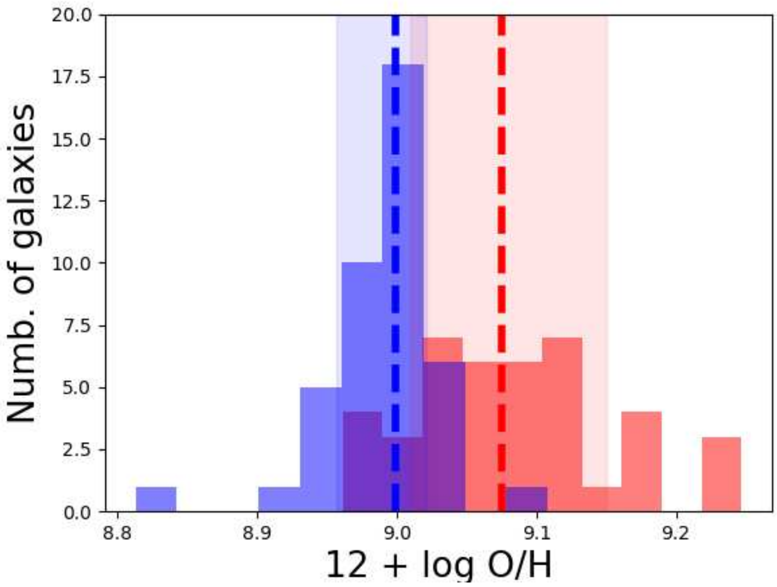

Figure 6.5: The blue histogram shows the 12 + log O/H at 0.3 R_e extrapolated from the linear fit of the H II regions in 42 MaNGA galaxies from the AGN-FS for which I was able to perform a linear fit of the gradient in the H II regions, as shown in Figure 6.4 for the galaxy ’8985-12703’. The red histogram shows the 12 + log O/H distribution of the values measured within 0.3 R_e (considering all the AGN, Composite and SF spaxels). The median measured value 12 + log O/H$_{r<0.3R_e}$ (red dotted line) is higher than the median extracted value of 12 + log O/H$_{r=0.3R_e}$ from the lineare fit (blue dotted line).

and those found in Section 6.1 are due the different methodology chosen to compute the gas phase metallicities, in particular the different and inhomogeneous calibrators used for AGN and SF regions.

6.2 Discussion and Summary

In Chapter 5 (based on the work presented in Peluso et al., 2023), I show how nuclear regions of AGN hosts are more metal-rich than those in star-forming galaxies, regardless of RPS. Possible mechanisms able to explain the observed metal enhancement due to the central AGN are discussed in details in the review by Maiolino & Mannucci (2019) (e.g.

dust destruction, top-heavy IMF star formation in the accretion disk, etc.). After being a vigorous topic of research since 1980s, also the hypothesis of a starburst-AGN activity connection is now back in fashion (see e.g. Lai et al., 2022) thanks to the JWST capability to overcome observational challenges such as heavy dust obscuration. A reservoir of gas in the host galaxy is clearly necessary for both ongoing star formation and black hole growth, but Kauffmann et al. (2023) show that the AGN-starburst connection also depends on the local ISM conditions around the SMBH.

In this context, the compression of gas during the merging of galaxies or a ram-pressure stripping event (which can trigger the AGN activity, see Chapter 1) is potentially able to induce starburst activity (e.g. Vulcani et al., 2018) which eventually fosters the metal pollution of the gas in the inner regions of the galaxy through SN expositions.

By studying the spatially-resolved gas-phase metallicity in the AGN and SF samples of galaxies presented in Peluso et al. (2023) I further characterize the metallicities around AGNs by showing that the metal enhancement is limited to the very inner regions (R $< 0.3\ R_e$) of the galaxy. Particularly, AGN hosts have metallicity gradients steeper than SF galaxies of a factor 0.04 dex for stellar masses below $\log(M_*/M_\odot) = 10.8$, while the steepness is two times higher (i.e. 0.08 dex) in the stellar mass bin $10.8 < \log(M_*/M_\odot) < 11.1$.

The metallicities are computed using the Cloudy photo-ionization models presented in Peluso et al. (2023), which ensured the homogeneity of the estimates among the SF/Composite/AGN regions in the galaxy. I argue that the use of these models is the main reason for the discrepancy between my result and those shown in Do Nascimento et al. (2022), which found that NLR are less metal enriched on average that H II regions in the galaxy disk. To test this hypothesis, I computed the quantity $< D >$ as in Do Nascimento et al. (2022) (i.e. the difference between the O/H abundance of the AGN and the intersect oxygen abundances derived from the radial abundance gradients, Y_0.) for the AGN galaxies drawn from the MaNGA survey and I found that the NLR metal content is higher than the extracted value from the SF gradients, computed considering the extranuclear H II regions, meaning that the discrepancy does not depend on the linear fit extrapolation used to compare the metal content in the AGN-ionized and H II regions.

7 CONCLUDING REMARKS AND FUTURE PROSPECTS

The aim of this Thesis is to investigate the link between the presence of active galactic nuclei (AGN) and the ram pressure stripping (RPS) phenomenon in nearby galaxies, through the use of Integral Field Spectroscopy (IFS) data. In the following, I summarise the main results reached during these three years of research activity, with an highlight on future prospectives.

Exploring the AGN-RPS Connection in the local universe

The influence of the large-scale environment on AGN activity is a vibrant field of research (e.g. Lopes et al., 2017). The RPS phenomenon, that is the pressure exerted by the intracluster medium (ICM) on the galaxy interstellar medium (ISM), is one of the most advocated mechanisms that affect the properties of cluster galaxies. One open question is if there is a link between the central active black hole (BH) and the gas physical conditions in RP-stripped galaxies, thus a connection between the AGN activity and RPS phenomenon.

Hydrodynamical simulations in Akerman et al. (2023) (but see also Tonnesen et al., 2009) showed that RPS is able to increase the mass inflows to the galaxy centre regardless of the wind impact angle and that this increase is mainly driven by the mixing of ISM and non-rotating ICM at all wind angles. Also, the mass inflow rates can be increased by pressure torques on the inner disk gas, which in turn are driven by rising gradients of ram pressure. Observationally, Poggianti et al. (2017b) (P17b) already found tentative evidence of a connection between the two phenomena in a small sample of RP-stripped galaxies, by observing 6 optical AGN out of a sample of 7 galaxies strongly affected by the stripping. However, a statistically robust study to clarify the existence of a link between RPS and AGN was missing.

To test this hypothesis, in Chapter 2 I present a sample of 51 RP-stripped galaxies observed by the GAs Stripping Phenomena (GASP) survey (PI: Poggianti, see e.g. Poggianti et al., 2017a) and a control sample of 782 normal galaxies, selected to be star-forming according to their specific Star Formation Rate (sSFR) and late-type according to their optical morphological classification drawn for the MaNGA survey. Even though the resolution of ∼ 2“ in MaNGA is comparable to the GASP resolution (seeing-limited) of ∼ 1“, I performed a redshift cut at $z < 0.07$ for the MaNGA galaxies to ensure that the spatial physical resolution was ∼ 1 kpc in both GASP and MaNGA samples. In addition to the RP-stripped galaxies in GASP, to increase the statistics I also collected a sample of RP-stripped galaxies by performing a systematic search in the literature, ending up with a sample of 115 RP-stripped galaxies located in clusters at low redshifts (z < 0.1).

Using the Baldwin, Philips and Telervich (BPT, Baldwin et al., 1981) diagrams, I distinguished regions within the galaxy where the ionization of the gas and its consequent emission is linked to the radiation coming from a central AGN, from young stars or from a mixed contribution of both stars and AGN. Since the three samples (GASP, ManGA and literature) have different stellar mass distributions, I computed the AGN fractions matching them with a Montecarlo extraction. I found statistical evidence that the AGN-

RPS connection does exist: the results show that the AGN fraction rises to 53% when ram-pressure stripping is acting, selecting galaxies with $M_* > 10^{10}M_\odot$. This fraction is higher than the AGN fraction of 19% in normal galaxies, in the same mass bin. The hypothesis of an AGN-RPS connection is also supported by the fact that the AGN hosts in the RPS sample are located in the infall-region of the phase space diagram, which is also the region where the stripping is the most intense. In conclusion, this work represents the first statistical study aimed at exploring the hypothesis of an AGN-RPS connection

Gas-phase metallicity of local AGN in the MaNGA and GASP surveys: the role of ram-pressure stripping

The chemical evolution of a galaxy is regulated by a plethora of processes, from stellar winds and supernovae explosions within the galaxy body (e.g., Maiolino & Mannucci, 2019, for a review) to the exchange of material with its environment (e.g., Ellison et al., 2009; Peng & Maiolino, 2014). The global gas-phase metallicity is well-known to be strongly correlated with the assembled stellar mass of a galaxy (e.g., Lequeux et al., 1979) through the so-called mass-metallicity relation (MZR) which has been shown to hold from low z (e.g., Tremonti et al., 2004; Pérez-Montero et al., 2013) to high z (up to $z \sim 6.5$ based on recent JWST measurements, e.g. Shapley et al., 2023). In addition to stellar evolution and environmental effects, also the presence of a central AGN can potentially have an impact on the galaxy metallicity (e.g., Groves et al., 2006).

However, the effect of the AGN on the metal content of the galaxy's central regions is highly debated: regardless of the stellar mass of the host galaxy, some works find that the AGN leads to an enrichment of metals, and in particular AGN hosts show higher metallicity than star-forming galaxies of similar mass (e.g., Thomas et al., 2019), while other works measure lower metallicity in AGN than in star-forming regions (e.g., Armah et al., 2023). In this context, a dedicated study of the gas-phase metallicity in the nuclear regions of galaxies hosting an AGN and its scaling relation with the host galaxy stellar mass in different environments is still missing. A possible link between the AGN metallicity and the environment may have roots in the fact that environmental processes such as the RPS phenomenon has been proven to work in synergy with the AGN feedback in quenching the star formation in galaxies falling into clusters (Ricarte et al., 2020; George et al., 2019; Radovich et al., 2019). This is due to the fact that the AGN feedback heats the gas, thus quenching star formation in the galaxy nuclear regions, and helps to re-distribute the gas in the outer part of the galaxy, which is then more easily stripped by the RP (Ricarte et al., 2020). As a consequence, the RPS and AGN feedback working together are potentially able to induce a particularly rapid halt of the metals's production in the galaxy nuclear regions.

For these reasons, I have developed spatially resolved maps of the oxygen abundance for SF and AGN galaxies in field and in clusters experiencing strong RPS. Using these maps, I measured the gas-phase metallicity in the nuclear regions and the mass-metallicity relation in 52 optical AGNs and in a mass-matched sample of 377 SF galaxies, restricting the samples to $z \leq 0.07$ in order to have the same spatial resolution (~ 1 kpc) in the MaNGA and GASP samples, already used to compute the AGN fractions.

To measure oxygen abundances, I exploited IFS data from the GASP and MaNGA surveys, photoionization models generated with the code Cloudy and the code NebulaBayes (Thomas et al., 2018a) to compare models and observations. In particular, I made use of Cloudy models built up to reproduce line ratios induced by photoionization from stars or AGN (that will be made available in Radovich et al. in prep.)and I also learned how to manipulate these grids of models, by mixing the contribution from stars and AGN to reproduce the nebular emission in regions classified as Composite in the BPT diagnostic diagrams. I considered the effects on the final estimates of the central metallicities of using different apertures (e.g., with radius $r < 0.5\ R_e$ or $r < 1$ kpc) centered on the galaxy. I show that the gas-phase metallicity in the nuclei of AGN hosts is enhanced with respect to those of SF galaxies by an average factor of ~ 0.05 dex. Independently of the RPS, I did not find a correlation between stellar mass and AGN metallicity in the mass range $\log M_*/M_\odot \geq 10.4$, while for the star-forming galaxies I observed the well-known MZR between $9.0 \leq \log M_*/M_\odot \leq 10.8$ with a scatter mainly driven by the star-formation rate (SFR), as expected from the FMZR (Mannucci et al., 2010), and a plateau around log $M_*/M_\odot \sim 10.5$. I have also tested the inadequacy of applying SEL calibrators developed independently by different works for HII and AGN-ionized regions, since this approach leads to a strong dependence of the results on the different methods employed to obtain the calibrators.

This is the first study to compute the nuclear metallicity in AGN galaxies affected by RPS and to investigate the impact of the RPS (thus of the environment) on this by comparing the results between RP- and non-RP- stripped AGN host galaxies.

Metallicity gradients

A detailed study of the spatially resolved ISM gas-phase metallicity around SMBHs, in order to investigate the impact of the AGN activity on the chemical composition on the galaxy inner regions, is something mostly lacking in the literature.

Chemical abundance composition of the inner regions in AGN hosts was already studied by Do Nascimento et al. (2022), which found a decrement of the metal content in the NLR with respect to the one extrapolated from metallicity gradients, measured in the outer H II regions. This result is in contrast to what is found by Peluso et al. (2023), as an increase of metals is observed, in this work, in the nuclear regions of AGN in both cluster and field galaxies.

To further investigate this topic, I use the spatially-resolved metallicity maps, computed for a sample of 52 AGN hosts and 377 SF galaxies for which the MZR was already studied in Peluso et al. (2023), to find whether nuclear regions are more or less metal-enriched in AGN galaxies than in SF galaxies, at given metallicity of the galactic disk.

To this end, I measure the metallicity within 0.3 effective radius (i.e. R_e, 12 + log O/H$_{r<0.3R_e}$) and the metallicity inside the annulus covering the area between $r = 0.9\ R_e$ and $r = 1.1\ R_e$ (12 + log O/H$_{r=1R_e}$), finding that AGN hosts on average show higher metallicities in their inner regions (12 + log O/H$_{r<0.3R_e}$) than star-forming galaxies, regardless from the galaxy stellar mass.

In other words, AGN hosts have steeper gradients but show a higher steepness in the high-mass bin. Particularly, I find that the slopes of the AGN hosts are a factor Δ (O/H) $= 0.04^{+0.13}_{-0.01}$ higher than in SF galaxies, in the mass bin $10.5 \leq \log(M_*/M_\odot) \leq 10.8$

and Δ (O/H) = $0.08^{+0.14}_{-0.02}$ in the mass bin $10.9 \leq \log(M_*/M_\odot) \leq 11.1$.

This result is opposed to Do Nascimento et al. (2022), but I also tested that this is not linked to the method used to quantify the difference between predicted (from the H ɪɪ regions' gradients) and the measured value of the NLR. I argue that the reason for this discrepancy is due to the use of photoionization models generated in Peluso et al. (2023), as opposed to Do Nascimento et al. (2022) which made use of SEL calibrators obtained in different works.

Future prospects

Taking advantage of the new observational window opened in the near-IR by instruments such as JWST (space-based) and ERIS (ground-based), it is possible to explore the potentiality of the (Near- and Mid-) IR range to study the AGN feeding and feedback processes in RP stripped galaxies. Thanks to the unprecedented high spatial (i.e. $0.1''$) and spectral (R = $11'500$ for ERIS and R = $2'700$ for JWST/NIRSpec) resolutions, it will be possible to look for non-circular motions (inflows and outflows) by modelling the molecular gas kinematics. This will permit to unveil the presence of gas inflows which eventually trigger/enhance the BH activity in galaxies experiencing RPS, as predicted by simulations (Akerman et al., 2023). Moreover, IR diagnostic diagrams (DDs) involving [FeII], Paschen and Bracket lines can be used to trace the gas ionized by shocks, since these DDs are able to distinguish ionization from shocks rather than from AGN or star-formation (Maiolino et al., 2017), unlikely the optical diagnostics. This will allow to study the AGN feedback on the ISM (hence on the RPS) surrounding the nuclear regions. For these reasons, I submitted an ERIS proposal to observe the RP-stripped galaxy JO201 (z = 0.0446, 1" ~ 1kpc, Bellhouse et al., 2021) with the spectrograph SPIFFIER, assisted by its Adaptive Optics module.

The main goal of the proposal will be to observe the Paα line and the H_2 S(1) line which trace the ionized (T ~ 10^4 K) and the molecular warm (T ~ 1000K) gas components, respectively, in the inner regions around the AGN inside the SPIFFIER FoV of $3'' \times 3''$.

The wealth of ancillary multi-wavelength (Chandra, HST, APEX, VLA, ALMA, MUSE) data ranging from the radio wavelengths to X-ray, the presence of strong ionized outflows detected with MUSE and ad-hoc simulations showing inflows pushed by RPS towards the center make JO201 (Bellhouse et al., 2021) the perfect candidate to look for non-circular molecular gas motions among all the RP-stripped galaxies in the local universe.

The detection of such non-circular motions would be particularly striking for the understanding of the AGN-RPS connection, since the enhanced AGN frequency in RP galaxies is only indirect proof of this connection.

An interesting outcome of my previous research would be to obtain SEL calibrators, which are easier to apply than photoionization models. This would be the first set of calibrators obtained in a coherent way (e.g. based on consistent assumptions among the SF and AGN models) to compute the metallicity in both HII regions and AGN-dominated regions, which is in fact something still lacking in the literature. By comparing the AGN calibrators with those already available in the literature (e.g., Storchi-Bergmann et al., 1998; Carvalho et al., 2020; Dors et al., 2015), it will be also possible to estimate the impact of making different assumptions (while generating the models, or comparing models and observations) on the final results about the AGN hosts metallicities presented by different works (see e.g., Pérez-Díaz et al., 2023).

BIBLIOGRAPHY

Abazajian, K. N., Adelman-McCarthy, J. K., Agüeros, M. A., et al. 2009, ApJS, 182, 543, doi: 10.1088/0067-0049/182/2/543

Abdurro, Accetta, K., Aerts, C., et al. 2022, The Astrophysical Journal Supplement Series, 259, 35, doi: 10.3847/1538-4365/ac4414

Abell, G. O. 1958

Abramson, A., Kenney, J., Crowl, H., & Tal, T. 2016, AJ, 152, 32, doi: 10.3847/0004-6256/152/2/32

Aguado, D. S., Ahumada, R., Almeida, A., et al. 2019, ApJS, 240, 23, doi: 10.3847/1538-4365/AAF651

Aihara, H., Allende Prieto, C., An, D., et al. 2011, ApJS, 193, 29, doi: 10.1088/0067-0049/193/2/29

Akerman, N., Tonnesen, S., Poggianti, B. M., Smith, R., & Marasco, A. 2023, The Astrophysical Journal, 948, 18, doi: 10.3847/1538-4357/acbf4d

Alexander, T. 2005, Physics Reports, 419, 65, doi: 10.1016/j.physrep.2005.08.002

Anderson, S. F., Margon, B., Voges, W.,

et al. 2007, AJ, 133, 313, doi: 10.1086/509765

Antonucci, R., Antonucci, & Robert. 1993, ARAA, 31, 473, doi: 10.1146/ANNUREV.AA.31.090193.002353

Araujo, B. L., Storchi-Bergmann, T., Rembold, S. B., Kaipper, A. L., & Dall'Agnol de Oliveira, B. 2023, Monthly Notices of the Royal Astronomical Society, Volume 522, Issue 4, pp.5165-5179, 522, 5165, doi: 10.1093/MNRAS/STAD1340

Arav, N., Gabel, J. R., Korista, K. T., et al. 2007, ApJ

Argudo-Fernández, M., Lacerna, I., Duarte Puertas, S., et al. 2018, AA, 620, A113, doi: 10.1051/0004-6361/201833328

Armah, M., Rog´, R., Riffel, R., et al. 2023, MNRAS, 520, 1687, doi: 10.1093/mnras/stad217

Arnold, T. J., Martini, P., Mulchaey, J. S., Berti, A., & Jeltema, T. E. 2009, The Astrophysical Journal, 707, 1691, doi: 10.1088/0004-637X/707/2/1691

Arrigoni, M., Trager, S. C., Somerville, R. S., & Gibson, B. K. 2010, Monthly Notices of the Royal Astronomical Society, 402, 173, doi: 10.1111/j.1365-2966.2009.15924.x

Bacon, R., M., A., L., A., et al. 2010, SPIE, 7735, 773508, doi: 10.1117/12.856027

Bacon, R., Conseil, S., Mary, D., et al. 2017, Astronomy and Astrophysics, 608, A1, doi: 10.1051/0004-6361/201730833

Badnell, N. R., Ferland, G. J., Gorczyca, T. W., Nikolić, D., & Wagle, G. A. 2015, ApJ, doi: 10.1088/0004-637X/804/2/100

Baldwin, J. A., Phillips, M. M., Terlevich, R., et al. 1981, PASP, 93, 5, doi: 10.1086/130766

Barnes, J. E., Hernquist, L., King, A., & Pounds, K. 2015, ARAA, 53, 115, doi: 10.1146/ANNUREV-ASTRO-082214-122316

Bartko, H., Martins, F., Trippe, S., et al. 2010, ApJ, 708, 834, doi: 10.1088/0004-637X/708/1/834

Beckmann, V., & Shrader, C. R. 2012, agn, 351. https://ui.adsabs.harvard.edu/abs/2012agn..book.....B/abstract

Bekki, K. 2013, Monthly Notices of the

Royal Astronomical Society, 438, doi: 10.1093/mnras/stt2216

Bekki, K., Shioya, Y., & Couch, W. J. 2002, ApJ, 577, 651, doi: 10.1086/342221

Belfiore, F., Westfall, K. B., Schaefer, A., et al. 2019, AJ, doi: 10.3847/1538-3881/ab3e4e

Belfiore, F., Santoro, F., Groves, B., et al. 2022, AA, 659, 26, doi: 10.1051/0004-6361/202141859

Bell, E. F., de Jong, R. S., Bell, E. F., & de Jong, R. S. 2001, ApJ, 550, 212, doi: 10.1086/319728

Bellhouse, C., McGee, S. L., Smith, R., et al. 2021, MNRAS, 500, 1285, doi: 10.1093/MNRAS/STAA3298

Berton, M., Foschini, L., Ciroi, S., et al. 2015, AA, 578, 28, doi: 10.1051/0004-6361/201525691

Best, P. N., Heckman, T. M., Best, P. N., & Heckman, T. M. 2012, MNRAS, 421, 1569, doi: 10.1111/J.1365-2966.2012.20414.X

Best, P. N., von der Linden, A., Kauffmann, G., et al. 2007, MNRAS, 379, 894, doi: 10.1111/J.1365-2966.2007.11937.X

Bialas, D., Lisker, T., Olczak, C., Spurzem, R., & Kotulla, R. 2015, Astronomy and Astrophysics, 576, A103, doi: 10.1051/0004-6361/201425235

Bicknell, G. V., Gingold, R. A., Bicknell, G. V., & Gingold, R. A. 1983, ApJ, 273, 749, doi: 10.1086/161410

Birchall, K. L., Watson, M. G., Aird, J., et al. 2020, MNRAS, 492, 2268, doi: 10.1093/MNRAS/STAA040

Blanc, G. A., Kewley, L., Vogt, F. P. A., & Dopita, M. A. 2014, The Astrophysical Journal, 798, 99, doi: 10.1088/0004-637X/798/2/99

Bland-Hawthorn, J., Bryant, J., Robertson, G., et al. 2011, OExpr, 19, 2649, doi: 10.1364/OE.19.002649

Blandford, R. D., Netzer, H., Woltjer, L., Courvoisier, T. J. L., & Mayor, M. 1990, agn, 97. https://ui.adsabs.harvard.edu/abs/1990agn..conf.....B/abstract

Blanton, M. R., Kazin, E., Muna, D., Weaver, B. A., & Price-Whelan, A. 2011, Astronomical Journal, 142, 31, doi: 10.1088/0004-6256/142/1/31

Blanton, M. R., & Roweis, S. 2007, The

Astronomical Journal, 133, 734, doi: 10.1086/510127

Blanton, M. R., Bershady, M. A., Abolfathi, B., et al. 2017, The Astronomical Journal, 154, 28, doi: 10.3847/1538-3881/aa7567

Böhm, A., Wisotzki, L., Bell, E. F., et al. 2013, Astronomy and Astrophysics, 549, A46, doi: 10.1051/0004-6361/201015444

Boissier, S., Boselli, A., Duc, P. A., et al. 2012, AA, 545, A142, doi: 10.1051/0004-6361/201219957

Boselli, A., Cortese, L., Boquien, M., et al. 2014, Astronomy and Astrophysics, 564, A66, doi: 10.1051/0004-6361/201322312

Boselli, A., Fossati, M., & Sun, M. 2022, The Astronomy and Astrophysics Review 2022 30:1, 30, 1, doi: 10.1007/S00159-022-00140-3

Boselli, A., & Gavazzi, G. 2006, Publications of the Astronomical Society of the Pacific, 118, 517, doi: 10.1086/500691

Boselli, A., Boissier, S., Cortese, L., et al. 2005, ApJL, 623, L13, doi: 10.1086/429377

—. 2006, ApJ, 651, 811, doi: 10.1086/507766

Boselli, A., Fossati, M., Gavazzi, G., et al. 2015, yCat, J/A+A/579/A102. https://ui.adsabs.harvard.edu/abs/2015yCat..35790102B/abstract

Boselli, A., Cuillandre, J. C., Fossati, M., et al. 2016, AA, 587, A68, doi: 10.1051/0004-6361/201527795

Boselli, A., Fossati, M., Cuillandre, J. C., et al. 2018, AA, 615, A114, doi: 10.1051/0004-6361/201732410

Boselli, A., Epinat, B., Contini, T., et al. 2019, AA, 631, A114, doi: 10.1051/0004-6361/201936133

Bravo-Alfaro, H., Cayatte, V., van Gorkom, J. H., & Balkowski, C. 1999, AJ, 119, 580, doi: 10.1086/301194

Bravo-Alfaro, H., Cayatte, V., Van Gorkom, J. H., & Balkowski, C. 2001, Astronomy Astrophysics, 379, 347, doi: 10.1051/0004-6361:20011242

Brinchmann, J., Charlot, S., Heckman, T. M., et al. 2004. https://arxiv.org/abs/0406220

Bruzual, G., & Charlot, S. 2003, Monthly Notices of the Royal Astronomical Society, 344, 1000, doi: 10.1046/j.1365-8711.2003.06897.x

Bryant, J. J., Bland-Hawthorn, J., Lawrence, J., et al. 2012, SPIE, 8446, 84460X, doi: 10.1117/12.925115

Bundy, K., Bundy, & Kevin. 2015, IAUS, 311, 100, doi: 10.1017/S1743921315003476

Byler, N. 2018, zndo, doi: 10.5281/ZENODO.1156412

Byler, N., Dalcanton, J. J., Conroy, C., & Johnson, B. D. 2017, The Astrophysical Journal, 840, 44, doi: 10.3847/1538-4357/aa6c66

Byrd, G., Valtonen, M., Byrd, G., & Valtonen, M. 1990, ApJ, 350, 89, doi: 10.1086/168362

Caglar, T., Burtscher, L., Brandl, B., et al. 2020, AA, 634, A114, doi: 10.1051/0004-6361/201936321

Caldwell, N., Rose, J., & Dendy, K. 1999, AJ, 117, 140, doi: 10.1086/300679

Calvi, R., Poggianti, B. M., Vulcani, B., et al. 2011, MNRAS, 416, 727, doi: 10.1111/J.1365-2966.2011.19088.X

Cappellari, M. 2017, MNRAS, 466, 798, doi: 10.1093/mnras/stw3020

Cardelli, J. A., Clayton, G. C., & Mathis, J. S. 1989, ApJ, 345, 245, doi: 10.1086/167900

Carter, B., Luminet, J. P., Carter, B., & Luminet, J. P. 1982, Natur, 296, 211, doi: 10.1038/296211A0

Carvalho, S. P., Dors, O. L., Cardaci, M. V., et al. 2020, Monthly Notices of the Royal Astronomical Society, 492, 5675, doi: 10.1093/MNRAS/STAA193

Castro, C. S., Dors, O. L., Cardaci, M. V., & Hägele, G. F. 2017, Monthly Notices of the Royal Astronomical Society, 467, 1507, doi: 10.1093/mnras/stx150

Chabrier, G., Chabrier, & Gilles. 2003, PASP, 115, 763, doi: 10.1086/376392

Chandrasekhar, & Subrahmanyan. 1961, hhs. https://ui.adsabs.harvard.edu/abs/1961hhs..book.....C/abstract

Charlot, S., & Longhetti, M. 2001, Monthly Notices of the Royal Astronomical Society, 323, 887, doi: 10.1046/j.1365-8711.2001.04260.x

Chemin, L., Cayatte, V., Balkowski, C., et al. 2005, AA, 436, 469, doi: 10.1051/0004-6361:20041664

Chen, H., Sun, M., Yagi, M., et al. 2020, MNRAS, 496, 4654, doi: 10.1093/MNRAS/STAA1868

Chen, J., Shi, Y., Dempsey, R., et al. 2019, MNRAS, 489, 855, doi: 10.1093/mnras/stz2183

Cherinka, B., Andrews, B. H., Sánchez-Gallego, J., et al. 2019, AJ, doi: 10.3847/1538-3881/ab2634

Choi, E., Ostriker, J. P., Hirschmann, M., Somerville, R. S., & Naab, T. 2022, The Astrophysical Journal, 929, 113, doi: 10.3847/1538-4357/ac5d47

Choi, J., Dotter, A., Conroy, C., et al. 2016, ApJ, doi: 10.3847/0004-637X/823/2/102

Chung, A., van Gorkom, J. H., Kenney, J. D. P., & Vollmer, B. 2007, The Astrophysical Journal, 659, L115, doi: 10.1086/518034

Chung, A., van Gorkom, J. H., Kenney, J. D. P., et al. 2009, AJ, 138, 1741, doi: 10.1088/0004-6256/138/6/1741

Chyży, K. T., Ehle, M., Beck, R., et al. 2007, AA, 474, 415, doi: 10.1051/0004-6361:20077497

Cid Fernandes, R., Stasińska, G., Mateus, A., & Vale Asari, N. 2011, Monthly Notices of the Royal Astronomical Society, 413, 1687, doi: 10.1111/j.1365-2966.2011.18244.x

Cisternas, M., Jahnke, K., Inskip, K. J., et al. 2011, Astrophysical Journal, 726, 57, doi: 10.1088/0004-637X/726/2/57

Coil, A. L., Aird, J., Reddy, N., et al. 2015, The Astrophysical Journal, 801, 35, doi: 10.1088/0004-637X/801/1/35

Coldwell, G. V., Pereyra, L., Alonso, S., et al. 2017, MNRAS, 467, 3338, doi: 10.1093/MNRAS/STX294

Collin, S., & Zahn, J. P. 2008, Astronomy and Astrophysics, 477, 419, doi: 10.1051/0004-6361:20078191

Congiu, E., Contini, M., Ciroi, S., et al. 2017, MNRAS, 471, 562, doi: 10.1093/mnras/stx1628

Conroy, C., Gunn, J. E., & White, M. 2009, The Astrophysical Journal, 699, 486, doi: 10.1088/0004-637X/699/1/486

Consolandi, G., Gavazzi, G., Fossati, M., et al. 2017, AA, 606, A83, doi: 10.1051/0004-6361/201731218

Cortese, L., Marcillac, D., Richard, J., et al. 2007, MNRAS, 376, 157, doi: 10.1111/J.1365-2966.2006.11369.X

Cowie, L. L., & Songaila, A. 1977, Nature 1977 266:5602, 266, 501, doi: 10.1038/266501a0

Cramer, W. J., Kenney, J. D. P., Sun, M., et al. 2019, ApJ, 870, 63, doi: 10.3847/1538-4357/AAEFFF

Croom, S. M., Lawrence, J. S., Bland-Hawthorn, J., et al. 2012, Monthly Notices of the Royal Astronomical Society, 421, 872, doi: 10.1111/j.1365-2966.2011.20365.x

Croom, S. M., Owers, M. S., Scott, N., et al. 2021, Monthly Notices of the Royal Astronomical Society, 505, 991, doi: 10.1093/mnras/stab229

Crowl, H. H., & Kenney, J. D. P. 2006, The Astrophysical Journal, 649, doi: 10.1086/508344

Crowl, H. H., Kenney, J. D. P., van Gorkom, J. H., et al. 2005, ASPC, 331, 281. https://ui.adsabs.harvard.edu/abs/2005ASPC..331..281C/abstract

Curti, M., Mannucci, F., Cresci, G., & Maiolino, R. 2020, Monthly Notices of the Royal Astronomical Society, 491, 944, doi: 10.1093/mnras/stz2910

Curti, M., Carniani, S., Maiolino, R., et al. 2023a, MNRAS, 518, 425, doi: 10.1093/mnras/stac2737

Curti, M., Maiolino, R., Carniani, S., et al. 2023b, ApJ. https://arxiv.org/abs/2304.08516v1

Damas-Segovia, A., Beck, R., Vollmer, B., et al. 2016, ApJ, 824, 30, doi: 10.3847/0004-637X/824/1/30

Davies, R., Baron, D., Shimizu, T., et al. 2020, MNRAS, 498, 4150, doi: 10.1093/MNRAS/STAA2413

Dessauges-Zavadsky, M., Pindao, M., Maeder, A., & Kunth, D. 1987, ApJS, 63, 295, doi: 10.1086/191166

Díaz, A. I., Terlevich, E., Vílchez, J. M., Pagel, B. E., & Edmunds, M. G. 1991, Monthly Notices of the Royal Astronomical Society, 253, 245, doi: 10.1093/MNRAS/253.2.245

Dietrich, M., Hamann, F., Shields, J. C., et al. 2003, ApJ, 589, 722, doi: 10.1086/374662

Diniz, S. I., Pastoriza, M. G., Hernandez-Jimenez, J. A., et al. 2017, Monthly Notices of the Royal Astronomical Society, 470, 1703, doi: 10.1093/mnras/stx1322

Do Nascimento, J. C., Dors, O. L., Storchi-Bergmann, T., et al. 2022, Monthly Notices of the Royal Astronomical Society, 513, 807, doi: 10.1093/MNRAS/STAC771

D'Odorico, V., Cristiani, S., Romano, D., Granato, G. L., & Danese, L. 2004, Mon. Not. R. Astron. Soc, 351, 976, doi: 10.1111/j.1365-2966.2004.07840.x

Dopita, M. A. 1997

Dopita, M. A., Kewley, L. J., Heisler, C. A., & Sutherland, R. S. 2000, The Astrophysical Journal, 542, 224, doi: 10.1086/309538/FULLTEXT/

Dopita, M. A., Sutherland, R. S., Nicholls, D. C., Kewley, L. J., & Vogt, F. P. A. 2013, The Astrophysical Journal Supplement Series, 208, 10, doi: 10.1088/0067-0049/208/1/10

Dors, O. L., Cardaci, M. V., Hägele, G. F., et al. 2015, MNRAS, 453, 4102, doi: 10.1093/mnras/stv1916

Dors, O. L., Dors, & L., O. 2021, MNRAS, 507, 466, doi: 10.1093/MNRAS/STAB2166

Dors, O. L., Maiolino, R., Cardaci, M. V., et al. 2020a, Monthly Notices of the Royal Astronomical Society, 496, 3209, doi: 10.1093/MNRAS/STAA1781

Dors, O. L., Freitas-Lemes, P., Amôres, E. B., et al. 2020b, MNRAS, 492, 468, doi: 10.1093/mnras/stz3492

Dors, O. L., Valerdi, M., Riffel, R. A., et al. 2023, Monthly Notices of the Royal Astronomical Society, 521, 1969, doi: 10.1093/mnras/stad635

Dotter, A. 2016, The Astrophysical Journal Supplement Series, 222, 8, doi: 10.3847/0067-0049/222/1/8

Dressler, A., Thompson, I. B., & Shectman, S. A. 1985, ApJ, 288, 481, doi: 10.1086/162813

Drory, N., MacDonald, N., Bershady, M. A., et al. 2015, Astronomical Journal, 149, 77, doi: 10.1088/0004-6256/149/2/77

Ebeling, H., Edge, A. C., & Henry, J. P. 2001, The Astrophysical Journal, 553, 668, doi: 10.1086/320958

Ebeling, H., Kalita, B. S., Ebeling, H., & Kalita, B. S. 2019, ApJ, 882, 127, doi: 10.3847/1538-4357/AB35D6

Ebeling, H., Stephenson, L. N., Edge, A. C., et al. 2014, ApJL, 781, L40, doi: 10.1088/2041-8205/781/2/L40

Ehlert, S., von der Linden, A., Allen, S. W., et al. 2014, MNRAS, 437, 1942, doi: 10.1093/MNRAS/STT2025

Elagali, A., Staveley-Smith, L., Rhee, J., et al. 2019, MNRAS, 487, 2797, doi: 10.1093/MNRAS/STZ1448

Ellison, S. L., Simard, L., Cowan, N. B., et al. 2009, Monthly Notices of the Royal Astronomical Society, 396, 1257, doi: 10.1111/J.1365-2966.2009.14817.X/2/M_MNRAS0396-1257-MU1.GIF

Epinat, B. 2010, International Astronomical Union, doi: 10.1017/S1743921311022617

Evans, I. N., Primini, F. A., Miller, J. B., et al. 2020, AAS, 235, 154.05. https://ui.adsabs.harvard.edu/abs/2020AAS...23515405E/abstract

Fabian, A. C., Johnstone, R. M., Sanders, J. S., et al. 2008

Fan, L., Han, Y., Fang, G., et al. 2016, The Astrophysical Journal, 822, L32, doi: 10.3847/2041-8205/822/2/l32

Fasano, G., Marmo, C., Varela, J., et al. 2006, AA, 445, 805, doi: 10.1051/0004-6361:20053816

Feltre, A., Charlot, S., & Gutkin, J. 2016, Monthly Notices of the Royal Astronomical Society, 456, 3354, doi: 10.1093/mnras/stv2794

Ferland, G. J. 1984, 286, 42

Ferland, G. J., Porter, R. L., van Hoof, P. A. M., et al. 2013, RMxAA, 49, 137. https://arxiv.org/abs/1302.4485

Ferland, G. J., Chatzikos, M., Guzmán, F., et al. 2017, RMxAA, 53, 385. http://www.chiantidatabase.org/

Fernandes, R. C., Stasinska, G., Mateus, A., & Asari, N. V. 2010, Monthly Notices of the Royal Astronomical Society

ety, Volume 413, Issue 3, pp. 1687-1699., 413, 1687, doi: 10.1111/j.1365-2966.2011.18244.x

Finoguenov, A., Briel, U. G., Henry, J. P., et al. 2004, Astronomy and Astrophysics, v.419, p.47-61 (2004), 419, 47, doi: 10.1051/0004-6361:20035765

Flury, S. R., & Moran, E. C. 2020, Monthly Notices of the Royal Astronomical Society, 496, 2191, doi: 10.1093/MNRAS/STAA1563

Fossati, M., Gavazzi, G., Boselli, A., et al. 2012, AA, 544, A128, doi: 10.1051/0004-6361/201219933

Fossati, M., Fumagalli, M., Boselli, A., et al. 2016, MNRAS, 455, 2028, doi: 10.1093/MNRAS/STV2400

Fossati, M., Mendel, J. T., Boselli, A., et al. 2018, Astronomy and Astrophysics, 614, A57, doi: 10.1051/0004-6361/201732373

Franchetto, A., Vulcani, B., Poggianti, B. M., et al. 2020, The Astrophysical Journal, 895, 106, doi: 10.3847/1538-4357/AB8DB9

Fritz, J., Moretti, A., Gullieuszik, M., et al. 2017, ApJ, 848, 132, doi: 10.3847/1538-4357/AA8F51

Fruscione, A., Gavazzi, G., Fruscione, A., & Gavazzi, G. 1990, AA, 230, 293. https://ui.adsabs.harvard.edu/abs/1990A&A...230..293F/abstract

Fumagalli, M., Gavazzi, G., Scaramella, R., et al. 2011, AA, 528, A46, doi: 10.1051/0004-6361/201015463

Fumagalli, M., Fossati, M., Hau, G. K. T., et al. 2014, MNRAS, 445, 4335, doi: 10.1093/MNRAS/STU2092

Gabor, J. M., Impey, C. D., Jahnke, K., et al. 2009, ApJ, 691, 705, doi: 10.1088/0004-637X/691/1/705

Gal, R. R., de Carvalho, R. R., Lopes, P. A. A., et al. 2003, AJ, 125, 2064, doi: 10.1086/368240

Gallagher, R., Maiolino, R., Belfiore, F., et al. 2019, MNRAS, 485, 3409, doi: 10.1093/mnras/stz564

Gaspari, M. 2016, Proceedings of the International Astronomical Union, 11, 17, doi: 10.1017/S1743921315010455

—. 2017, The Astrophysical Journal, 837, 149, doi: 10.3847/1538-4357/aa61a3

Gaspari, M., Brighenti, F., & Temi, P.

2015, Astronomy and Astrophysics, 579, A62, doi: 10.1051/0004-6361/201526151

Gaspari, M., Ruszkowski, M., & Oh, S. P. 2013, Monthly Notices of the Royal Astronomical Society, 432, 3401, doi: 10.1093/mnras/stt692

Gatti, M., Lamastra, A., Menci, N., Bongiorno, A., & Fiore, F. 2015, AA, 576, 32, doi: 10.1051/0004-6361/201425094

Gavazzi, G., Catinella, B., Carrasco, L., Boselli, A., & Contursi, A. 1998, AJ, 115, 1745, doi: 10.1086/300314

Gavazzi, G., Consolandi, G., Yagi, M., et al. 2017, AA, 606, A131, doi: 10.1051/0004-6361/201731372

Gavazzi, G., Gavazzi, & Giuseppe. 1989, ApJ, 346, 59, doi: 10.1086/167985

Gavazzi, G., O'Neil, K., Boselli, A., & van Driel, W. 2005, Astronomy and Astrophysics, Volume 449, Issue 3, April III 2006, pp.929-935, 449, 929, doi: 10.1051/0004-6361:20053844

Gavazzi, G., Tarenghi, M., Jaffe, W., et al. 1984, AA, 137, 235. https://ui.adsabs.harvard.edu/abs/1984A&A...137..235G/abstract

Gavazzi, G., Contursi, A., Carrasco, L., et al. 1995, AA, 304, 325. https://ui.adsabs.harvard.edu/abs/1995A&A...304..325G/abstract

Gavazzi, G., Boselli, A., Mayer, L., et al. 2001, ApJL, 563, L23, doi: 10.1086/338389

Gavazzi, G., Consolandi, G., Gutierrez, M. L., et al. 2018, AA, 618, A130, doi: 10.1051/0004-6361/201833427

George, K., Poggianti, B. M., Bellhouse, C., et al. 2019, MNRAS, 487, 3102, doi: 10.1093/MNRAS/STZ1443

Giovanelli, R., Haynes, M. P., Salzer, J. J., et al. 1994, AJ, 107, 2036, doi: 10.1086/117014

Giunchi, E., Gullieuszik, M., Poggianti, B. M., et al. 2023, The Astrophysical Journal, 949, 72, doi: 10.3847/1538-4357/acc5ee

Glikman, E., Glikman, & Eilat. 2012, hst, 12942. https://ui.adsabs.harvard.edu/abs/2012hst..prop12942G/abstract

Glikman, E., Simmons, B., Mailly, M., et al. 2015, Astrophysical Journal, 806, 218, doi: 10.1088/0004-637X/806/2/218

Gordon, Y. A., Pimbblet, K. A., Owers, M. S., et al. 2018, Monthly Notices of the Royal Astronomical Society, Volume 475, Issue 3, p.4223-4234, 475, 4223, doi: 10.1093/MNRAS/STY115

Gregg, M., West, M., Gregg, M., & West, M. 2017, AAS, 229, 427.07. https://ui.adsabs.harvard.edu/abs/2017AAS...22942707G/abstract

Grogin, N. A., Conselice, C. J., Chatzichristou, E., et al. 2005, ApJL, 627, L97, doi: 10.1086/432256

Groves, B. A., Heckman, T. M., & Kauffmann, G. 2006, Mon. Not. R. Astron. Soc, 371, 1559, doi: 10.1111/j.1365-2966.2006.10812.x

Gu, L., Yagi, M., Nakazawa, K., et al. 2013, ApJL, 777, L36, doi: 10.1088/2041-8205/777/2/L36

Gullieuszik, M., Poggianti, B., Fasano, G., et al. 2015, AA, 581, A41, doi: 10.1051/0004-6361/201526061

Gullieuszik, M., Poggianti, B. M., McGee, S. L., et al. 2020, ApJ, 899, 13, doi: 10.3847/1538-4357/ABA3CB

Gullieuszik, M., Giunchi, E., Poggianti, B. M., et al. 2023, The Astrophysical Journal, Volume 945, Issue 1, id.54, <NUMPAGES>13</NUMPAGES> pp., 945, 54, doi: 10.3847/1538-4357/acb59b

Gunn, J. E., Gott, J. Richard, I., Gunn, J. E., & Gott, J. Richard, I. 1972, ApJ, 176, 1, doi: 10.1086/151605

Gunn, J. E., Siegmund, W. A., Mannery, E. J., et al. 2006, AJ, 131, 2332, doi: 10.1086/500975

Gutkin, J., Charlot, S., & Bruzual, G. 2016, Monthly Notices of the Royal Astronomical Society, 462, 1757, doi: 10.1093/mnras/stw1716

Hamann, F., & Ferland, G. 1999, ARAA, 37, 487, doi: 10.1146/annurev.astro.37.1.487

Hamann, F., Ferland, G., Hamann, F., & Ferland, G. 1993, ApJ, 418, 11, doi: 10.1086/173366

Helfer, T. T., Thornley, M. D., Regan, M. W., et al. 2003, ApJS, 145, 259, doi: 10.1086/346076

Hernández-Toledo, H. M., Cortes-Suárez, E., Vázquez-Mata, J. A., et al. 2023, Monthly Notices of the Royal Astronomical Society, 523, 4164, doi: 10.1093/mnras/stad1425

Hernández-Toledo, H. M., Vázquez-Mata, J. A., Martínez-Vázquez, L. A., et al. 2010, AJ, 139, 2525, doi: 10.1088/0004-6256/139/6/2525

Hester, J. A., Seibert, M., Neill, J. D., et al. 2010, ApJL, 716, L14, doi: 10.1088/2041-8205/716/1/L14

Hickox, R. C., & Alexander, D. M. 2018, Annu. Rev. Astron. Astrophys, 56, 1, doi: 10.1146/((please)

Ho, L. C., Filippenko, A. V., & Sargent, W. L. W. 1997, The Astrophysical Journal Supplement Series, Volume 112, Issue 2, pp. 315-390., 112, 315, doi: 10.1086/313041

Hopkins, P. F., Kocevski, D. D., & Bundy, K. 2014, Monthly Notices of the Royal Astronomical Society, 445, 823, doi: 10.1093/mnras/stu1736

Hota, A., Saikia, D. J., & Irwin, J. A. 2007, MNRAS, 380, 1009, doi: 10.1111/j.1365-2966.2007.12114.x

Hwang, H. S., Park, C., Elbaz, D., & Choi, Y.-Y. 2012, Astronomy Astrophysics, 538, A15, doi: 10.1051/0004-6361/201117351

Jáchym, P., Combes, F., Cortese, L., et al. 2014, ApJ, 792, 11, doi: 10.1088/0004-637X/792/1/11

Jáchym, P., Sun, M., Kenney, J. D. P., et al. 2017, ApJ, 839, 114, doi: 10.3847/1538-4357/AA6AF5

Jáchym, P., Kenney, J. D. P., Sun, M., et al. 2019, ApJ, 883, 145, doi: 10.3847/1538-4357/AB3E6C

Jiang, J., Parker, M. L., Fabian, A. C., et al. 2018, Monthly Notices of the Royal Astronomical Society, 477, 3711, doi: 10.1093/mnras/sty836

Juneau, S., Dickinson, M., Alexander, D. M., et al. 2011, ApJ, 736, 104, doi: 10.1088/0004-637X/736/2/104

Kalita, B. S., Ebeling, H., Kalita, B. S., & Ebeling, H. 2019, ApJ, 887, 158, doi: 10.3847/1538-4357/AB5184

Kantharia, N. G., Rao, A. P., Sirothia, S. K., et al. 2008, MNRAS, 383, 173, doi: 10.1111/J.1365-2966.2007.12525.X

Kapferer, W., Sluka, C., Schindler, S., Ferrari, C., & Ziegler, B. 2009, Astronomy Astrophysics, 499, doi: 10.1051/0004-6361/200811551

Karas, V., Šubr, L., Karas, V., & Šubr, L. 2012, EPJWC, 39, 01003, doi: 10.1051/EPJCONF/20123901003

Karouzos, M., Jarvis, M. J., & Bonfield, D. 2013, MNRAS, 439, 861, doi: 10.1093/mnras/stu009

Kauffmann, G., Millán-Irigoyen, I., Crowther, P., & Maraston, C. 2023, Monthly Notices of the Royal Astronomical Society, 527, 150, doi: 10.1093/mnras/stad3096

Kauffmann, G., White, S. D. M., Heckman, T. M., et al. 2004, MNRAS, 353, 713, doi: 10.1111/J.1365-2966.2004.08117.X

Kauffmann, G., Heckman, T. M., Tremonti, C., et al. 2003, MNRAS, 346, 1055, doi: 10.1111/J.1365-2966.2003.07154.X

Kenney, J. D., Abramson, A., & Bravo-Alfaro, H. 2015, Astronomical Journal, 150, doi: 10.1088/0004-6256/150/2/59

Kenney, J. D. P., Rubin, V. C., Planesas, P., & Young, J. S. 1995, The Astrophysical Journal, 438, 135, doi: 10.1086/175060

Kenney, J. D. P., van Gorkom, J. H., Vollmer, B., et al. 2004, AJ, 127, 3361, doi: 10.1086/420805

Kenney, J. D. P., Tal, T., Crowl, H. H., et al. 2008, ApJL, 687, L69, doi: 10.1086/593300

Kenney, J. D. P., Geha, M., Jáchym, P., et al. 2014, ApJ, 780, 119, doi: 10.1088/0004-637X/780/2/119

Kennicutt, R. C. 1998, https://doi.org/10.1146/annurev.astro.36.1.189, 36, 189, doi: 10.1146/ANNUREV.ASTRO.36.1.189

Kewley, L. J., & Ellison, S. L. 2008, The Astrophysical Journal, 681, 1183, doi: 10.1086/587500

Kewley, L. J., Groves, B., Kauffmann, G., & Heckman, T. 2006, Monthly Notices of the Royal Astronomical Society, 372, 961, doi: 10.1111/j.1365-2966.2006.10859.x

Kewley, L. J., Nicholls, D. C., Sutherland, R., et al. 2019a, ApJ, doi: 10.3847/1538-4357/ab16ed

Kewley, L. J., Nicholls, D. C., & Sutherland, R. S. 2019b, Australia Annu. Rev. Astron. Astrophys, 57, 511, doi: 10.1146/annurev-astro-081817

Kewley, L. J., Dopita, M. A., Sutherland, R. S., et al. 2001, ApJ, 556, 121, doi: 10.1086/321545

King, A., & Pounds, K. 2015, Annual Review of Astronomy and Astrophysics, 53, 115, doi: 10.1146/annurev-astro-082214-122316

Kocevski, D. D., Faber, S. M., Mozena, M., et al. 2012, Astrophysical Journal, 744, 148, doi: 10.1088/0004-637X/744/2/148

Kormendy, J., Ho, L. C., Kormendy, J., & Ho, L. C. 2013, ARAA, 51, 511, doi: 10.1146/ANNUREV-ASTRO-082708-101811

Koss, M., Mushotzky, R., Veilleux, S., & Winter, L. 2010, Astrophysical Journal Letters, 716, L125, doi: 10.1088/2041-8205/716/2/L125

Koulouridis, E., Ricci, M., Giles, P., et al. 2018, AA, 620, A20, doi: 10.1051/0004-6361/201832974

Kronberger, T., Kapferer, W., Ferrari, C., Unterguggenberger, S., & Schindler, S. 2008, Astronomy Astrophysics, 481, doi: 10.1051/0004-6361:20078904

Krumholz, M. R., Fumagalli, M., da Silva, R. L., Rendahl, T., & Parra, J. 2015, Monthly Notices of the Royal Astronomical Society, 452, 1447, doi: 10.1093/mnras/stv1374

Lai, T., Bianchin, M., Remigio, R. P., et al. 2022. https://arxiv.org/abs/2209.01210v2

Larson, R. B. 1974, Monthly Notices of the Royal Astronomical Society, 169, 229, doi: 10.1093/MNRAS/169.2.229

Larson, R. B., & Dinerstein, H. L. 1975, Publications of the Astronomical Society of the Pacific, 87, 911, doi: 10.1086/129870

Larson, R. B., Tinsley, B. M., & Caldwell, C. N. 1980, The Astrophysical Journal, 237, 692

Laudari, S., Av el, P. J., Sun, M., et al. 2022, MNRAS, 509, 3938, doi: 10.1093/mnras/stab3280

Law, D. R., Yan, R., Bershady, M. A., et al. 2015, Astronomical Journal, 150, 19, doi: 10.1088/0004-6256/150/1/19

Law, D. R., Cherinka, B., Yan, R., et al. 2016, AJ, 152, 83, doi: 10.3847/0004-6256/152/4/83

Law, D. R., Ji, X., Belfiore, F., et al. 2021, ApJ, 915, 35, doi: 10.3847/1538-4357/ABFE0A

Lee, B., Chung, A., Lee, B., & Chung, A. 2018, ApJL, 866, L10, doi: 10.3847/2041-8213/AAE4D9

Lee, B., Chung, A., Tonnesen, S., et al. 2017, Monthly Notices of the Royal Astronomical Society, 466, 1382, doi: 10.1093/mnras/stw3162

Lehmer, B. D., Brandt, W. N., Alexander, D. M., et al. 2007, The Astrophysical Journal, Volume 657, Issue 2, pp. 681-699., 657, 681, doi: 10.1086/511297

Lejeune, T., Cuisinier, F., & Buser, R. 1997, Astronomy and Astrophysics Supplement Series, 125, 229, doi: 10.1051/aas:1997373

Lequeux, J., Peimbert, M., Rayo, J. F., et al. 1979, AA, 80, 155. https://ui.adsabs.harvard.edu/abs/1979A&A....80..155L/abstract

Livio, M., Regev, O., Shaviv, G., et al. 1980, ApJL, 240, L83, doi: 10.1086/183328

Lopes, P. A. A., Ribeiro, A. L. B., Rembold, S. B., et al. 2017, MNRAS, 472, 409, doi: 10.1093/MNRAS/STX2046

López-Cobá, C., Sánchez, S. F., Anderson, J. P., et al. 2020, The Astronomical Journal, 159, 167, doi: 10.3847/1538-3881/ab7848

Magliocchetti, M., Popesso, P., Brusa, M., & Salvato, M. 2018, agn, 13, 26, doi: 10.5281/ZENODO.1472829

Magliocchetti, M., Pentericci, L., Cirasuolo, M., et al. 2020, MNRAS, 493, 3838, doi: 10.1093/MNRAS/STAA410

Mahajan, S., Haines, C. P., Raychaudhury, S., et al. 2010, MNRAS, 404, 1745, doi: 10.1111/J.1365-2966.2010.16432.X

Maier, C., Ziegler, B. L., Haines, C. P., & Smith, G. P. 2019, Astronomy and Astrophysics, 621, A131, doi: 10.1051/0004-6361/201834290

Maiolino, R., & Mannucci, F. 2019, De re metallica: the cosmic chemical evolution of galaxies, doi: 10.1007/s00159-018-0112-2

Maiolino, R., Russell, H. R., Fabian, A. C., et al. 2017, Nature 2017 544:7649, 544, 202, doi: 10.1038/nature21677

Malina, R. F., Bowyer, S. C., International Astronomical Union. Commission 29., International Astronomical Union. Commission 44., & International Astronomical Union. Commission 48. 1991, eua, 341. https://ui.adsabs.harvard.edu/abs/1991eua..coll..341M/abstract

Man, Z.-y., Peng, Y.-j., Kong, X., et al. 2019, MNRAS, 488, 89, doi: 10.1093/MNRAS/STZ1706

Mannucci, F., Cresci, G., Maiolino, R., Marconi, A., & Gnerucci, A. 2010, Mon. Not. R. Astron. Soc, 408, 2115, doi: 10.1111/j.1365-2966.2010.17291.x

Martini, P., Mulchaey, J. S., Kelson, D. D., et al. 2007, ApJ, 664, 761, doi: 10.1086/519158

Martini, P., Miller, E. D., Brodwin, M., et al. 2013, ApJ, 768, 1, doi: 10.1088/0004-637X/768/1/1

Marziani, P., D'Onofrio, M., Bettoni, D., et al. 2017, Astronomy Astrophysics, 599, A83, doi: 10.1051/0004-6361/201628941

Mastropietro, C., Moore, B., Mayer, L., et al. 2005, MNRAS, 364, 607, doi: 10.1111/J.1365-2966.2005.09579.X

Mathews, W. G., Ferland, G. J., Mathews, W. G., & Ferland, G. J. 1987, ApJ, 323, 456, doi: 10.1086/165843

Mathis, J. S., Rumpl, W., Nordsieck, K. H., et al. 1977, ApJ, 217, 425, doi: 10.1086/155591

Matsuoka, K., Nagao, T., Marconi, A., et al. 2018, AA, 616, 4, doi: 10.1051/0004-6361/201833418

Matsuoka, K., Nagao, T., Marconi, A., Maiolino, R., & Taniguchi, Y. 2010, AA, 527, A100, doi: 10.1051/0004-6361/201015584

McPartland, C., Ebeling, H., Roediger, E., et al. 2016, MNRAS, 455, 2994, doi: 10.1093/MNRAS/STV2508

Mechtley, M., Jahnke, K., Windhorst, R. A., et al. 2016, The Astrophysical Journal, 830, 156, doi: 10.3847/0004-637x/830/2/156

Menci, N., Gatti, M., Fiore, F., & Lamastra, A. 2014, AA, 569, A37, doi: 10.1051/0004-6361/201424217

Mendel, J. T., Simard, L., Palmer, M., et al. 2014, yCat, J/ApJS/210/3. https://ui.adsabs.harvard.edu/abs/2014yCat..22100003M/abstract

Merluzzi, P., Mercurio, A., Haines, C. P., et al. 2010, MNRAS, 402, 753, doi: 10.1111/J.1365-2966.2009.15929.X

Merluzzi, P., Busarello, G., Dopita, M. A., et al. 2013, MNRAS, 429, 1747, doi: 10.1093/MNRAS/STS466

—. 2016, MNRAS, 460, 3345, doi: 10.1093/MNRAS/STW1198

Merritt, D., Merritt, & D. 1984, ApJ, 276, 26, doi: 10.1086/161590

Miller, C. J., Nichol, R. C., Gomez, P., Hopkins, A., & Bernardi, M. 2003, The Astrophysical Journal, 597, 142, doi: 10.1086/378383

Miller, L. 1986, MNRAS, 220, 713, doi: 10.1093/MNRAS/220.3.713

Miller, N. A., Hornschemeier, A. E., Mobasher, B., et al. 2009, AJ, 137, 4436, doi: 10.1088/0004-6256/137/5/4436

Minchin, R. F., Taylor, R., Köppen, J., et al. 2019, AJ, 158, 121, doi: 10.3847/1538-3881/AB303E

Mingozzi, M., Belfiore, F., Cresci, G., et al. 2020, AA, 636, 42, doi: 10.1051/0004-6361/201937203

Moore, B., Katz, N., Lake, G., Dressler, A., & Oemler, A. 1996, Nature 1996 379:6566, 379, 613, doi: 10.1038/379613a0

Moore, B., Lake, G., & Katz, N. 1997, ApJ, 495, 139, doi: 10.1086/305264

Moretti, A., Poggianti, B. M., Gullieuszik, M., et al. 2018, MNRAS, 475, 4055, doi: 10.1093/mnras/sty085

Moustakas, J., & Kennicutt, R. C. 2006, ApJ, 651, 155, doi: 10.1086/507570

Nagao, T., Maiolino, R., & Marconi, A. 2006, Astronomy and Astrophysics, 447, 863, doi: 10.1051/0004-6361:20054127

Navarro, J. F., Frenk, C. S., White, S. D. M., et al. 1997, ApJ, 490, 493, doi: 10.1086/304888

Nayakshin, S., & Sunyaev, R. 2005, Monthly Notices of the Royal Astronomical Society: Letters, 364, L23, doi: 10.1111/J.1745-3933.2005.00097.X

Nicholls, D. C., Dopita, M. A., & Sutherland, R. S. 2012, The Astrophysical Journal, 752, 148, doi: 10.1088/0004-637X/752/2/148

Nicholls, D. C., Sutherland, R. S., Dopita, M. A., Kewley, L. J., & Groves, B. A. 2017, Monthly Notices of the Royal Astronomical Society, 466, 4403, doi: 10.1093/mnras/stw3235

Nucita, A. A., Manni, L., De Paolis, F., et al. 2017, ApJ, 837, 66, doi: 10.3847/1538-4357/AA5F4F

Nulsen, P. E. J., Nulsen, & J., P. E. 1982, MNRAS, 198, 1007, doi: 10.1093/MNRAS/198.4.1007

O'Donnell, J. E., O'Donnell, & E., J. 1994, ApJ, 422, 158, doi: 10.1086/173713

Oh, K., Koss, M. J., Ueda, Y., et al. 2022, The Astrophysical Journal Supplement Series, 261, 4, doi: 10.3847/1538-4365/AC5B68

Oosterloo, T., Morganti, R., & Murthy, S. 2023. https://arxiv.org/abs/2312.00917v1

Oosterloo, T., van Gorkom, J., Oosterloo, T., & van Gorkom, J. 2005, AA, 437, L19, doi: 10.1051/0004-6361:200500127

Osterbrock, D. E. 2006, Astrophysics of gaseous nebulae and active galactic nuclei. 2006agna.book.....O

Owen, F. N., Keel, W. C., Wang, Q. D., et al. 2006, AJ, 131, 1974, doi: 10.1086/500573

Owers, M. S., Couch, W. J., Nulsen, P. E. J., et al. 2012, ApJL, 750, L23, doi: 10.1088/2041-8205/750/1/L23

Pace, Z. J., Tremonti, C., Chen, Y., et al. 2019a, ApJ, doi: 10.3847/1538-4357/ab3723

—. 2019b, The Astrophysical Journal, 883, 83, doi: 10.3847/1538-4357/ab3726

Padovani, P. 1997, Memorie della Societa Astronomica Italiana, Vol. 68, p. 47-54 (1997), 68, 47, doi: 10.48550/ARXIV.ASTRO-PH/9701074

Padovani, P., Padovani, & Paolo. 2017, FrASS, 4, 35, doi: 10.3389/FSPAS.2017.00035

Peluso, G., Radovich, M., Moretti, A., et al. 2023, ApJ, 958, 147, doi: 10.3847/1538-4357/acf833

Peluso, G., Vulcani, B., Poggianti, B. M., et al. 2022, ApJ, doi: 10.3847/1538-4357/ac4225

Peng, Y., Maiolino, R., & Cochrane, R. 2015, Natur, 521, 192, doi: 10.1038/nature14439

Peng, Y.-J., & Maiolino, R. 2014, MNRAS, 438, 262, doi: 10.1093/mnras/stt2175

Pérez-Díaz, B., Masegosa, J., Márquez, I., & Pérez-Montero, E. 2021, MNRAS, 505, 4289, doi: 10.1093/mnras/stab1522

Pérez-Díaz, B., Pérez-Montero, E., Fernández-Ontiveros, J. A., Vílchez, J. M., & Amorín, R. 2023. https://arxiv.org/abs/2306.14843v1

Pérez-Montero, E. 2014, MNRAS, 441, 2663, doi: 10.1093/mnras/stu753

Pérez-Montero, E., & Contini, T. 2009a, Monthly Notices of the Royal Astronomical Society, 398, 949, doi: 10.1111/J.1365-2966.2009.15145.X/2/MNRAS0398-0949-F13.JPEG

—. 2009b, Monthly Notices of the Royal Astronomical Society, 398, 949, doi: 10.1111/j.1365-2966.2009.15145.x

Pérez-Montero, E., Dors, O. L., Vílchez, J. M., et al. 2019, MNRAS, 489, 2652, doi: 10.1093/mnras/stz2278

Pérez-Montero, E., Contini, T., Lamareille, F., et al. 2013, Astronomy Astrophysics, 549, A25, doi: 10.1051/0004-6361/201220070

Pettini, M., & Pagel, B. E. 2004, Monthly Notices of the Royal Astronomical Society, 348, L59, doi: 10.1111/j.1365-2966.2004.07591.x

Pimbblet, K. A., Shabala, S. S., Haines, C. P., Fraser-McKelvie, A., & Floyd, D. J. 2013, Monthly Notices of the Royal Astronomical Society, 429, 1827, doi: 10.1093/mnras/sts470

Poggianti, B. M., Fasano, G., Omizzolo, A., et al. 2016, yCat, J/AJ/151/78. https://ui.adsabs.harvard.edu/abs/2016yCat..51510078P/abstract

Poggianti, B. M., Moretti, A., Gullieuszik, M., et al. 2017a, The Astrophysical Journal, 844, 48, doi: 10.3847/1538-4357/AA78ED

Poggianti, B. M., Jaffé, Y. L., Moretti, A., et al. 2017b, Natur, 548, 304, doi: 10.1038/NATURE23462

Poggianti, B. M., Gullieuszik, M., Tonnesen, S., et al. 2019, MNRAS, 482, 4466, doi: 10.1093/MNRAS/STY2999

Popesso, P., & Biviano, A. 2006, AA, 460, L23, doi: 10.1051/0004-6361:20066269

Radovich, M., Poggianti, B., Jaffé, Y. L., et al. 2019, MNRAS, 486, 486, doi: 10.1093/MNRAS/STZ809

Rahman, N., Bolatto, A. D., Wong, T., et al. 2011, ApJ, 730, 72, doi: 10.1088/0004-637X/730/2/72

Rakshit, S., Stalin, C. S., Chand, H., et al. 2017, yCat, J/ApJS/229/39. https://ui.adsabs.harvard.edu/abs/2017yCat..22290039R/abstract

Ramos-Martínez, M., Gómez, G. C., & Pérez-Villegas, Á. 2018, MNRAS, 476, 3781, doi: 10.1093/MNRAS/STY393

Rawle, T. D., Altieri, B., Egami, E., et al. 2014, MNRAS, 442, 196, doi: 10.1093/MNRAS/STU868

Reines, A. E., & Volonteri, M. 2015, Astrophysical Journal, 813, doi: 10.1088/0004-637X/813/2/82

Ricarte, A., Tremmel, M., Natarajan, P., et al. 2020, ApJL, 895, L8, doi: 10.3847/2041-8213/AB9022

Riffel, R. A., Dors, O. L., Armah, M., et al. 2021, Monthly Notices of the Royal Astronomical Society: Letters, 501, L54, doi: 10.1093/mnrasl/slaa194

Roberts, I. D., Parker, L. C., Roberts, I. D., & Parker, L. C. 2020, MNRAS, 495, 554, doi: 10.1093/MNRAS/STAA1213

Roediger, E., & Hensler, G. 2008, AA, 483, 121, doi: 10.1051/0004-6361:200809438

Roman-Oliveira, F. V., Chies-Santos, A. L., del Pino, B. R., et al. 2018, Monthly Notices of the Royal Astronomical Society, 484, 892, doi: 10.1093/mnras/stz007

Ruszkowski, M., Brüggen, M., Lee, D., & Shin, M. S. 2014, Astrophysical Journal, 784, doi: 10.1088/0004-637X/784/1/75

Sabater, J., Best, P. N., & Argudo-Fernández, M. 2013, MNRAS, 430, 638, doi: 10.1093/MNRAS/STS675

Salim, S., Boquien, M., Lee, J. C., et al. 2018, ApJ, 859, 11, doi: 10.3847/1538-4357/AABF3C

Salim, S., Lee, J. C., Janowiecki, S., et al. 2016, ApJS, 227, 2, doi: 10.3847/0067-0049/227/1/2

Salpeter, E. E., Salpeter, & E., E. 1955, ApJ, 121, 161, doi: 10.1086/145971

Sánchez, S. F., Kennicutt, R. C., Gil De Paz, A., et al. 2010, Proceedings of the 9th Scientific Meeting of the Spanish Astronomical Society - Highlights of Spanish Astrophysics VI, SEA 2010, 851. https://arxiv.org/abs/1012.3002

—. 2012, Astronomy and Astrophysics, 538, A8, doi: 10.1051/0004-6361/201117353

Sánchez, S. F., Perez, E., Sánchez-Blazquez, P., et al. 2016, Revista Mexicana de Astronomia y Astrofisica, 52, 21. https://arxiv.org/abs/1509.08552

Sánchez, S. F., Avila-Reese, V., Hernandez-Toledo, H., et al. 2018, Revista Mexicana de Astronomia y Astrofisica, 54, 217. https://arxiv.org/abs/1709.05438

Satyapal, S., Ellison, S. L., McAlpine, W., et al. 2014, Monthly Notices of the Royal Astronomical Society, 441, 1297, doi: 10.1093/mnras/stu650

Schlegel, D. J., Schlegel=durham, D. J. A., And, D. P., & Davis, M. F. 1998, THE ASTROPHYSICAL JOURNAL, 500, 525

Schmutz, W., Leitherer, C., Gruenwald, R., et al. 1992, PASP, 104, 1164, doi: 10.1086/133104

Schulz, S., & Struck, C. 2001, MNRAS, 328, 185, doi: 10.1046/J.1365-8711.2001.04847.X

Scott, T. C., Usero, A., Brinks, E., et al. 2013, Monthly Notices of the Royal Astronomical Society, 429, 221, doi: 10.1093/mnras/sts328

Scott, T. C., Bravo-Alfaro, H., Brinks, E., et al. 2010, Monthly Notices of the Royal Astronomical Society, Volume 403, Issue 3, pp. 1175-1192., 403, 1175, doi: 10.1111/J.1365-2966.2009.16204.X

SDSS. 2004, Galaxy Properties for DR8 spectra from MPA-JHU | SDSS. https://www.sdss.org/dr12/spectro/galaxy_mpajhu/

Shapley, A. E., Reddy, N. A., Sanders, R. L., Topping, M. W., & Brammer, G. B. 2023, The Astrophysical Journal Letters, 950, L1, doi: 10.3847/2041-8213/acd939

Sharp, R., Saunders, W., Smith, G., et al. 2006, Ground-based and Airborne Instrumentation for Astronomy, 6269, 62690G, doi: 10.1117/12.671022

Sharp, R. G., Bland-Hawthorn, J., Sharp, R. G., & Bland-Hawthorn, J. 2010, ApJ, 711, 818, doi: 10.1088/0004-637X/711/2/818

Silverman, J. D., & David, J. 2015, IAUGA, 29, 2246407. https://ui.adsabs.harvard.edu/abs/2015IAUGA..2246407S/abstract

Silverman, J. D., Kovač, K., Knobel, C., et al. 2009, The Astrophysical Journal, 695, 171, doi: 10.1088/0004-637X/695/1/171

Simon, L. E., & Hamann, F. 2010, Monthly Notices of the Royal Astronomical Society, 409, 269, doi: 10.1111/J.1365-2966.2010.17306.X/3/M_MNRAS0409-0269-MU17.GIF

Sirianni, M., Jee, M. J., Benitez, N., et al. 2005, PASP, 117, 1049, doi: 10.1086/444553

Sivakoff, G. R., Martini, P., Zabludoff, A. I., et al. 2008, ApJ, 682, 803, doi: 10.1086/589686

Sivanandam, S., Rieke, M. J., & Rieke, G. H. 2010, The Astrophysical Journal, Volume 717, Issue 1, pp. 147-162 (2010)., 717, 147, doi: 10.1088/0004-637X/717/1/147

Sivanandam, S., Rieke, M. J., Rieke, G. H., et al. 2014, ApJ, 796, 89, doi: 10.1088/0004-637X/796/2/89

Smee, S. A., Gunn, J. E., Uomoto, A., et al. 2013, AJ, 146, 32, doi: 10.1088/0004-6256/146/2/32

Smith, R. J., Lucey, J. R., Hammer, D., et al. 2010, Monthly Notices of the Royal Astronomical Society, 408, 1417, doi: 10.1111/J.1365-2966.2010.17253.X

Sobral, D., Stroe, A., Dawson, W. A., et al. 2015, MNRAS, 450, 630, doi: 10.1093/MNRAS/STV521

Stasińska, G., Cid Fernandes, R., Mateus, A., Sodré, L., & Asari, N. V. 2006, Monthly Notices of the Royal Astronomical Society, 371, 972, doi: 10.1111/j.1365-2966.2006.10732.x

Stein, Y., Bomans, D. J., Ferguson, A. M. N., et al. 2017, AA, 605, A5, doi: 10.1051/0004-6361/201730589

Storchi-Bergmann, T., Schmitt, H. R., Calzetti, D., & Kinney, A. L. 1998, AJ, 115, 909, doi: 10.1086/300242

Storchi-Bergmann, T., & Schnorr-Müller, A. 2019, Nature Astronomy, 3, 48, doi: 10.1038/s41550-018-0611-0

Stroe, A., Sobral, D., Harwood, J., et al. 2015, AAS, 225, 304.02. https://ui.adsabs.harvard.edu/abs/2015AAS...22530402S/abstract

Stroe, A., Hussaini, M., Husemann, B., et al. 2020, ApJL, 905, L22, doi: 10.3847/2041-8213/ABCB04

Sun, M., Donahue, M., & Voit, G. M. 2007, The Astrophysical Journal, Volume 671, Issue 1, pp. 190-202., 671, 190, doi: 10.1086/522690

Sun, M., & Vikhlinin, A. 2004, ApJ, 621, 718, doi: 10.1086/427728

Sun, M., Vikhlinin, A., Sun, M., & Vikhlinin, A. 2005, ApJ, 621, 718, doi: 10.1086/427728

Sun, M., Jones, C., Forman, W., et al. 2006, ApJL, 637, L81, doi: 10.1086/500590

Sun, M., Donahue, M., Roediger, E., et al. 2010, ApJ, 708, 946, doi: 10.1088/0004-637X/708/2/946

Sutherland, R. S., & Dopita, M. A. 2017, ApJS, doi: 10.3847/1538-4365/aa6541

Temi, P., Amblard, A., Gitti, M., et al. 2018, The Astrophysical Journal, 858, 17, doi: 10.3847/1538-4357/aab9b0

Tempel, E., Tamm, A., Gramann, M., et al. 2014, yCat, J/A+A/566/A1. https://ui.adsabs.harvard.edu/abs/2014yCat..35660001T/abstract

Thomas, A. D., Dopita, M. A., Kewley, L. J., et al. 2018a, The Astrophysical Journal, 856, 89, doi: 10.3847/1538-4357/aab3db

Thomas, A. D., Groves, B. A., Sutherland, R. S., et al. 2016, The Astrophysical Journal, 833, 266, doi: 10.3847/1538-4357/833/2/266

Thomas, A. D., Kewley, L. J., Dopita, M. A., et al. 2018b, The Astrophysical Journal, 861, L2, doi: 10.3847/2041-8213/aacce7

—. 2019, The Astrophysical Journal, 874, 100, doi: 10.3847/1538-4357/ab08a1

Toba, Y., Oyabu, S., Matsuhara, H., et al. 2014, ApJ, 788, 45, doi: 10.1088/0004-637X/788/1/45

Tonnesen, S., Bryan, G. L., Tonnesen, S., & Bryan, G. L. 2009, ApJ, 694, 789, doi: 10.1088/0004-637X/694/2/789

Tonnesen, S., Bryan, G. L., & van Gorkom, J. H. 2007, The Astrophysical Journal, 671, 1434, doi: 10.1086/523034

Treister, E., Schawinski, K., Urry, C. M., & Simmons, B. D. 2012, ApJL, 758, L39, doi: 10.1088/2041-8205/758/2/L39

Tremonti, C. A., Heckman, T. M., Kauffmann, G., et al. 2004, The Astrophysical Journal, 613, 898, doi: 10.1086/423264/FULLTEXT/

Tschöke, D., Bomans, D. J., Hensler, G., et al. 2001, AA, 380, 40, doi: 10.1051/0004-6361:20011354

Urrutia, T., Lacy, M., & Becker, R. H. 2008, The Astrophysical Journal, 674, doi: 10.1086/523959

Valluri, M. 1993, BASI, 21, 377. https://ui.adsabs.harvard.edu/abs/1993BASI...21..377V/abstract

—. 1994, ApJ, 430, 101, doi: 10.1086/174385

Van Den Bosch, F. C., Aquino, D., Yang, X., et al. 2008, Monthly Notices of the Royal Astronomical Society, 387, 79, doi: 10.1111/j.1365-2966.2008.13230.x

Van Hoof, P. A. M., Weingartner, . C., Martin, . G., Volk, K., & Ferland, G. J. 2004, Mon. Not. R. Astron. Soc, 350, 1330, doi: 10.1111/j.1365-2966.2004.07734.x

van Hoof, P. A. M., Weingartner, J. C., Martin, P. G., et al. 2001, ASPC, 247, 363, doi: 10.48550/ARXIV.ASTRO-PH/0107183

Van Loon, M. L., Mitchell, P. D., & Schaye, J. 2021, MNRAS, 504, 4817, doi: 10.1093/mnras/stab1254

Veilleux, S., Cecil, G., & Bland-Hawthorn, J. 2005, Annual Review of Astronomy and Astrophysics, 43, 769, doi: 10.1146/annurev.astro.43.072103.150610

Veilleux, S., & Osterbrock, D. E. 1987, The Astrophysical Journal Supplement Series, 63, 295

Veron-Cetty, M. P., Veron, P., Veron-Cetty, M. P., & Veron, P. 2003, yCat, VII/235. https://ui.adsabs.harvard.edu/abs/2003yCat.7235....0V/abstract

—. 2006, yCat, 7248, 0. https://ui.adsabs.harvard.edu/abs/2006yCat.7248....0V/abstract

Vieser, W., & Hensler, G. 2007, Astronomy and Astrophysics, 472, 141, doi: 10.1051/0004-6361:20042120

Villforth, C., Hamann, F., Rosario, D. J., et al. 2014, Monthly Notices of the Royal Astronomical Society, 439, 3342, doi: 10.1093/mnras/stu173

Villforth, C., Hamilton, T., Pawlik, M. M., et al. 2017, Monthly Notices of the Royal Astronomical Society, 466, 812, doi: 10.1093/mnras/stw3037

Vollmer, B., Beck, R., Kenney, J. D. P., et al. 2004, AJ, 127, 3375, doi: 10.1086/420802

Vollmer, B., Cayatte, V., Balkowski, C., & Duschl, W. J. 2001, The Astrophysical Journal, 561, 708, doi: 10.1086/323368

Vollmer, B., Soida, M., Beck, R., et al. 2007, AA, 464, L37, doi: 10.1051/0004-6361:20066980

Vollmer, B., Soida, M., Chung, A., et al. 2008, AA, 483, 89, doi: 10.1051/0004-6361:20078139

Vollmer, B., Vollmer, & B. 2003, AA, 398, 525, doi: 10.1051/0004-6361:20021729

Vollmer, B., Soida, M., Chung, A., et al. 2009, AA, 496, 669, doi: 10.1051/0004-6361/200811140

Von der Linden, A., Wild, V., Kauffmann, G., White, S. D. M., & Weinmann, S. 2010, Monthly Notices of the Royal Astronomical Society, Volume 404, Issue 3, pp. 1231-1246., 404, 1231, doi: 10.1111/J.1365-2966.2010.16375.X

Vulcani, B., Poggianti, B. M., Smith, R., et al. 2022, The Astrophysical Journal, 927, 91, doi: 10.3847/1538-4357/ac4809

Vulcani, B., Poggianti, B. M., Gullieuszik, M., et al. 2018, ApJ, doi: 10.3847/2041-8213/aae68b

Vulcani, B., Poggianti, B. M., Tonnesen, S., et al. 2020, The Astrophysical Journal, 899, 98, doi: 10.3847/1538-4357/ABA4AE

Vulcani, B., Poggianti, B. M., Moretti, A., et al. 2021, ApJ, doi: 10.3847/1538-4357/abf655

Vulcani, B., Moretti, A., Poggianti, B. M., et al. 2023, eprint arXiv:2311.13486, arXiv:2311.13486, doi: 10.48550/ARXIV.2311.13486

W. J., C., J. D. P., K., J. R., C., et al. 2020, The Astrophysical Journal, 901, 95, doi: 10.3847/1538-4357/abaf54

Wake, D. A., Bundy, K., Diamond-Stanic, A. M., et al. 2017, The Astronomical Journal, 154, 86, doi: 10.3847/1538-3881/aa7ecc

Wang, H., Zhou, H., Yuan, W., & Wang, T. 2012, ApJL, 751, L23, doi: 10.1088/2041-8205/751/2/L23

Wang, J., Xu, W., Lee, B., et al. 2020, ApJ, 903, 103, doi: 10.3847/1538-4357/ABB9AA

Webb, N. A., Coriat, M., Traulsen, I., et al. 2020, yCat, IX/59. https://ui.adsabs.harvard.edu/abs/2020yCat.9059....0W/abstract

Werle, A., Poggianti, B., Moretti, A., et al. 2022, The Astrophysical Journal, 930, 43, doi: 10.3847/1538-4357/ac5f06

Westfall, K. B., Cappellari, M., Bershady, M. A., et al. 2019, The Astronomical Journal, 158, 231, doi: 10.3847/1538-3881/AB44A2

Weżgowiec, M., Bomans, D. J., Ehle, M., et al. 2012, AA, 544, A99, doi: 10.1051/0004-6361/201117652

Winkler, H., Winkler, & H. 1992, MNRAS, 257, 677, doi: 10.1093/MNRAS/257.4.677

Xu, F., Bian, F., Shen, Y., et al. 2018, Monthly Notices of the Royal Astronomical Society, 480, 345, doi: 10.1093/MNRAS/STY1763

Yagi, M., Komiyama, Y., Yoshida, M., et al. 2001, ApJ, 561, 708, doi: 10.1086/323368

Yagi, M., Yoshida, M., Komiyama, Y., et al. 2010, AJ, 140, 1814, doi: 10.1088/0004-6256/140/6/1814

Yagi, M., Gu, L., Fujita, Y., et al. 2013, ApJ, 778, 91, doi: 10.1088/0004-637X/778/2/91

Yagi, M., Yoshida, M., Gavazzi, G., et al. 2017, ApJ, 839, 65, doi: 10.3847/1538-4357/AA68E3

Yan, R., Bundy, K., Law, D. R., et al.

2016, The Astronomical Journal, 152, 197, doi: 10.3847/0004-6256/152/6/197

Yoshida, M., Yagi, M., Okamura, S., et al. 2002, ApJ, 567, 118, doi: 10.1086/338353

—. 2004, IAUS, 217, 386. https://ui.adsabs.harvard.edu/abs/2004IAUS..217..386Y/abstract

Yoshida, M., Yagi, M., Komiyama, Y., et al. 2012, ApJ, 749, 43, doi: 10.1088/0004-637X/749/1/43

Zhang, B., Sun, M., Ji, L., et al. 2013, ApJ, 777, 122, doi: 10.1088/0004-637X/777/2/122